A molecular dynamics investigation of tetrahedral liquids and aqueous solutions in bulk (SiO_2) and confinements (SiO_2, H_2O, water-octanol mixtures)

Molekulardynamische Untersuchung von tetrahedralen netzwerken und wässrigen Lösungen im Bulk und unter geometrischen Einschränkungen

Zur Erlangung des Grades eines Doktors der Naturwissenschaften (Dr. rer. nat.)
genehmigte Dissertation von M.Sc. Elvira Sanjon aus Yaounde, Kamerun
Tag der Einreichung: 10.07.2018, Tag der Prüfung: 29.10.2018
Darmstadt — D 17

1. Gutachten: Prof. Dr. Barbara Drossel
2. Gutachten: Prof. Dr. Michael Vogel

TECHNISCHE UNIVERSITÄT DARMSTADT

Fachbereich Physik
Institut für Festkörperphysik

A molecular dynamics investigation of tetrahedral liquids and aqueous solutions in bulk (SiO_2) and confinements (SiO_2, H_2O, water-octanol mixtures)
Molekulardynamische Untersuchung von tetrahedralen netzwerken und wässrigen Lösungen im Bulk und unter geometrischen Einschränkungen

Genehmigte Dissertation von M.Sc. Elvira Sanjon aus Yaounde, Kamerun

1. Gutachten: Prof. Dr. Barbara Drossel
2. Gutachten: Prof. Dr. Michael Vogel

Tag der Einreichung: 10.07.2018
Tag der Prüfung: 29.10.2018

Darmstadt — D 17

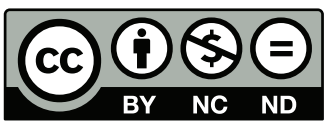

Erklärung zur Dissertation

Hiermit versichere ich, die vorliegende Dissertation ohne Hilfe Dritter nur mit den angegebenen Quellen und Hilfsmitteln angefertigt zu haben. Alle Stellen, die aus Quellen entnommen wurden, sind als solche kenntlich gemacht. Diese Arbeit hat in gleicher oder ähnlicher Form noch keiner Prüfungsbehörde vorgelegen.

Darmstadt, den 17.12.2018

(Elvira Sanjon)

’I saw that wisdom is better than folly,
just as light is better than darkness.
The wise have eyes in their heads,
while the fool walks in the darkness;
but I came to realize that the same fate overtakes them both.
Then I said to myself,
"The fate of the fool will overtake me also. What then do I gain by being wise?"
I said to myself, "this too is meaningless." ’

(Ecclesiastes 2: 13-15)

Abstract

Water is an essential material in our everyday life and is the solvent mostly used for chemical and biological reactions. In particular, water in living cells are surrounded by macromolecules and behaves as a confined fluid. Confined water does not only occur in biology but also in geology for example in porous rocks, or in technology as for example nanofluidic devices. For all these systems, an understanding of the transport mechanism of water is necessary. Water molecules are highly polar and can form hydrogen-bonded networks. They can also share hydrogen bonds with other molecules. In particular, aqueous mixtures of water confined within nanoscale geometries of hydrophilic surfaces is subject to several competing interactions: liquid-liquid interaction between the liquid species composing the mixture and surface-liquid interactions.
In the first part of the work, the behavior of water molecules in partially filled pores is investigated while comparing conventional silica models. We show that water droplets can undergo several configurations in the pore when the silica surface described by the model is not highly hydrophilic. For the expected highly hydrophilic silica surface, the pore surface is always completely wetted by water, agreeing with experimental observations. We have as well evaluated the contact angle of a water droplet on top of a silica slab and finds out that the interaction becomes more hydrophilic with increasing slab thickness and saturates around $2.5 - 3$ nm, consistent with experimentally found value.
Having verified the silica model capturing adequately the wetting mechanism of water in silica surfaces, we have then examined the behavior of water/octanol mixture in silica confinement. Octanol is a long chain alcohol and resembles lipid macromolecules which are main components of biological membranes. It is a peculiar choice because its long hydrocarbon chain plays an important role in the competitive process of interaction near the pore surface. We show indeed evidence of a bilayer-like structure in pore when the pore size is approximately 2 times larger as the octanol chain length. We show that the water/octanol ratio does not significantly affect the orientation of octanol or water molecules near the pore surface. Whereas, the amount of water molecules accumulating near the pore surface increases with water content. We interpret these findings by referring to the relative facility of water molecules to fit near the pore surface in comparison to octanol molecules. Combined with the fact that when water reach the pore wall, it almost gets stack in the surface and its motion considerably slows down due to the effect of the restriction imposed by the fixed atoms of the wall together with the restriction arising from the slower mobility of octanol near the pore.

The ensuing part consists in understanding the dramatic dynamical slowdown of glass forming liquids. To approach the problem, we study liquid silica in bulk and in neutral confinement. Alike water, silica molecules are polar molecules which can build tetrahedral networks due to their directed bonds. They exhibit analogous anomalous features such as a density maximum upon cooling, dynamical transitions such as the fragile-to-strong transition and possibly thermodynamic transitions. Specifically, the fragile-to-strong transition in liquid silica is followed by a structural change to lower density and higher tetrahedral order. In order to clear up the effect of Coulomb electrostatic interactions on the structure and dynamics of silica, we modify the bond polarity by varying the partial charges attached to silicon and oxygen.
We find out that density, tetrahedral order and structural relaxation times decrement when the bond polarity is reduced. Interestingly, the density maximum and the fragile-to-strong transition shift to lower temperatures and disappear when the partial charges are decremented below roughly 75 % of their standard value. We as well show that the temperature-independent energy barriers associated to strong dynamics at low temperature and to the activated dynamics at high temperature both decrease faster than linearly with charges. We then demonstrate that the fragile-to-strong transition is closely related to structural changes happening between the first and the second neighboring shell which influence both a lowering of density and an increase in local ordering. We have further applied the recently introduced relations to describe the intermediate fragile dynamics of silica. This new model decomposes the

temperature-dependent activation barrier into a single particle contribution (that is the high-temperature activation energy) and a temperature-dependent collective contribution (which should pictured dynamical correlations). It describes qualitatively well intermediate fragile dynamics of silica variants although universal relations expected from the out-coming model parameters are not quantitatively reproduced for silica.

Finally, the dynamics slowdown of silica variants in neutral confinements have been addressed. We would like to check whether one can see a trend in the possible growing mechanism of correlated clusters. And in particular, we would like to sort out the effect of bond polarity. Assuming that the emergence of correlated clusters upon cooling can be pictured by typical length scales related to the size of the clusters, we have accessed structural, elastic and dynamical length scales from our analysis in neutral confinements. We show that these length scales increase upon cooling. Another important aspect is the effect of the fragile-to-strong crossover on the temperature variation of length scales. We perform an in-depth analysis of the temperature-dependent length scales by comparing the trend between silica-like liquids and additionally by relating length scales with bulk-like structural relaxation times. We find out no simple relations between studied length scales and activation energy barriers. We postulate that length scales characterizing strong dynamics increase slower with time scale in comparison with length scales describing fragile dynamics.

Zusammenfassung

Wasser ist ein unverzichtbarer Bestandteil unseres täglichen Lebens und das Lösungsmittel, das am häufigsten für chemische und biologische Reaktionen verwendet wird. Insbesondere Wasser in lebenden Zellen ist von Makromolekülen umgeben und kann als begrenzt angesehen werden. Kondenswasser kommt nicht nur in der Biologie vor, sondern auch in der Geologie wie zum Beispiel in porösen Gesteinen oder in der Technik wie zum Beispiel in der Nanofluidik. Für alle diese Systeme ist ein Verständnis des Transportmechanismus von Wasser notwendig. Wassermoleküle sind hochpolar und können wasserstoffgebundene Netzwerke bilden und Wasserstoffbrücken mit anderen Molekülen teilen. Insbesondere wässrige Mischungen, die in nanoskaligen Geometrien von hydrophilen Oberflächen eingeschlossen sind, sind die hydrophile Wechselwirkung zwischen jedem Flüssigkeitstyp der Mischung untereinander und zwischen jeder Flüssigkeit, die die Mischung bildet, und den Oberflächenmolekülen.
Im ersten Teil der Arbeit wird das Verhalten von Wassermolekülen in teilweise gefüllten Poren beim Vergleich konventioneller Silica-Modelle untersucht. Wir zeigen, dass Wassertropfen mehrere Konfigurationen in der Pore durchlaufen können, wenn die vom Modell beschriebene Silica-Oberfläche nicht sehr hydrophil ist. Für die zu erwartende hoch hydrophile Silica-Oberfläche wird die Porenoberfläche immer vollständig mit Wasser benetzt, was mit experimentellen Beobachtungen übereinstimmt. Wir haben auch den Kontaktwinkel des Wassertropfens auf der Silica-Platte ausgewertet und festgestellt, dass die Wechselwirkung mit zunehmender Plattendicke hydrophiler wird und um 2,5 - 3 nm sättigt, was dem experimentell ermittelten Wert entspricht.

Nachdem wir das Silica-Modell verifiziert haben, das den Benetzungsmechanismus von Wasser in Silica-Oberflächen adäquat erfasst, haben wir das Verhalten des Wasser/Oktanol-Gemisches im Silica-Einschluss untersucht. Octanol ist ein langkettiger Alkohol und ähnelt Lipidmakromolekülen, die Hauptbestandteile biologischer Membranen sind. Es ist eine besondere Wahl, weil seine lange Kohlenwasserstoffkette eine wichtige Rolle im konkurrierenden Prozess der Interaktion in der Nähe der Porenoberfläche spielt. Wir zeigen tatsächlich eine zweischichtige Struktur in der Pore, wenn die Porengröße etwa 2 mal größer ist als die Oktanolkettenlänge. Wir zeigen, dass das Wasser/Oktanol-Verhältnis die Orientierung von Oktanol oder Wassermolekülen in der Nähe der Porenoberfläche nicht wesentlich beeinflusst. Die Menge der Wassermoleküle, die sich in der Nähe der Porenoberfläche ansammeln, nimmt dagegen mit dem Wassergehalt zu. Wir interpretieren diese Ergebnisse so, dass Wassermoleküle eine höhere relativ Fähigkeit als Oktanolmoleküle aufweisen in die Nähe der Porenoberfläche zu passen. Kombiniert mit der Tatsache, dass sich das Wasser, wenn es die Porenwand erreicht, fast in der Oberfläche stapelt und seine Bewegung durch die Wirkung der Einschränkung durch die festen Atome der Wand zusammen mit der Einschränkung, die durch die langsamere Mobilität des Oktanols in der Nähe der Pore entsteht, erheblich verlangsamt.

Der anschließende Teil der Arbeit besteht darin, die dramatische dynamische Verlangsamung von glasbildenden Flüssigkeiten zu verstehen. Um das Problem anzugehen, untersuchen wir flüssige Kieselsäure im Bulk und im neutralen Confinements. Ähnlich wie Wasser sind Silica-Moleküle polare Moleküle, die aufgrund ihrer gerichteten Bindungen tetraedrische Netzwerke bilden können. Sie zeigen analoge Anomalien wie ein Dichtemaximum beim Abkühlen, dynamische Übergänge wie den fragil-stark Übergang und möglicherweise thermodynamische Übergänge. Konkret folgt auf den fragil-stark Übergang in flüssiger Kieselsäure ein Strukturwandel zu geringerer Dichte und höherer tetraedrischer Ordnung. Um die Wirkung der elektrostatischen Coulomb-Wechselwirkung auf die Struktur und Dynamik von Siliziumdioxid zu klären, modifizieren wir die Bindungspolarität durch Variation der an Silizium und Sauerstoff gebundenen Partialladungen.
Wir stellen fest, dass Dichte, tetraedrische Ordnung und strukturelle Relaxationszeiten abnehmen, wenn die Bindungspolarität reduziert wird. Interessanterweise verschieben sich das Dichtemaximum und der fragil-stark Übergang zu niedrigeren Temperaturen und verschwinden, wenn die Teilladungen unter

etwa 75 % ihres Standardwertes gesenkt werden. Wir zeigen auch, dass die temperaturunabhängigen Energiebarrieren, die mit einer starken Dynamik bei niedrigen Temperaturen und der aktivierten Dynamik bei hohen Temperaturen verbunden sind, schneller als linear mit der Ladung abnehmen. Wir zeigen dann, dass der fragil-stark Übergang eng mit strukturellen Veränderungen zwischen der ersten und der zweiten Nachbarschale zusammenhängt, die sowohl eine Verringerung der Dichte als auch eine Zunahme der lokalen Ordnung beeinflussen. Wir haben die kürzlich eingeführten Beziehungen weiter angewandt, um die intermediäre zerbrechliche Dynamik von Kieselsäure zu beschreiben. Dieses neue Modell zerlegt die temperaturabhängige Aktivierungsbarriere in einen einzigen Teilchenbeitrag, der die Hochtemperatur-Aktivierungsenergie beschreibt, und einen temperaturabhängigen kollektiven Beitrag, der dynamische Zusammenhänge abbildet. Es beschreibt die intermediäre fragile Dynamik von Silica-Varianten qualitativ gut, obwohl universelle Beziehungen, die von den ausstehenden Modellparametern erwartet werden, für Silica nicht quantitativ reproduziert werden.

Schließlich sind wir die Verlangsamung der Dynamik von Kieselsäure-Varianten in neutralen Umgebungen eingegangen. Wir möchten prüfen, ob man einen Trend im möglichen Wachstumsmechanismus von korrelierten Clustern sehen kann. Und vor allem möchten wir den Effekt der Bindungspolarität herausfinden. Unter der Annahme, dass die Entstehung von korrelierten Clustern beim Abkühlen durch typische Längenskalen in Bezug auf die Größe der Cluster dargestellt werden kann, haben wir auf strukturelle, elastische und dynamische Längenskalen aus unserer Analyse in neutralen Grenzen zurückgegriffen und zeigen, dass sie beim Abkühlen zunehmen. Ein weiterer wichtiger Aspekt ist der Einfluss der fragil-stark Übergang auf die Temperaturschwankungen der typischen Längenskala. Wir untersuchen eingehend die temperaturabhängigen Längenskalen, indem wir den Trend zwischen kieselsäureähnlichen Flüssigkeiten und Zusatzstoffen durch Bezugnahme auf volumenähnliche strukturelle Relaxationszeiten vergleichen. Wir finden keine einfachen Beziehungen zwischen untersuchten Längenskalen und Aktivierungsenergiebarrieren und wir postulieren, dass Längenskalen, die eine starke Dynamik charakterisieren, langsamer zunehmen als Längen, die eine fragile Dynamik beschreiben.

Contents

Acronyms

BO: Bridging oxygen
BDS: Broadband dielectric spectroscopy
BZ: Bródka–Zerda
CRR: Cooperatively rearranging regions
ECNLE: Elastically collective non-linear Langevin equation
FS: Fragile-to-strong
GT: Gulmen-Thompson
H-bonds: Hydrogen bonds
HDL: High density liquid
HDA: High density amorphous
ISF: Intermediate scattering function
KWW: Kohlrausch-Williams-Watts
LJ: Lennard Jones
LDL: Low density liquid
LDA: Low density amorphous
LLCP: Liquid liquid critical point
LLPT: Liquid liquid phase transition
MC: Monte Carlo
MCT: Mode-coupling theory
MD: Molecular dynamics
MSD: Mean-squared displacement
NAMD: Nanoscale Molecular Dynamics
NBO: Nonbridging oxygen
NMR: Nuclear magnetic resonance
OF: Overlap function
OAC: Orientational autocorrelation
PBC: Periodic boundary conditions
PEL: Potential energy landscape
PME: Particle-Mesh Ewald
QENS: Quasielastic neutron scattering
RFOT: Random First-Order Theory
SPC/E: Simple point charge extended
VdW: Van der Waals
VFT: Vogel-Fulcher-Tamman

1 Introduction

The focus of this thesis is on the understanding of the molecular mechanism governing the structure and dynamics of network-forming liquids such as water (water/alcohol mixtures), silica mainly in the supercooled (metastable) phase. Our survey is made using molecular dynamics (MD) simulations. Our first emphasis is on water and aqueous mixtures. Water is an essential liquid in our everyday life and is the solvent mostly used for chemical and biological reactions. For example water in the human body is surrounded by large biomolecules [1, 2] and can be considered as confined water with the confinement size lying in the range from at 1 to 100 nm. Understanding the properties of confined water is thus relevant for life science, in particular describing the behavior of water near surfaces is relevant to answer the questions about the role of water in biological processes occurring in cells. For this task, it might be helpful to check how the structure and dynamics of water are modified in the vicinity of surfaces. Indeed, water molecules are highly polar, forming hydrogen-bonded networks and also connecting to other molecules with hydrogen bonds. Interestingly, water confined within nanoscale geometries presenting hydrophilic surfaces feel two competing interactions: the hydrophilic interactions between water molecules and those between water and surface molecules. In the particular case of aqueous mixtures as for example water/octanol mixtures in hydrophilic confinements, the amphiphilic nature of alcohols induces the ability to share hydrogen bonds with water, [3] thus adds another contribution to the preferential interacting process happening near the hydrophilic surface of the confinement. More importantly, a thorough study of the behavior of confined water/alcohol mixtures may help in optimizing separation techniques such as lubrication, oil recovery and elimination of contamination. [4, 5, 6] The behavior of water as well as aqueous mixtures in silica confinements are thus the prime topics covered in the thesis.

One of the standard systems for studying hydrophilic interactions of confined water are silica nanopores such as sols-gels, [7] mesoporous silica (MCM-41), [8, 9, 10, 11, 12, 13] Vycor-glasses, [14, 15, 16] controlled pore glasses (CPG). [17, 18, 19, 20, 21] A survey of the behavior of water in silica nanopores is the topic which has brought considerable attention, [22, 23, 24, 25, 26, 27, 28] due to the relevance of the water-silica interaction in understanding water transport in porous rocks, [29] nanofluidic devices, [30] heterogeneous catalysis in mesoporous materials, [31, 20] and permeation through membrane channels. [32] Several experimental researches of water in silica nanopores have been carried out using NMR spectroscopy, [11, 19] X-ray and neutron diffraction, [15, 33, 16, 34, 9, 12] quasi-elastic neutron scattering (QENS), [8, 10] small-angle neutron scattering (SANS), [14] and optical Kerr-effect spectroscopy, [7] all agreeing in the fact that the dynamics of water in such pores is slow in comparison to the dynamics of bulk water. This originates from the strong binding of water molecules with silica surfaces molecules as found by experimental measurements [11, 19] resulting in a complete coverage of the pore surface at even moderate pore filling percentage. It is therefore necessary to capture accordingly the intermolecular interactions between water and silica surfaces in MD simulations. This task would be useful for the next set of simulations consisting of water and aqueous mixtures in silica confinements.
Previous MD simulations [35, 36, 37, 38, 39] have used the *Bródka and Zerda* (BZ) [40] silica model in which the (12-6) Lennard-Jones (LJ) parameters assigned to oxygen atoms of the silica wall are approximated from the *Kirkwood-Mueller* formula, [41] while no LJ interaction centers are assigned to silicon and hydrogen (of the silanol groups) as they are small in size and possess a low polarizability. The BZ model also defines the set of partial charges which should be attached to each silica atom site accordingly in order to get a hydrophilic surface. What lacks from those preceding MD investigations (using the BZ model) is an explicit description of the extent to which the pore surface is wetted. One could not conclude whether it is only partially wetted or rather completely covered (as expected from measurements [11, 19]). In addition, the pore filling ratio influences substantially the dynamic behavior of confined water droplets [25, 37] but in the case of incomplete wetting it might be difficult to draw conclusions on the link between dynamics and the possible configurations of water inside partially filled pores. Therefore, a detailed understanding of the effect of the filling ratios on the wetting properties of

water in silica nanopores is necessary. Investigating partially filled pores is as well relevant for experimentalists since in experiments the pore filling procedure starts with a fluid which is placed on top of a porous surface and can flow to enter inside the pore. As a consequence, the pore used in experiments is generally only partially filled.
Within our thorough investigation, we have shown that water molecules do not completely wet the BZ silica model surface at intermediate pore fillings. Therefore, the silica model recently introduced by *Gulmen and Thompson* [42] (GT) has been tested. The GT [42] potential differs from the BZ [40] silica potential by the weak short-ranged LJ interaction which is added for silicon and hydrogen atoms as well as the partial charges attached to each atom sites which are slightly incremented. We study the wetting behavior of water on silica surfaces as predicted by both silica models and we make a comparison to the experimental expectations. [43, 11, 19, 44, 45] We show that the GT potential proposes a highly hydrophilic silica surface that reproduces accurately the wetting mechanism of water in silica surfaces. [46] We further show the different configurations undertaken by water droplet in partially filled BZ silica pore and we propose a theoretical explanation for the different shapes obtained. We then conclude our analysis by making a survey of the contact angle of water on flat silica slabs. We analyze the dependency of the contact angle on the thickness slab and proposes the minimum thickness slab for silica surfaces to reproduce accurately the wetting properties of water in silica surfaces. The results are presented in chapter 5.

Having ensured a silica model surface describing qualitatively and quantitatively well the wetting properties of water in silica surfaces, we then use this model surface to study the behavior of confined water and octanol mixtures of different mixing percentages. Here the mixing percentage is defined with respect to the molar water content. As for alcohol, octanol is chosen as with its long hydrocarbon chain, it shows similar properties as lipid molecules. Knowing that lipid molecules are the main component of biological membranes, octanol can be used as a model to understand the process in membranes mimetics. [47, 48] Furthermore, given the fact that water and octanol are not miscible, the water octanol partition coefficient is often employed to estimate the partitioning of solutes between aqueous (hydrophilic) and organic (lipophilic) phases. [49, 50, 51] For example, the water-octanol partition coefficient is universally utilized to check the pharmacokinetic properties of drug molecules. [52, 53, 54]
In this prospect, inspecting the structure and dynamics of water/alcohol (or other aqueous) mixtures in confinements is a current field of research as they are still unsettled questions about the arrangements of each liquid component in the porous volume. Indeed, previous experimental [55, 56, 57, 58, 59] and MD simulations [60, 61, 62, 63] results have proposed that almost independently of the water content, water molecules show a strong preference to attach to the hydrophilic pore surface, and occupy more the pore center with increasing water/alcohol mole fractions; to the detriment of the alcohol molecules which accumulate in the pore center. Examples of alcohol chosen for the mixing with water are glycerol [56, 55, 57] or propylene glycol (PG) and propylene glycol monomethyl ether (PGME) [58, 59] as well as acetonitrile [60] and ethanol (in alumina pores). [63] Oppositely, other simulations [64] as well as experimental [65] reports have claimed that water form clusters in the pore center region while ethanol molecules are more willing to attach to the silica surface especially when the water content is smaller than 80 mol% as recently suggested. [65] Using a simulation framework, *Schmitz et al.* [66] have shown evidence for ethylene-glycol enriched surface layer and water-enriched surface layers in the silica pore confinement, but such privileged adsorption is governed by both liquid-matrix interactions and the liquid-liquid interactions, and thus more water are pushed to the pore center while less water molecules are aggregating near the pore wall when ethylene-glycol is considered in its gauche conformation as compared to its trans conformation. All these previous works practically agree on the fact that the system undergoes a micro-phase separation, where one of the components has an increased concentration in the immediate vicinity of the hydrophilic surface. In all cases, the observed structures are a highly nontrivial outcome of the complex interplay of the various interactions between molecules, and with the surface. What is new with our work is that we used a long chain alcohol presenting a long hydrophobic

tail, that might add an interesting contribution to the ongoing debate. Our MD results of the water and octanol mixtures in confinements are then compared to NMR spectroscopy findings (collaboration with experimentalists from the group of *Professor Buntkowsky* at the TU Darmstadt) and summarized in Ref. [67].
Combining both techniques (Solid-state NMR investigations and MD simulations), we have shown that the hydroxyl groups of octanol and water are attached to the pore surface via hydrogen bonding with silica sites, while the hydrocarbon chains are located in the range between surface and center. The orientation of the hydroxyl groups of water and octanol located near the pore surface seems to be almost independent from the ratio between water and octanol molecules. However, the mixing ratio significantly alters the formation of hydrogen bondings between octanol-octanol and octanol-silica, thus with incrementing the water content, water replaces octanol in the vicinity of the pore surface, such that silica prefer to link with water molecules instead of octanol. In simulations, we have also found the presence of a bilayer-like formation for a pore size of roughly 2 nm in which some octanol and water hydroxyl groups can also occupy the pore center region. But such bilayer formation is intrinsically related to the size of an octanol molecule $\sim$ 0.9 nm thus with bigger pore size ($\sim$ 3 nm, 4 nm), the layering process gets less pronounced. The results of this study are detailed in chapter 6.

Besides the possible induced micro-phase separation process, the confinement effects can also be used to avoid the spontaneous crystallization of water at low temperature (approximately 150-230 K at ambient pressure) and thus to enter in the "no-man's land" region of water. [68, 69] This method has therefore been implemented by a number of authors as summarized in the latest review of *Cerveny and coworkers*. [70] An outcome is that the structure of water is strongly altered within non neutral matrices (as for example silica nanopores), in comparison to neutral confinements which offer the advantage of maintaining the structure of water even near the pore surface as bulk-like. [71, 64] Thus, it is not straightforward to relate structural relaxations of confined supercooled water with supercooled bulk water. [70] It is worth to mention that independently of the confinements nature, water layers in the vicinity of the pore surface show a slower dynamics than water layers in the pore center region. Consequently, it has been found that the temperature dependent relaxation data of confined water also displays a dynamic crossover. [72, 73, 71, 74] This dynamic crossover is mainly important for understanding both behavior of confined and bulk supercooled water. Indeed, The possibility of a fragile-to-strong (FS) crossover in bulk water is heavily discussed. [75, 76, 77, 78, 79] A fragile supercooled liquid displays a non-Arrhenius temperature-dependent dynamics which is often the case for ionic and Van der Waals systems. Strong glass formers show instead a temperature-dependent dynamics related to the Arrhenius law. Such trend is noticed for materials with strong directed bonds leading to an ordered network structure. Besides the FS crossover in water, several other anomalies are observed in bulk water at low temperature such as the density maximum, the maximum appearing in thermodynamic quantities as the isothermal compressibility, and constant-pressure specific heat capacity upon crossing the Widom line. These anomalies have been rationalized by proposing the possible existence of a liquid-liquid phase transition (LLPT) [68] which separates two distinct fluids: a low-density liquid (LDL) phase at low pressure and a high-density liquid (HDL) at high pressure.
The origin of these anomalies as well as the connection between thermodynamic, structural and dynamical properties is highly debated. A simple three-state model implementing the density- and entropy-reducing effects of polar bonds [80] has demonstrated that in general networks-forming liquids might exhibit a thermodynamic phase transition between a HDL and a LDL. Nevertheless, it manifests itself depending on the values of the parameters characterizing the molecular interactions. Another suitable example of network-forming liquid is silica. Water and silica resemble each other in different ways, they are composed of polar molecules and are both able to build tetrahedral structures. Hence, silica also present similar anomalies as water. Indeed, the occurrence of a LLPT has also been claimed in silica and a connection between the FS and the critical end point of a LLPT was proposed for silica [81, 82, 83, 84, 85, 86, 87, 88, 89] as well as for water. [68, 81, 87, 88, 78, 79] In the special case of

silica, the FS transition is a well-established and accepted phenomenon shown by experimental studies [90, 91, 92] and also simulation results. [93, 94, 95, 96, 84, 97, 98, 99] Therefore, silica might be a good alternative for comprehending the genesis of the anomalies as it is not concerned with the issue arising from the immediate crystallization process happening in water.
In this work, we check the possible relation between LLPT and the FS crossover by an analysis of the influence of the microscopic properties on the FS crossover happening in silica. [100] We systematically modify the intermolecular interactions between silica atoms. We change the electrostatic part by altering in a generic manner the partial charges attached to silicon and oxygen atoms. Analogous studies were recently performed in water [101] and in WAC silica. [89, 102] For water, the outcome was that the high-temperature activation energy relates universally to the glass transition temperature T_g, while the fragility remains constant when the molecular polarity is varied. [101] In the case of silica, the *Woodcock-Angell-Cheeseman* (WAC) [103] silica model was used. The WAC model includes only electrostatic interactions and short-range repulsions which is different from the modified version[104] of the *van Best, Kramer, and van Santen* (BKS) model [105] (here studied) that clearly incorporates an additive short range repulsive contribution. With the WAC model, *Lascaris and coworkers* [89, 102] have prospected the change occurring in thermodynamic properties with a variation of the partial charges. They give evidence for the existence of a liquid-liquid critical point (LLCP) when the partial charges were decremented from their standard values (+4e for silicon and -2e for oxygen) of the original WAC model. [103]
In the current work, we make a complementary investigation to the work of *Lascaris et al.* on the WAC model. [89, 102] We use the modified version BKS model. [104] The initial values of the partial charges in the BKS [105] model amount to only 60% of those defined in the WAC model. By varying the partial charges of the silicon and oxygen atoms around the standard BKS values, we rather explore a range of partial charges smaller than that investigated for the WAC model. Rather than looking at the thermodynamic properties of a more abstract class of models as shown by *Lascaris et al.*, [89, 102] we probe the effect of the electrostatic interaction on the structural and dynamical properties of a chemically more realistic silica model. The results are presented in chapter 7. We show that as charges are decremented and the liquid becomes more similar to a Lennard-Jones (LJ) liquid, the density anomaly becomes less pronounced and the liquid behaves more as fragile a glass former see Ref. 100. We present a direct correlation between structural changes and the FS transition, with both features vanishing when the partial charges are lower than approximately 75% of the BKS initial values.

The focus of the bulk behavior study was to explore the properties of liquid silica and to obtain equilibrated systems which will then be used to generate neutral pores. As previously mentioned, studies in confinements [72, 73, 74] can be useful in shedding light on the dynamical behavior of supercooled liquids. However, the comparison with bulk dynamics is still questionable [106, 107, 70] especially when the confined liquid is different than the confining matrix (for example water confined in silica pore). Lately, neutral confinements [71, 22, 101] have been proposed as they offer the possibility to study a almost undistorted confined liquid. The majority of neutral confinements analysis have based the research on the ideal case of LJ liquids. [108, 109, 110, 111] It was also recently applied for a realistic model of supercooled water by *Klameth et al*. [71, 112] and of silica [101] but the conclusions were almost similar as in the case of LJ liquids. Indeed, as intuitively expected the structure of the confined liquid is not disturbed by the confining matrix and remains identical to the bulk structure. [71, 112] This result is understandable as the immobile atoms of the pore wall impose a static energy landscape [22] to the mobile particles and therefore only gives rise to slight fluctuations of the density near the surface in neutral confinements. [71, 101] Meanwhile, the dynamics hugely slow down in the vicinity of the pore surface, offering the possibility to sort out the confinement effect without worrying about surface effects. Moreover investigations confined systems offer the possibility to check the different theories proposing the emergence of growing length scales in the liquids associated with the rapid slow-down at low temperature. These theoretical predictions are for example the *Adam-Gibbs* relation [113] which suggests that

the slowing down of the dynamics upon reducing temperature is driven by the vanishing configurational entropy which is intrinsically connected to a large growth of the size of possible existing cooperatively rearranging region (CRR); the random first-order theory (RFOT) [114, 115] which offers a more general view by proposing that the typical length scale of the CRR increases sharply when reducing temperature, and this is not merely due to a lowering of the configurational entropy but also related to a huge energy cost associated with the creation of interfaces between different possible states. There is also the elastically collective nonlinear Langevin (ECNLE) theory [116, 117, 118] which splits the energy barrier associated to structural relaxations into two terms: a term accounting for local activated hopping and second term accounting for cage expansion represented by long-range collective displacements of particles outside the cage. This second term is the one involving the typical length scale of the CRR. The open question [119, 120] are whether one can relate the rapid slow-down in dynamics upon approaching the glass transition to the emergence of one or more growing length scales in dynamics and whether the length scales can be connected to collective motion happening in supercooled liquids. The topic of chapter 8 will be based on the results obtained from simulations of the bulk silica families (differing by bond polarity) confined in neutral matrices. Our results [121] confirm the monotonic increase of structural and dynamical length scales already previously proposed. [108, 110, 111, 71, 112, 101] We further show a general trend in the slowing down process of atoms near the pore wall. We check whether the process is different between silica liquids showing no FS in bulk to those where the FS has been observed in bulk. We as well check the different theoretical predictions and we discuss the success and limits of each theory when applied to BKS silica.

The last part of this research was based on comprehending why radon accumulates more in fat (neutral solvents) than in liquid water (or more generally in polar solvents). We study the most stable isotope ^{222}Rn which has a half-life of 3.8 days. Exposure to radon represents the largest proportion of annual radiation dose from natural sources. [122, 123] Significant doses of radon can accumulate in the human body organs. [124, 122, 125, 126, 127, 123] The highest dose is deposited in lungs, enhancing the probability of lung cancer infection. [128, 129] However, radon are playing a crucial role for therapy of inflammatory diseases like rheumatoid arthritis. The prevailing molecular mechanisms explaining the healing effect of radon are still not known. [130, 131] Radon can diffuse into the bloodstream and was observed to accumulate preferentially in fatty tissues. [132, 133, 134] The physical and chemical origin underlying this inhomogeneous distribution in the human body have not been thoroughly explored. Though, this might be helpful for understanding the effect of radon therapy as well as the possible health risks. To achieve this task, we use a combination of γ-spectroscopy (Collaboration with the biophysics group of *Prof. Gerhard Kraft* and *Prof. Claudia Fournier* in the GSI institute of Darmstadt) and MD simulations [135] to study the solubility of radon in water and fat. We used an isotonic alkaline solution as a model for standard body cells and fatty acids to represent fatty cells. Additionally to fat and water-salt solutions, we also used pure SPC/E water [136] (labeled as Q_0) and water with a polarization that was artificially reduced (Q_-) or enhanced (Q_+) by 15% from the initial value of the SPC/E water model (Q_0), [136] and also hexane in order to check the assumption that the polarization of the solvent is a main determinant of radon solubility.

The rest of this work is organized as followed. Chapter 4 makes a review about the theory behind supercooled liquids and the different proposed theoretical models. Chapter 2 shortly illustrates the principle of MD simulations with its success and limits. It is immediately followed by chapter 3 which defines the main observables which are evaluated with the MD trajectories. The simulation details and the simulated systems description of each project is always made at the beginning of each chapter (chapter 5, 6, 7, 8, 9) where the results of the projects are presented. Each chapter showing the results ends with a small summary recapitulating the highlighted message. Thereupon, the most relevant points are reiterated in the thesis summary (chapter 10). Furthermore, a listing of references, publications by the author, as well as a short curriculum vitae and acknowledgments end the manuscript.

2 Molecular dynamics (MD) simulations

Classical molecular dynamics (MD) is a simulation method describing the molecular motion by the equation of motion of Newton's classical mechanics. The basics of MD simulations will be introduced in this chapter. The first section will emphasize on the technical details of the MD simulations, in particular the settings of the NAMD software program [137] with which all simulations have been performed. The second part will discuss how good is the MD performance in comparison to the other molecular modeling techniques. We will also show how MD simulations results can be related to experimental results.

2.1 Basics of MD

MD simulations compute atomic trajectories while solving Newton's equations of motion numerically using empirical force fields to approximate the actual atomic interaction in the system. Thus the starting point is the Newton's equation of motion.

$$m_i \frac{\mathrm{d}^2 \vec{r}_i}{\mathrm{d}t^2} = -\vec{\nabla}_i V_{\text{total}}(\vec{r}_1, \vec{r}_2, ..., \vec{r}_N)\,. \tag{1}$$

The potential energy $V_{\text{total}}(\vec{r}_1, \vec{r}_2, ..., \vec{r}_N)$ only describes the positions of atoms and using the Born-Oppenheimer approximation, the electrons are assumed to always remain in the ground state and to instantaneously adjust their position to the center of mass motions of the atom. The accuracy of the microscopic description of the systems that we obtain strongly depend on the precision of the potential energy $V_{\text{total}}(\vec{r}_1, \vec{r}_2, ..., \vec{r}_N)$ between atoms of the systems. It is generally expressed in terms of intra-molecular energy contributions (bonded energy) (see Fig. 1) and the intermolecular (non-bonded) energy.

$$V_{\text{total}} = V_{\text{bond}} + V_{\text{angle}} + V_{\text{dihedral}} + V_{\text{VdW}} + V_{\text{electrostatic}} + V_{\text{ext}}\,. \tag{2}$$

The intra-molecular energy involves the description of bonds in molecules, the angles between different bonds, and possible bonds rotation giving rise to molecules conformations. We have for example:

$$V_{\text{bond}} = \frac{1}{2} k_{\text{bond}} (r - r_0)^2\,, \tag{3}$$

which corresponds to the bond stretching between adjacent pairs of atoms distant by r around the equilibrium distance r_0.

$$V_{\text{angle}} = \frac{1}{2} k_{\text{angle}} (\theta - \theta_0)^2\,, \tag{4}$$

which defines bonds bending between successive bond vectors of angle θ oscillating around the equilibrium angle θ_0. The harmonic approximations of the bond and angle deformation are accurate enough at ordinary temperature and in the absence of chemical reactions. There are also dihedral angle potential between atoms pairs separated by exactly three atomic covalent bonds. They are defined as

$$V_{\text{dihedral}} = \begin{cases} k(1 + \cos(n\psi + \phi)) & \text{if } n > 0, \\ k(\psi - \phi)^2 & \text{if } n = 0; \end{cases} \tag{5}$$

and describe the torsion energy term consisting of the dihedral angle between the planes formed by the first three and last three atoms of a consecutively bonded (i_1, i_2, i_3, i_4) atoms quadrupole. Here ψ is the torsional angle in radians between the (i_1, i_2, i_3) atoms bond plane and the (i_2, i_3, i_4) atoms bond

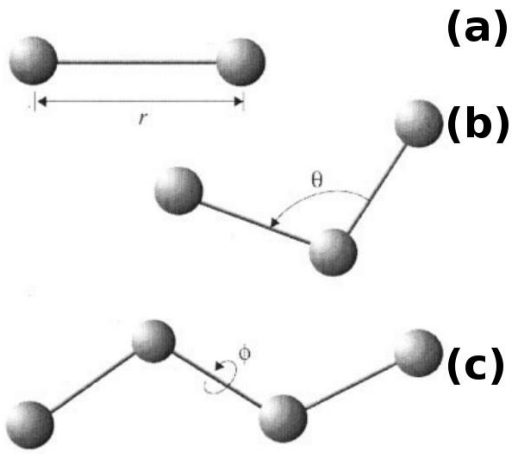

Figure 1: Scheme of the different bonding energy terms. (a) displays the vibrational deformation bond energy, (b) illustrates the angle bending term and (c) shows the dihedral bond rotation term. θ and ϕ are respectively the bond and dihedral angles. Figure adapted from Ref. 137.

plane. n are the different periodicities for a given set of (i_1, i_2, i_3, i_4) atoms quadrupole. k represents the multiplicative constant and ϕ is the phase shift angle.
Next to the intra-molecular energy, we also have intermolecular energy between molecules or atoms which are mostly split into the Van der Waals (VdW) term V_{VdW} and the electrostatic contribution. V_{VdW} describes the dispersive forces or the charge fluctuations forces in which one contribution is the Pauli electron cloud repulsion between atoms. The default VdW interaction implemented in NAMD are Lennard-Jones (LJ) like expression

$$V_{\mathrm{VdW}}^{\mathrm{LJ}} = 4\epsilon\left(\frac{\sigma^{12}}{r_{i,j}^{12}} - \frac{\sigma^{6}}{r_{i,j}^{6}}\right). \tag{6}$$

However, Buckingham-like VdW potential $V_{\mathrm{VdW}}^{\mathrm{B}}(r) = A\exp(-br) - c/r^6$ can also be parametrized in NAMD using for example the energy tabulated method. We will use both functional types depending on the systems which is investigated.

$$V_{\mathrm{electrostatic}} = \frac{1}{4\pi\epsilon_0}\frac{q_i q_j}{r}, \tag{7}$$

is the electrostatic term which is basically in the Coulomb form. Depending of the system of interest, other contributions might be required in the potential energy such as the improper energy which account for chirality, extended dipolar energy that explicitly account for the hydrogen bonds interaction, or other external forces depending on the constraint applied to the system; these other possible energy parts are represented by V_{ext}.

Periodic boundary conditions (PBC) are often set in MD simulations in order to remove the effect of system boundary. A periodic box is defined accordingly to the system size and as a particle moves out of the periodic box, it is immediately replaced by an image particle which moves inside the box. Accessing the exact total potential energy involving all atoms (as well as possible image atoms) of the systems is thus computationally demanding. Therefore, reasonable truncations are made in order to facilitate the problem. The interaction of the VdW force is smoothly truncated at a cut-off distance which depends on the studied system. That means for atoms which are far apart than the cut-off distance, the VdW term is neglected which is accurate enough since the $1/r^6$ term converges quickly to 0. Simultaneously, within

the cut-off distance, the electrostatic interaction between atoms pairs are calculated exactly while long-range electrostatic interactions are estimated with the help of the particle-mesh Ewald (PME) algorithm. [138] The PME summation divides the total electrostatic energy into a term in direct space and a term in reciprocal space allowing the long-range part to be calculated via fast Fourier transform. Therefore, PME only works when using PBC. The solution of the Newton equation can not be solved analytically since it involves the calculation of potential energy between a large number of coordinates. NAMD uses then the Verlet algorithm [139] in which the position at time $t + \Delta t$ is determined by the position and velocity at time t and $t + \Delta t/2$, and by the force at time t.

$$\begin{aligned} v_{n+\frac{1}{2}} &= v_n + \tfrac{1}{m} F_n \tfrac{\Delta t}{2}\,, \\ r_{n+1} &= r_n + v_{n+\frac{1}{2}} \Delta t\,, \\ F_{n+1} &= F(r_{n+1}), \\ v_{n+1} &= v_{n+\frac{1}{2}} + \tfrac{1}{m} F_{n+1} \tfrac{\Delta t}{2}\,. \end{aligned} \tag{8}$$

The choice of the time step Δt is determinant because if it is too large the motion of molecule becomes unstable due to the very big error occurring in the integration. If it is too small, then it increases the computational cost. A good choice is dictated by the time step Δt which scales up to the period of the highest vibrational frequency of the molecule. The Verlet algorithm performs quite well in predicting the time evolution of atoms coordinates. It is exactly time reversible and easy to program, and it also requires only one (expensive) force evaluation for each evaluation step. More importantly, it conserves both linear and angular momentum.

Furthermore, one can simulate several thermodynamical ensemble with NAMD. The ones used within this research are either NPT where the pressure and the temperature are fixed, or NVT which is similar to NPT but instead of the pressure, the volume is fixed. To control and fix the temperature, the Langevin dynamics, [140, 137] in which additional damping and random forces are introduced to the system, is utilized. It generates a Boltzmann distribution of the atoms kinetic energy distribution at the maintained temperature. The pressure can also be settled by using the Langevin-Piston method [141] in which the volume of the system is allowed to vary to enable the convergence of the internal and applied pressures to the same value.
Given the interacting parameters constants of each atom, interactions between the different atoms are governed by the *Lorentz—Berthelot* mixing rules. [142] In general, simulation parameters either describing the molecular structure or the intermolecular interactions are determined after a comparison with available experimental data and/or when using quantum chemical computations. [105, 136, 143, 144]

2.2 Success and limits of MD

Computer simulations in general help in understanding the microscopic properties of molecules assemblies and act as a complement to conventional experiments. The two main simulation techniques are molecular dynamics (MD) and Monte Carlo (MC). There is as well a couple of hybrid techniques [145] which combine features from both but will be not discussed in this section.
The advantages of MD over MC are quite obvious, as they allow a study of the dynamical properties of systems such as transport coefficients, time-dependent responses to perturbations in the microscopic scale such that a spatial resolution of each properties is also accessible. They provide an estimate of the nanosized interactions between molecules, and often lead to accurate predictions of bulk properties. They as well act as a bridge to experiment as they allow to test theoretical assumptions by comparing simulation with experimental results. In addition, it is also possible to check what might occur at extreme temperature or pressure conditions, which is sometimes hardly manageable in experiments.
MD and MC differs by the way the atoms positions are obtained. While MD is a deterministic method based on solving Newton's equations of motion, MC is a stochastic method which may predict different possible configurations of the system. [146] The system is allowed to take different configurations and

the energies of the different configurations are compared. The configurations providing the lower energies are accepted. One limit of the MC techniques is that it allows quick barrier crossings between energy minima and thus quick exchange between sample conformations. That might not be advantageous when probing for example fragile liquids at very low temperature since there is a large probability of selecting configurations of the phase space with comparable local energy minima and rejecting other configurations with a bit higher energy minima, though the later can also significantly affect the properties of the liquid. Second, MC is not suited when one is interested on the transport properties of the system. In those cases MD techniques are quite appropriate.

There are two MD families: classical MD and ab-initio MD. The difference between both is that in classical MD, the interactions between particles is given by empiric potentials (force fields) which are in most cases a function of the atomic coordinates. Generally, the force field consider terms only up to three-particle interactions and neglect the many-particle terms. While in the ab-initio MD, the inter-atomic forces are determined accurately. They are calculated at each time by solving time-independent Schroedinger equation for the many-body wave function of electrons and invoking the Born-Oppenheimer approximation in which the nuclei is fixed at the instantaneous positions of the atoms. The resulting energy is a function of the nuclear coordinates and is used as the inter-atomic potential required to compute the forces in Newton's equation of motion for the nuclei. Although, in this way, the molecular bonding, the molecular polarization, the charge transfer, the many-body effects are exactly approximated, ab-initio are quite computationally expensive and only allow the simulations of relatively small systems sizes in short time scales (several picoseconds). As the dynamics of glass forming liquids is very slow in the low temperature range, one necessitates a long time simulations of ns to μs which are easily achievable with classical MD. Along with the long time dynamics, the studied system should be sufficiently large to limit finite size-effects on the observed behavior.
Obviously, classical MD simulations performance depend on the force field utilized to depict inter-atomic forces. Therefore, a comparison with experimental techniques is often necessary. This is one of the main benefits of MD simulations as the dynamics for each atom of the system is accessible and can be directly related with experimental results probing related structural relaxation process of particles such as broadband dielectric spectroscopy (BDS), Nuclear magnetic resonance (NMR), and quasielastic neutron scattering (QENS). A non negligible drawback of MD originates from the use of systems of finite size, up to 100000 particles can be simulated rising the question of finite size effects. To circumvent this problem, the use of periodic images from PBC are then necessary. Nonetheless, they can still be limited in capturing the length scales over which micro-phase separation or phase transition happens; as the length scales at low temperature can even go beyond the box size set in PBC. Usually, for liquids approaching phase transition, the correlation length is infinitely large and thus requires an infinitely large system size. Similarly, an investigation of liquid mixtures showing macroscopic phase separation in which the process can require about several μs and the system should be sufficiently large is often not possible in MD. In the present investigation, we choose the systems size accordingly large than any possible growing correlation lengths (see chapter 8) and we focus on temperature ranges in which only dynamical transition are possible. Lastly, the force fields chosen for the systems investigated have often been previously tested and approved. [105, 136, 147, 148, 143, 104]

3 Observables

This chapter will present the quantities that can be inferred from the MD trajectories. We will classify them as structural properties for the ones which describe the structural changes happening in the system and the dynamical properties for the ones depicting atoms dynamics.

3.1 Structural quantities

3.1.1 Density

The mass density of the bulk system is defined as:

$$\rho = \frac{\text{Mass}}{V} = \frac{N_1 \cdot M_1 + N_2 \cdot M_2}{V}, \tag{9}$$

in which N_1 (N_2) are the number of atoms type of mass M_1 (M_2), while the atoms density is defined as followed.

$$\rho_\text{a} = \frac{N_\text{a}}{V}. \tag{10}$$

For the simulations in confinements, the number density profile is usually evaluated. As we simulate approximately cylindrical confinements, the number density profile of atoms in a given cylindrical shell located between R_i and R_{i+1} (which define the radial positions) is defined as:

$$n(R_i) = \left\langle \frac{N[R_i : R_{i+1}]}{\pi(R_{i+1} - R_i)^2 l} \right\rangle. \tag{11}$$

in which $N[R_i : R_{i+1}]$ are the number of atoms counted in the radial interval $[R_i : R_{i+1}]$ and l is the length of the confinement. The brackets $\langle\rangle$ indicate the time average.

3.1.2 Radial distribution function

Using neutron scattering experiment, the local structure of system can be probed via the structure factor. For an isotropic system, it is defined as followed:

$$S(k) = \left\langle \frac{1}{N} \sum_{i,j} \frac{\sin k\left[\vec{r}_i - \vec{r}_j)\right]}{k\left[\vec{r}_i - \vec{r}_j)\right]} \right\rangle, \tag{12}$$

in which k is the scattering vector (change in the incident wave vector compared to the scattering wave vector). For a sufficiently large number of atoms, we can inferred the radial distribution function: [149]

$$g(r) = \frac{1}{2\pi^2 \rho r} \int_0^\infty [k(S(k) - 1)] \sin kr \mathrm{d}k, \tag{13}$$

in which ρ is the average density and r is the distance at which the distribution is evaluated. In MD simulations, the radial distribution is calculated by evaluating the number of atoms pairs $n(r)$ within a spherical shell of thickness $\mathrm{d}r$.

$$g(r) = \lim_{\mathrm{d}r \to 0} \frac{n(r)}{4\pi(N_\text{pair}/V) r^2 \mathrm{d}r}. \tag{14}$$

N_{pair} is the total number of pairs of atoms within the volume V. When we are looking for similar atoms types, $N_{\text{pair}} = N_1(N_1-1)$, in the case of pairs of different atoms type $N_{\text{pair}} = N_1 N_2$ in which N_1 (N_2) is the total number of atoms of each type.

The local coordination environment of a given atom type (for example silicon in silica) is analyzed using partial radial distribution functions $g^{(i)}(r)$ of the ith nearest neighbors, which are related to the total radial distribution $g(r)$ via

$$g(r) = \sum_{i=1}^{\infty} g^{(i)}(r)\,. \tag{15}$$

Thus, $4\pi r^2 g^{(i)}(r)\mathrm{d}r$ is the probability that the distance between a silicon atom and its ith nearest silicon neighbor is between r and $r + \mathrm{d}r$.

3.1.3 Hydrogen bonds

Hydrogen bonds (H-bonds) are often useful in probing the local ordering in water and also hydrogen bonding liquids such as alcohol, carboxilic acids. They can be accessed experimentally when using for example X-ray diffraction, [150, 151] neutron diffraction, [152, 153] Infrared and Raman spectroscopy [154, 155, 156] and X-ray spectroscopy [157] depending on the probed entity (electron cloud, nuclei) in molecules. The difficulty in comparing the values of H-bonds obtained between different techniques reside in the way a bond can be considered as H-bonds or not. Sometimes energy thresholds of the intermolecular energy between water molecules are used as criterion [158, 159, 160, 161] to depict whether they are H-bonded. Others define both energetic assignments and geometrical assignments. [157] Generally, various cut-off in distance and angle are often used [162, 163, 35, 164, 157] to assign a H-bond. Given a geometric criterion, the problem still resides on the stability of such bonds since it can accidentally form for very short time. Some experimental data have claimed that liquid water displays two classes of H-bonds domains: intact and broken, [165] which should depend on the H-bond lifetime. A combination of temperature-dependent spontaneous Raman spectroscopy with Monte Carlo simulations in Ref. 165 have revealed that some of the supposed evidence for a multi-state system can arise from continuous distributions. Therefore, the definition of H-bonds presented by MD simulations data are somehow abstract.

In this investigation, the definition is based on the assumption of *Rovere and coworkers* [35] initially defined in Ref. [162, 163], which consider two molecules, as for example water molecules (see Fig. 2), as connected with H-bonds when the angle between the intramolecular O-H vector and the intermolecular O...O vector is less than 30°, provided that the O...O separation is less than 0.335 nm. Similar definitions can be applied between different molecules or atoms groups, for example between octanol and silanol groups. The work of *Shi* & *Tanaka* [166] has shown the robustness of this geometric criterion as it detects more than 80% of H-bonds shared between water molecules; they have also reported that the number of detected H-bonds barely change with various thermodynamic conditions.

3.1.4 Tetrahedral order parameter

The ability of water molecules to be connected via hydrogen bonds render them the tendency of forming tetrahedral networks as one can see in Fig. 2 (a). Similarly silica molecules can also form directional bonds between each other and build tetrahedral structures (Fig. 2 (b)). The degree of tetrahedrality or of local ordering is often estimated by calculating the tetrahedral order parameter and its distribution over the system. We define the tetrahedral order parameter Q by using the definition of Ref. [167, 168].

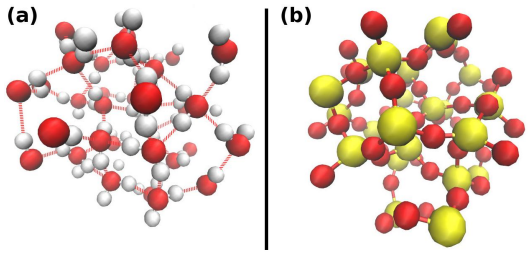

Figure 2: VMD snapshot (a) of a tetrahedral network formed by water molecules of the SPC/E water model [136] used in this study, (b) is a similar snapshot of BKS silica. [105] The red dashed lines in (a) illustrate the H-bonds formed between water molecules. In (b) one can see similar directional bonds between silica molecules.

The degree of local order is evaluated using the tetrahedral order parameter. For a given atom i, it is defined as

$$Q_i = 1 - \frac{3}{8}\sum_{j=1}^{3}\sum_{k=j+1}^{4}\left[\cos\theta_{ijk} + \frac{1}{3}\right]^2 , \tag{16}$$

with θ_{ijk} is the angle between the bonds connecting atom i and two of its four nearest silicon neighbors j and k. Q_i values are lying between -3 and 1. In a liquid, a distribution $f(Q_i)$ of values Q_i can be defined. The time and ensemble averaged order parameter $\langle Q_i(T)\rangle = \left\langle \sum_i f(Q_i,T)Q_i \right\rangle$ is 1 for perfect tetrahedral networks and vanishes for random distributions.
In analogy, a tetrahedral entropy [169] which measures the entropy in tetrahedral local ordering is easily evaluated within MD trajectories as compared to configuration entropy and is defined as:

$$S_Q(T) = S_0 + \frac{3}{2}K_B\left\langle \sum_i \ln(1-Q_i)f(Q_i,T) \right\rangle , \tag{17}$$

in which S_0 is considered as the entropy at high temperature where we actually approach the simple liquid limit. It is generally not known therefore, we rather plot $\frac{2K_B S_Q(T)}{3S_0}$.

3.2 Dynamical quantities

3.2.1 Mean-squared displacement (MSD)

When probing translational motions, the mean-squared displacement (MSD) of particles can be evaluated. It is defined as:

$$\left\langle \Delta r^2(t) \right\rangle = \left\langle \frac{1}{N}\sum_i^N [\vec{r}_i(t) - \vec{r}_i(0)]^2 \right\rangle , \tag{18}$$

given the total number of atoms N. It can be accessed experimentally e.g in neutron scattering. We will define the quantity:

$$\left\langle u^2 \right\rangle = \left\langle \Delta r^2(t = 1\,\mathrm{ps}) \right\rangle , \tag{19}$$

which is generally related to the Debye-Waller factor. [170] In the limit of large k or equivalently in the long times limit, the diffusion regime is reached and the average diffusion coefficient (D) of particles can be estimated using the Stokes-Einstein relation for diffusivity.

$$\left\langle \Delta r^2(t) \right\rangle = 6D \cdot t . \tag{20}$$

3.2.2 Translational correlation functions

The incoherent intermediate scattering function (ISF) measures correlation translational dynamics in the Fourier space. It is calculated as the Fourier transform of the single particle displacement. It studies the particle motion at the length scale fixed by the scattering length k. In the case of isotropic samples of interest, it is given by

$$F_s(k,t) = \left\langle \frac{\sin\left(k\left|\vec{r}_i(t_0+t) - \vec{r}_i(t_0)\right|\right)}{k\left|\vec{r}_i(t_0+t) - \vec{r}_i(t_0)\right|} \right\rangle , \tag{21}$$

where $|\vec{r}_i(t_0+t) - \vec{r}_i(t_0)|$ is the particle displacement after a time interval t and k denotes the modulus of the scattering vector. The values of k used in this study correspond to the typical nearest neighbor distance in the different systems. In case of any variation, it would be mentioned.
The ISF and its Fourier transform can be directly compared to data from inelastic neutron scattering or X-ray scattering. The Fourier transform of the ISF leads to the self-part of the van Hove correlation function displaying microscopic mechanisms for structural relaxations.

$$G_s(|\vec{r}|,t) = \langle \delta\left[|\vec{r}_i(t_0+t) - \vec{r}_i(t_0)| - |\vec{r}|\right]\rangle . \tag{22}$$

$4\pi G_s(|\vec{r}|,t)$ indicates the probability that an atom has traveled the distance r during the time interval t.

3.2.3 Rotational autocorrelation function

In addition to the translational motion, rotation dynamics can be probed. We study the reorientation of the nuclear dipole vector of water which can be accessible experimentally in dielectric spectroscopy (DS) experiments. We can also define a dipole vector in other molecules as for example octanol molecules and probed similar correlations. The function is defined as:

$$F_1(t) = \left\langle \frac{1}{N}\sum_{i=1}^{N} \vec{e}_{i,\mathrm{dipole}}(t)\cdot\vec{e}_{i,\mathrm{dipole}}(0) \right\rangle . \tag{23}$$

The dipole vector defined in a octanol molecule is the vector connecting the carbon of the hydroxyl group with the carbon ending the octanol chain, i.e the carbon linked to three hydrogens.

3.2.4 Overlap function (OF)

In simulations, simple glass forming liquids [171] can crystallize at sufficiently long times. Thus, it is possible to find in supercooled liquids clusters with local structure resembling that of the equilibrium crystal. These clusters are expected to have a high lifetime such that a study of the formation and growth of such clusters may help in understanding the rapid slowing down of the liquid kinetics. These might be investigated by looking at correlations in the density fluctuations which can be probed using the point-to-set or overlap function (OF) introduced by *Berthier* & *Kob* in Ref. 110. The time evolution of the OF can be accessed by the following relation

$$P(t) = \frac{\sum_{i,j}\left\langle n_j(t+t_0)n_i(t_0)\right\rangle}{\sum_i n_i(t_0)} , \tag{24}$$

in which the time variation of the occupation of spherical cells are analyzed. $n_i(t)$ is the occupation number of a cell by the atom labeled i at time t. Assuming that the cell is occupied by atom i at time t_0, that means $n_i(t_0)$=1, if after time t_0+t, the cell gets instead occupied by atom j, then $n_j(t_0+t)$=1 otherwise $n_j(t_0+t)$=0. As expected, $P(t)$ is unchanged by an exchange of atom i and j. The size of the spherical cell is chosen accordingly such that only one atom entity (for example silicon atom of silica) can fit inside the cell. For silica systems, we set the radius of the sphere to r_{OF}=0.1 nm. The average is made over the total number of cells of the system. In general, the OF has also been used to probe possible overlapping in configurations of liquids structures in confined geometries. [172, 110, 173, 111, 174, 175, 176, 177]

4 Theoretical review

This section will give a short theoretical overview about the theory of glasses. The concepts and theoretical background which are necessary for the comprehension of the results presented in chapter 5, 6, 7, 8, 9 will be introduced. Basics of MD simulations have been already presented in chapter 2 followed by the evaluated quantities from the MD trajectories in chapter 3, we thus assume that the author is familiar with these notions.

4.1 Supercooled liquids and glasses

In the cooling process of a liquid down to the melting temperature, it is possible to keep the system in its metastable state and to avoid crystallization given certain conditions. That is the liquid supercooled phase. Supercooled liquids display a phenomenological behavior and the most prominent feature is the dynamic glass transition. When the supercooled phase has been reached, the temperature can be further decreased such that below a certain point, the relaxation time (as well as the viscosity) rises so sharply that the system can't be equilibrated within moderate experimental times. The glass state is reached. The glass state can be simply seen as a liquid that is unable to flow. It is structurally hardly distinguishable from its liquid state but behaves as disordered solids. The most interesting consequence of going off-equilibrium is that the system does not have enough time to properly explore the whole phase space, such that the number of degrees of freedom accessible to the system are considerably reduced. However, the entropy of the glass is not remarkably higher than that of the crystal state (see Fig. 3).

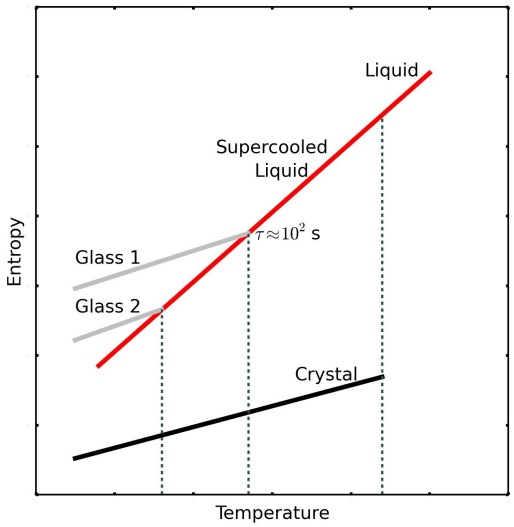

Figure 3: Sketch of the temperature-dependent entropy during a glass transition process. Glass 1 or Glass 2 illustrates that different glass states can be reached depending on the used cooling rate. One can also notice that in comparison to the abrupt change in entropy between liquid to crystal phase transition, the liquid to glass transition displays basically a smooth variation. Sketch adapted from Ref. 178.

The temperature of glass transition has been conventionally fixed as corresponding to the temperature at which the relaxation time (viscosity) has increased by 12-14 decades. Knowing that typical correlation times τ in simple liquids are on the picoseconds timescale, it was first proposed in Ref. 179 to correspond to

$$\tau(T_g) = 100 - 1000\,\mathrm{s}\,, \tag{25}$$

that is associated to a viscosity roughly equal to 10^{13} Poise which is pretty huge when we compare to the viscosity generally reached at the melting point $\sim 10^{-3}$-10^{-2} Poise. The definition of the glass transition is merely based on dynamics, thus the observables highlighting the onset of glassiness are generally dynamical correlation functions $C(t)$, such as the intermediate scattering function (ISF), the rotational correlation, etc. They are well defined by the *Kohlrausch-Williams-Watts* (KWW) relaxation function.

$$C(t) = C_0 \exp(-(t/\tau)^{\beta}) + C_{\infty} \,. \tag{26}$$

C(t) measures how rapid correlations happening in the system decay in time. It can also be applied to describe structural correlations function such as overlap correlation functions (OF) which have recently been introduced [110] and provide a very well insight into overlying between configurations of glassy systems. C_{∞} of Eq. 26 basically vanishes for most of the correlation functions, exception happens for function such as the OF for which it is proportional to the density fluctuations (see Fig. 3). It has been shown in Ref. 180 that for the overlap function, C_{∞} scales as

$$C_{\infty} \sim \frac{4}{3}\pi r_{\mathrm{OF}}^3 \rho_{\mathrm{T}} \,, \tag{27}$$

in which r_{OF} is the radius of the sphere in which the atom occupation number is studied, while ρ_{T} is the atom density at a specific temperature T.

A two-step relaxation process happens at sufficiently low temperature in $C(t)$ (which is more visible in the ISF curve of Fig. 4).

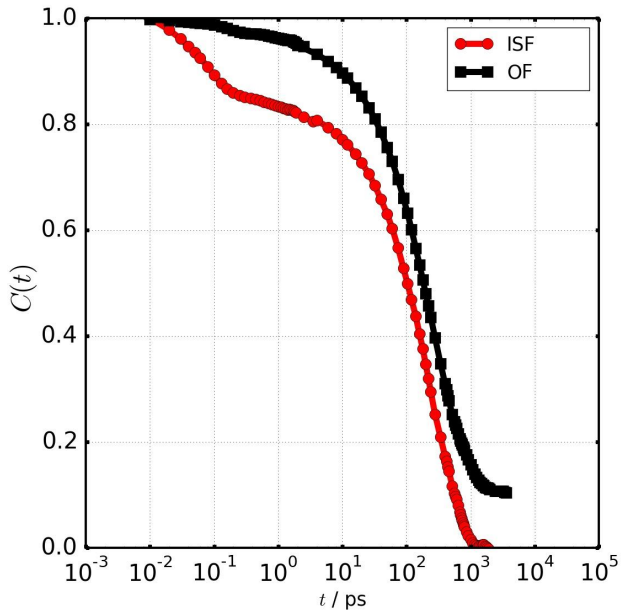

Figure 4: Intermediate scattering function (ISF) and overlap functions (OF) for an exemplary silica like-liquid plotted at a low temperature in order to see the two-step decay in ISF. Remarkably, the OF curve does not vanish at longer times but decays to a finite value.

The short time dynamics are dominated by particle vibrational motions and are often referred as the ballistic regime in which particles move freely without interacting with each other. They are followed by the so-called cage regime in which a particle is confined in the cage formed by its neighbors and is prevented from diffusing despite its many collisions with other particles. This corresponds to the plateau observed in $C(t)$ which comes directly after the vibrational decay. After a sufficiently long time,

proportional to the structural relaxation time τ, the particle can move out of the cage, and a standard diffusive dynamics sets in. This is sometimes referred as the α-relaxation process. As mentioned in Fig. 3, depending on the cooling rate used and the temperature reached, different glass can be formed. There are strong glasses for which the structural relaxation times follow the thermal Arrhenius activation over a constant energy barrier (similarly to high-temperature relaxations).

$$\tau(T) = \tau_{\mathrm{A}} \exp\left[\frac{E_{\mathrm{A}}}{T}\right]. \tag{28}$$

The following notations are used: the index A will be replaced by 0 in the low-temperature regime and by ∞ in the high-temperature regime (for simple liquids). In Eq. 28 and the following relations (Eq. 29-. 32), the activation energy is scaled with the Boltzmann constant $\mathrm{K_B}$ and has the unit of temperature. There are also fragile glasses in which the energy barrier grows sharply with decreasing temperature (see Fig. 5). Here the well-known *Vogel-Fulcher Tamman* (VFT) law is used:

$$\tau(T) = \tau_{\mathrm{VFT}} \exp\left[\frac{E_{\mathrm{VFT}}}{T - T_{\mathrm{VFT}}}\right], \tag{29}$$

where E_{VFT} is a quantity related with the activation Energy barrier. T_{VFT} is the so-called "*Vogel* ideal glass transition temperature" at which the relaxation time diverges. Nevertheless, the physical origin of the VFT relation has not yet been fully understood. [181, 182, 183] More recent relations have been defined for describing the τ-temperature dependence for fragile glasses. That is the *Rössler* approach, which was recently tested in experimental studies [184, 185, 186] on various molecular and polymeric glass formers and in simulation works [101, 100] on water and silica-like liquids respectively.

$$\tau(T) = \tau_{\infty} \exp\left[\frac{E_{\infty} + E_{\mathrm{c}}(T)}{T}\right]. \tag{30}$$

The temperature-dependent contribution to the energy barrier $E_{\mathrm{c}}(T)$, is interpreted as a collective excitation energy accounting for cooperativity in the motions between particles and is assumed to have an exponential temperature dependence. It can be accessed through this relation:

$$E_{\mathrm{c}}(T) = T \log(\tau/\tau_{\infty}) - E_{\infty}\,, \tag{31}$$

or by means of an exponential fit giving as output μ and T_A.

$$E_{\mathrm{c}}(T) = E_{\infty} exp\left[-\mu\left(\frac{T - T_{\mathrm{A}}}{E_{\infty}}\right)\right]. \tag{32}$$

Here, μ can be considered as a generalized fragility and T_{A} as a reference temperature defined such a way that $E_{\mathrm{C}}(T_{\mathrm{A}}) = E_{\infty}$.

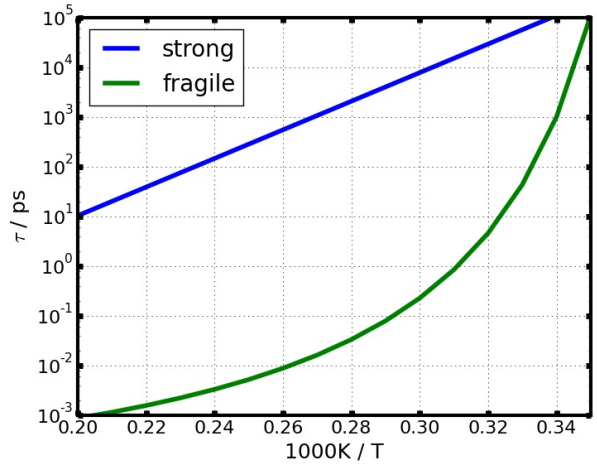

Figure 5: Strong relaxation process characterized by a constant energy barrier in comparison to fragile relaxation process defined by a temperature dependent energy barrier.

Several theories and views have been proposed to picture the behavior of particles in the system during the glass transition. We will briefly present some of them in the succeeding paragraphs.

4.2 Adam-Gibbs theory

The temperature of singularity T_{VFT} implies the possibility of an existing phase transition in glass forming liquids which might be dynamic or thermodynamic related. The prediction of *Kauzmann* [187] suggests that this transition should be thermodynamic related, by proposing that the transition is accompanied by a vanishing of the excess entropy at a finite temperature (the *Kauzmann* temperature T_K). T_K is supposedly nearly similar to T_{VFT} as pointed in Ref. 188. Following the idea of a thermodynamic glass transition, *Gibbs and Di Marzio* [189] have also developed a theoretical framework based on the entropy vanishing idea. Starting from the definition of the excess entropy of supercooled liquids which is the difference between the liquid entropy to the crystal entropy (assuming that the liquid vibrational entropy is almost equal to the crystal entropy); it can be approximated as the entropy related with possibly distinct liquid configurations and is also generally called configurational entropy. *Adam and Gibbs* proposed a relation of such vanishing configurational entropy (S_c) to dynamical slow down leading to the following *Adam-Gibbs* relation [113]

$$\tau(T) \propto \exp\left(\frac{CN}{TS_c}\right), \tag{33}$$

which suggests that the time scales growing with reduced temperature is driven by the vanishing excess entropy. C is proportional to E_∞ and N is the total number of particles in the system. This relation has been validated by experimental and computer simulation data showing relaxation times and viscosities of several supercooled liquids. [190, 188, 191, 192] A simple understanding of this relation is that as the configurational entropy decreases and eventually goes to 0, the dynamics hugely slow down since they remain smaller available configurations that particles can undertake and this considerably restrict the mobility of particles. *Adam and Gibbs* have then proposed in Ref. 113 that a supercooled liquid progressively organizes in large and large regions that have to cooperatively rearrange as the temperature decreases. These regions are referred as 'cooperatively rearranging' regions (CRR) and sketch in Fig. 6. One can see that the diffusion of an atom from the orange position to the pink position in the low density liquid (Fig. 6(a)) is pretty easy. However, for the atom to move from the orange to pink position in the high density liquid (Fig. 6(b-c)), the surroundings atoms (green circles) have to accommodate in order to provide a free empty site as shown in Fig. 6(c). But these regions are small

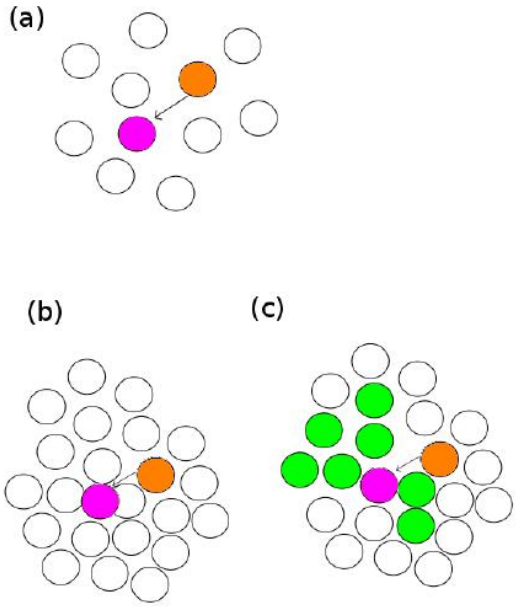

Figure 6: Schematic view of the rearranging process of CRR. (a) shows the diffusion of an atom from the orange to the pink position in a low density liquid, while (b) and (c) corresponds to the process in a high density liquid in which the diffusion of the orange atom to the pink position involves the rearrangement of the neighboring atoms (green color) in order to provide a free site where it can sits. Sketch adapted from Ref. 180 originating from Richard Jones, Soft Condensed Matter (2002). [193]

enough such that they can rearrange independently of their surroundings and they can hence undertake a constant number of states Ω (which neither varies with temperature or with the size of the CRR) in such a way that the total number of configurations of the system N_{total} reads $N_{\text{total}} = \Omega^{\frac{N}{n}}$ with n numbers of particles present in CRR. The configurational entropy S_{c} can be expressed as the logarithmic density of the number of stable states.

$$S_{\text{c}} = \frac{\log N_{\text{total}}}{N} = \frac{\log \Omega}{n}\,. \tag{34}$$

If we assign a typical length scale ξ as the size of these cooperative regions, then n should be related to ξ^d in which d depends on the shape of the CRR. n should also be inversely connected to the energy barrier crossed during a rearranging process, this relation then leads again to eq. 33. The *Adam-Gibbs-Di Marzio* (AGDM) theory provides a simple viewing of the *Kauzmann* entropy crisis in terms of a thermodynamic phase transition, it also relates configurational entropy and size of the correlated regions (and thus energy barriers) such that it can picture the super-Arrhenius increase of the relaxation time in fragile systems. The theory assumes that the liquid–crystal difference of the specific heat ΔC_{p} is almost not temperature dependent. Knowing that by definition the $S_{\text{c}}(T_{\text{K}})$=0, the configuration entropy at a specific temperature can be written as

$$S_{\text{c}}(T) \sim \Delta C_{\text{p}} \frac{T - T_{\text{K}}}{T_{\text{K}}}\,. \tag{35}$$

When combining Eq. 33 and Eq. 35, one can thus write:

$$\tau(T) \propto \exp\left(\frac{A}{T - T_{\text{K}}}\right), \tag{36}$$

analogous to the VFT relation of Eq.29. Nevertheless, this theory presents some limit. First of all it does not take into account the possible transition from non-activated to activated dynamics. Moreover, the assumption that CRR of size ξ can occupy a finite number of configurations such that it is sufficient for a relaxation of the system seems less probable. Since it means that the few number of configurations that they can undergo does not depend on the size of the domains. Therefore, the theory has been revisited by *Kirkpatrick, Thirumalai and Wolynes* [114] when defining the mosaic theory which solves this ambiguity by allowing that the number of states available to a CRR exponentially increases with the size of domains.

4.3 Random first-order theory (RFOT) or mosaic theory

The following explanation of the RFOT theory can be found in the reviews of *Cavagna* [119] and *Biroli&Bouchaud* [194] as well as the paper of *Karmakar et al.* [120]. *Kirkpatrick, Thirumalai and Wolynes* [114] have proposed that one should consider the possible existence of a dynamic transition at a finite temperature bigger than T_{K}. For temperatures situated between the temperature of dynamic transition and T_{K}, a large amount of metastable states are possible and their multiplicity tends to vanish close to T_{K}. Following the dynamic transition idea, they have also suggested [114, 115] that there exists a finite length scale beyond which it becomes entropically favorable for regions of a liquid initially in one configuration to make a transition to any one of the equivalent metastable states. The free energy drive to rearrange a droplet of size R is ensured by the fact that such region has an exponentially large number of available states and is related to the excess entropy of the most probable metastable states at the given temperature. It can be expressed as followed.

$$\Delta F_1 = -TS_{\text{c}}(T)R^d\,. \tag{37}$$

While there is a price to pay arising from the surface tension of the created interfaces between the different structures associated to the different metastable states. Considering a system at a given temperature

T, a certain region in it of size R may rearrange due to thermal fluctuations and undertake the next available metastable state, such that there is a mismatch of the interfaces between the old and the new state. The free energy cost corresponding to this transition can be written as:

$$\Delta F_2 = \gamma(T) R^{\theta}\,, \text{ with } \theta \leq d-1\,; \tag{38}$$

where $\gamma(T)$ is a generalized surface tension and θ is an exponent which both depend on the shape of the rearranging region. For a spherical shape, θ is 2 and γ is related to the energy per unit area.

In analogy to the classical problem of nucleation of crystal, for small R, ΔF_2 wins over and the formation of a droplet is not favored, while for any size R larger than the so-called 'mosaic length' ξ, the entropic drive dominates. Thus ξ is fixed by the balance between Eq. 37 and 38.

$$\xi = \left(\frac{\gamma(T)}{TS_{\mathrm{c}}(T)}\right)^{\frac{1}{d-\theta}}\,. \tag{39}$$

This means that the typical length scale ξ increases with a decrease of the excess entropy which is consistent with the AGDM theory of the last section. However, the number of accessible metastable states are not constant in the case of large nucleating droplet of size $R > \xi$ but scales as $\exp(R^d S_{\mathrm{c}})$. In case $R < \xi$, the surface tension energy cost ΔF_2 between interfaces is larger than the entropic gain ΔF_1 in going to the next available states such that the number of explored states scales as 1. At end, one can further make a direct comparison between the AGDM and the RFOT theory by expressing ξ in dependence of temperature starting from Eq. 35, and remembering that within the AGDM $\xi \sim n^{1/d} \sim (1/Sc)^{1/d}$.

$$\xi_{\mathrm{RFOT}} \approx \left(\frac{1}{T-T_{\mathrm{K}}}\right)^{\frac{1}{d-\theta}} \,, \xi_{\mathrm{AGDM}} \approx \left(\frac{1}{T-T_{\mathrm{K}}}\right)^{\frac{1}{d}}\,. \tag{40}$$

One can observe that the RFOT theory predicts a sharper increase as compared to the AGDM theory.

4.4 Mode Coupling theory (MCT)

The brief overview of the MCT here presented can be found in the paper of *Ediger et al.*, [195] *Reichmann* & *Charbonnea*, [196] and *Karmakar et al.* [120]. MCT approach [197, 198, 199] is a nonlinear dynamical theory for the behavior of density correlation functions in fluids. The original work, [197] generally referred as the 'idealized' MCT predicts a divergence of relaxation times at a temperature $\mathrm{T_{MCT}}$ as a power law with a universal exponent ϕ.

$$\tau \approx (T - \mathrm{T_{MCT}})^{-\phi}\,. \tag{41}$$

MCT can clearly depict the relaxation processes as a composition of different dynamical regimes in the density correlation function $C(t)$ (see Fig. 7) namely the cage regime (also named as β-relaxation) and the structural α-relaxation.

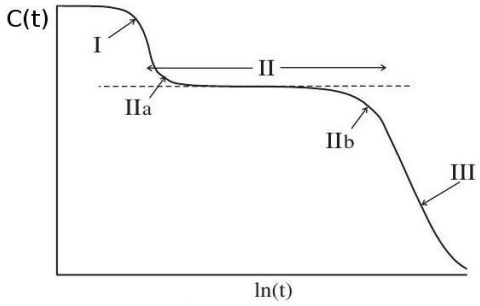

Figure 7: Schematic view of the correlation decay in MCT, the vibrational regime (I) is not the target of the MCT. But the decay occurring immediately before (IIa) and after (IIb) the plateau regime as well as the α-process (III) are qualitatively well pictured by the MCT. This figure is adapted from *Reichmann* & *Charbonneau*. [196]

The early decay IIa is described by a power-law decay.

$$c(t) \sim f + At^{-a}\,. \tag{42}$$

The decay IIb from the plateau is also described by a similar power law.

$$c(t) \sim f - Bt^{-b}\,. \tag{43}$$

The exponent a and b are related as shown in Ref. 196. Finally, at very long times, this decay is followed by the α-decay which is a stretched exponential of the KWW type. This sequence of quantitative relaxations processes has been verified experimentally for fragile liquids using light scattering [200, 201] and neutron scattering. [202, 203]
The major failure of the MCT is its prediction of a sharp τ divergence near T_{MCT}. Since T_{MCT} is greater than T_g, this divergence itself is somehow abstract as it implies a kinetic arrest to a non-ergodic phase at temperatures where the system is still ergodic (fluid). Another weakness is that it does not describe real systems below the crossover temperature T_{MCT}. Lastly, the power-law divergence performs poorly (see Ref. 195) over a wide range of temperatures in comparison to the VFT law (Eq. 29) or the *Rössler* approach (Eq. 30).

4.5 Potential energy landscape description

The description above will be based on the review of *Cavagna*. [119] *Goldstein* [204] studies the evolution of the system in the space of all the configurational degrees of freedom namely the phase space. The potential energy landscape (sketched in Fig. 8) of the system can be defined, which is the surface of the total potential energy of the system. Each of the different states available to the system is represented by a point in the phase space, and the dynamics of the system can be thought of as the motion of this point over the potential energy landscape. The local energy minima represented in the potential energy landscape correspond to locally stable configurations of the system. The configuration of the absolute minimum (the ground state) is the crystal. The excitations over the crystalline ground state can be caused by the presence of defects into the crystal. Next to these defected and polycrystalline minima, there will be many local minima associated to configurations that do not have long-range crystalline order. These are amorphous, or glassy energy minima possessing a potential energy lying at higher energy niveau in comparison to the crystal one. The *Goldstein* view of the glassy state is that at low enough temperature, supercooled liquids may explore the space of all system coordinates through activated jumps between different amorphous minima of comparable energy, separated by potential energy barriers.

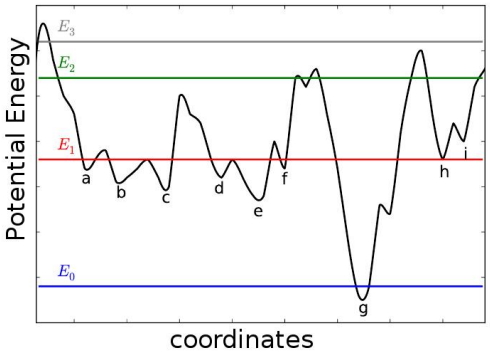

Figure 8: Sketch of the potential energy landscape showing different energy mimima. g is the crystal ground state and with a thermal energy E_0, particles can vibrate around this absolute minimum. With the thermal energy E_1, the system can occupy any avalaible state of lower energy mimimum as compared with E_1, these are states a-f. Local hoppings can arise between equivalent states such as between b and c, as well d and e. With the thermal energy E_2, the system can flow between states a-f, or from state h to i. With the higher thermal energy E_3, the system can flow over the whole phase space and behaves as a simple liquid. This figure is adapted from Ref. 180.

Within *Goldstein*'s picture, activation is the principal mechanism which drives diffusion and thus at very low T the system vibrates within an amorphous minimum of the potential energy during a certain time but can also jump to equivalent energy minima. At much higher temperature, the *Goldstein*'s scenario breaks down at the point where the thermal energy becomes higher or comparable to the typical potential energy barriers. Hence at high temperature, the theory of the activation itself is a very rough approximation of the truly high-T dynamics as activation only holds when the barrier is much larger than thermal fluctuations. Indeed in the high-temperature regime, local rearrangements are dictated by particles flowing. One can hence define a conceptually useful threshold temperature (T_x) which separates a low-T activated viscous regime from a high-T non-activated and fluid regime. 2 dynamical processes can be distinguished from the *Goldstein*'s scenario below T_x. The time regime due to the vibrational relaxation within a potential energy minimum, and a long time relaxation manifested by hoppings between different energy minima which grow up exponentially with reduced temperature. This view agrees very well with the two step relaxation of the dynamical correlation function and one can state that vibrations in the phase space around a single potential energy minimum are associated to vibrations of particles within their cages, while crossing a potential energy barrier, the system looses the memory of the starting configuration.

The limit of the *Goldstein* prediction is that at temperature bigger than T_x, two step relaxation processes also occur through in this temperature range activated dynamics are not the main mechanism of diffusion. Thus, simply assigning the α decay to activated barrier crossing does not apply at all temperatures, specifically in the fragile regime, while this mere picture applies well for strong glass formers.

4.6 Elastic models (Shoving model)

The starting point of the elastic models is that viscous liquids are viewed as 'solids which flow'. The view is rationalized by considering the extremely large viscosity of glass-forming liquid upon approaching

the glass transition. Meaning that more molecular motions are dominated by vibrations within energy minima as in the case of solids, and only some molecules are able to flow, thus we have less molecular rearrangement events. The model assumes that viscous liquid are almost not distinguishable from disordered solids. Therefore, *Hall&Wolynes* [205] have proposed to discuss viscosity by adopting a harmonic approximation to define the intermolecular potential. The idea was to connect the potential energy minima in which atoms move to the elastic constants such that the viscous flow process can be pictured by estimating the rates with which molecules move from one equilibrium position to the next. This leads to the prediction that the activation energy is related to the MSD of molecules in their vibrations around a potential energy minimum ($\langle u^2 \rangle$).

$$\frac{E}{K_B T} \propto \frac{a^2}{\langle u^2 \rangle}. \tag{44}$$

Here a is the intermolecular distance. The shoving model introduced by *Dyre et al.* [206, 207, 208] proposes that the displacements events are generated by thermal fluctuations triggering a sufficient expansion of a local free volume, leading to the conjecture that the structural relaxations time are related to the high-frequency shear modulus. This assumes that the barrier height is mainly defined from shoving aside the surrounding liquid and the energy cost from separating the flowing event molecules are neglected. In this way the energy barrier is proportional to the instantaneous shear modulus: $E(T) \sim a^3 G_\infty$. The relaxation times can then be expressed as:

$$\tau(T) \approx \exp \frac{a^3 G_\infty}{K_B T} \exp \approx \frac{\rho^{-2/3}}{\langle u^2 \rangle}, \tag{45}$$

in which ρ is the density and $\langle u^2 \rangle$ is the local cage size. It is often mentioned as the Debye-waller factor [170] and considered as the MSD after a typical time of 1 ps. This last point constitutes one limit of this model since the well determination of the cage onset is sometimes blurred up by the vibrational decay. [101]

4.7 Elastically collective nonlinear Langevin equation (ECNLE)

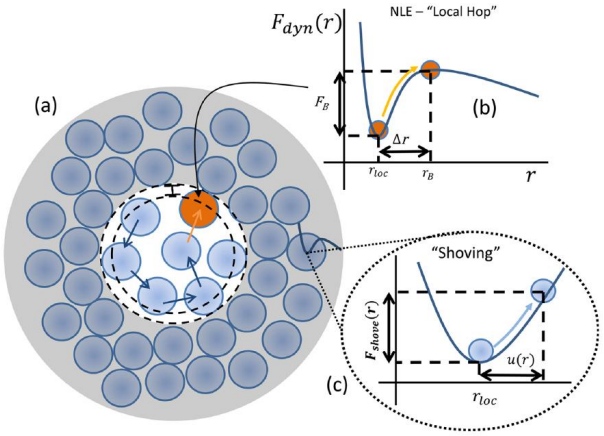

Figure 9: Sketch of the different elements described by the ECNLE theory: (a) local hopping process and cage expansion leading to a long ranged collective elastic barrier, b) dynamic free energy defining the rearrangement of the local cage, (c) collective displacements of all particles outside the cage.

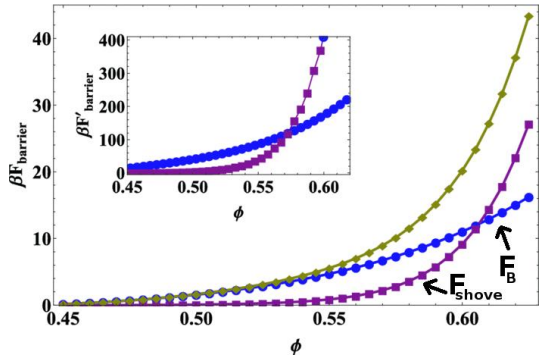

Figure 10: Different contributions to the total energy barrier: the blue circles are the NLE local barrier (F_B), the red squares are collective elastic barrier (F_{shove}) , and the yellow diamonds represent the total barrier. These are calculated for various volume fraction of hard sphere suspensions. Figure adapted from Ref. 117. The inset curves show the corresponding first derivatives.

The ECNLE theory elaborated by *Schweizer et al.* [116, 117, 118] is a more general approach starting from the shoving idea but explicitly accounting the rearrangement of the neighboring atoms. It splits the energy barrier associated to structural relaxations into two terms: a term describing local activated hopping and a second term accounting for cage expansion represented by long-range collective displacements of particle outside the cage. The second term then involves the typical length scale of CRR. Fig. 9 illustrates the idea of the theory, Fig. 9 (a) is a scheme of the local hopping process and the corresponding cage expansion which together contribute to the long range collective elastic barrier. Fig. 9 (b) shows F_B the dynamical free energy barrier (derived from the nonlinear Langevin equation (NLE) approach [209, 210]) required for the rearrangement of the local cage. While F_{shove} is the elastic energy contribution of the energy barrier which originates from the collective motion due to the expansion of neighboring clusters for free volume creation.

$$\frac{F_B}{K_B T} \approx \frac{A}{\sqrt{\langle u^2 \rangle}}, \qquad \frac{F_{elastic}}{K_B T} \approx \frac{\xi^2}{\langle u^2 \rangle}. \tag{46}$$

The structural relaxation in the ECNLE theory thus reads

$$\tau(T) \propto \exp\left(\frac{F_B + F_{elastic}}{K_B T}\right) \propto \exp\left(\frac{A}{\sqrt{\langle u^2 \rangle}} + \frac{B \cdot \xi^2}{\langle u^2 \rangle}\right). \tag{47}$$

Both energy contribution calculated for the case of hard sphere suspensions of various volume fraction are shown in Fig. 10. F_B dominates at low volume fraction (equivalent to the high-temperature regime for supercooled liquids) while F_{shove} ($F_{elastic}$) dominates at large volume fraction (equivalent to the low-temperature regime for supercooled liquids). The ECNLE somehow combines the *Goldstein* approach with the MCT approach but tries to overcome the limitations of MCT by enabling cooperative collective rearrangements below T_C. However, a limit of this ECNLE view is that it somehow underestimates energy barriers by the definition of its single particle dynamic which is mean-field like.

4.8 Water in the supercooled regime

As already stated in the introduction (chapter. 1), liquid water at low temperature is a convenient example of supercooled liquid. While simple liquids get compressed with reducing temperature, liquid water starts expanding when its temperature drops below roughly 277 K, [69, 211] temperature close to the melting temperature T_M of Fig. 11. This can be visible in nature for example in seas of cold

regions in which one can observe ice floating at the sea surface. At much lower temperature, that is in supercooled water (metastable) phase, the coefficient of thermal expansion, isothermal compressibility, and constant-pressure specific heat capacity increase sharply and reach a maximum at a certain temperature below which it becomes difficult to access experimentally liquid water as water immediately crystallize (via homogeneous nucleation). This limit defines the "no-man's land" and is located down to the temperature T_H (temperature marking the homogeneous nucleation curve) indicated in Fig. 11. The liquid-liquid phase transition (LLPT) hypothesis [68] is an approach that has been introduced to describe the enriched behavior of liquid water at low temperature. The LLPT approach is based on MD studies of the structural properties of water as well as the state equation. It states the existence of a critical point at low temperature separating water into two distinct fluid phases: a low-density liquid (LDL) phase at small pressure and a high-density liquid (HDL) at large pressure. The separating line is indicated by the gray line of the "no-man's land" terminating exactly at the critical point ($T_C \approx 220$ K, $P_C \approx 0.1$ GPa). [69] The LLPT prediction has been approved by several authors. [212, 213, 214, 215, 216, 87, 217, 218, 219, 88, 220, 78] Moreover, it was proposed that the critical end point of a LLPT might instigate the crossover from the dynamical FS behavior in its vicinity in water [68, 81, 87, 88, 78, 79] as well as in silica [81, 82, 83, 84, 85, 86, 87, 88, 89] but it is still a hot topic of debate [220, 221, 222] on which we will add our contribution by looking at silica liquid families differing by the bond polarity (topic covered in chapter. 7).

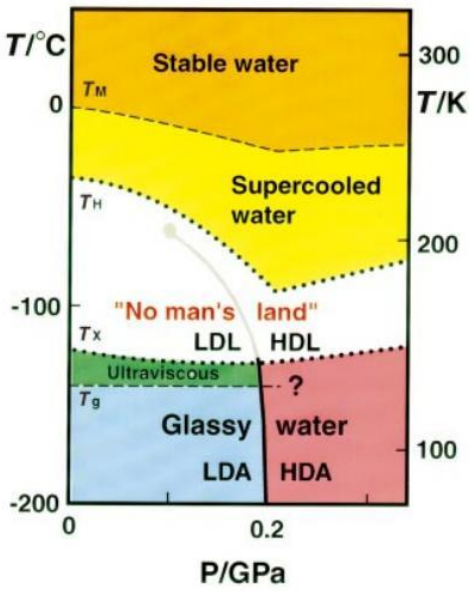

Figure 11: Schematic P-T diagram illustrating the various phases of liquid water while modifying the pressure and the temperature consistently. This figure is adapted from Ref. 211.

Below the "no-man's land" region, glassy water can be obtained and the glass transition of water is estimated as $T_g \sim 130$ K. All amorphous solids type of water are generally partitioned into low-density amorphous ice (LDA) and high-density amorphous ice (HDA), which slightly differ to each other by the microscopic structure and are reachable depending on the preparation method and procedure. [223, 224, 225, 226, 227, 228]

4.9 Contact angle theory

As we are also looking at the wetting properties of aqueous mixtures in silica surface, it is necessary to review some intrinsic principles such as the adhesion process in surface. Surface energy determines the

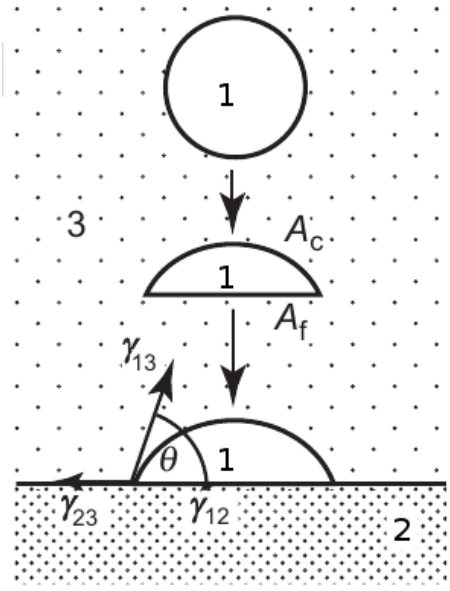

Figure 12: Scheme of a water droplet (labeled as medium 1) initially in vacuum (medium 3) processing to wet a flat silica surface (medium 2). A_f is the surface directly in contact with medium 1 while A_C is the curved surface in contact with vacuum. This figure is adapted from Ref. 229.

deformation of macroscopic liquid droplets while adhering to a surface. Generally, a droplet of constant volume develops an angle in order to minimize the total surface energy of the system: this is the contact angle. To test how well is a surface wetted by water, the contact angle is a good tool as it directly shows the interplay between the different surface forces involved during the wetting process. Starting from Fig. 12 showing a water droplet (medium 1) in vacuum (medium 3) approaching and settling on a flat silica surface (medium 2). The final total surface energy (W_{tot}) of the system can be expressed as

$$W_{\text{tot}} = \gamma_{13}(A_c + A_f) - W_{123}A_f \,. \tag{48}$$

The equation of an equilibrated wetting droplet reads

$$\gamma_{13}(\mathrm{d}A_c + \mathrm{d}A_f) - W_{123}\mathrm{d}A_f = 0\,, \tag{49}$$

and knowing that $\mathrm{d}A_c/\mathrm{d}A_f = \cos\theta$, then one obtains

$$\gamma_{13}(1+\cos\theta) = W_{123} = \gamma_{23} + \gamma_{13} - \gamma_{12}\,. \tag{50}$$

Here, γ_{13}, γ_{23}, γ_{12} are respectively the surface energy between water and vacuum, silica and vacuum, and water and silica. W_{123} is the adhesion work of water and silica in vacuum. Eq (50) can be rewritten as followed leading to the Young's equation:

$$\gamma_{13}\cos\theta = \gamma_{23} - \gamma_{12}\,. \tag{51}$$

In the case of a hydrophilic silica surface, the surface energy between water and silica γ_{12} wins over the surface energy between silica and vacuum γ_{23}, and thus $\gamma_{23} - \gamma_{12} < 0$. The opposite applies for hydrophobic surfaces.

5 Wetting of water on silica surfaces

At this stage, we have gone trough all the prerequisites which are necessary to understand the outcome of this thesis. We probe the physical properties by inspecting the behavior of liquids in bulk (for example silica bulk) or in confinements. As for the confinement, we can define either a neutral confinement in which the confined mobile liquid and the confining immobile matrix are of the same nature, namely are composed of the same atom types; or we can examine the case for which the molecular entities of the fixed matrix are different than the ones of the mobile liquid. This would be the subject of the two following chapters.

The first topic of our results is on the wetting mechanism of water droplets on silica surfaces. This chapter will show the results of the simulations of water droplets in partially filled pores at first, and secondly of a water droplet wetting silica slabs. In each case, the silica models utilized are the BZ [40] and the GT [42] potentials. The study has been inspired by experimental reports [11, 17] from the group of *Professor Buntkowsky* from the TU Darmstadt which have shown that water in partially filled silica pores fully wets the silica surface. These findings were based on a measurement of the absorption of water in MCM-41, SBA-15 [11] and in CPG [17] pore material within the ^{1}H-MAS solid state NMR spectroscopy. From the spectra obtained, they then infer the ^{1}H chemical shifts of the hydrogen atoms of water dipole in the pore and reported that during the filling process, the inner surface of the pore is initially entirely covered, and with increasing water content in the pore, the center of the pore gets occupy by the remaining water molecules. These findings that water wets the pore surface wholly was not corroborated by our first simulations using the standard BZ silica model. Hence, we tested another model successfully.

5.1 Simulation set-up

Simulation details

An amorphous cylindrical nanopore of roughly 4 nm of diameter and silica slabs of different thicknesses have been fabricated in our group. [230] A crystalline cell of SiO_2 with a box length of approximately 6.08 nm is built. The system is initially melted at 5000 K and cooled to room temperature with the method described in Ref. [230], after that a cylindrical cavity of ~ 4 nm diameter is cut. Details about the fabrication process are presented in Ref. 230. The surface of the silica pore and slab established show a surface concentration of hydroxyl groups of about 7.5 nm^{-2} which corresponds to highly hydrated silica. Two types of oxygen atoms can be found in the silica nanopore or the silica slab relying on the number of silicon atoms with which they are connected. Bridging oxygens (O_{Si}) are bonded to two adjacent silicons and non-bridging oxygens (O_H) are attached to only one silicon and are mainly positioned at the surface. Hydrogen atoms are bonded to the O_H atoms so that the silanols groups (SiOH, $Si(OH)_2$) of the surface are formed. The bonded interaction parameters for silica atom sites are the ones of *Hill and Sauer*. [231] Apart from the hydrogen atoms of the silanols groups which can rotate, all other atoms in the silica pore and slab are immobile and constrained to a fixed position. Instead, water molecules are allowed to move within the pore. Liquid water is defined using 2 models: a set of 3 rigid sites given by the SPC/E [136] model and a set of 4 sites provided by the TIP4P/2005 [143] model. The main difference between both models is that TIP4P/2005 water model proposes a more ordered tetrahedral structure (as can be noticed when comparing the pore center data in Fig. 15 between each model). Nevertheless, these are two popular models which are useful to understand the dynamics of supercooled water. [232, 215, 233, 79, 101] The atoms of the silica substrate are interacting with the water sites via the Coulomb and the LJ potential in Eq. (60) (the LJ part represents the VdW contribution). The LJ parameters and the fractional charges for the silica sites are given in Table 1.

All simulations are performed within the NVT ensemble with a fixed room temperature $T = 298$ K

using a Langevin thermostat [137] with a coupling coefficient of 1.0 ps^{-1} and with the hydrogen atoms included in the Langevin dynamics. [140, 137] An integration time step of 2 fs is utilized and the trajectories are acquired for at least 30 ns after 5 to 10 ns of equilibration. PBC are set for the simulations of water inside the pore for calculating the long-range Coulombic electrostatic interactions with the PME summation using a cut-off of 1.2 nm. No PBC are defined for the simulation of water wetting silica slabs such as the full electrostatic and VdW interactions between all water droplet atoms and silica slab atoms are calculated.

Table 1: LJ potential parameters for silica interaction centers. * Constants are not indicated in the model and are chosen arbitrarily small.

Parameters	Sites	σ (nm)	ε (Kcal/mol)	q (e)
BZ [40]	Si	0.0178*	0.00000	1.283
	O_{Si}	0.27	0.45705694	-0.629
	O_H	0.3	0.45705694	-0.533
	H	0.0178*	0.00000	0.206
GT [42]	Si	0.25	0.0001	1.28
	O_{Si}	0.27	0.457	-0.64
	O_H	0.307	0.17	-0.74
	H	0.1295	0.0003657	0.42

Systems Description

The first part is based on simulations of water droplets inside the cylindrical pore of radius 2 nm. We use different pore filling ratios (with respect to the volume of the pore) varying from roughly 15 to 97 %. We approximate the filling percentage by assuming that in average 2700 water molecules are needed to completely fill a pore of this size. This estimation has been proposed in Ref. 38. In the case of moderate filling ratios, we test whether the initial configuration of the water droplet inside the pore has an effect to the obtained final configuration. We thus change the starting configuration of water and generate two sets of simulations: one in which water is initially placed at the pore center, the other in which water covers the pore surface. Each starting configuration is pictured by the VMD snapshot of Fig. 13(a)-(b). The position of atoms inside the pore are resolved from their radii (R) to the pore center as illustrated in Fig. 58. The results of the 15 % filling ratio are added in appendix (Fig. 88, Fig. 89).

Secondly, a flat silica surface is used as a hydrophilic substrate and we deposit on it a water droplet (see Fig. 13(c)). We perform several simulations with silica slabs of different thicknesses in the range 1-3 nm. The slab surface is 12.35x12.35 long and is chosen large enough to avoid that water molecules flow till the side of the surface. The water cluster used in this case contains roughly 469 water molecules.

5.2 Results I: water in partially filled silica pores

In this part, we show the results of the configurations of water in a partially filled silica pore for the two different silica models. We as well compare these results with a analytical calculation of the different possible phases of water in a cylindrical pore enabling us to interpret the findings. The analytical calculation has been performed by *Julian Geske* and presented in detailed in Ref [180].

5.2.1 Computational results

All quantities presented in this part are averaged over 15 ns after at least 5 ns of equilibration for each simulation. The opening simulations are on a pore completely filled with SPC/E (or TIP4P/2005) water molecules with a filling percentage approaching 97%. The aim is to check the structure of water

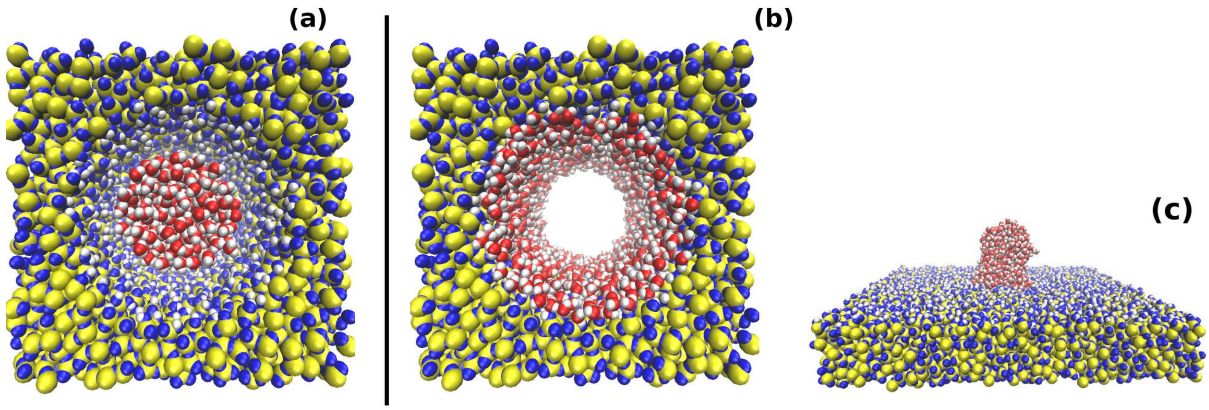

Figure 13: Top view of the two initial configurations used for the simulations in pore, labeled in the corresponding snapshots with "center" (a) and "surface" (b). The figures presented are for the case of 30% pore filling ratio. The side view of the initial configuration used for the simulation on a flat surface is added in (c), the thickness slab is roughly 2.5 nm. Si, $O_{Si,H}$, H are drawn in yellow, blue and white, whereas water atoms O, H are highlighted by red and white respectively. The snapshots are generated using the VMD program. [234]

molecules near respectively the GT and the BZ silica surface. The radial density profile plotted (as function of the distance to the pore center R) in Fig. 14 illustrates the number density of oxygens divided by the bulk density. The top curves (a)-(b) represent the profile with the SPC/E water model and the down curves (c)-(d) with the TIP4P/2005 water model. In the case of 97% filling ratio, the density in the pore center is nearly equal to the bulk density for both silica surfaces and water models, while a layering of water in the vicinity of the pore surface can be identified. This layering is consequent to the static energy landscape imposed by the fixed surface atoms of silica pore. Interestingly, the layering process is slightly more pronounced near the BZ surface (Fig. 14 (a)) in comparison to the GT surface (Fig. 14 (b)) for both water models. We then further analyze the local ordering of water molecules in the vicinity of both surfaces and also in the pore center, see Fig. 15. The local structure of water in the pore center is analogous for both silica model for a given water model. The distribution of the local order of water in the pore middle region shows a peak at $Q_i \sim 0.77$ and a small kink at $Q_i \sim 0.5$ for both water model. We can also state that TIP4P/2005 water shows a more ordered local structure as compared to SPC/E water. Oppositely, near the silica surface of both models, the local structure is distorted by the surface such that the distribution has a well pronounced peak at $Q_i \sim 0.5$ and a peak (TIP4P/2005) or kink (in the case of SPC/E water) at $Q_i \sim 0.77$. However, the local structure of water near the silica surface is somewhat more disturbed near the GT surface than near the BZ surface, since the small kink (or peak) at $Q_i \sim 0.77$ is considerably reduced in the case of the GT surface (see opened hexagons of Fig. 15). These are first indications that the GT silica surface interacts more with water molecules.

To get more insights about the equilibrated configurations of water in the pore for the GT and BZ surfaces, we simulate smaller filling ratios and different starting configurations. The pore filling ratios are in the range 30% - 65%. The density of water in partially filled pores is also plotted in Fig. 14. In order to see the extent to which the final configurations depend on the initial configuration, we tested the two different initial configurations shown in Fig. 13, where water is concentrated around the cylinder axis which is identified by "center", and at the pore surface which is represented by "surface". The "center" starting means that a water droplet is placed in the center of the pore and there is void between the water droplet and the silica surface; while the "surface" starting illustrates the results in which water layers are originally placed in the pore surface and creating a void in the pore center.

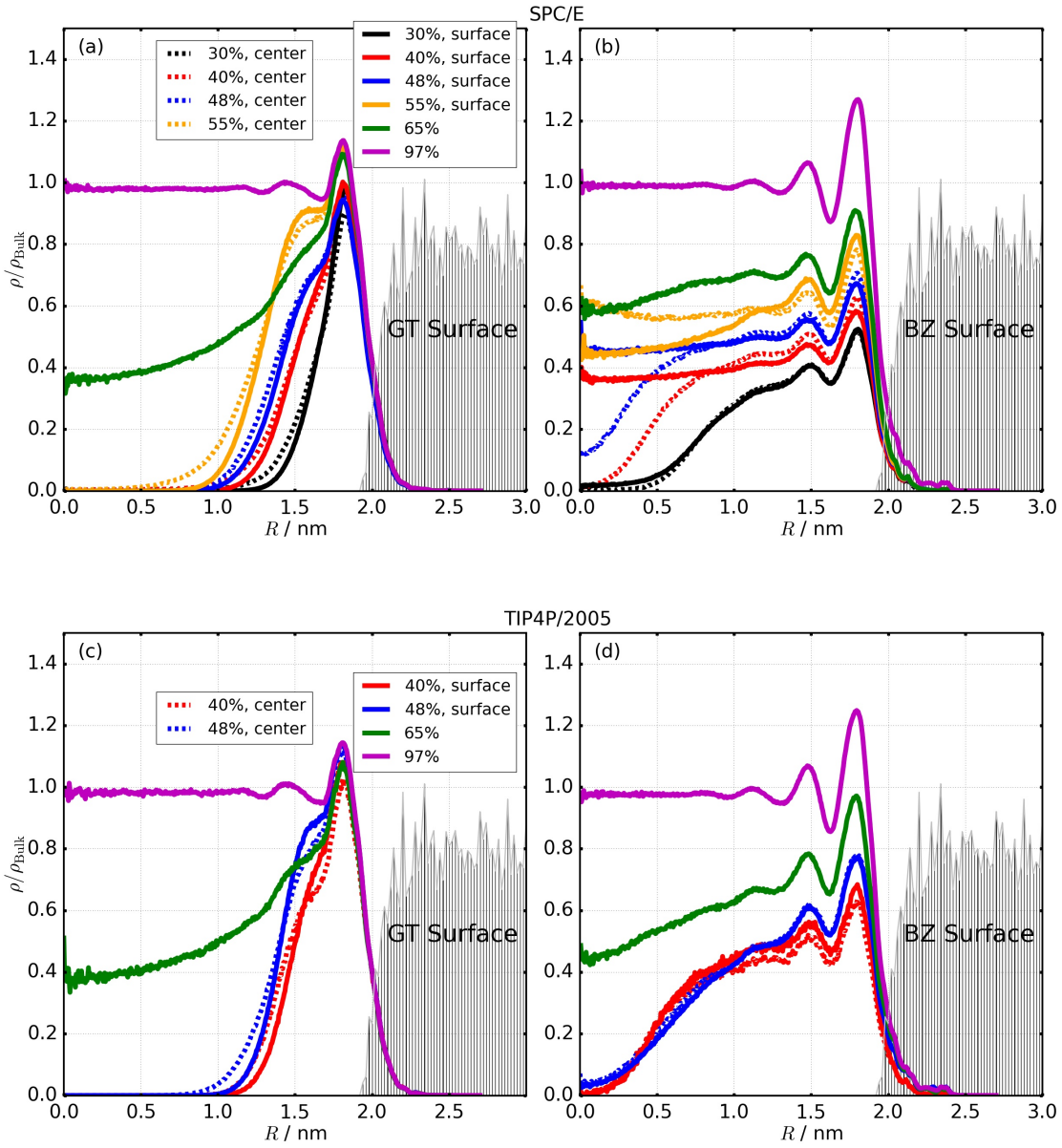

Figure 14: Radial density profile of water in the pore for different filling ratios and starting configurations, for the (a),(c) GT surface and the (b),(d) BZ surface. The gray area indicates the silica oxygens distribution and is arbitrarily scaled for an easy comparison. The number density of oxygens is weighted to the bulk density ρ_{Bulk}. The top figures (a)-(b) are for the oxygens of SPC/E water and the down (c)-(d) ones are for oxygens of TIP4P/2005 water.

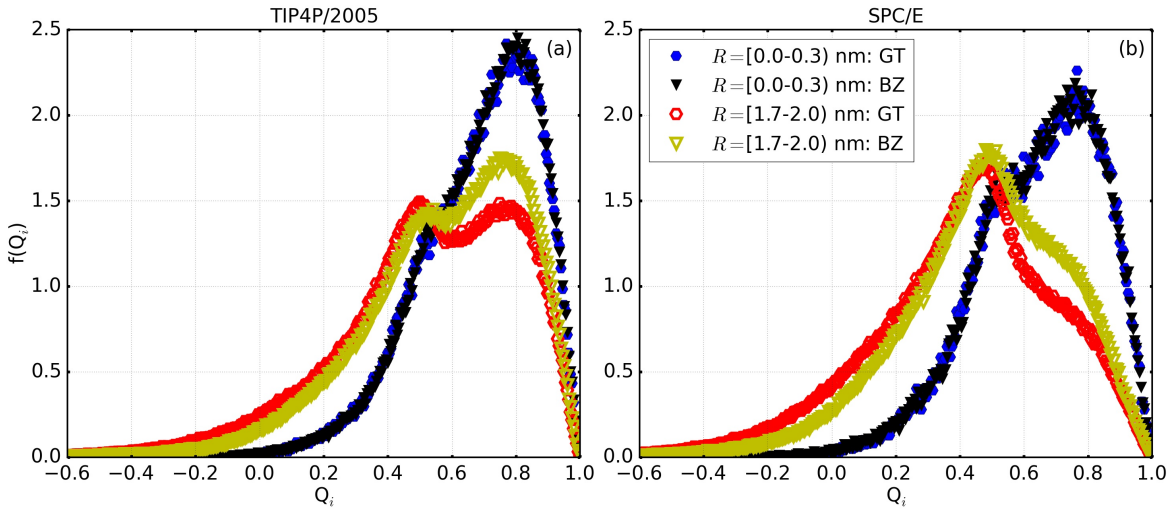

Figure 15: Distribution of the tetrahedral order parameter of water molecules lying near the pore center (close symbols) in comparison to water molecules lying near the pore wall (opened symbols) within 0.3 nm of the pore wall. This is plotted for the BZ and the GT silica surface. The left panel (a) indicates the distribution of TIP4P/2005 water molecules, and the right panel (b) the corresponding ones for SPC/E water molecules.

The radial density profile (Fig. 14) of water molecules (SPC/E or TIP4P/2005) in moderate filling ratios shows that water is closer to the GT surface. Indeed, The GT density profile displays only one peak for a filling ratio of 30%, indicating that all water molecules are in contact with the pore surface. Only after the first layer forms, a second layer develops, as is visible for the curves for filling ratios between 40 and 55%. Then at 65% filling ratio, water molecules also occupy the interior of the pore, revealing a configuration with a completely wetted surface and a compact water droplet in the pore interior. More importantly, these observations are independent of the water models investigated. The density profiles of SPC/E and TIP4P/2005 oxygens near the BZ surface in the case of intermediate filling ratios, show several layers of water within the pore, with a peak height that depends on the filling ratio. Moreover, the density profile strongly depends on the initial configuration (specially in the case of SPC/E water) with the initial configurations at the surface leading to final configurations with rather flat density profiles in the pore center. This suggests that for the initial configuration at the boundary ("surface"-starting), the water droplet forms a "plug" in the pore interior, while for the initial configuration in the center ("center"-starting), water forms some type of droplet sitting at the surface. Since the pore surface is rough, some water molecules can also be found inside the silica pore material.

In order to check the intuition obtained for the configurations of water inside the pore based on the density profiles, we next evaluated the distribution of SPC/E water molecules within a distance of 0.3 nm of the surface. This corresponds approximately to the first layer wetting the surface. Fig. 16 displays the resulting surface coverage by water molecules, with cylinder coordinates. This figure confirms that for the GT surface, the water droplet initially covers the surface completely, before filling the pore interior. In the case of the BZ surface, the pore surface is only partly wetted with water, and the final configuration often depends on the starting configuration for intermediate filling ratios. For instance, for 40% filling ratio with the "center" starting configuration, water molecules are localized in one angular segment of the surface but are covering the entire pore length, while for the "surface" starting configuration they are concentrated in only a part of the z range, but occupy all angles. These final configurations for moderate filling ratios are in a sense very plausible if one imagines how the initial configurations can

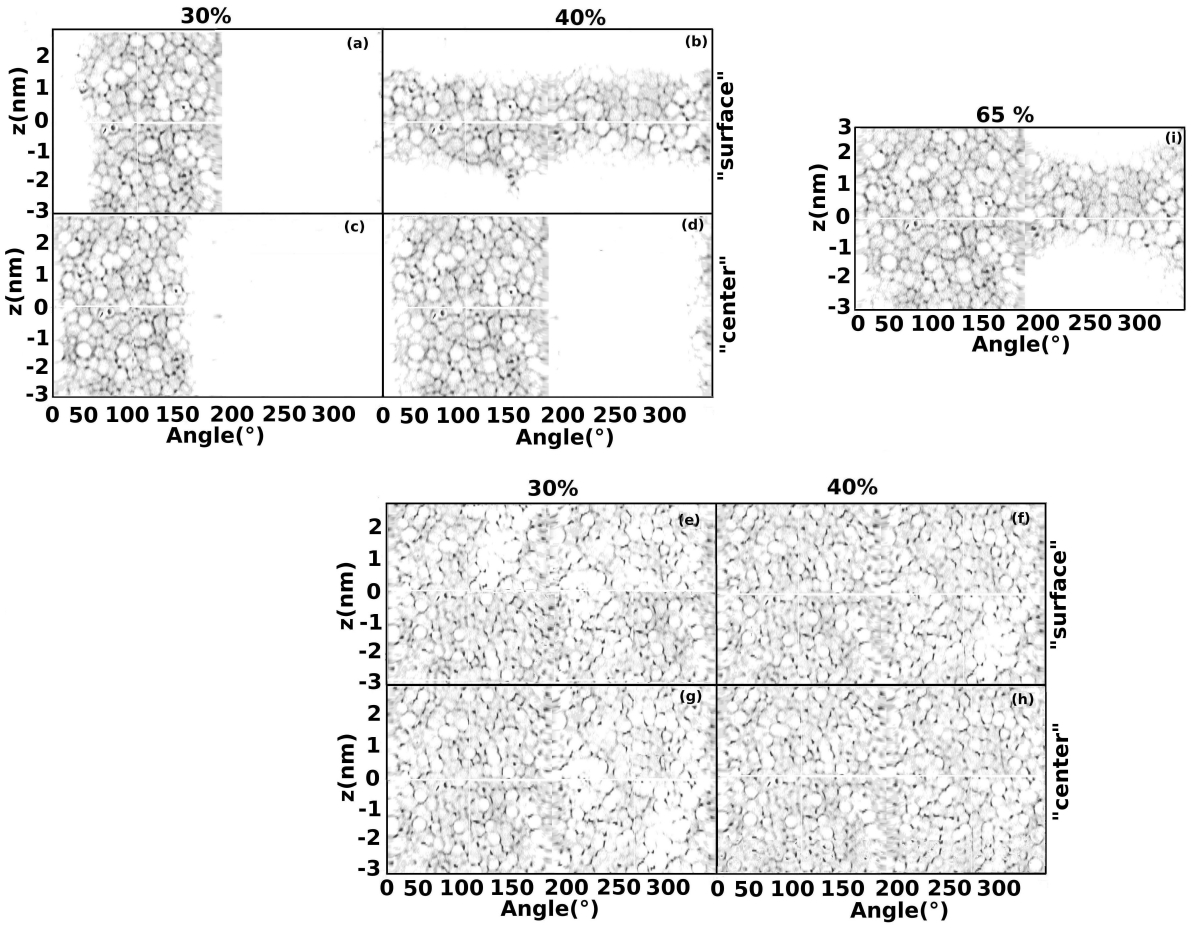

Figure 16: The water density at the pore surface, showing water molecules that are within a distance of 0.3 nm of the silica surface. For the GT surface (e-h), only filling ratios of 30 and 40% are displayed, since for larger filling ratios the surface is completely wetted. For the BZ surface, the top (a-b) graphs represent the "surface" starting configuration and the bottom graphs (c-d) stands for the "center" starting configuration, (i) represents the density at 65% filling ratio.

evolve with time in such a way that the water-surface interaction is not strong enough to favor an entire wetting of the surface. In fact, when the initial configuration has a water cylinder in the pore center, the whole cylinder gets attracted by the silica molecules under the effect of electrostatic and VdW interaction and moves as a whole towards the pore surface, covering a specific angular region of the surface. When the starting droplet sits at the pore surface, the water film may rupture along an angular line, and the droplet contracts itself to form a plug. Of course one of the two final configurations can lie at a lower free energy, however this free energy difference should not be large, though the transition between them will involve a sufficiently huge barrier that might not be overcome during the simulation time. When the filling ratio is lower (as can be seen for 30%), there is only one stable configuration which is observed independently of the initial configuration, that is the whole cylinder occupying a certain angular range over the pore length. These two possibly final configurations observed merge also for higher filling ratios (as can be seen for 65%), where the void left by the water droplet takes the shape of a droplet that sits at the pore surface.

This connection between the final configuration and the starting configuration is less noticeable with the TIP4P/2005 water model as shown in Fig. 14 and one might get the impression that the SPC/E water droplet at low filling ratios (particularly at 40 %) needs more time to be fully equilibrated. We have check that by plotting the evolution of the total electrostatic energy between water molecules of the water droplet at first, and between water molecules and the atoms of the pore wall in the particular case of 40 % filling. This can be easily computed using the NAMDENERGY code. [137] Fig. 17 shows the total energy obtained for the equilibrated configuration when the starting configuration of water is either at the center (dashed lines) or the surface (solid lines). We find out that near a specific surface (e.g GT), the energy of the equilibrated configurations always converges to a similar value for both starting configurations. Interestingly, the value of the energies (water-water or water-silica) at equilibrium near a specific surface are comparable between both water models. This suggest that the different ending configurations of the SPC/E water droplet in the 40 % center or surface startings (see Fig. 16), might be plausible metastable states of comparable energy. The energy plot also approximates a electrostatic energy between water and GT silica 8 times larger than the corresponding one between water and BZ silica, which goes in accordance with the previous observations.
Furthermore, we as well check how the stronger hydrophilicity of the GT surface influences in the formation of molecular bonds by evaluated the average number of hydrogen bonds (H-bonds) formed between water molecules, and between water molecules and silica molecules. We use the geometric criterion presented in chapter. 3. The resulting H-bonds profiles are shown in Fig. 18, in which we compare the profile near the BZ surface and the GT surface. For the BZ surface, the number of H-bonds between water molecules is comparable to the bulk value in the inner part of the pore for a filling ratio larger than 40% with the "surface" initial configuration. Also for the "center" initial condition, the bulk value is obtained for the water molecules in the interior of the water droplet. Not surprisingly, in the GT surface, the bulk value is only reached for filling ratios above 60%. This illustrates the fact that the BZ surface distorts the bulk water structure less than the GT surface. Accordingly, the number of hydrogen bonds formed between the silica surface and the water molecules is larger for the GT surface.
Interestingly, for both models it can be observed that the maximum number of water-silica H-bonds is already reached at $\approx$ 40% filling ratio, confirming that one and half layer of water molecules is sufficient to completely wet the GT silica surface. It is at first surprising that for the BZ surface, the number of water-silica H-bonds does not rise for filling ratios larger than 40% and stays considerably below the value of the GT surface (similar results have also been found with the TIP4P/2005 water in Fig. 90). In the particular case of 97 % where the surface is inevitably completely covered by water molecules, the H-bonds shared with the BZ molecules are still smaller. This can only be explained by different water orientations near the surface in the two models as revealed by the locally ordered structure near each surface in Fig. 15. In the appendix (see Fig. 91), we have also added the distribution of the scalar product between water OH bonds and the unit vector along the z-axis. It indicates that near the BZ surface

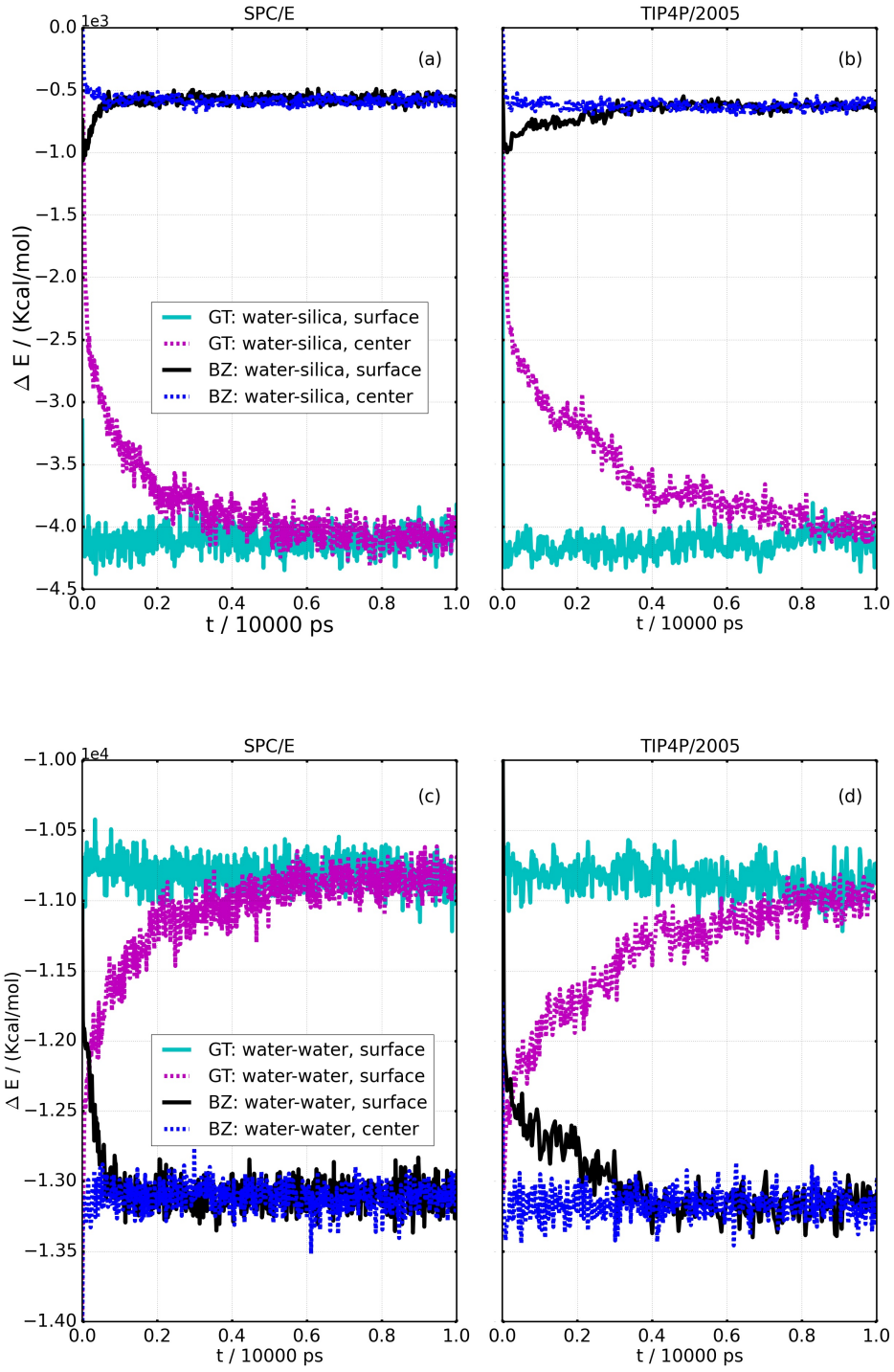

Figure 17: Total electrostatic energy between all molecules of the SPC/E (a) or the TIP4P/2005 (b) water in the systems and atoms of the silica wall of the GT model and the BZ model. (c)-(d) shows the corresponding energy between all water molecules of the systems near each silica surface type. The dashed lines are indicates the energy in the case for which water is initially placed at the pore center ("center"); while the solid lines corresponds to the equilibration of the surface initial configuration. These plots are for the 40 % filling percentage.

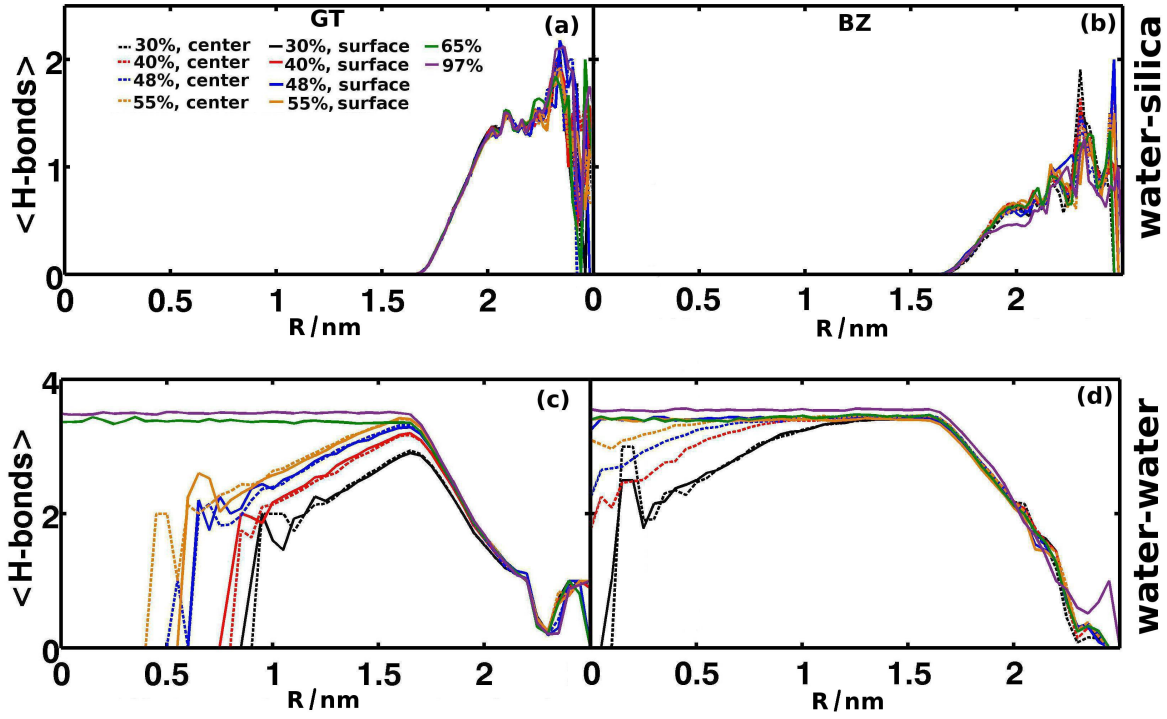

Figure 18: Average number of hydrogen bonds per water molecules between water and silica molecules (a-b) as well as water molecules to each other (c-d), for various initial conditions and filling ratios, as indicated in the legends. The results for the GT silica surface are plotted on the left-hand side in (a) and (c), and those for the BZ silica surface on the right-hand side in (b) and (d).

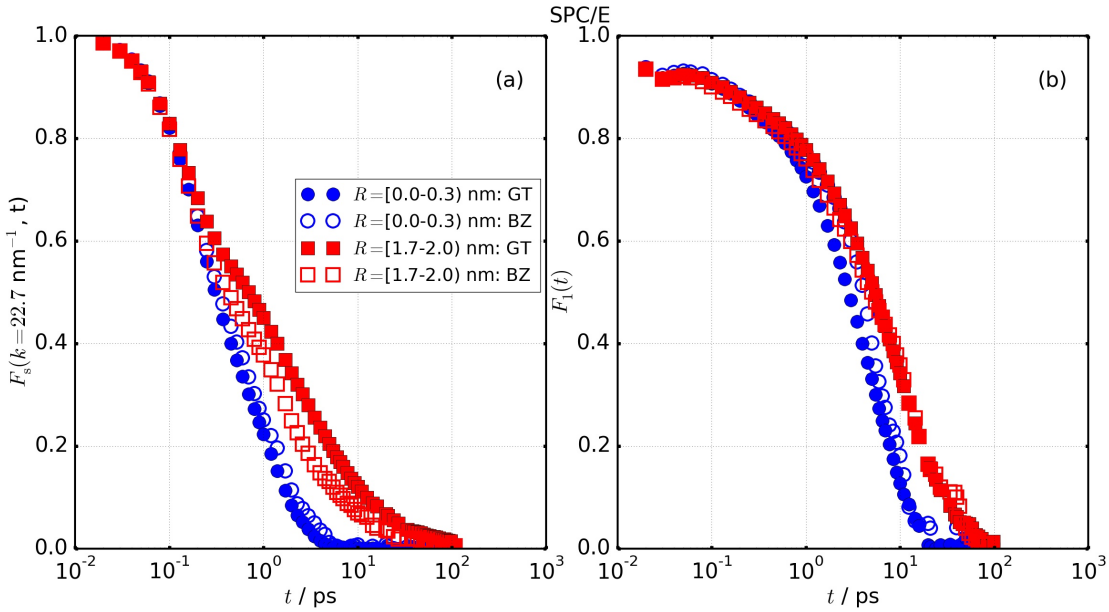

Figure 19: Intermediate scattering function (ISF) and orientational correlation function (OAC) of SPC/E water layers within 0.3 nm respectively to the pore center or the pore surface. The open symbols are with the BZ surface, and the closed corresponds to the GT surface. The scattering vector is k=22.7 nm^{-1} corresponding to the nearest neighbor atomic distance in SPC/E water.

the OH bonds of water molecules have a strongly preferred orientation, while this is not the case near the GT surface. This can be interpreted as only part of the water molecules can act as a hydrogen bond donor or acceptor near a BZ silica molecule, while near the GT surface all the water molecules have in overall the same tendency to share H-bonds with the surface atoms.

Finally, we have investigated a bit the dynamics of the water molecules in the GT and the BZ pore, by looking at the ISF and the OAC function of water molecules within 0.3 nm near the pore center or near the pore wall. We have analyzed (see Fig. 19) the ISF (probing the translational motion) and the OAC (probing the rotation of the water dipole moment) function for each layers near the BZ surface (opened symbols) and the GT surface (closed symbols). As expected the dynamics of the water molecules is slowed near each pore wall. However, the translation motion is faster near the BZ surface in comparison to the GT surface, suggesting that the hopping of water molecules between silica sites of the GT type is slower as they are tightly bound to the H-bonds contacts of the GT surface.

5.2.2 Theoretical evaluation of the phase diagram

This part has been performed by Julian Geske during his doctoral study, [180] but we will briefly show the main results since they are important to understand the different phases undertaken by water in partially filled pores. The different water configurations in the pore should be related to the competitive process between the different energies responsible to the formation of bonds between water molecules to each other and water molecules with surface molecules. We have thus performed a theoretical analysis that is based on surface energy minimization. We need, the surface area between the water droplet and vacuum which is denoted with A_1 and the surface area between the water droplet and the pore material that is labeled as A_2. The corresponding surface tensions are γ_1 which is the surface tension between water and vacuum, γ_2 representing the difference between the surface tension of silica and water with

the surface tension of silica and vacuum. The total surface energy of the wetting droplet can thus be written as

$$E_S = \gamma_1 \cdot A_1 + \gamma_2 \cdot A_2 \,. \tag{52}$$

By neglecting the entropy change between different phases, the configuration of the water droplet in the pore can be predicted by minimizing E_S for a given filling ratio. To simplify the analytical calculation, we approximate the different possible phases using merely geometrical shapes, in this way the energy minimization can be performed by varying at most 2 parameters that characterize the phase. The ratio of the pore radius to the pore length is settled to the value $R/L = 2/6.1$ used in the simulations and the phase diagram is determined in dependence of the filling ratio and the ratio between the two surface energies. We check hydrophilic ($\gamma_2 < 0$) as well as hydrophobic surfaces ($\gamma_2 > 0$) knowing that the surface tension γ_1 is a positive quantity. Fig. 20 shows the eight phases considered and the resulting phase diagram obtained from minimizing E_S. The phase diagram reveals clearly three qualitatively different

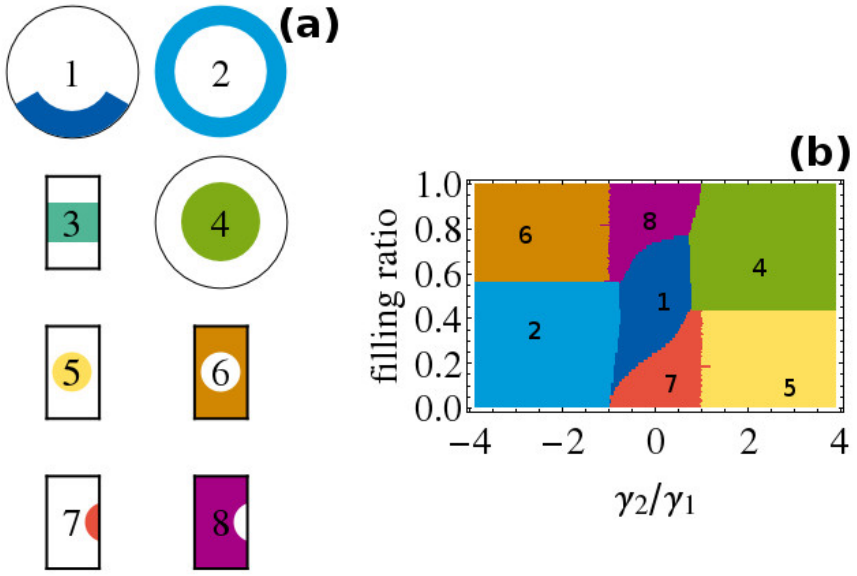

Figure 20: (a) The eight different phases used for energy minimization and (b) the phase diagram in dependence of the ratio of the water-vacuum and water-silica surface energies and of the filling ratio. The aspect ratio r/l between radius and length of the cylindrical pore is 2/6.1.

regions that depend on the ratio γ_2/γ_1. With the insights gained from these analytical calculations, we can suitably clarify the results of the MD simulations shown in Figs. 14-16. For the BZ surface, phase 1,3 and 8 occur depending on the filling ratio, and the surface is always partly wetted by water for all simulated filling ratios. As predicted by the phase diagram, the transition to phase 8 occurs at sufficiently large filling ratio of approximately 60%. Oppositely for smaller filling ratios below 15%, phase 7 also develops as shown in Fig. 88 in appendix. Knowing that the surface is hydrophilic ($\gamma_2 < 0$), this means that the ratio of surface energies lies in the interval $\gamma_2/\gamma_1 \in (-1, 0)$. With the GT surface, we observed a complete wetting of the silica surface (phases 2 and 6) for all simulated filling ratios, and of course a transition between these two phases at a higher filling ratio of about 60%. This suggests that $\gamma_2/\gamma_1 < -1$ which appears to be the more realistic scenario, as it agrees well with experimental results and indicates a highly hydrophilic surface. [11] In order to get an additional perspective on the different interaction between water and a silica surface described by each model, the final part of the work consists in investigating the contact angle of water on top of a flat silica slab using both models.

5.3 Results II: Water on top of a silica slab

5.3.1 MD Simulation

Secondly, a flat silica surface is used as hydrophilic substrate and we deposit on it a water droplet in order to estimate the contact angle. This is another appropriate method to examine the performance of silica potentials. We performed additional MD simulations of a water droplet on a flat surface of amorphous silica and estimated the contact angle. No PBC are set for these simulations in order to get rid of the influence of the neighboring water periodic images. Thus, the Coulomb and the VdW (LJ) interaction energies between all atoms in the water droplet and the silica slab have been calculated exactly.
For evaluating the contact angle θ, the density profile of all horizontal water layers of 0.05 nm thickness has been determined, and from these a contour plot of the density is sketched. The contour plot is then fitted to a circular segment, this allows the deduction of the contact angle from the tangential line to the base of the circular segment. The result is shown in Fig. 21 for both types of silica models, with a slab of thickness approaching $T = 2.5$ nm. For the GT model, the droplet wets the entire surface and has a very small contact angle of roughly 7°. Similar simulation with PBC considered lead to an entirely flat water layer. In contrast, a larger contact angle of the water droplet on top of the BZ surface avoisinating 25° is recorded. These results corroborates the findings of the previous subsections, that the GT silica surface is so hydrophilic that water wets it fully, in comparison to the less hydrophilic BZ surface which is partially wetted.

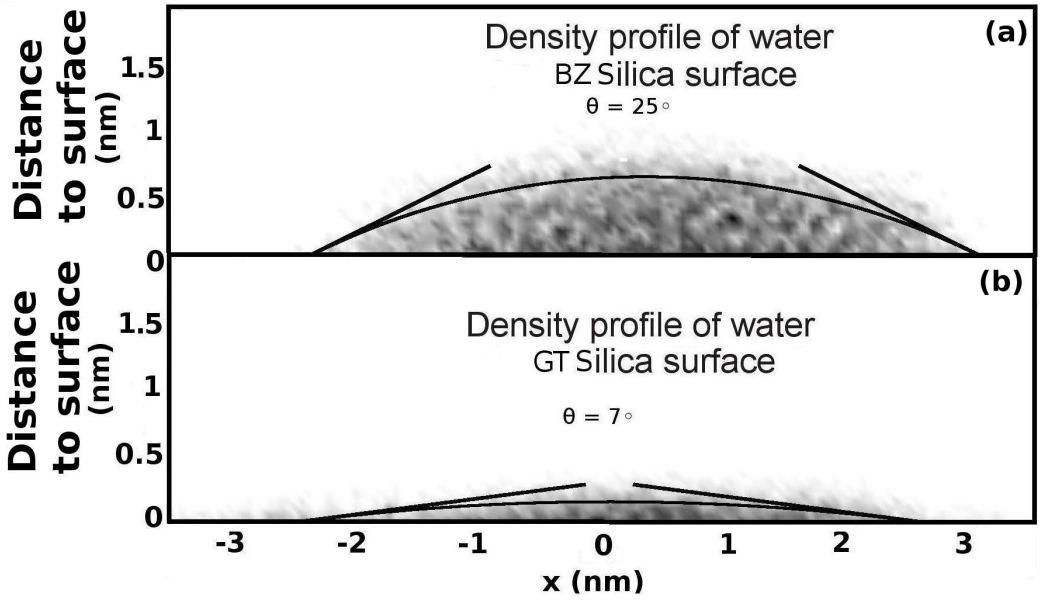

Figure 21: Contact angle of a water droplet on top of a silica slab of thickness $T = 2.5$ nm. (a) and (b) correspond respectively to the BZ and the GT silica surface.

The contact angle is closely connected to the surface energies that we used for evaluating the phase diagram. For an equilibrated droplet of constant volume, the total surface energy (E_S) of water wetting a silica surface must be minimal, i.e. $dE_s = 0$ implying the relation:

$$\frac{dA_1}{dA_2} = -\frac{\gamma_2}{\gamma_1} = \cos\theta\,. \tag{53}$$

A detailed derivation of this relation is reviewed in section. 4.9 of Chapter. 4. The contact angle of 25° for the BZ surface matches considerably well with our conclusion that $-1 < \gamma_2/\gamma_1 < 0$ and leads more

precisely to $\gamma_2/\gamma_1 \simeq -0.9$. Instead for the GT surface, we had obtained that $\gamma_2/\gamma_1 < -1$, implying a contact angle of about zero and a whole wetting. This is compatible with our observation that the droplet spreads on the surface and tends to form the 1.5 layers required for absolute wetting. The very small contact angle for the GT surface is in accordance with previous experimental findings. [43, 44, 45] In those experiments, the absolute value of the angle depends on whether the advancing or receding droplet is considered, and on the thickness of the slab, and it ranges from 0° to 7°. Since the interaction strength between water and silica is known to vary with the slab thickness, [43, 44, 45, 235] we evaluated the contact angle for different values of the thickness T (within the GT model), see Fig. 22. The cosine of the contact angle increases with thickness and approaches its limit when $T = 2.5$ nm, for which the contact angle is $\approx 7°$. A similar relation of the cosine of the contact angle on thickness has been measured. [43] It suggests that, to entirely reproduce the wetting properties of a water droplet on a silica slab, the slab should possess at least a thickness in the range 2.5-3 nm. This result is nearly similar to the experimental value 3 nm found by Williams and Goodman. [43] The variation of the contact angle with thickness

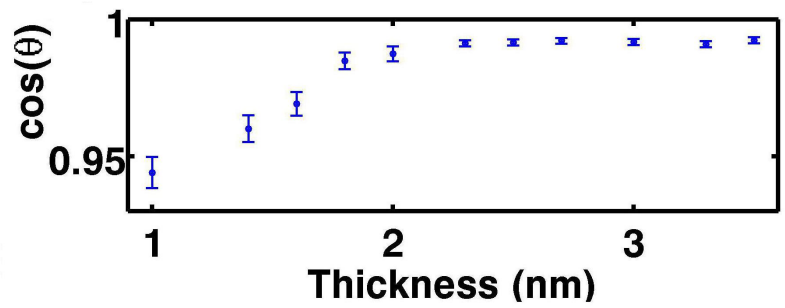

Figure 22: Dependence of the cosine of the contact angle θ of the water droplet on the thickness of the silica slab. MD simulations were performed with the GT model, using 469 water molecules.

indicates also that water does not entirely wet the surface when thin slabs are used. This means that the ratio γ_2/γ_1 moves from a value > -1 to a value < -1 with increasing thickness, implying that this ratio is necessary very close to -1. This in turn implies that small differences in the preparation of the surface can shift the ratio over the threshold -1, and this may explain why some experiments record a nonzero contact angle, while others find full wetting.

	ϵ_{GT}, q_{GT}	$1\%\epsilon_{GT}, q_{GT}$	$\epsilon_G, (q=0)$
$T = 1.6$ nm	14.3°	17.2°	105°
$T = 2.0$ nm	9.0°	12.3°	88°
$T = 2.5$ nm	7.0°	11.1°	87°

Table 2: Contact angle obtained for different slabs types: ϵ_{GT}, q_{GT} represent the GT model surface as defined in Table 1. $1\%\epsilon_{GT}, q_{GT}$ represents the GT model in which ϵ of each atoms is reduced to 1% of the original value in the GT model; $\epsilon_{GT}, (q = 0)$ stands for a slab without partial charges assigned to atoms but with LJ sites corresponding to the GT model.

To perceive the effect of each interaction type on the wetting properties, we evaluate the contact angle on different silica slabs in which we vary the interacting parameters accordingly. The idea was to test previous investigations of *Jacobs and coworkers* [45, 44] showing that VdW interactions play a determinant role in the adhesion of biomolecules on surfaces, in particular silica surfaces. We define 2 other slabs. In the first case, the partial charges of all silica atoms were set to 0 so that silica can only interact by means of VdW interactions. A second case has been set in which the partial charges were unchanged but only 1% of the original LJ interaction parameters were used to describe VdW forces. Table 2 confront

the resulting contact angles for various slab thicknesses.
With no partial charges attached to silica sites, one obtains a contact angle of 105° for thin slabs suggesting that the surface has become hydrophobic, with $\gamma_2/\gamma_1 \simeq 0.26$. It gets slightly hydrophilic with thicker slabs. This modification in the hydro-affinity with increasing thickness indicate the effect of VdW interactions. Oppositely, reducing the VdW interaction energy between water and silica molecules diminishes their interaction force and consequently the equilibrium distance between water and silica molecules increases. Due to that effect, the electrostatic strength is reduced as it is proportional to the inverse distance and hence the contact angle increases with a reduction of the VdW interaction energy.
Indeed, for 1% VdW interaction ($\theta = 11.1°$) the surface gets moderately less hydrophilic as with 100% VdW interaction ($\theta = 7.0°$). These findings reveal that the effect of VdW interaction are not negligible but are still considerably weak in comparison to the electrostatic forces influencing more the wetting properties.

5.3.2 Theoretical understanding of the contact angle variation with slab thickness

The idea is to approximate γ_2 in terms of the VdW and the electrostatic Coulomb interaction between the water droplet atoms and the silica atoms: $\gamma_2(T) = \mathrm{VdW}(T) + \mathrm{Elect}(T)$ (per unit area). $\mathrm{VdW}(T)$ stands for the VdW energy between the liquid droplet atoms and the atoms of the block while $\mathrm{Elect}(T)$ stands for the electrostatic energy, T represents the thickness of the block and γ_1 is the water surface energy, $\gamma_1 = 72.85\ \mathrm{mj/m^2} = 10.48\ \mathrm{Kcal/mol \cdot nm^2}$.
In order to systematically study the influence of the thickness of the block on the contact angle, one can calculate $\gamma_2(T)$ of water on top of silica slabs with varying thicknesses T. Let's assume that we have a homogeneous silica block of density ρ_1 and each molecule of the silica block interacts with each water molecule via an effective VdW potential of the form $\frac{-C_{\mathrm{VdW}}}{r^6}$ and an effective dipole-dipole electrostatic potential of the form $\frac{-C_{\mathrm{Elect}}}{r^3}$. Following the framework used in, [229] one can calculate the VdW (electrostatic) energy between the molecule OH_2 (located at $z = 0$) and the silica molecules in equation 54, 55. Figure 23 (a) shows a sketch for the integration of the energy. To simplify the integral calculation, cylindrical coordinates are used, and the molecules are assumed to be uniformly distributed: ρ_1 and ρ_2 are respectively the volume densities of the silica block and the water droplet. The number of silica molecules located in a circular ring of cross-sectional area $\mathrm{d}x\mathrm{d}z$ and radius x are given by $n_{\mathrm{ring}} = 2\pi\rho_1 x\mathrm{d}x\mathrm{d}z$. The VdW and the electrostatic energies between the water molecule and the silica molecules is given by

$$\begin{aligned} VdW_{\mathrm{OH_2-silica}} &= -2\pi C_{\mathrm{VdW}}\rho_1 \int_D^T \mathrm{d}z \int_0^\infty \frac{x\mathrm{d}x}{(x^2+z^2)^3} \\ &= \frac{-2\pi C_{\mathrm{VdW}}\rho_1}{4} \int_D^T \frac{\mathrm{d}z}{z^4} = \frac{-2\pi C_{\mathrm{VdW}}\rho_1}{12}\left(\frac{1}{T^3} - \frac{1}{D^3}\right), \end{aligned} \tag{54}$$

$$\begin{aligned} Elect_{\mathrm{OH_2-silica}} &= -2\pi C_{\mathrm{elect}}\rho_1 \int_D^T \mathrm{d}z \int_0^\infty \frac{x\mathrm{d}x}{(x^2+z^2)^{3/2}} \\ &= -2\pi C_{\mathrm{Elect}}\rho_1 \int_D^T \frac{\mathrm{d}z}{z} = -2\pi C_{Elect}\rho_1 \ln\left(\frac{T}{D}\right). \end{aligned} \tag{55}$$

Starting from equation 54, 55, one can at this level calculate the total VdW and electrostatic energy between all molecules in the water droplet and the molecules in the silica block. By considering that the water droplet is a flat surface, the number of water molecules in a thin slab of thickness $\mathrm{d}z$ (Figure 23

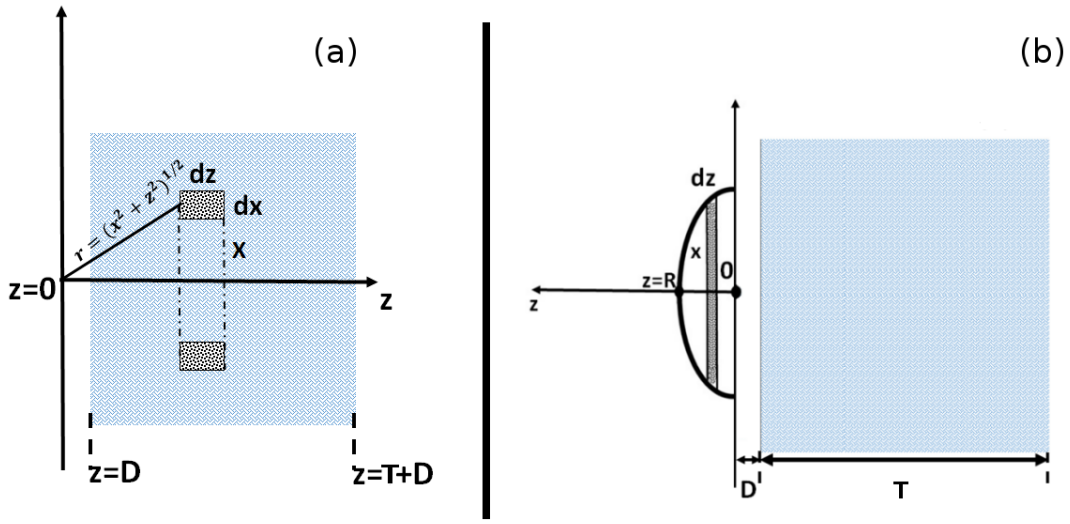

Figure 23: (a) Integration of the interaction energy between a water molecule at $z = 0$ and the atoms of the silica block. (b) Energy summation for all atoms of the water molecules. The sketch is adapted from Ref. 229.

(b)) is $\rho_2 \mathrm{d}z$. The total VdW (electrostatic) energy between all the water droplet molecules and the silica atoms in the block reads

$$\begin{aligned} VdW(T) &= \frac{\pi C_{\mathrm{VdW}} \rho_1 \rho_2}{6} \int_0^R \mathrm{d}z \left(\frac{1}{(T+z)^3} - \frac{1}{(D+z)^3} \right) \\ &= -\frac{\pi C_{\mathrm{VdW}} \rho_1 \rho_2}{12} \left(\frac{1}{T^2} - \frac{1}{D^2} - \frac{1}{(T+R)^2} + \frac{1}{(D+R)^2} \right), \end{aligned} \tag{56}$$

$$\begin{aligned} Elect(t) &= -2\pi C_{\mathrm{Elect}} \rho_1 \rho_2 \int_0^R \mathrm{d}z \ln\left(\frac{T+z}{D+z} \right) \\ &= -2\pi C_{\mathrm{Elect}} \rho_1 \rho_2 \left((T+R) \ln\left(\frac{T+R}{T} \right) - (D+R) \ln\left(\frac{D+R}{D} \right) \right). \end{aligned} \tag{57}$$

C_{VdW} is deduced from the *Hamaker* constants of silica and water tabulated in Ref. [229], while C_{Elect} has been considered equal to unity, this is accurate enough to follow the variation trend with the thickness, and can be modify accordingly as soon as the exact absolute values of the energy calculated are required. T is the slab thickness, D is the distance between the OH_2 molecule (located at $z = 0$) and the first layer of silica atoms, it represents how close the OH_2 can come to a silica molecule. It scales as the diameter of a water molecule which is roughly 0.3 nm. R is the water droplet thickness which normally changes slightly with the contact angle (and the thickness of the silica slab) between 0.35-0.56 nm. To calculate γ_2, we have assumed R constant and equal to 0.4 nm. The resulting $\gamma_2(T)$ is plotted in figure 24 (b).

Figure 24 reveals that the energy should increase with the thickness and reaches a limit at roughly 3 nm, that is close to the value 2.5 nm predicted by $\cos\theta(T)$ in figure 22. It means that, to accurately reproduce the wetting properties of a water droplet on a silica slab, the slab should have at least a thickness in the range $2.5-3$ nm. This result is close to the experimental value 3 nm found in Ref. [43]. Moreover, the convergence of the adhesion energy shows that, the amount of energy needed for the water droplet to completely adhere the silica surface is already reached with a silica block of $2.5-3$ nm thick.

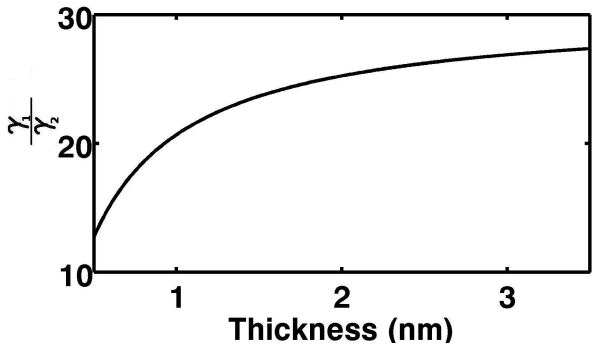

Figure 24: Change of the adhesion work γ_2 of the water droplet adhering a GT silica model block, evaluated from the MD trajectories (a) and derived from the theoretical approach (b), with respect to the thickness of the silica slab.

5.4 Summary

We have studied the wetting properties of water in partially filled silica pores and on flat silica surfaces using MD simulations with two extensively used intermolecular potentials [40, 42] for the interaction between water and silica surface atoms. This investigation has been motivated by former experimental findings [11, 17] from the group of *Professor Buntkowsky* from the TU Darmstadt displaying that water in low filled silica pores fully wets the silica surface. We have simulated water in a cylindrical silica pore and we have calculated the radial density, angular density and the H-bond profiles of water molecules in the pore. We have as well in the special case of 97% filling ratio compared how each surface distorts the local ordering of water molecules, as well as how are dynamics influenced by each surface. We have also looked at the energy evolution with time for a lower filling ratio (e.g 40%) to check whether the system is equilibrated. A phase diagram has been proposed (originating from the work of *Julian Geske* [180]) based on the possible configurations of water in a moderately filled pore. Lastly, we have performed the simulation of a water droplet on top of a flat surface, to contrast the contact angle of a water droplet on top of both silica model surface.

With the help of the evaluation of radial and angular density profiles, we show that the GT silica model surface is entirely covered by water molecules even at moderate filling percentages (30 %, 40 %). Interestingly, we could conclude that approximately one and a half layer of water is sufficient for a complete wetting of the surface. Moreover, these results are independent of the water models used and of the initial configuration of the water droplet inside the silica pore. Whereas, the arrangement of the water droplet near the BZ model surface depends considerably on the filling ratio and also on the starting configuration. By means of a simple analytical evaluation of the possible water phases in a pore, we propose that for the BZ model, the interfacial energy of the water droplet with the silica wall is even less than the interfacial energy of water with vacuum, influencing the formation of water configurations sharing small interfaces with vacuum, while the opposite applies for the GT surface, for which the interface between water and the silica surface is maximized.
Near the BZ surface, we find a preferred formation of a double water layer at all studied filling ratios, agreeing well with the reports of other authors. [35, 38, 36] Nevertheless, our results complement their work as we make a full study of the proportion of the pore surface that is covered by water, and reported the coexistence of different phases of water inside the pore at intermediate filling ratios. The phases obtained with MD trajectories could not be completely reproduced by the phase diagram that was solely based on surface tensions, without considering entropy and thus we propose that the entropy effect might induced the formation of a more compact "plug" phase appearing in MD simulations.

Furthermore, we show that the contact angle of a water droplet wetting a silica slab is nearly similar to zero for the GT silica model, while it is around 25° for the BZ model. That is, the GT model agrees well with previous experimental reports. [44, 45] In addition, the contact angle diminishes with slab thickness and converges at approximately $T = 2.5\,\text{nm}$. This result matches qualitatively well the experimentally proposed value $T = 3\,\text{nm}$ [43] and is of more interest for simulations of aqueous mixtures in silica pore. Because it can help in reducing the computational cost of MD studies by limiting the thickness of the silica slab to roughly $T = 3\,\text{nm}$.

Altogether, our results reveal that the behavior of water confined in the GT silica model is similar to the experimental findings that water in partially filled silica pores covers the surface entirely. [11, 17] Our thorough analysis shows that the GT silica model [42] surface is more hydrophilic than the standard BZ silica model [40] surface. This should be related to the different partial charges attached to silica atoms in the two models, which agrees with our results that the electrostatic energy evaluated between water and GT silica atoms is much more larger than the corresponding one between water and BZ silica atoms. It also goes in accordance with the findings shown in the last sections where additional simulations were made for comparing the effects of rescaling the partial charges of silica atoms, to the effect of rescaling the LJ parameters. It results that the electrostatic interaction plays a prominent role in the wetting properties of water on silica surfaces.

6 Water and octanol mixture in silica confinements

In the last chapter, we have approved the silica model (GT model) which provides a highly hydrophilic surface while checking the wetting processes of water droplet in porous as well as flat silica surfaces. We can now investigate the behavior of octanol/water mixtures in silica pore. This system is interesting to investigate the competition between liquid-liquid and liquid-matrix interactions given the long hydrophobic hydrocarbon chain of octanol and its hydroxyl group. This work is mainly motivated by the collaboration with experimentalists from the group of *Professor Buntkowsky* at the TU Darmstadt enabling direct comparison between experiments and simulations. With the solid-state NMR spectroscopy method, they have investigated the ^{1}H chemical shifts of the hydrogens of the silanol in the silica surface of a dried SBA-15 pore mixed with either 1-octanol or aqueous solutions composed of water and octanol at room temperature. The NMR results suggest the orientation and interaction process of octanol/water near the pore surface region. It is also important to point out that *Sandra Forg* has worked on the initial steps of this topic during her master proposal [236] under my supervision.

6.1 System description and simulation details

The bulk of 1-octanol liquid containing 3600 molecules is at first simulated using the CHARMM22 force field for hydrocarbon atom interactions, [237] associated with the force field parameters of *Debolt and Kollman* [147] for the interaction with the hydroxyl group part. The density of the equilibrated 1-octanol liquid approximates 0.8380 g/cm^3, which is only 1.4% higher than the known experimental value (0.8263 g/cm^3) at ambient pressure. [47, 238]

Using the SPC/E [136] water model, three liquid mixtures containing 10 mol% of water (90 mol % of 1-octanol) molecules, and 30 mol% of water (70 mol % of 1-octanol) molecules as well as 50 mol% of both species are respectively investigated. In the bulk simulations case, the starting configurations are designed by water molecules almost equally distributed in octanol (see Fig. 26 (a)-(b)), which then clustered when the system gets equilibrated (at normal pressure and room temperature) as observed in Fig. 26. For the 10 mol% water content, one can notice a complete mixing between water and octanol oxygens. Whereas, by increasing the water content to 30 mol%, a partial demixing can be noticed in which large water clusters agglomerate near the oxygens centers of octanol molecules. This observation goes in accordance with the proposed demixing ratio of 26 mol% [47, 147, 48] at room temperature.

The equilibrated bulk mixtures are then inserted in the silica pore of 4 nm diameter manufactured by *Geske and Vogel.* [230] While applying a similar methodology, larger pore of 6 and 8 nm in diameter have also been produced. These have been established by starting from the equilibrated cooled silica block

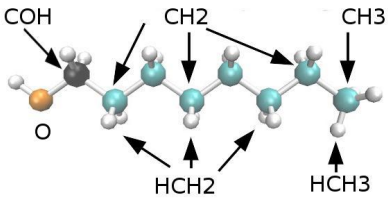

Figure 25: Visual representation of an octanol molecule with the atom types defined to describe the interactions potential specified. The first carbon of the chain is designated by a black sphere and is linked to the hydroxyl group (also represented by the oxygens in orange to which a hydrogen (HOH) is attached). All hydrogens are represented by white spheres. The rest of atoms are the hydrocarbons CH2 each linked to 2 hydrogens (HCH2) and CH3 attached to 3 hydrogens (HCH3).

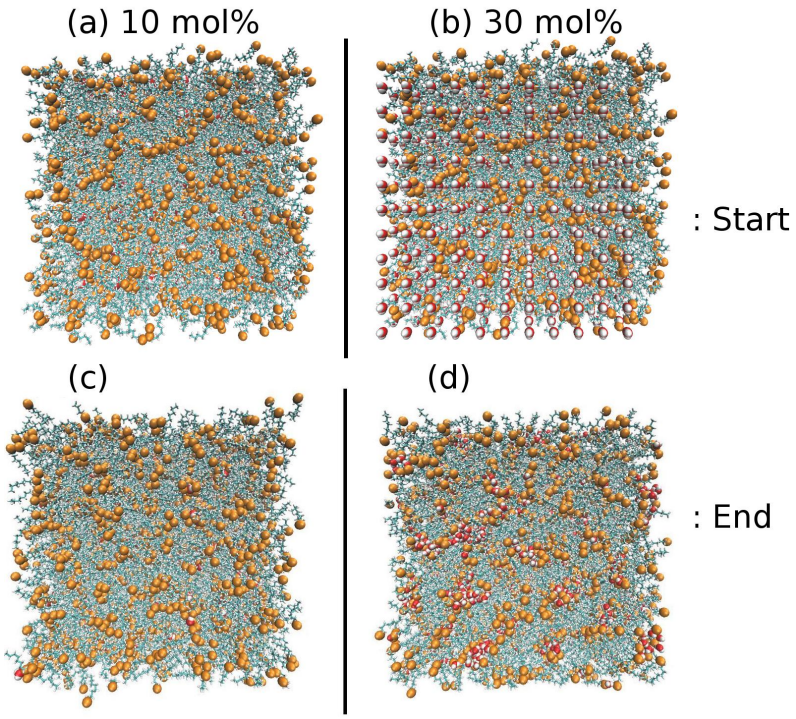

Figure 26: Snapshot of the starting (a)-(b) and the equilibrated (c)-(d) configurations used when simulating water octanol mixtures at room temperature T=300 K. (a) and (c) corresponds to the 10 mol% case, while (b) and (d) are for the 30 mol% case. The red, and orange spheres indicate respectively the location of water and octanol oxygens. The snapshots are generated using the VMD program. [234]

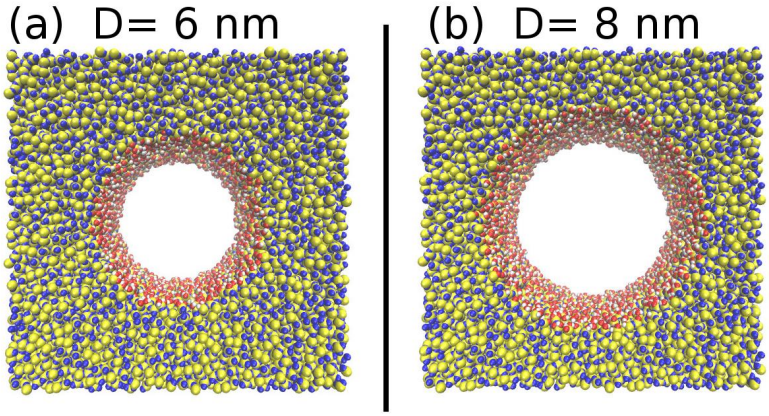

Figure 27: Top views of the bigger pore created in this thesis: (a) is the pore of roughly 6.0 nm in diameter and (b) is the pore of roughly 8 nm in diameter. Si, O_{Si}, O_H, and H are drawn respectively in yellow, blue, red and white. The snapshots are generated using the VMD program. [234]

Table 3: LJ parameters for the 1-octanol sites. The atoms are labeled as followed: O and HOH are the oxygen and hydrogen of the hydroxyl group, respectively. COH is the carbon linked to the hydroxyl group of the 1-octanol molecule. The hydrocarbons carbons are designated by CH3 connected to 3 and and CH2 to 2 hydrogens. The corresponding hydrogens are HCH3 linked to CH3 and HCH2 linked to CH2. The hydrocarbons atoms parameters are extracted from the CHARMM22 force field, [237] while the atoms linked to the hydroxyl groups parameters are mostly taken from the force field parameters of *Debolt and Kollman*. [147]

Sites	σ (nm)	ε (Kcal/mol)	q (e)
O	3.070	0.170	-0.710
HOH	1.782	0	0.435
COH	3.904	0.118	0.270
CH3	3.634	0.078	-0.270
CH2	3.581	0.056	-0.180
HCH2	2.387	0.035	0.009
HCH3	2.387	0.024	0.009

[230] of length 6.08 nm, then duplicating it 4 times to create a larger block (see Fig. 92 of appendix). The box size is given by 12.16 nm x 12.16 nm x 6.08 nm. A cylindrical cut has then been used to create the pore leading to some defects at the surface with missing closed neighbors. Within the functionalized surface layer of approximately 0.55 nm thick from pore center to pore wall, silicons and oxygens with smaller valence than 4 or 2 (for oxygens) are either saturated with hydroxyl groups or deleted if the valence after cutting is smaller than 2 for silicons and 1 for oxygens. Snapshots of the obtained larger pore are added in Fig. 27. The different atoms constituting the pore wall (Si, O_{Si}, O_H, and H) have been introduced in Chapter. 5. In the snapshot of Fig. 27, the oxygens O_H of the silanol groups are colored in red to differentiate with the bridging oxygens O_{Si} which are represented by blue spheres. The surface density of hydroxyl groups can be approximated by assuming a perfect cylindrical pore and a uniformly distributed surface. They are given by 7.9 nm^{-2} for the pore of 6 nm in diameter and 7.6 nm^{-2} for the pore of 8 nm in diameter, which is nearly similar to the expected surface density with the pore creation methodology. [230] Of course, these values are comparable to the surface density of the already introduced 4 nm pore in chapter. 5.

Atoms of 1-octanol and water are enabled to interact with silica atoms through the Coulomb and the Lennard-Jones (LJ) potential. The GT [42] model is used to define the LJ parameters and the partial charges assigned to each silica sites (see Table. 1). The LJ parameters for the octanol sites are given in Table. 3. Interactions between the different atoms are as well dictated by the *Lorentz—Berthelot* mixing rules. [142]

Table 4: Periodic box size of the different simulated systems.

Simulation Types	Systems	L_X (nm)	L_Y (nm)	L_Z (nm)
Bulk	Octanol	9.76	9.76	9.76
	10 mol%	9.81	9.81	9.81
	30 mol%	9.93	9.93	9.93
Pore	$\sim$ 4 nm pore	6.08	6.08	6.08
	$\sim$ 6 nm pore	12.16	12.16	6.08
	$\sim$ 8 nm pore	12.16	12.16	6.08

Table 5: Number of molecules N in the mixture simulated. NPT ensemble is used for bulk simulations with the atmospheric pressure of 1 bars. NVT ensemble is implemented for the confinement simulations.

Simulation Types	Systems	N_{water}	$N_{octanol}$
Bulk	10 mol%	405	3600
	30 mol%	1543	3600
4 nm Pore	10 mol%	30	278
	30 mol%	108	253
6 nm Pore	30 mol%	295	689
8 nm Pore	30 mol%	451	1053

The covered temperature range is within 300 K-425 K for all simulations in confinements. The bulk systems are only equilibrated at room temperature before cutting the droplet for confinement simulations. A minimal equilibration time of 5 ns to 10 ns is necessary for the bulk simulations before acquiring the analysis data from further trajectories. This is necessary for the bulk mixture simulations as water and 1-octanol tend to demix in bulk. For the confinements, the minimal equilibration amounts 5 to 20 ns as the long octanol molecule close to the pore surface slowly rotates. A time step of 0.5 fs was necessary to avoid instabilities in the motions of octanol hydrocarbons near the pore wall which are subject to a static landscape. Whereas, 1 fs of time step is a good choice for bulk simulations. PBC were applied with the size of the cell described in Table. 4. A cut-off at 1.5 nm and a switching distance of 1.2 nm is defined. In the NPT simulations, the pressure is maintained to 1 bar using the Langevin—Piston method. [141] For the pore confinement simulations, NVT simulations are performed using the Langevin thermostat, [137] with a coupling coefficient of 1.0 ps^{-1}, and while hydrogen atoms are included in the Langevin dynamics. The number of molecules simulated in each systems are summarized in Table. 5. The Coulomb interactions are evaluated using the PME summation.

6.2 Simulation results

6.2.1 Pure (unconfined) mixture

Water and octanol show a large miscibility gap as shown in Fig. 28 that displays the mixture percentage (in terms of octanol moles content) at which both liquids do not mix. Both liquids usually do not mix when the water content is larger (or comparable as) 30 mol%. The simulations of the water/octanol mixtures are necessary first to equilibrate the system before confining it. Secondly to identify the temperature at which the system demix under atmospheric pressure (1 bar). Fig. 29 (a) shows the distribution of oxygens in the mixture, irrespective of whether they are belonging to a octanol or a water molecule. The different mol% indicate the water content (in terms of number of molecules) in the liquid, of course 0 mol% represents pure octanol. A short range ordered characteristic of liquid can be identified in the plots. Interestingly, the inclusion of water decreases the number of closest oxygens which are then pushed to positions between the second and the third neighboring shells. The effect is more visible in the 30 mol% curve and this should be related to the presence of much large water clusters in the nearby of octanol oxygens (see Fig. 26(d)) which then distorts the local structure of octanol. Similar observation can also be drawn when looking at the distribution of the carbon COH (directly connected to the hydroxyl groups) with respect to octanol oxygens as plotted in Fig. 29(b).

6.2.2 Confinement

Given the equilibrated bulk at 300 K, we have cut a cylindrical droplet that is then inserted in the silica pore (see Fig. 30 (a)). We first look at the density profile of oxygens and carbons near the 4 nm silica

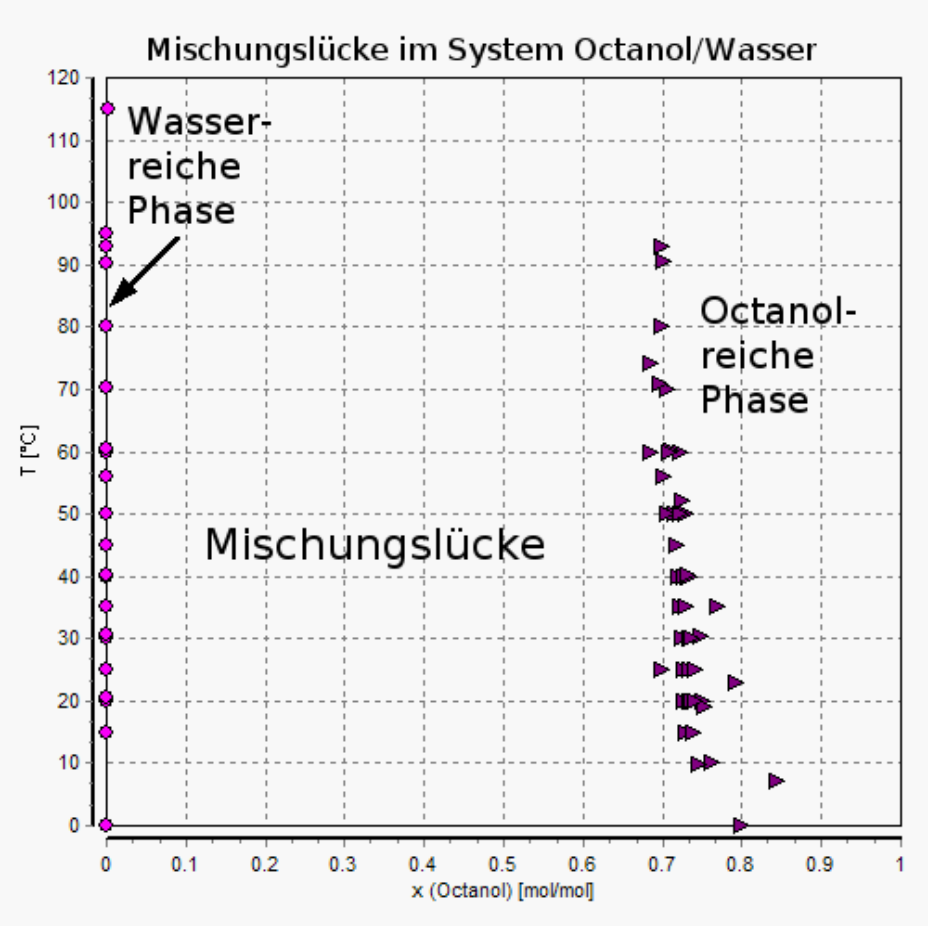

Figure 28: Phase diagram between water and octanol extracted from Wikipedia.

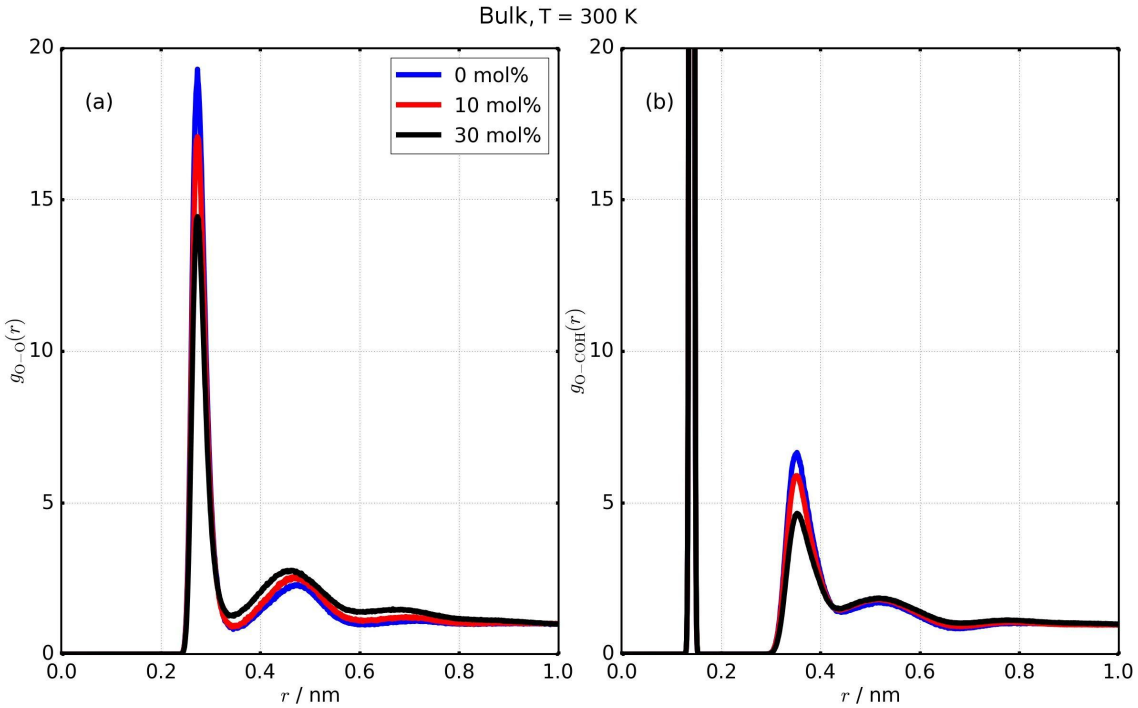

Figure 29: Radial density distribution between oxygens (a) and between oxygens and carbons (b). The target carbons are the carbons connected to the hydroxyl group labeled as COH. The distribution corresponds to the different liquid mixture simulated. 0 mol% represents bulk octanol. The first peak in (b) represents the carbon which belongs to the same molecule as the targeted oxygen.

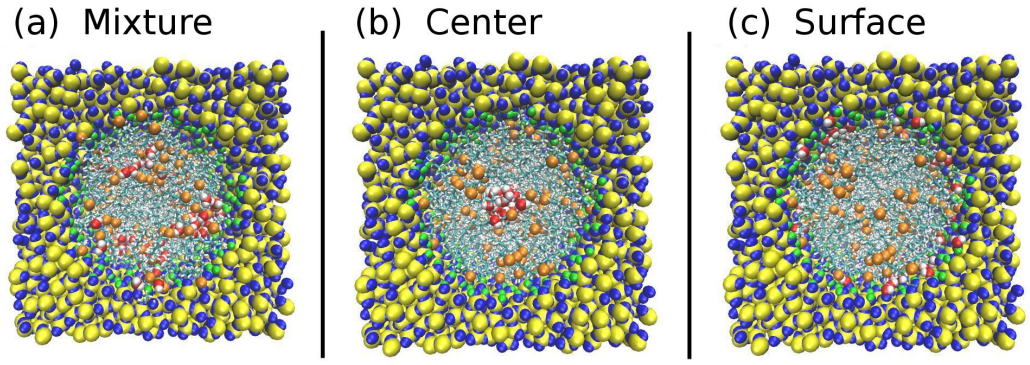

Figure 30: Snapshot showing the top views of the starting configurations of the simulations of a mixture of 30 mol% water and 70 mol% 1-octanol in silica pore. (a) Initial configuration obtained when cutting a cylinder from the equilibrated bulk mixture at 300 K (see Fig. 26(d)), (b) and (c) are the initial configurations for which a water droplet are initially inserted in the pore center or in the vicinity of the pore surface, respectively. The yellow, blue and green spheres are the silicon, oxygen and hydrogen atoms of the silica pore, respectively. The red and white spheres are oxygen and hydrogen atoms of water molecules. The octanol oxygen atoms are represented as orange spheres. The snapshots are generated using the VMD program. [234]

pore as displayed in Fig. 31 (a)-(b). It exhibits the number density profile of oxygen atoms of water and 1-octanol, displaying that oxygen atoms of water and 1-octanol are concentrated near the pore surface as well as in the pore center. The density distributions of the first (COH) and last (CH3) carbon of the 1-octanol chain, plotted in Fig. 31(b), shows a similar tendency. COH accumulates in the vicinity of the pore surface as well as in the pore center, while CH3 displays a peak roughly in the intermediate pore region. For the other carbons of octanol (the ones connected each to 2 hydrogens) labeled as C2-C7 the overall number density profiles are given in Fig. 32(a)-(b) and shows the maximum concentration in the range between the wall and the intermediate pore region. The effect of water content on the density distribution of COH and CH3 is almost not visible when comparing the distribution obtained in systems containing 0, 10 and 30 mol% water. In general the distributions of the carbons are not significantly affected by the inclusion of water. The opposite case happens with the number density of water molecules. Indeed, with increasing water content, water molecules accumulate somehow closer to the pore center and near the pore surface. This influences the distribution of octanol oxygens which consequently decreases near the pore wall and increases near the pore center. These observations that water tends to concentrate more in the pore wall vicinity but are still present in the pore middle region is not very surprising since the tendency of water molecules is to stay close to the hydrophilic centers presented by 1-octanol or by the silica surface. As we have seen in chapter. 5, water completely wets the GT silica surface even at very small pore filling percentage (see the case of 15 % in Fig. 89 and Fig. 88(a) of the appendix.). Therefore, the presence of some water molecules at the pore center can only be explained by the attraction of some water molecules to the hydroxyl groups of octanol in the pore center. From the observations made in Fig. 31 (a)-(b) and Fig. 32 (a)-(b), we propose that a bilayer formation occurs in the 4 nm pore and this is understandable since the length of an 1-octanol molecule is roughly 0.9 nm corresponding to half the pore radius, suggesting that two layers of 1-octanol molecules can arrange inside the 4 nm pore.
We get more understandings when we compare with the simulations data in bigger pores (6 nm and 8 nm). The tendency of octanol oxygens to accumulate somewhat less near the pore wall and more in the pore center region due to the inclusion of water is also visible here, while the carbons are less sensible (see Fig. 31(c)-(d)). The bilayer-like formation gets less visible here and instead a flattening of the distribution and a bulk like number density is observed in the pore center region. Overall, only a peak in the distribution of oxygens and carbons COH near the pore wall is remarkable originating from the effect of the energy landscape imposed by the fixed wall atom. Next to these peaks, are the peaks of the other carbons C2-C7, CH3 which is a little bit shifted to the intermediate pore region, however the distribution of all atoms is constant and equal to the bulk density in the pore center region (see panels (c)-(d) of Fig. 31 and Fig. 32). The density profiles in the 6 nm pore are plotted in Fig. 93 of the appendix.

In this investigation, we also check the influence of the initial configuration of the liquid mixture confined in pore by using three different starting configurations of the confined mixture. At first, the equilibrated bulk mixture droplet is inserted inside the pore (see Fig. 30 (a)) and the results have been presented in the previous paragraphs. Secondly, water is initially inserted in the pore center region (see Fig. 30 (b)) and surrounded by 1-octanol molecules and we refer this as center starting, third water is attached to the pore surface and the rest of the pore is filled with 1-octanol molecules and this is labeled as surface starting (see Fig. 30 (c)). The number density profiles obtained in each case are compared in Fig. 33 and show that the number of oxygens or carbons aggregating near the pore wall or in the intermediate pore region do not depend on the starting configurations. The results are independent of the pore size as can be seen in Fig. 33. In the appendix (see Fig. 94), the snapshots of the system at different time are added such that one can clearly inspect the behavior of water molecules in the case of center starting. Water molecules initially positioned in the pore center are attracted by the surface silica sites and their density considerably decrease in the pore center region. In general, water always accumulate preferably at the pore surface. The distribution obtained in the center of the pore is almost not changing with starting configuration, nevertheless small fluctuations are noticeable especially in the oxygens density. These might be related to the entropy created by the presence of carbons in the pore

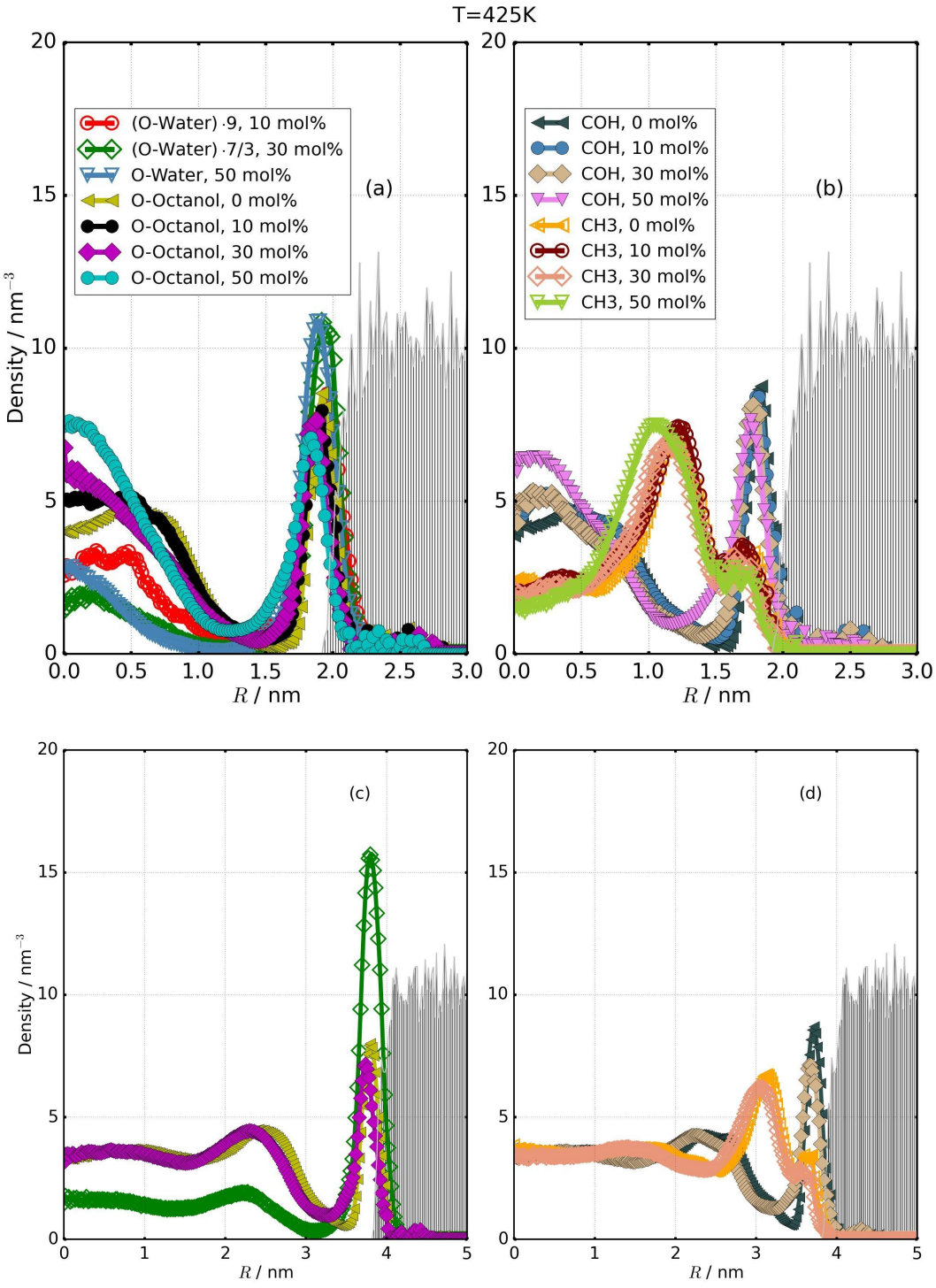

Figure 31: Number density profile of (a),(c) oxygens of water and 1-octanol molecules and (b), (d) of carbons (first carbon COH and last carbon of the chain CH3) of 1-octanol molecules, for 0, 10 and 30 mol% of water content. The density of water molecules is multiplied by the indicated factor for a better comparison. The top curves (a)-(b) correspond to the simulation in the 4 nm pore diameter, while (c)-(d) are data acquired for the simulation in the pore of double size. These data correspond to a simulation at 425 K and for a starting configuration for which the equilibrated mixture droplet is inserted in the pore.

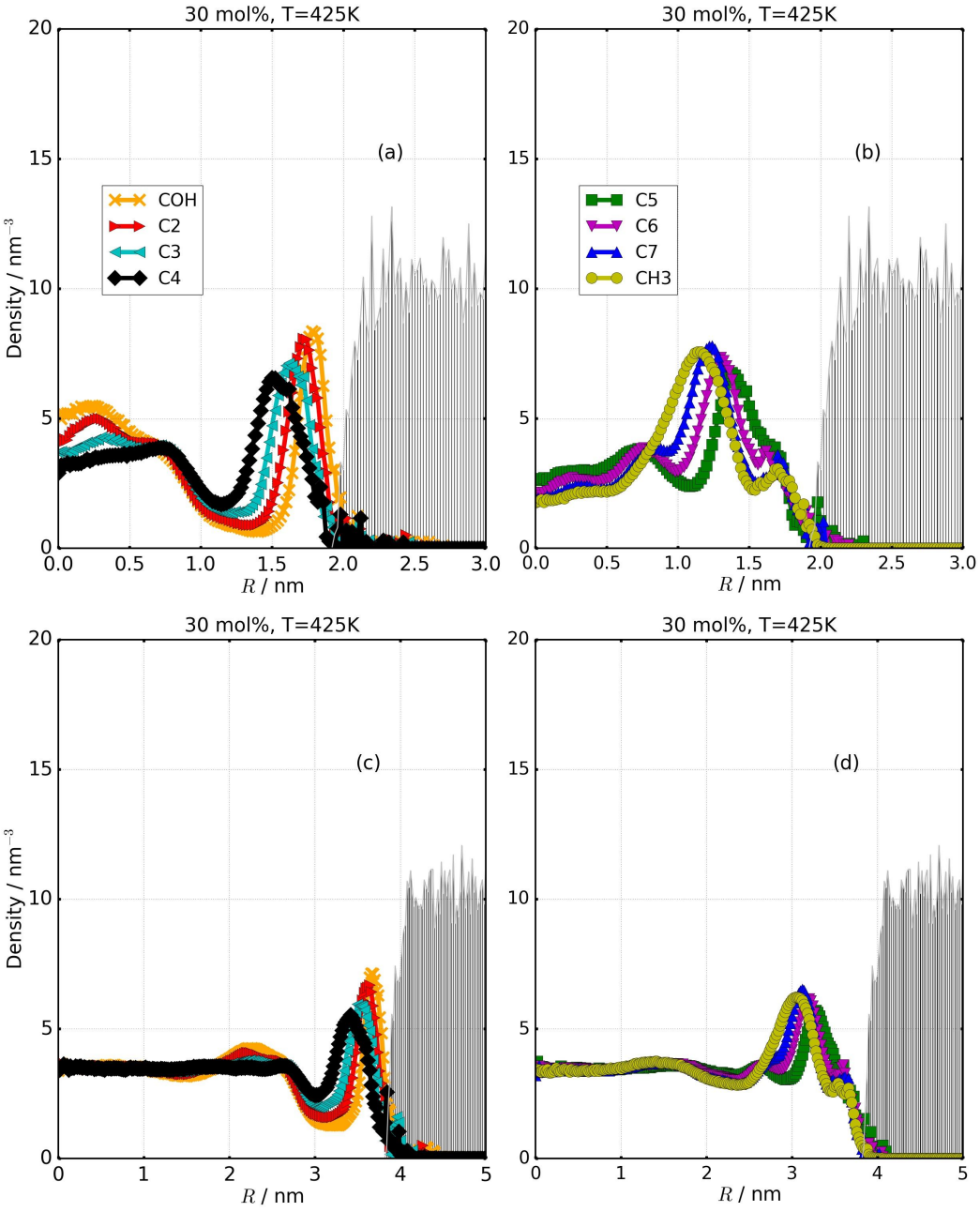

Figure 32: Number density profile of carbons of 1-octanol for 30 mol% at T=425 K for the 4 nm pore (a)-(b) and the 8 nm pore (c)-(d). In panel (a) COH, C2-C4 are more concentrated in the pore center or the pore surface region whereas C5-C7, CH3 (b) aggregate preferentially in the intermediate pore region. In a pore of double size, on top of the features observed for the smaller pore, a bulk-like behavior is noticeable in the pore center region.

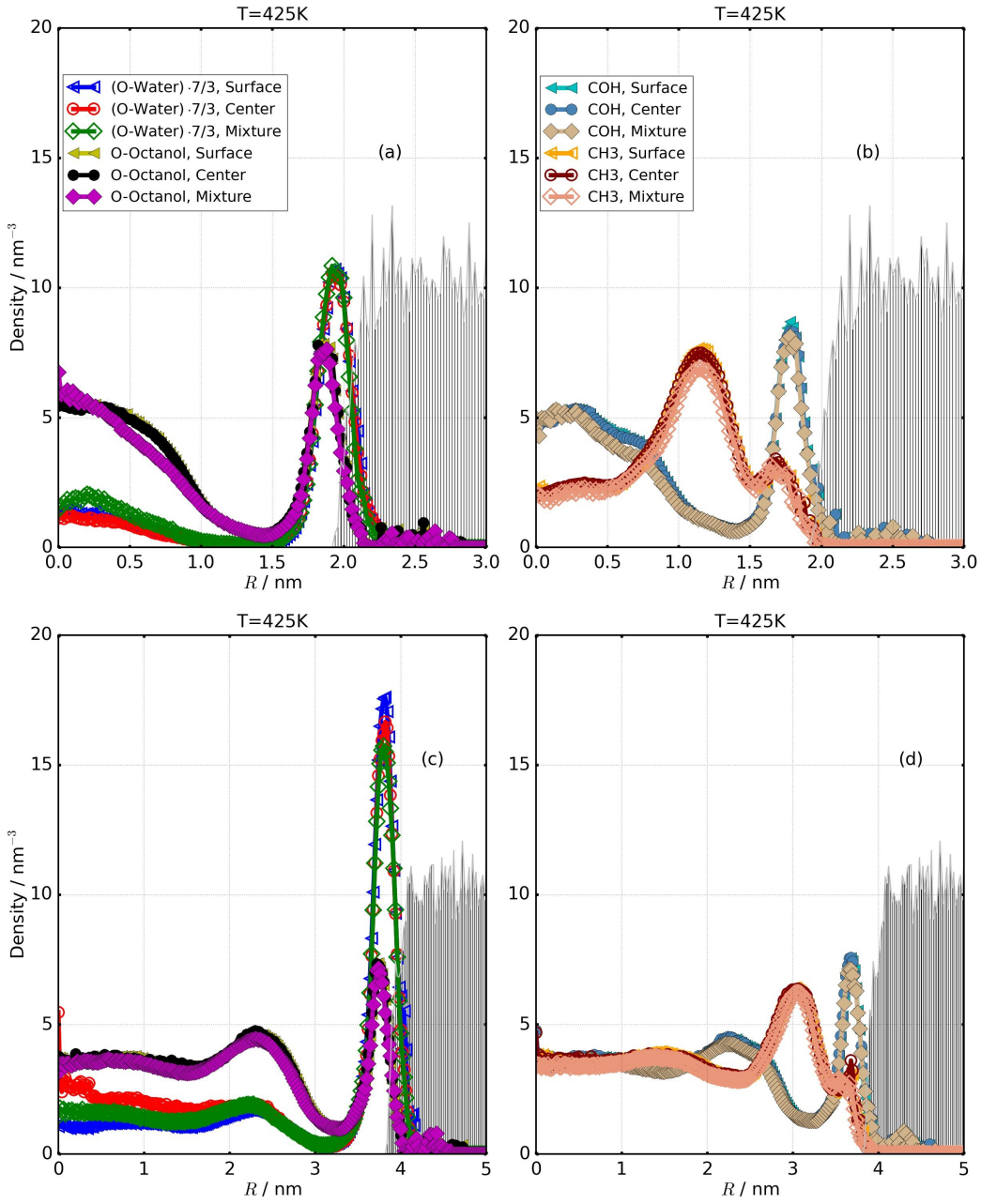

Figure 33: Number density profile for 30 mol% mixture in pore at 425 K of (a) the oxygens of water and octanol molecules, and (b) the carbons (first carbon (COH) and last carbon (CH3) of the chain) of 1-octanol molecules, for the surface, center and mixture starting configurations. The density of water molecules is enhanced by the indicated factor 7/3 to be easily compared with the other atoms profiles. The top panels (a)-(b) are for the 4 nm pore while the down figures (c)-(d) are for the 8 nm pore.

center which force the oxygens of water to accommodate in order to maximize the formation of H-bonds with octanol hydroxyl groups. These effects might induce some fluctuations in the obtained density of oxygens near the pore center as well as carbons of the hydroxyl groups.

We have in the next steps compared the energy of the equilibrated systems obtained for each initial configurations (see Fig. 34 (a)). It is interesting to notice that the water-silica energy decreases for the center and mixture starting configuration, and it moderately increases for the surface starting configuration, until reaching the balanced energy. Simultaneously, the water-water energy increases for the center as well as for the mixture starting condition, while for the surface starting configuration the energy at equilibrium is almost reached after very short simulation times. Fig. 34 (b) enables to compare the electrostatic energy between water and silica with the ones between octanol and silica. The octanol-silica energy is slightly reduced (in absolute) when water is added while the water-silica energy tends to increase (in absolute values). This trend agrees with the previous observation that octanol density decreases near the pore wall when water is added.

To get more insights to these findings, we have additionally evaluated the average number of hydrogen bonds per octanol molecule (see Fig. 35 (a)) and per water molecule (see Fig. 35 (b)) inside the pore for different water/1-octanol ratios, as they play a crucial role at determining the configuration of lowest energy. First, it is observed that the average number of hydrogen bonds per octanol molecule shared between octanol molecules (octanol-octanol) in the pore reduces when water is added. This is expected because some of the octanol molecules will be involved with hydrogen bonding with water molecules. The average number of hydrogen bonds shared between water and octanol molecules (water-octanol) is almost independent of the mixing ratio as shown in Fig. 35 (b). Moreover, nearly 1.5 H-bonds per octanol (and per water) molecules are shared with the silica sites, which suggests that the electrostatic energy between octanol and surface molecules is of the same order of magnitude as the one between water and surface molecules. This observation is somewhat confirmed by the evaluated electrostatic energy of Fig. 34, since the energy between water and silica almost converges to the same value as the energy between octanol and silica. The tiny differences visible in the H-bond profile near the pore surface might be related to the presence of very few octanol hydroxyl tails in the silica wall as well as water molecules, impacting on the calculation of the average number of the hydrogen bonds in the vicinity of the silica surface.

The results show till now where mostly for T = 425 K where the system is certainly well equilibrated. The influence of the temperature of the obtained distribution of water and octanol is shown in Fig. 36. The carbon peaks near the pore wall is almost not influenced by the temperature, oppositely to the distribution in the pore center region. The oxygens peaks are the ones much more affected with a tendency of water to concentrate more in the pore center region. This can be rationalized by the fact that when the system is not sufficiently heated, the octanol molecules having a long chain might need longer time to completely rotate particularly in the 4 nm pore where the layer in the pore center region is directly in contact to the layer involved with the pore surface. These slow motion of octanol can hindered the motions of water molecules which might be trapped in small hydrocarbons aggregates.

In the last step, we probe dynamics by looking at the ISF of octanol oxygens sites situated either with 5 nm of the pore center region or near the pore wall (see Fig. 37 (a)-(c)), or the rotational correlation function of the dipole formed by the the first (COH) and the end carbon (CH3) of the chain (see Fig. 37 (b)-(d)). In overall, the dynamics is slow in the pore wall, but the effect is more visible in the rotational motion in which the decay happens at a time at least one order of magnitude larger. The effect of water content displays by panels (a) and (b) of Fig. 37 suggest that the confinements effect on octanol dynamics reduces with water content agreeing with our former observations that water replace octanol near the pore wall. The effect of pore size on octanol dynamics illustrated in panels (c) and (d) is less pronounced, though the dynamics gets a bit slower when the pore size shrinks as the dynamics is dominated by the interfacial octanol molecules (which are H-bonded with silica sites). Surprisingly, the rotational correlation function does not decay to 0 near the pore surface but to a plateau with height

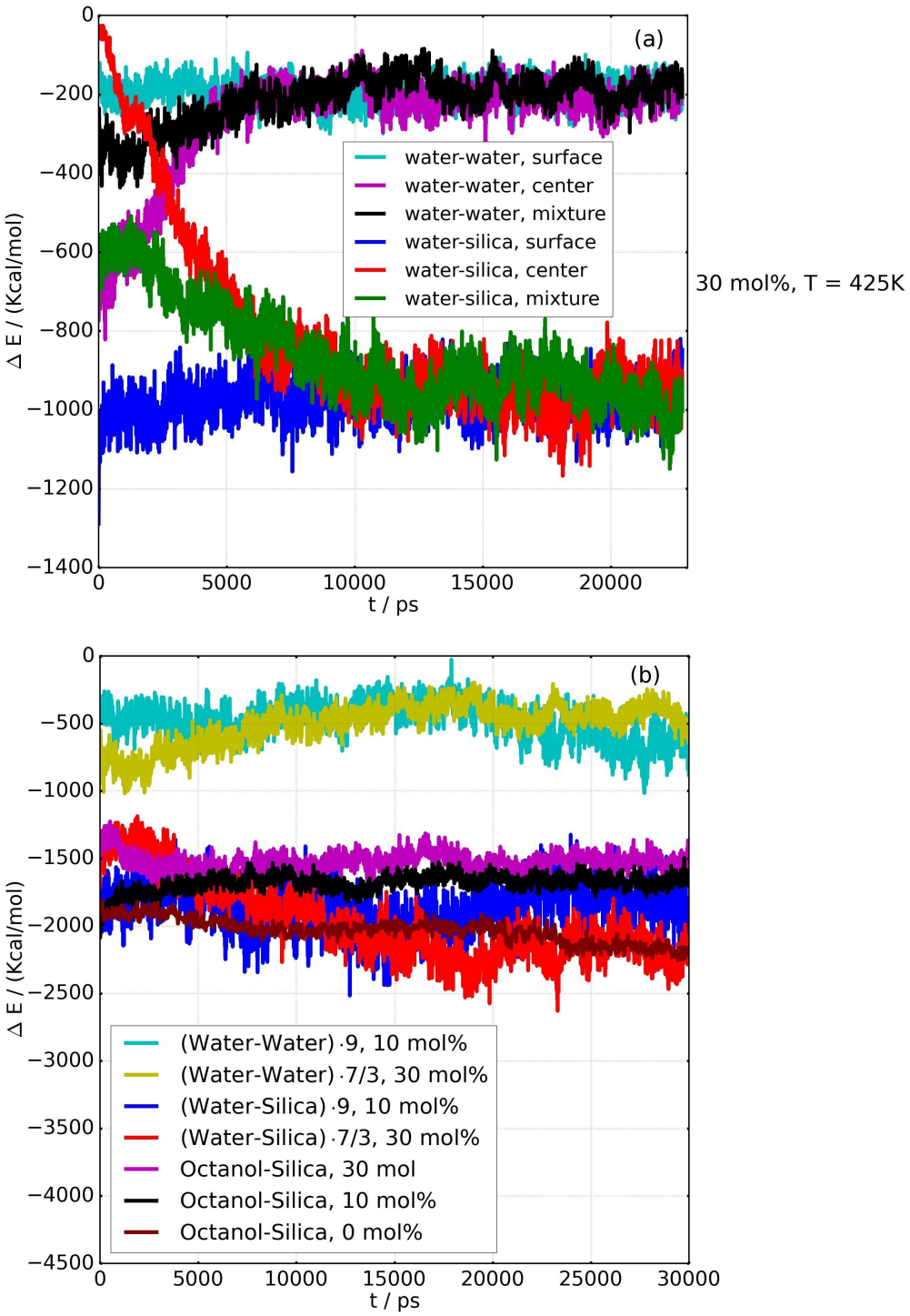

Figure 34: (a) Electrostatic energy between water molecules, and between water molecules and silica surface molecules for surface, center and mixture starting condition for the simulation of 30 mol% water content at 425 K. (b) is the electrostatic energy between water and water, water and silica, octanol and silica for the mixture starting condition for the 0, 10, 30 mol% simulations. Assuming that the energy is related to the number of water molecules, it has been multiplied by the indicator factor for a comparison with octanol. The energy plots are for the simulation in the 4 nm pore.

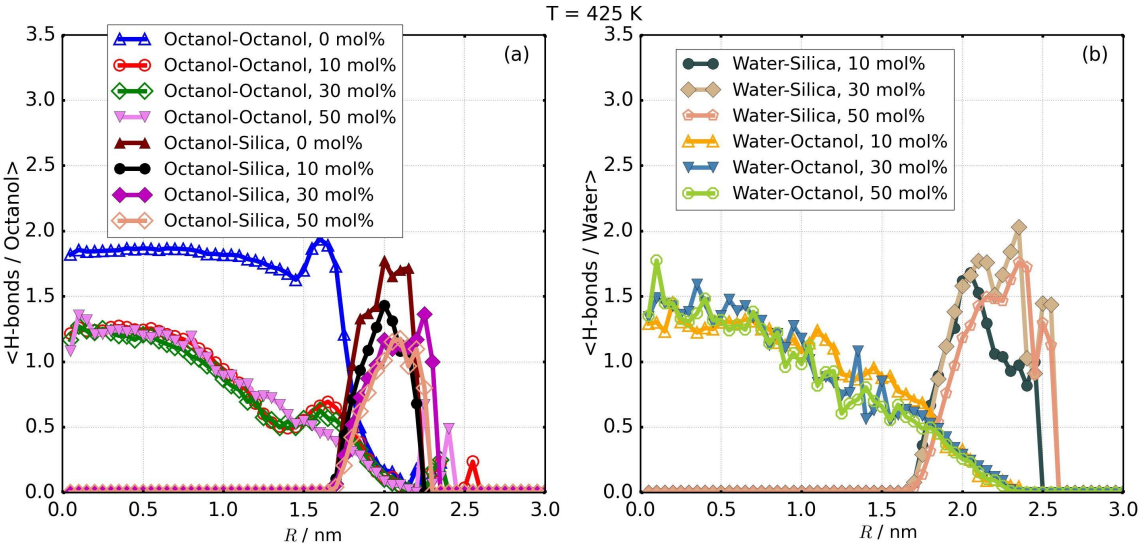

Figure 35: (a) Profile of the average number of hydrogen bonds per octanol molecule shared with octanol molecules (octanol-octanol) and silanol groups (octanol-silica). (b) The equivalent profile for water, including the hydrogen bonds between water and silanol groups (water-silica), and water and octanol molecules (water-octanol).

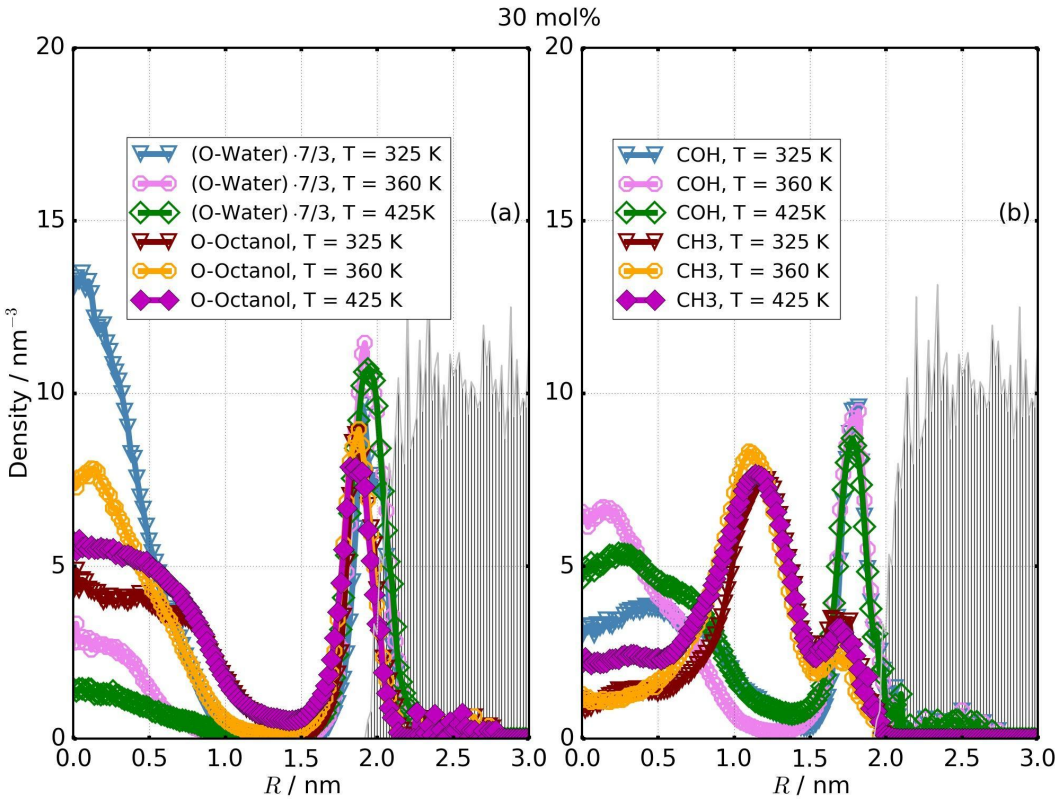

Figure 36: Number density profile of (a) oxygens of water and 1-octanol molecules and (b) of carbons (first carbon COH and last carbon of the chain CH3) of 1-octanol molecules, for 30 mol% of water content at different temperature. The density of water molecules is multiplied by the indicated factor for a better comparison. This corresponds to a simulation in the 4 nm pore.

somewhat depending on the water content and on the pore size. It means that interfacial octanols are enforced to fluctuate around certain angles to ensure H-bonds between octanol hydroxyl groups and silica sites and to accommodate with the possible exchange of H-bonds between a octanol molecule and free available silica sites.

6.3 Summary

We present the results of water and octanol mixtures in silica confinements. Since an octanol molecule is roughly 0.9 nm long, that is twice the pore radius of the silica pore fabricated by *Geske and Vogel*, [230] we use a similar methodology to fabricate bigger pores. In this way, we could check the effect of the mixing ratio as well as the pore size in the distribution undertaken in the pore. We further briefly analyze the effect of temperature.
Our MD simulation results clearly indicate that the hydroxyl groups from water and octanol tend to accumulate near the pore surface and form hydrogen bonds with the hydrophilic sites of the silica surface, agreeing with NMR experimental results. [67] Moreover, octanol and water also form hydrogen bonds with each other. MD simulations show evidence of the formation of a bilayer-like structure inside the 4 nm pore with hydroxyl groups oriented to the pore surface and in the pore center, and hydrocarbon chain in the pore intermediate region. This possibility to form bilayer-like structures is also demonstrated by NMR studies, which suggest an alignment of octanol molecules. However, the weak dipolar interaction of the protons in the second octanol layer with the silica surface makes it difficult to be accurately determined.
The effect of pore size has been checked using larger pore sizes of respectively 6 and 8 nm of diameter. We found out that the bilayer-like formation almost disappears in the bigger pores. In both cases the peaks in the pore center region are rather replaced by a flat density approaching octanol bulk density. The well pronounced peak of octanol and water oxygens density at the pore surface arise from the static energy landscape imposed by the immobile atoms of the pore surface. [22] The density peak of oxygens water accumulating in the pore wall vicinity can be confronted with the density peak of oxygens of octanol near the wall. We find out that the ratio between both peaks, is roughly 1.47 in a pore of 2 nm pore radius and then rises to 1.8 in the 3 nm pore radius, and reaches 2.1 in the 4 nm pore radius. This remark implies that the restriction imposed by a pore of smaller size prohibits some octanol molecules to quickly rotate and consequently water molecules are not effectively moving to the pore surface.
We have further analyzed the effect of water content and find out that it moves some octanol molecules from the pore surface to the pore center region leaving some free H-bonds sites in the silica surface to which water can bound. This process occurs irrespective of the pore size. Finally, the effect of temperature is to slow down the motions of molecules in the pore such that there is always a chance to find much more water molecules trapped within octanol molecules near the pore center.

Studies of water or water/octanol mixtures in silica confinements, reveal that the liquid structure is strongly distorted by the non-neutral pore surface such that it becomes difficult to distinguish the surface effects from the geometrical constraint effects on dynamics. Therefore the purpose of the successive chapters is to move to neutral confinements. We will choose silica since it offers the possibility to scrutinize dynamical transition. However, one would primarily inspect the bulk properties in the next chapter and then present neutral confinements effects in the later chapter.

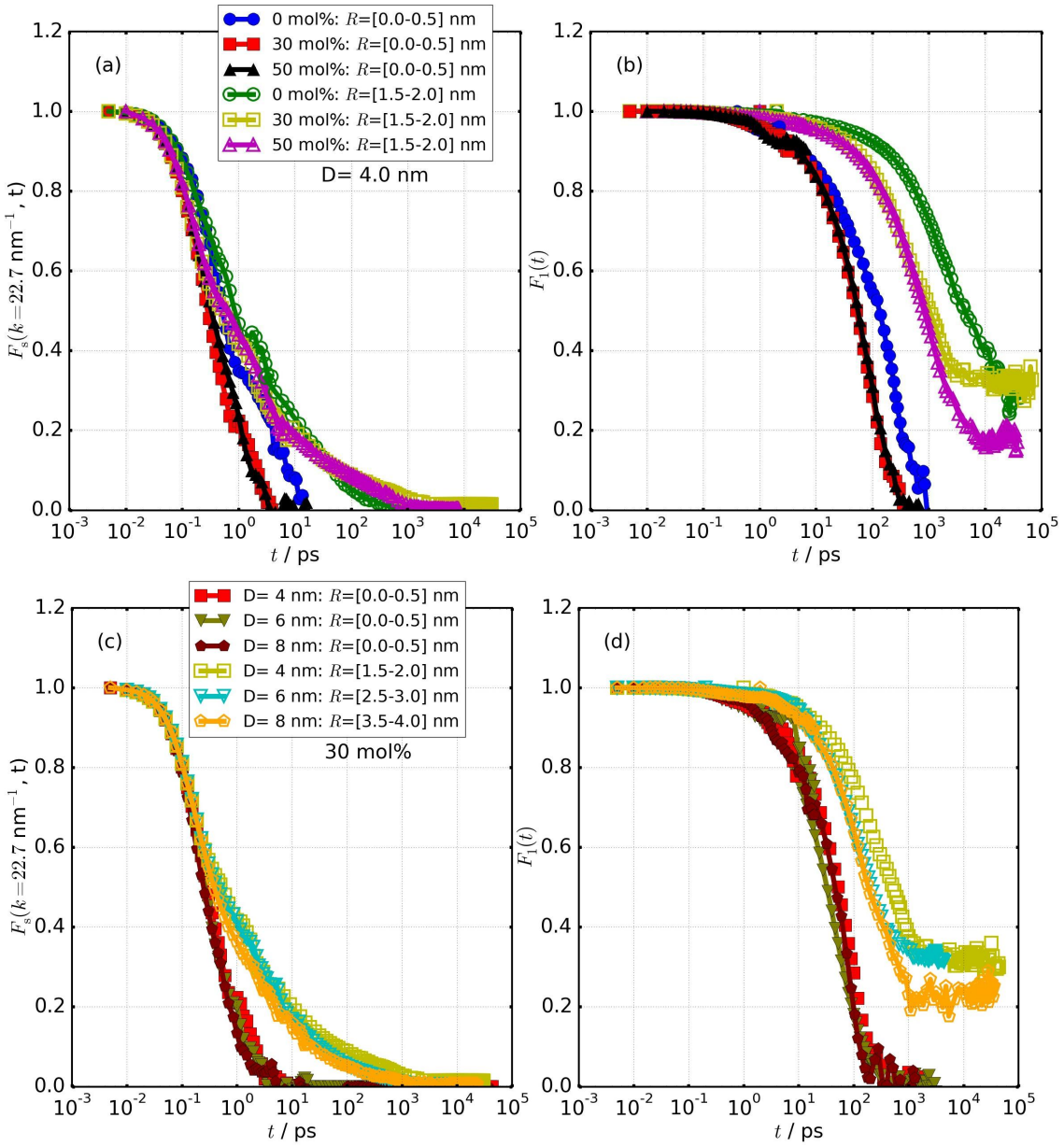

Figure 37: ISF (a)-(c) of octanol oxygens situated either within 5 nm of the pore center region or 5 nm of the pore surface. Similar curves are plotted for rotational correlation (b)-(d) functions of octanol sites when probing the dipole between the first (COH) and the end carbon (CH3) of the chain. The top panels indicate the effect of water content on dynamics, while the bottom are devoted to a fixed mixing ratio of 30 mol% but then study the effect of pore size is displayed.

7 Bulk silica with varying bond polarity

Silica and water molecules show several similarities: they have identical 2:1 stoichiometry, their networks form tetrahedral structure. They also exhibit analogous anomalous properties, [239, 240, 96, 85, 87] such as a density maximum upon temperature lowering, possible thermodynamic transitions between different liquids types presenting different degrees of ordering. In particular, the dynamical transition between fragile dynamics with a non-Arrhenius temperature dependence and strong dynamics with Arrhenius behavior is clearly established in silica. [104, 100] We would like to understand the foundation of these anomalies by inspecting structural and dynamical properties of silica-like liquids which differ by the bond polarity. These systems are obtained from the modified [104] BKS [105] silica model. The partial charges attached to silicons and oxygens are then systematically modified. In this way, we investigate in a generic manner the effect of electrostatic interactions in the glassy behavior of BKS silica. Most of the trajectories used for the regular BKS system (q/q_0=1.00) are outcoming from the work of *Julian Geske*. [180]

7.1 Simulation details

We study BKS silica [105] for which the pairwise potentials between silicon and oxygen atoms have been parametrized using ab-initio and experimental data in order to properly reproduce the nearest-neighbor interactions. This potential incorporates a Buckingham-like short-range interaction to the Coulomb electrostatic interaction, which can be expressed by assigning partial charges q_{Si} and q_{O} to silicons and oxygens. The following equations show the BKS pairwise potential.

$$V_{ij}(r) = \frac{q_i q_j}{r} + V_{ij}^{\mathrm{B}}(r)\,, \tag{58}$$

$$V_{ij}^{\mathrm{B}}(r) = A_{ij}\exp(-b_{ij}r) - \frac{c_{ij}}{r^6}\,. \tag{59}$$

The parameter values A_{ij}, b_{ij} and c_{ij} are given in Table, 6. The BKS potential between silicon and oxygen

Table 6: Parameters of the potential: A_{ij}, b_{ij} and c_{ij} are the values taken from the BKS potential, [105] while $C_{ij}^{(6)}$ and $C_{ij}^{(12)}$ are the modified values taken from. [241] The unit of the parameters presented here is K.

Site i	site j	A_{ij}	b_{ij}	c_{ij}	$C_{ij}^{(6)}$	$C_{ij}^{(12)}$
O	O	$1.61 \cdot 10^7$	$1.38 \cdot 10^3$	$2.03 \cdot 10^6$	$-1.14 \cdot 10^6$	$1.41 \cdot 10^8$
Si	O	$2.09 \cdot 10^7$	$2.45 \cdot 10^3$	$1.55 \cdot 10^6$	$5.65 \cdot 10^5$	$6.93 \cdot 10^6$
Si	Si	0	-	0	0	0

atoms negatively diverges at short interatomic distances, causing improbable dynamics at sufficiently large temperatures for which atoms have got enough thermal energy to cross the barrier separating the minimum region to this unrealistic range. To get rid of these non physical dynamics, the Buckingham part ($V_{ij}^{\mathrm{B}}(r)$) of the potential is slightly altered [104] at small distances by adding a repulsive contribution. This contribution can be visualized as followed: starting from the Buckingham form of the BKS model in the first relation of Eq. 58, [105] a cautious transition is made to a Lennard-Jones (LJ) potential

$$V_{ij}^{\mathrm{LJ}}(r) = C_{ij}^{(12)}/r_{ij}^{12} - C_{ij}^{(6)}/r_{ij}^{6}\,, \tag{60}$$

at short distances such that the potential remains continuously differentiable with distance. The resulting Buckingham form reads:

$$V_{ij}^{\mathrm{B}}(r) = \begin{cases} V_{ij}^{\mathrm{LJ}}(r)\cdot\left(\frac{r_{\max}-r}{r_{\max}}\right)^2 + V_{ij}^{B}(r_{\max}) & \text{for r<r}_{\max}\ , \\ V_{ij}^{\mathrm{B}}(r) & \text{for r}\geq\text{r}_{\max}\ . \end{cases} \tag{61}$$

with $r_{max} \approx 0.11$ nm. Fig 95 in appendix shows the obtained modified potential as compared to the original form. The ensuing potential remains identical to the original BKS potential for interatomic distances $\gtrsim 0.12$ nm, but for smaller distances the strong attractive part at small distances is replaced by a repulsive part (see Fig. 95 of appendix). Analogous modifications have been formerly implemented to remove the negatively divergent part in BKS silica. [83]

Starting from the standard modified BKS silica [104] for which the default partial charges of the BKS model are defined as $q_{Si} = 2.4e \equiv q_0$ and $q_O = -q_0/2 = -1.2e$., we have generated different silica by scaling the partial charges such that the partial charges range $0.65q_0$ and $1.4q_0$. This permits a thorough exploration of the effect of the Coulomb potential on the structure and dynamics of silica. The interacting potential between silicon and oxygen, combining the modified form of the Buckingham part and the Coulomb electrostatic interaction, is plotted in Fig. 38 for different partial charges. It shows two minima, a broad minimum at typical interatomic distances and a tight one at much shorter distances, which is artificially caused by the added repulsive term. For higher scaling factors $q/q_0 \gtrsim 1.21$, more atoms can occupy this artificial minimum even at intermediate and low temperature, leading to non-realistic liquid structural and dynamical characteristics, and specifically a decrease of tetrahedral order (see Fig. 40 (a) and Fig. 96 of appendix). We will therefore solely present results obtained with $q/q_0 \leq 1.21$. The lower limit of the scaling factor q/q_0 will be restricted to 0.65 since the density maximum and the strong dynamics appearing at low-temperature regime die out for $0.65q_0$ and smaller values of the charges. We performed MD simulations in the NPT ensemble, keeping the temperature T and the pressure P constant (1 bar) using the Langevin thermostat and the Langevin-Piston barostat, respectively. We simulate cubic systems of length changing with temperature but avoisinating 6 nm containing 5832 silicon and 11664 oxygen atoms. We apply PBC and estimate the long-range Coulomb interactions with the PME sum and a cut-off of 1.2 nm. The time step of the integration is generally set to 1 fs and in some cases 0.5 fs specifically for larger charges (q/q_0=1.09, 1.21) at high temperatures for which, otherwise, some atoms overcome the nearest-neighbor energy barrier to the unrealistic energy minimum at low r (Fig. 38). Before data acquisition, the system is always equilibrated for times at least comparable or much more longer than the structural relaxation time. The total simulation time reached during the simulations approaches 80-100 ns, relying on temperature and partial charges. The systems are each first equilibrated at high temperature in which structural relaxation times amount some ps and from the high temperature equilibrated configuration, the system is gradually cooled and then equilibrated at each designated lower temperature. The temperature range covered is between 1000 K to 9000 K but varies depending on the system. For example, for the sample corresponding to the lowest partial charge q/q_0=0.65, the temperature range is between 1000 K to 6000 K, while for the high partial charges case, the temperature are lying between 2700 K to 9000 K.

7.2 Results I: Structural properties

Fig. 39 shows the temperature-dependent density for different values of q/q_0. The density enlarges with increasing absolute values of the partial charges, which is expected as the attractive interaction gets then stronger and as the distance at which the interaction potential has its minimum reduces, see Fig. 38. The existence of a density maximum for conventional silica, is well known from experiments [242, 239] and simulations. [85, 81] We pinpoint that the density maximum as well as the density minimum in its vicinity are shifted to higher temperatures as the ratio q/q_0 increments. This can be rationalized while thinking about the fact that the contribution of the electrostatic energy (which is part of U) to the free energy $F = U - TS$ grows with increasing partial charge. As long as the potential energy part wins over the entropy contribution $-TS$ and dominates the trend of F, the density is mainly determined by the potential minimum, and the liquid assumes a low-density structure with high tetrahedral order and low entropy. When partial charges are incremented, a higher temperature is necessary to bring the system to the state of higher density and larger entropy, thus moving the density minimum to larger T. For partial charges $q/q_0 \lesssim 0.70$, the density minimum and maximum disappears and the liquid is similar

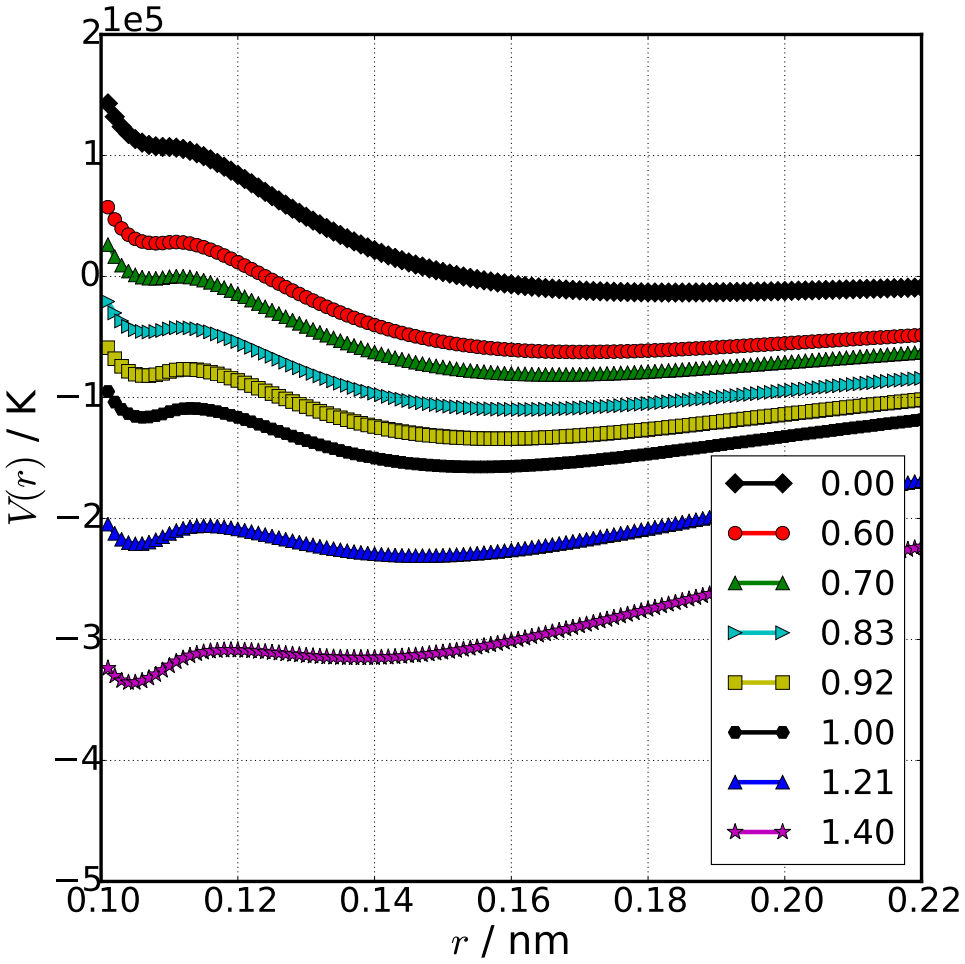

Figure 38: Interacting pairwise potential (measured in units of k_B times 1 Kelvin) between silicons and oxygens different partial charges q/q_0. The minimum at short distances arise from the definition of the potential to avoid the negatively diverging part. It strongly altered the system structure and dynamics when it gets lower than the realistic minimum related to the next-neighbor distance, only values $q/q_0 \leq 1.21$ are mainly considered for the simulations.

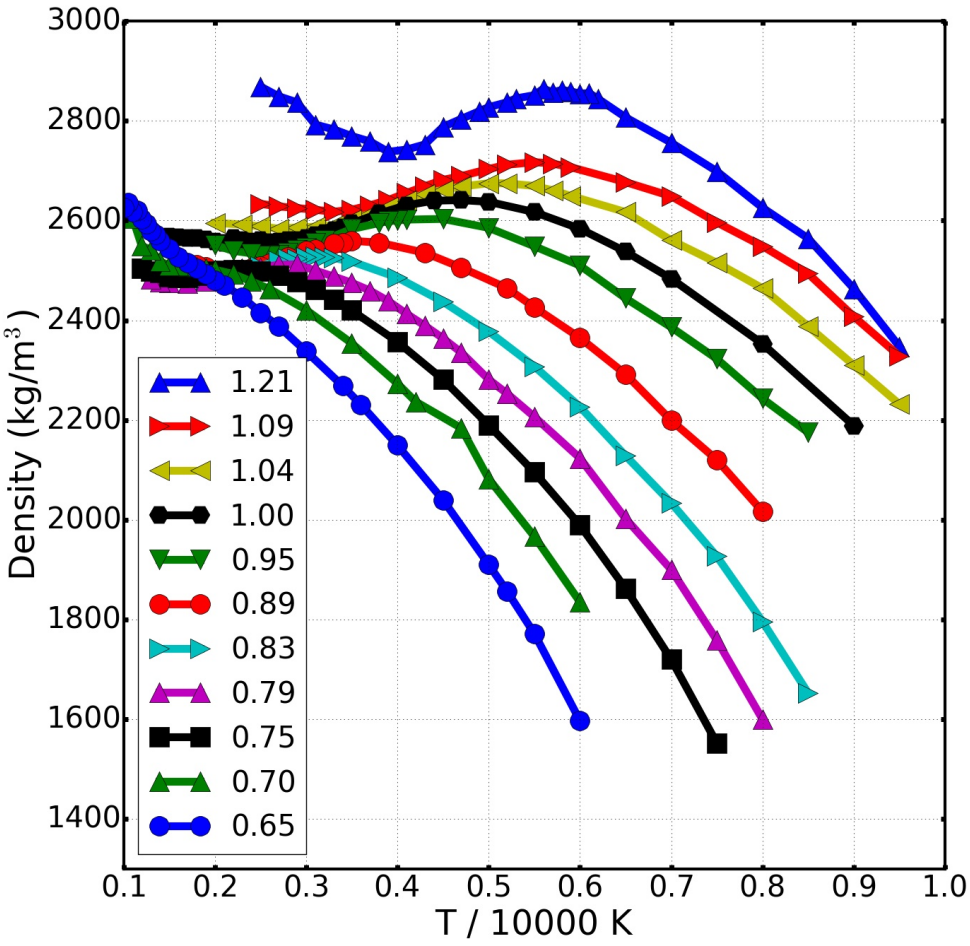

Figure 39: Density of silica models at a pressure of 1 bar over a wide temperature range, evaluated for different partial charges q. The numbers indicated in the legend denote the scaling factors q/q_0. The density values for $q/q_0 = 1.00$ are taken from Geske et al. [104]. For $q/q_0 = 1.21$, the equilibration periods for the 2-3 lowest temperatures were slightly smaller than the relaxation times so that one should be cautious when interpreting these data.

to a LJ liquid, which has no tetrahedral structure. This effect observed here while reducing the partial charges is similar to the effect of increasing pressure on regular silica [180] (i.e. q/q_0=1.00) since this also prohibits the formation of a lower-density ordered structure. An analogous vanishing of the density maximum with decreasing partial charges has also been recently shown for water-like liquids. [101] In this case, the density anomaly has been associated to the removal of molecules at interstitial positions located between the first and second neighbor shells. [101, 219, 243] The temperature at which this maximum occurs for the different silica systems (referred as T_{max}) is plotted in Fig. 54(a) and displays a rapid than linear increase with charges.

Next, we probe the local distribution of atoms by looking at the pair distribution function of silicon atoms to each other and between silicons and oxygens (Fig. 40). For the systems corresponding to the lowest partial charges, the distribution is plotted at a temperature avoisinating 1100 K while for the rest are evaluated at T_{FS} which is the crossover temperature between the strong dynamics and the fragile dynamics as displayed in Fig. 48 and plotted for the different systems in Fig. 54. Not surprisingly, the peak of the neighboring shells shift slightly to short distance when the partial charge increases, going in accordance with the density expansion with larger partial charges described below. While a similar effect can be conjectured in the second peak of $g_{Si-O}(r)$, the second peak of $g_{Si-Si}(r)$ changes additionally in broadness suggesting that the number of silicon atoms present in the second neighboring changes substantially with charges.

To clearly check the mechanism happening, we have evaluated the structure resolving it to each closest neighbor. We access it by looking at the partial radial distribution functions $g^{(i)}(r)$ of the ith nearest neighbors for silicon atoms introduced in Eq. 14 of Chapter. 3. We can then scrutinize the trend of each resolved radial distribution as presented by each systems. Fig. 41 display the local arrangement of the first to 8th neighbor, for q/q_0=1.21, 1.04, 0.65 in which one can identify a bimodal distribution appearing mostly in the peaks of the second coordination shell namely $g^{(5)}(r)$ and $g^{(6)}(r)$ for q/q_0=1.21, 1.04, which gets gets broader and extends from $g^{(6)}(r)$ till $g^{(8)}(r)$ for q/q_0=0.65 as the overall density diminishes. $g^{(1)}(r)$-$g^{(4)}(r)$ display mostly a unimodal distribution for all of them and which also gets wide for q/q_0=0.65.

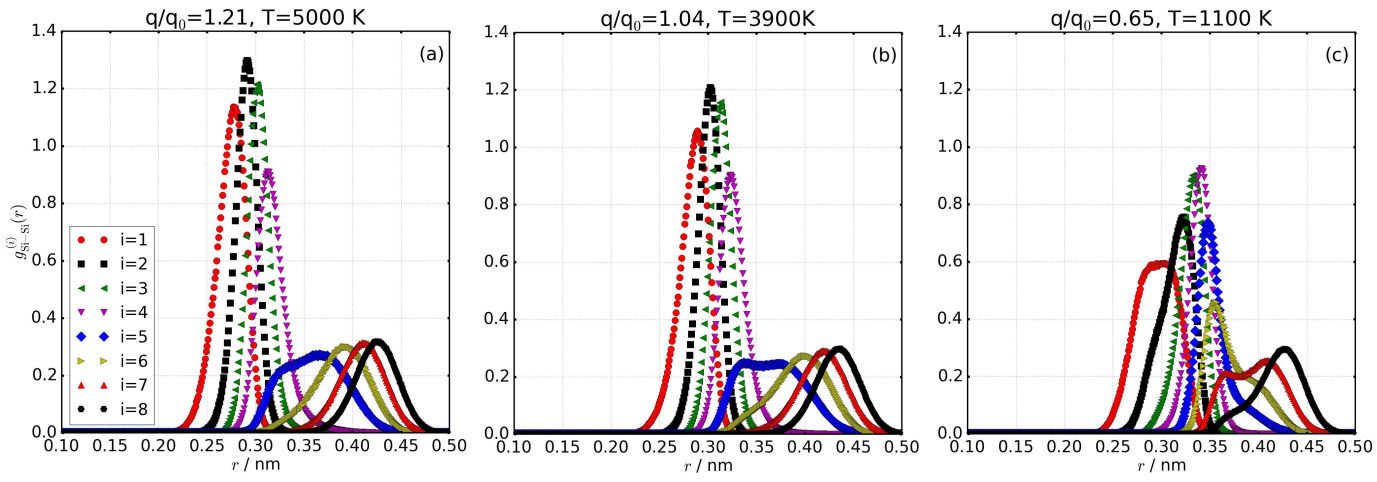

Figure 41: Distribution of $g^{(i)}$ (i)=1,..,8 (the first to 8 neighbors) for a fixed temperature (T=1100 K for q/q_0=0.65 (c), and T_{FS} for q/q_0=1.04 (b), 1.21 (a)).

We further study the temperature variation of the bimodal distribution observed in the second shell functions. Fig. 42 (a) exhibit $g^{(5)}(r)$ for q/q_0=1.04 and it can be noticed that this distribution is unimodal at high and low temperatures with peaks at $r \approx 0.34$ nm (short distances at high temperature)

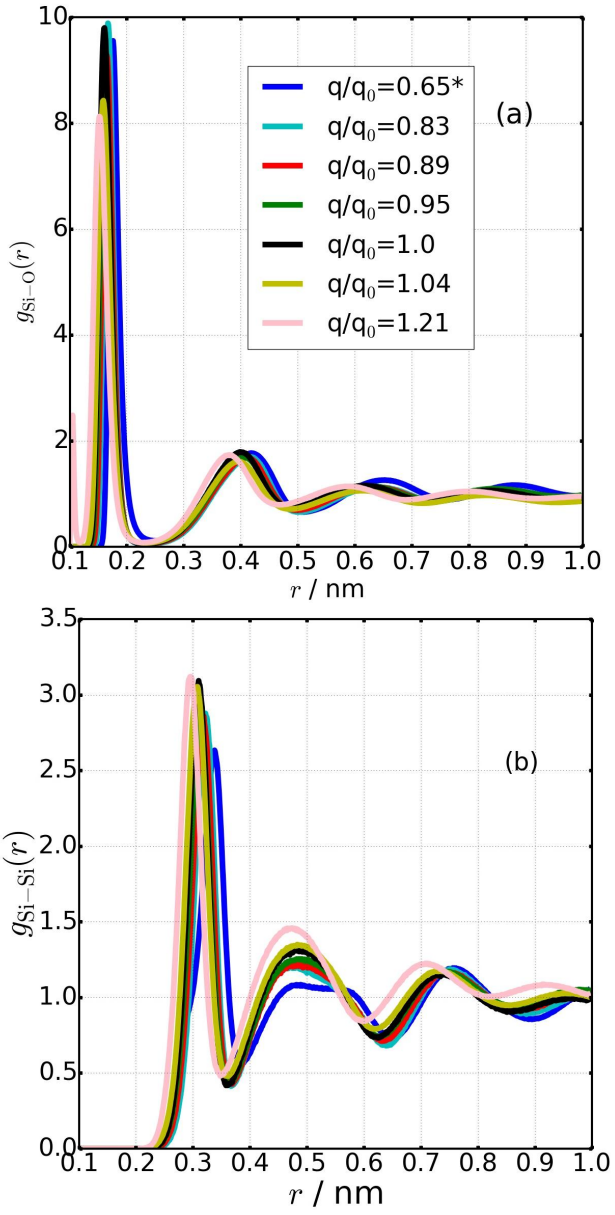

Figure 40: Nearest neighbor radial distribution between silicon and silicon (a) as well as silicon and oxygens (b) plotted for the different silica systems. For the three systems corresponding to the lowest partial charges and marked in the legend by an asterix symbol, the temperature chosen is roughly 1100 K. For the other systems, the distribution displayed is evaluated at the particular FS transition temperature T_{FS} (the crossover temperature between the low-temperature Arrhenius fit and the *Röessler*/VFT fit as illustrated in Fig. 48 and plotted in Fig. 54). The very first peak in $g_{\mathrm{Si-O}}(r)$ represents some oxygens which are occupying the unwanted energy minimum at short distance defined in Fig. 38.

and $r \approx 0.39\,\text{nm}$ (larger distances at low temperatures), respectively, both associated to distances between the first and second coordination shells of the total pair distribution function ($g_{\text{Si-Si}}(r)$) plotted in Fig. 40(b). In particular, when the temperature is closest to the temperature of density maximum (T_{max}) then $g^{(5)}(r)$ is unimodal with the maximum peak (see Fig. 42 (a) and Fig. 97 in the appendix.) and when the temperature is increased or decreased from T_{max} then the peak of the unimodal distribution diminishes, this could imply that the appearance of density maximum should be related to the maximum of 5th neighbors located in the nearby of the first neigboring shell (at around $r \approx 0.34\,\text{nm}$). Furthermore, at intermediate low temperatures, $g^{(5)}_{\text{Si-Si}}(r)$ is bimodal and the peak at larger r intensifies with respect to that at shorter r upon cooling. Interestingly, the modification from the first to the second peak happens in the vicinity of the FS transition, see Fig. 42(b). The bimodal trend in $g^{(5)}_{\text{Si-Si}}(r)$ suggests that, at ambient pressure and intermediate temperatures, liquid silica experiences two different types of local neighborhoods, which are each distinguishable through the spatial arrangement of atoms between the first and second coordination shells and, thus, the atoms density and the associated relative weight continuously changes with temperature. Besides the atom pair distribution, particles local arrangements can be examined by means of the tetrahedral order parameter introduced in Eq. 16 of Chapter. 3 describing explicitly the change in network structure. Fig. 43 displays the temperature change of the average tetrahedral order parameter $\langle Q_i \rangle$ for the different silica systems. $\langle Q_i \rangle$ expands when the temperature

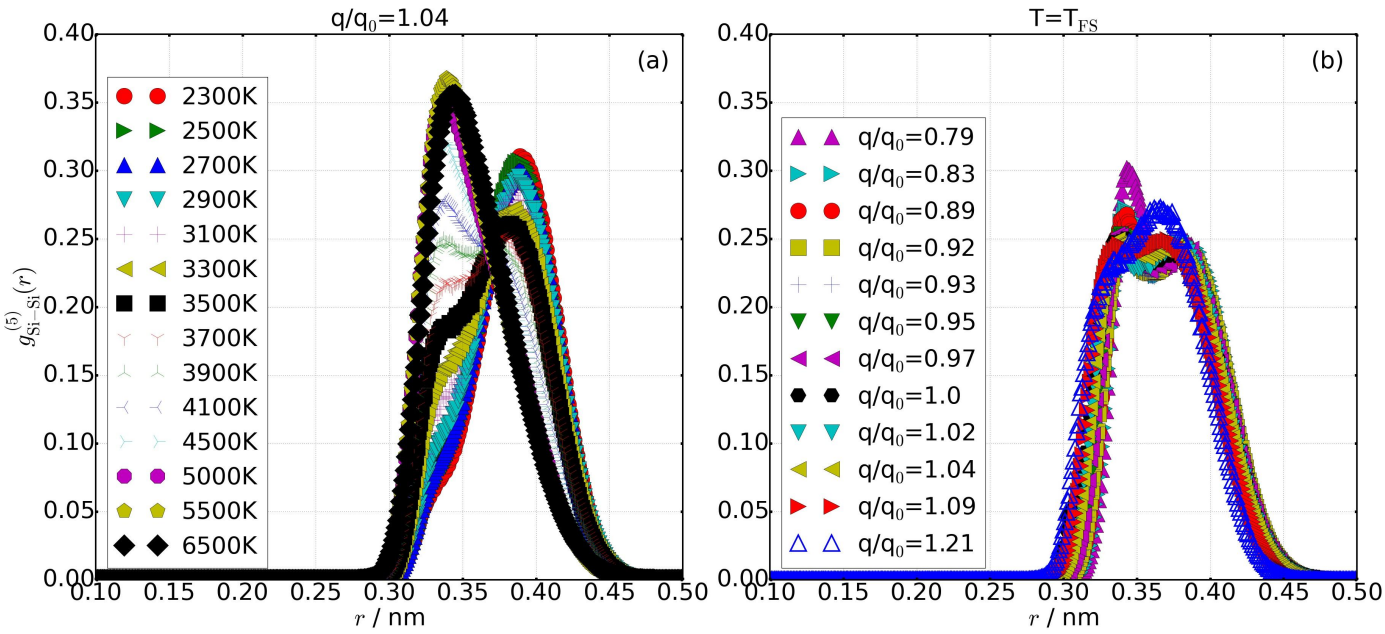

Figure 42: Radial distribution of the 5th nearest silicon neighbor of a silicon atom (a) for different temperatures and $q/q_0 = 1.04$ and (b) for the temperature of the FS transition, $T = T_{\text{FS}}$, and different partial charges. In (a), the distribution is unimodal and reaches its maximum around the temperature of density maximum.

lowers and the partial charges are incremented. Interestingly, the average order show a peculiar feature at some specific temperature for which it becomes independent of partial charge. In fact, it amounts to $\langle Q_i \rangle \approx 0.6$ at the temperature of the density maximum, T_{max} (plotted in Fig. 54(a)). At this temperature, the distribution of the tetrahedral order parameter is widest and its shape is analogous for different partial charges, see Fig. 44(a). This shape displays two peaks of roughly equal height, revealing that at T_{max}, the order is evenly distributed between $\langle Q_i \rangle \approx 0.5$ and $\langle Q_i \rangle \approx 0.75$. For the system ($q/q_0 < 0.65$) where the density maximum is absent, $\langle Q_i \rangle$ remains below 0.6. In Fig. 98 of appendix, we show the

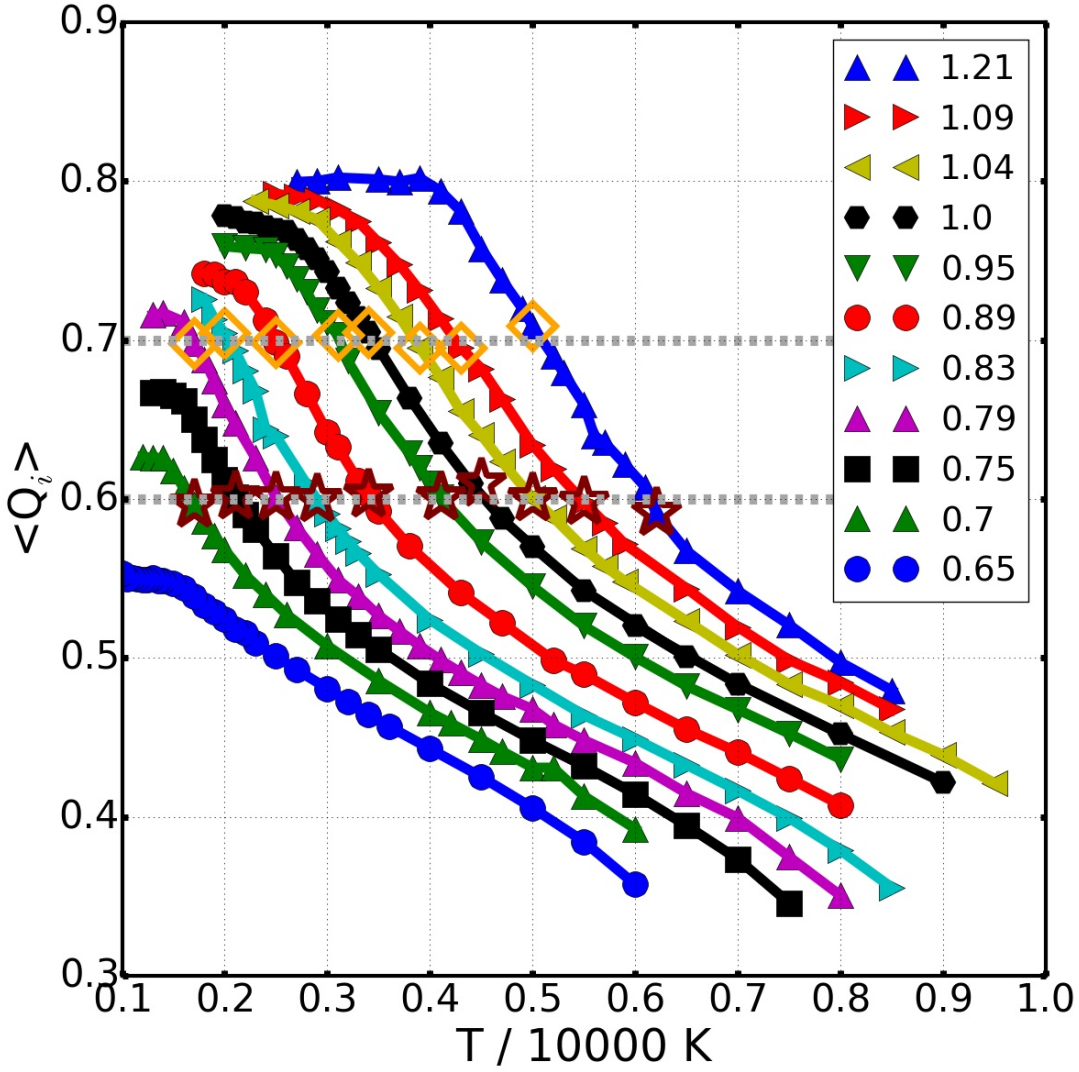

Figure 43: Temperature dependence of the average tetrahedral order parameter $\langle Q_i \rangle$ for different values of the scaling factor q/q_0. The temperatures T_{max} where the density has its maximum are marked with maroon stars and the temperatures T_{FS} where the dynamical FS transition occurs (see Fig. 48 below) are highlighted with orange diamonds. The tetrahedral order parameter values for $q/q_0 = 1.00$ are taken from *Geske et al.* [104].

evolution of the distribution of the tetrahedral order parameter from a peak at lower order to a peak at higher order when reducing temperature for fixed partial charge.

$\langle Q_i \rangle$ tends to levels off at low temperatures to a constant value which itself gets little for lower q/q_0. To check whether these low-temperature values correspond to a well equilibrated sample, we check the distribution of the local ordering when changing the initial configuration of the simulation. Fig. 45 shows the obtained distribution for q/q_0=0.65 when using as starting either the standard method as introduced in the previous paragraph, or using the equilibrated configuration at the given temperature but for the system associated with a higher partial charge q=0.79q_0. Here we choose two low temperatures 1300 K and 1400 K for q/q_0=0.79 which are below the FS crossover and the order parameter is above 0.7. We start from the equilibrated configuration got at these two temperatures and the system partial charges is scaled to q/q_0=0.65, 0.70; the derived distribution (as shown in Fig. 45) is identical. It means that when starting with initial states of high order (as in this case $\langle Q_i \rangle \approx 0.7$) or with starting states at low order (for example $\langle Q_i \rangle \approx 0.35$ obtained for q/q_0=0.65 and T=6000 K), one recovers the same balanced state at low temperatures and, hence the plateau observed does not arise from insufficient equilibration.

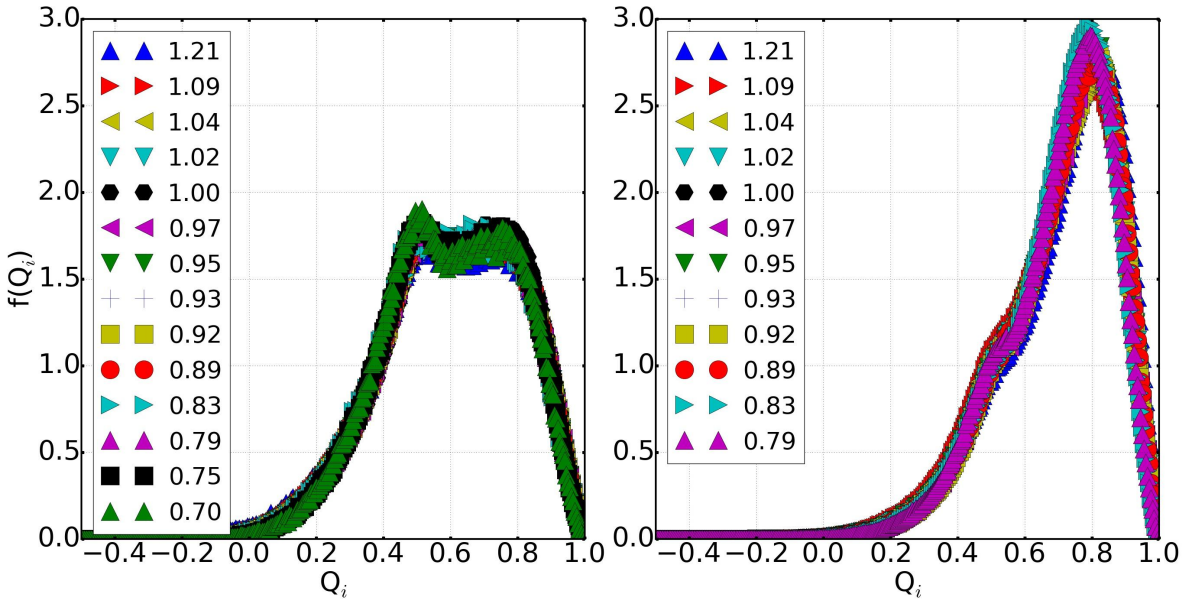

Figure 44: (a) Bimodal distribution $f(Q_i)$ with peaks of equal height of the tetrahedral order parameter for $T = T_{\max}$, which is the temperature of density maximum. (b) Unimodal distribution of the tetrahedral order parameter with a small shoulder at $T = T_{\mathrm{FS}}$, which is the temperature of the FS crossover, see Fig. 48 below.

7.3 Results II: Dynamical properties

We will now quest the dynamical features of the systems. In order to compare the motion of atoms on the same length scale, we will basically probe dynamics on the nearest neighbor length scale and use $k = 2\pi/d = 20\ \mathrm{nm}^{-1}$ corresponding to the average silicon-silicon nearest neighbor distance $d \simeq 0.31$ nm. In order to check to which extent our results can be generalized, we also tested other values of k in the range $k = 10-25\ \mathrm{nm}^{-1}$, and we show that the dynamics at intermediate and high temperatures depend considerably on k, but our general conclusions are not affected (see Fig. 51.).

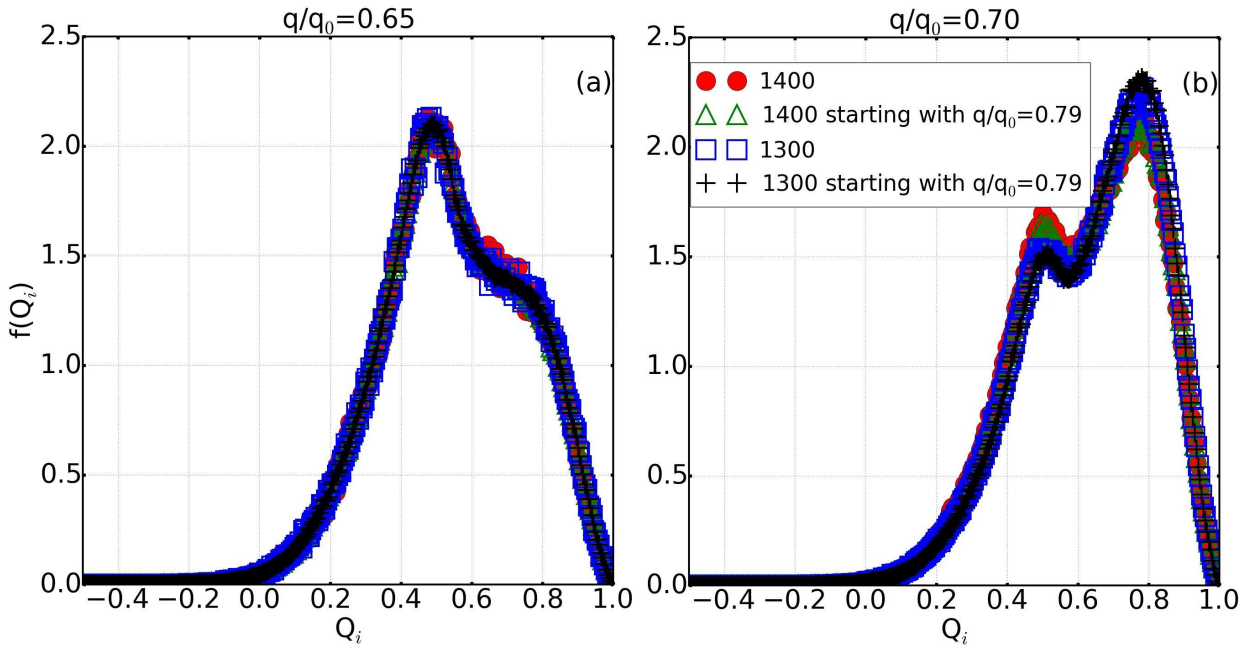

Figure 45: Distribution of the average tetrahedral order parameter plotted for two silica like liquids with q/q_0 = 0.65, 0.70, using either the standard starting configuration which is given by the equilibrated configuration at a higher temperature; or using the equilibrated configuration obtained at q/q_0 = 0.79 for the corresponding temperature of simulations.

Fig. 46 (a)-(b) display the ISF curves for various temperature for q/q_0=0.65, 1.21 in which the dashed lines indicates the value at which structural relaxation times are extracted. The typical two-step decay which fingerprint the low temperature dynamics of supercooled liquids can be recognized. The short time decay describes local vibrational motion, while the long time decay describes the structural relaxation processes. Both decays are hardly distinguishable at high temperature and this has a strong influence in the results concerned by the transition time between these decays. Similarly in Fig. 46 (c)-(d), the short-time dynamics characteristic of the vibrational motion can be identified, next to it comes the plateau regime also known as cage regime during which particle are trapped in cages formed by the nearest neighbors immediately followed by structural relaxations at longer times where particles are diffusing. The rapid slow down of dynamics with temperature can be observed.

Along with that, comes the charge dependent dynamics in which one compares the motion of particle of different liquid systems at a fixed temperature. Fig. 47 shows such trend observed at $T \approx 3100\,\mathrm{K}$ and different partial charges in ISF (a) and MSD (b). The effect of increasing q/q_0 is comparable to that of decreasing T. For sufficiently large q/q_0, the ISF data present a two-step decay. Likewise, for sufficiently high bond polarity, a prominent plateau separating vibrational and diffusive motions can be observed in the MSD. The observed massive slowdown of structural relaxation with increasing magnitude of the partial charges signifies that supercooled liquids dynamics are hugely affected by electrostatic interactions.

We continue our analysis by making a quantitative description of the slow down trough the determination of structural relaxation times τ from the ISF decays. Fig. 48 displays the variation of τ with respect to temperature for exemplary values of q/q_0. For most values of the partial charges, the data match well with an Arrhenius fit at high or low temperatures, yielding τ_∞ and E_∞ in the high-temperature regime and τ_0 and E_0 in the low-temperature regime. For ratios $q/q_0 \lesssim 0.75$, there are a high-temperature Arrhenius regime and a fragile regime, but a low-temperature Arrhenius regime is not observed in the temperature range accessible to our simulations. We use two approaches to probe the intermediate frag-

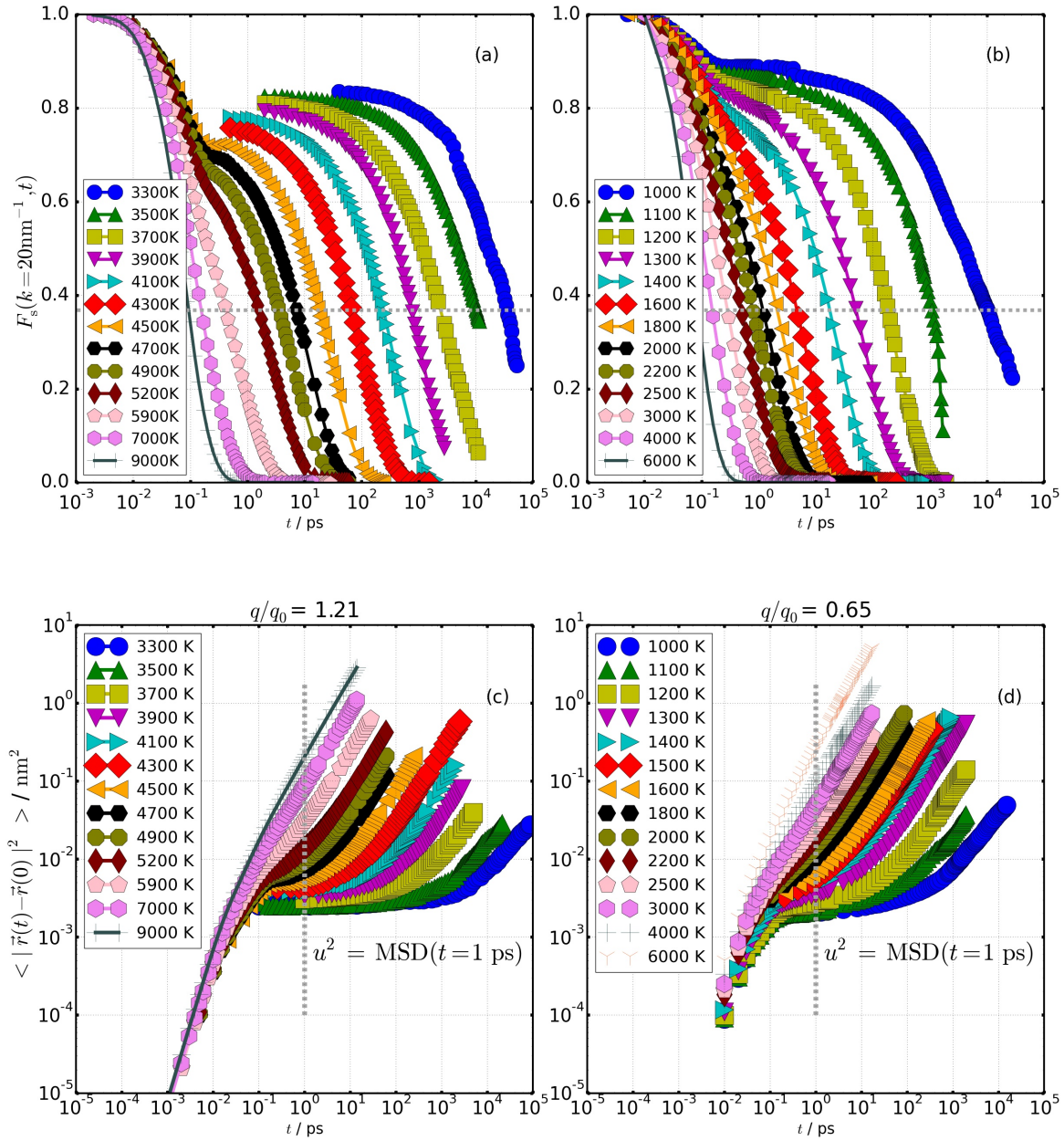

Figure 46: (a)-(b): ISF $F_s(k,t)$ for silicon atoms at $q/q_0 = 0.65$ (a) and $q/q_0 = 1.21$ (b) and different temperature. (c)-(d) the respective temperature curves of the MSD. The dashed horizontal line in panel (a) and (b) marks the value e^{-1} used for determining τ; while the dashed vertical line in (c) and (d) exhibits the time at which the Debye-wall factor u^2 is determined.

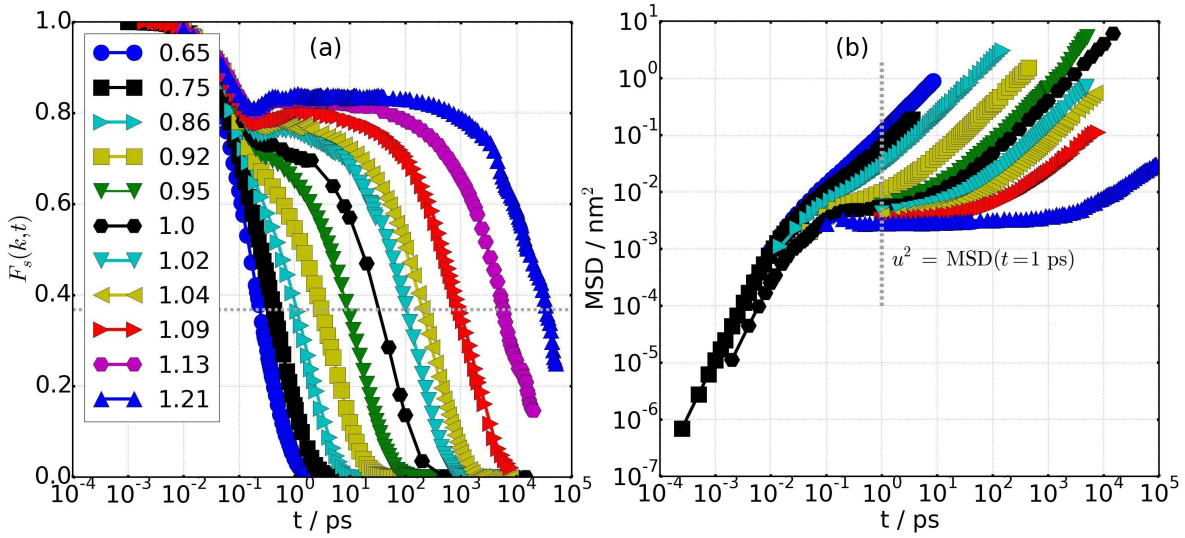

Figure 47: (a) ISF $F_s(k = \mathrm{nm}^{-1}, t)$ for silicon atoms at $T \approx 3100$ K and different values of q/q_0. The dashed horizontal line marks the value e^{-1} used for determining τ. (b) MSD as function of time for the same parameter values. The ISF and MSD for $q/q_0 = 1.00$ are taken from Geske et al. [104].

ile regime in silica systems namely the VFT law and the Rössler approach. [184, 185, 186] With both functionals, we confirm the occurrence of a FS transition governing the low-temperature dynamics of silica systems where the non-Arrhenius behavior crosses over to the low-temperature Arrhenius behavior. We deduce the temperature T_{FS} of the FS transition from the intersections of the interpolations of the fragile regime (purple or green curves) with the Arrhenius fit (blue line). For the given density of data points and statistical accuracy, we can extract this transition temperature with a precision of ∼100 K. The resulting temperature values are already designated in Figs. 43 - 42. In Fig. 54(a), we show that the crossover temperature T_{FS} roughly grows linearly with partial charge. A more appealing point is that at T_{FS} the distribution of the tetrahedral order parameter $f(Q_i)$ (see Fig. 44(b)) is nearly analogous for all scaling factors q/q_0, with a peak at $\langle Q_i \rangle \approx 0.77$ and a small shoulder at $\langle Q_i \rangle \approx 0.5$. Indeed, the average order parameter takes the common value $\langle Q_i \rangle \approx 0.7$ at T_{FS} (see Fig. 43) with no partial charge dependence. This findings combined with our results for the distribution of the 5th nearest neighbors at T_{FS} (displayed in Fig. 42) confirms that the FS transition is closely correlated to a transition from a high- to a low-density liquid and happens when a sufficiently high degree of local order is reached upon cooling. The values of T_{FS}, E_∞, and E_0 presented here are roughly identical to the ones obtained when doing a similar analysis with the oxygens correlation times as indicated in Figs. 103 and 104 of appendix.
The connection between the high- and low-temperature activation energies E_0 and E_∞ is shown in Fig. 49. For silica systems with partial charges lying within 5% of the original value q_0, the low-temperature activation energies E_0 remain in the range 4.7-5.5 eV $\widehat{=}$ 54500-63800 K consistent with previous reports. [244, 245, 99, 97, 93, 94, 104] Moreover, E_0 values do not depend on the length and time scales over which the dynamics are inspected, as we obtain analogous results from the ISF with $k = 20$ and $10\,\mathrm{nm}^{-1}$, or from the self diffusion coefficient extracted from the long-time behavior of the MSD. This is exhibited by Fig. 105 in appendix. In Fig. 50, we show that E_0 is mostly dominated by Coulomb interactions and roughly scales as the typical interatomic energy between neighboring atoms. This is plausible when thinking about the fact that low-temperature dynamics are controlled by hopping motions of oxygen and silicon atoms between neighboring sites, with energy barriers originating from the Coulomb repulsion with nearby atoms of the same type. Viewing again Fig. 49, one notices that when increasing the absolute value of the partial charges, E_0 increments faster than E_∞. The main

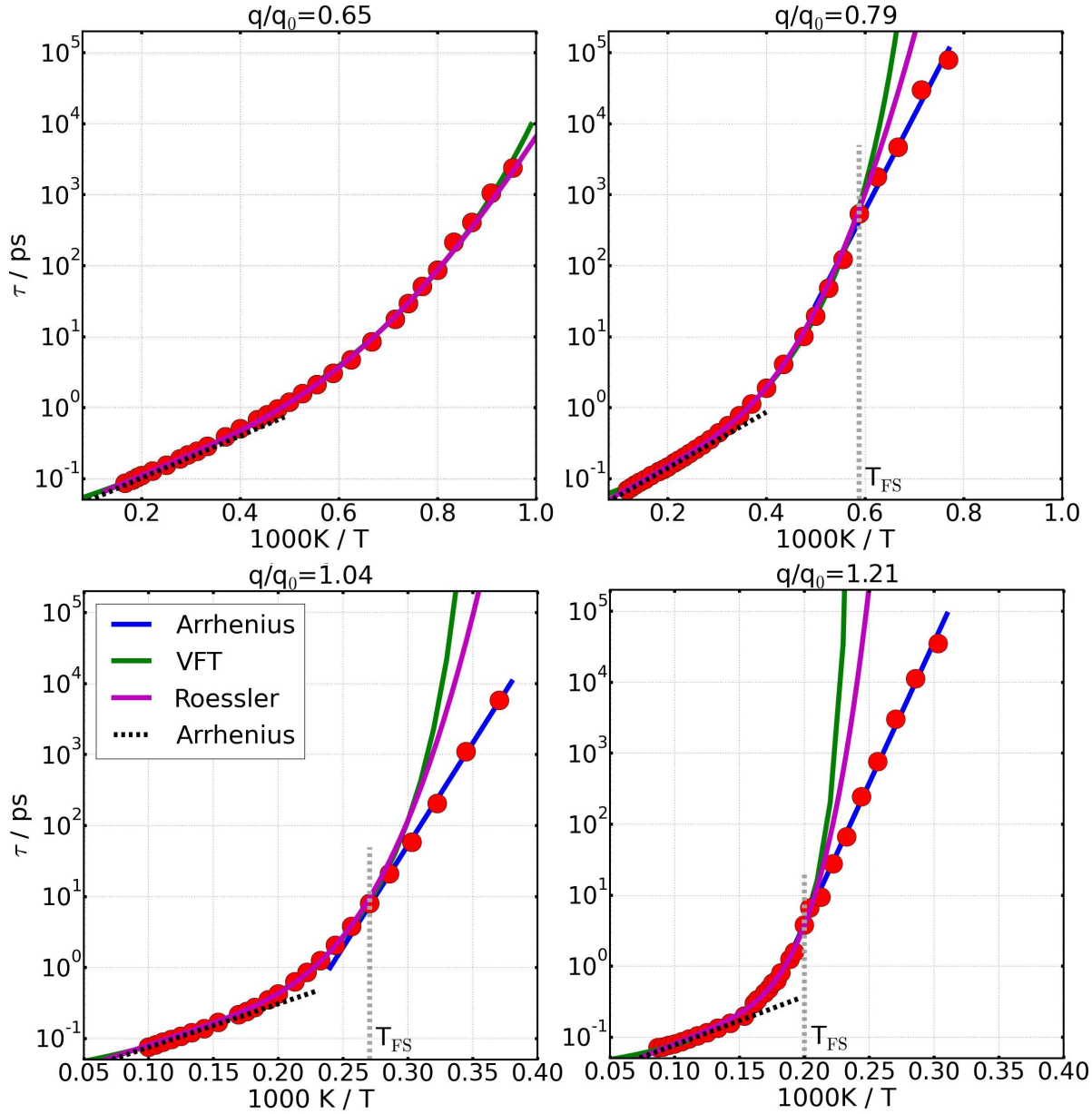

Figure 48: Structural relaxation times for silica-like liquids with various partial charges. Fits with the Arrhenius equation, Eq. 28, at high and low temperatures and with the VFT relation, Eq. 29, or the Rössler approach, Eq. 30, are included. The dotted vertical lines indicate the temperature of the fragile-to-strong transition T_{FS}. It is defined as the temperature where the non-Arrhenius behavior crosses over to the low-temperature Arrhenius behavior.

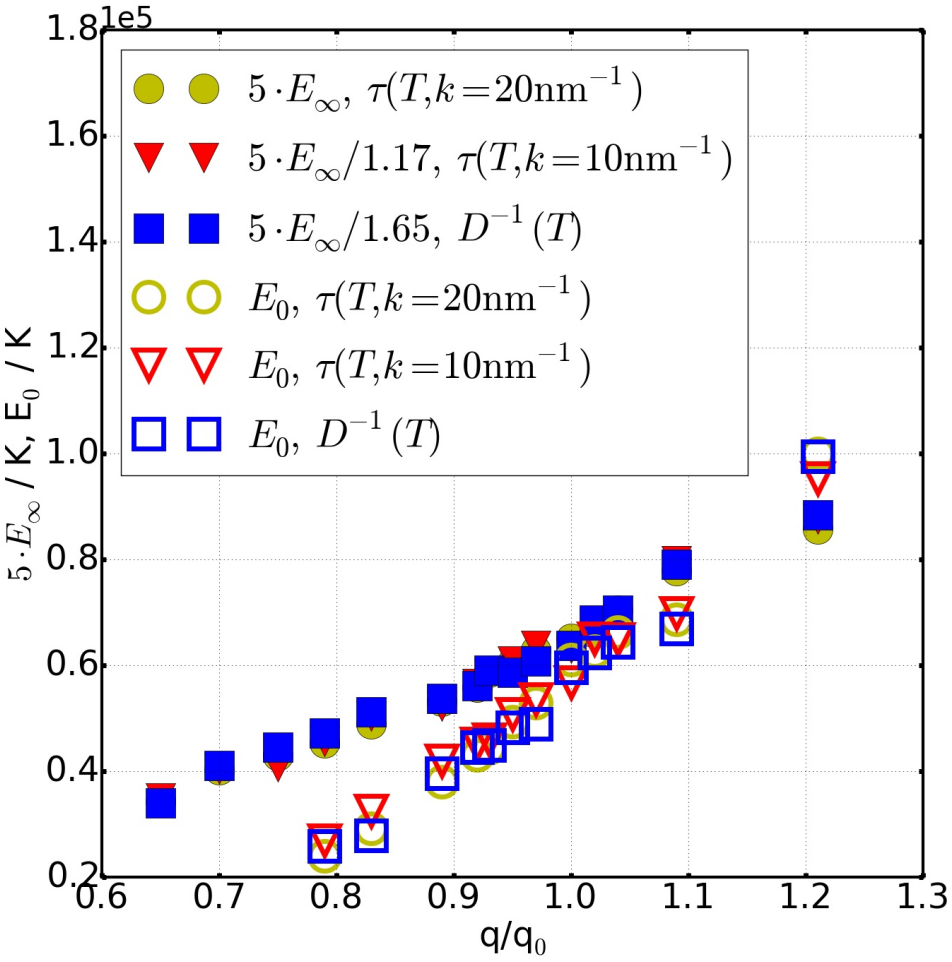

Figure 49: Charge dependence of the activation energies resulting from low-temperature (E_0) and high-temperature (E_∞) Arrhenius fits.

difference between E_0 and E_∞ should be related to the entropic contribution to motion. In the ordered low-temperature structure, entropy is small and the induced frustration on the Si-O bonds is weak, explaining our statement that E_0 depends linearly on the local bond strength. Oppositely, in the high-temperature liquid, thermal fluctuations should strongly influence dynamics, irrespective of the value of the partial charges.
Another important aspect is that when extrapolating the low-temperature Arrhenius fit to the point where $\tau = 100\,\mathrm{s}$, we find a glass transition temperature $T_g \sim 1450\text{-}1480\,\mathrm{K}$ for $q/q_0 \simeq 1$, see Fig. 54(a), which is comparable to the experimental value. [91, 246, 247, 88, 248] Thus the modified [104] BKS [105] model used in the present investigation reproduces qualitatively well dynamical features of liquid silica. Over the entire range of q/q_0, the glass transition temperature T_g varies by a factor of 4.

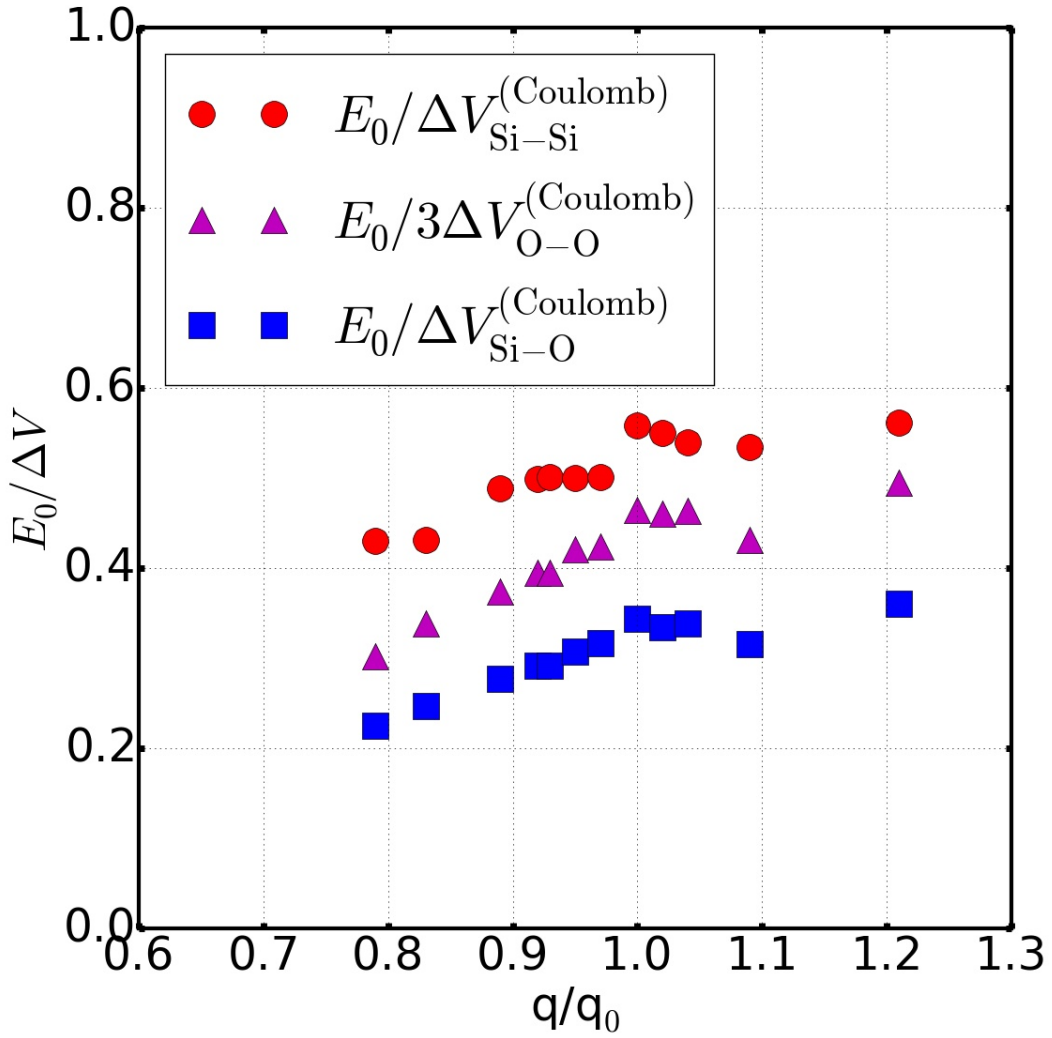

Figure 50: Activation energy compared to the value of the typical interatomic Coulomb interaction energies between two atoms positioned respectively in the first and the second coordination shell. The scaling factor 3 is used in the case of oxygen-oxygen interacting potential for a better comparison.

Furthermore, Fig. 49 reveals that the high-energy barriers E_∞ resulting from different length and time scales vary by some factor. This discrepancy might arise from the difficulty to discriminate the decays as-

sociated with vibrational motion and structural relaxation in the ISF at high temperature. Therefore, one should be very cautious when employing ISF and MSD data at high temperatures to investigate relations between structural relaxation times and self diffusion coefficients, e.g., the Stokes-Einstein (SE) relation. In this prospect, Fig. 51 shows the k-dependent dynamics of silicon atoms for two exemplary systems represented by q/q_0=0.83, 1.04, and 1.21. The difference in curvature happening at intermediate temperature can be identified in each curve, while the low-temperature dynamics particularly display less k-dependency. An attempt to establish the SE relation for different k's lead to Fig. 52 in which the SE

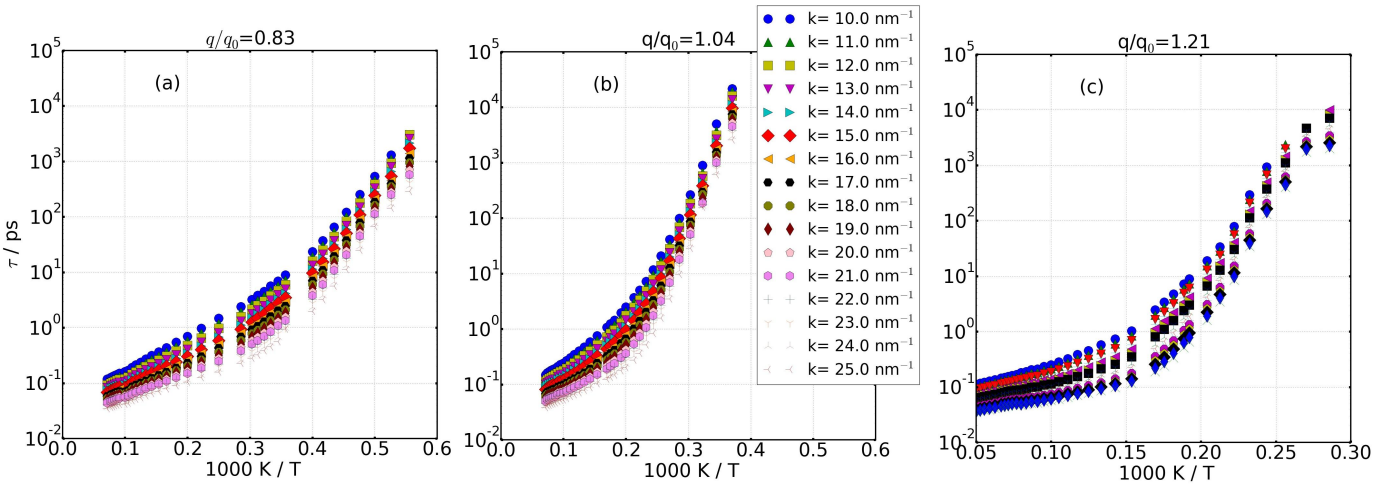

Figure 51: Temperature dependence of τ for different k-momentum. In the fragile regime, the curves are steeper for larger k-momentum. The low-temperature evolution shows almost no k-dependence. The plots correspond to three scaling factors (a) q/q_0=0.83, (b) q/q_0=1.04, and (c) q/q_0=1.21.

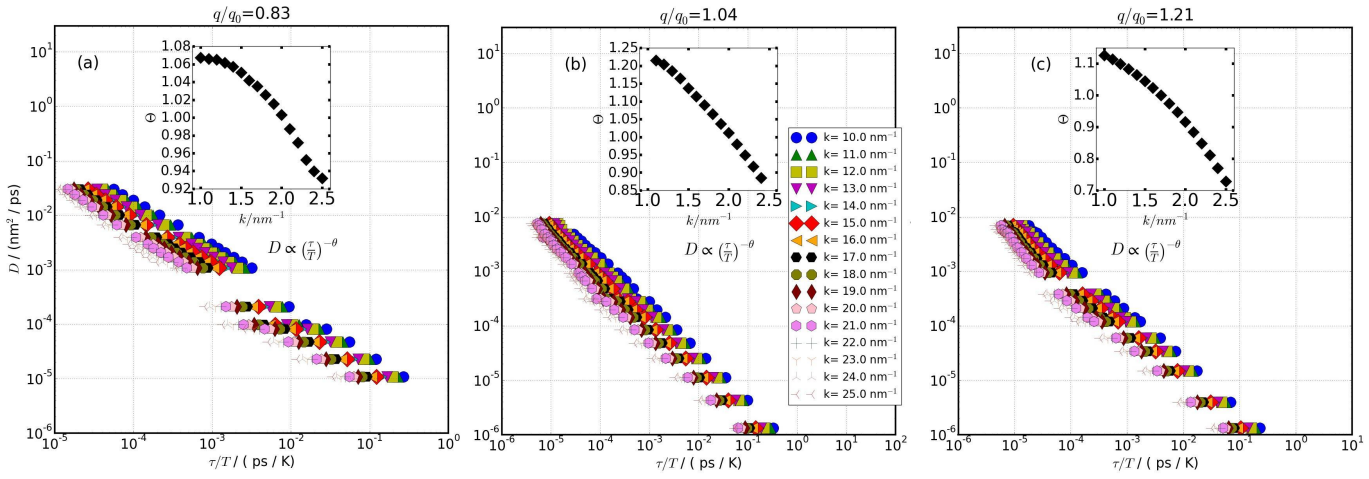

Figure 52: SE representation of D with respect to τ/T: the inset shows the inferred θ values when fitting the curves with the SE relation as expressed in the figure panel. The plots correspond to three scaling factors (a) q/q_0=0.83, (b) q/q_0=1.04, and (c) q/q_0=1.21.

relation is checked for q/q_0=0.83, 1.04, and 1.21. The ensuing values of θ are almost changing linearly with k and tends to saturate closely to 1 for the short k corresponding to larger length scales. This suggest that the SE relation break-down might only arise due to the strong influence of the length scale over

which dynamics are probing to inspect fragile dynamics. This is somehow intuitive because one might think that the shorter is the length scale over which dynamics are inspected, the more heterogeneous are the emanating particle dynamics.
Additionally, reinspecting the intermediate temperature regime of Fig. 48 enables us to explore in detailed the fragile regime. We observe that both VFT and *Rössler* fit functions well capture the fragile dynamics. The fit parameters deduced from the VFT law are plotted in Fig. 101, T_{VFT} present a faster than linear incrementation with partial charges, in contrast to the values of E_{VFT} which are almost not changing and are of the same order of magnitude as previously recorded data. [104] The fit with the *Rössler* functions [184, 185, 186] is performed as followed: in the preliminary step, τ_∞ and E_∞ are deduced from the obtained Arrhenius high-temperature fits and are used to calculate $E_{\mathrm{c}}(T)$ with Eq.(31); then a two-parameter fit using Eq.(32) is performed, giving as output a generalized fragility μ and a characteristic temperature T_A. The curves showing the resulting fit (with k =10 nm^{-1} and k =20 nm^{-1}) for $E_{\mathrm{c}}(T)$ are plotted in Fig. 53. It can be observed that E_{c} decays to 0 with enlarging temperature as expected as the particle dynamics correlation should decrease and become similar to simple liquids motions. Last, we inserted the fitted $E_{\mathrm{c}}(T)$ into Eq.(30).

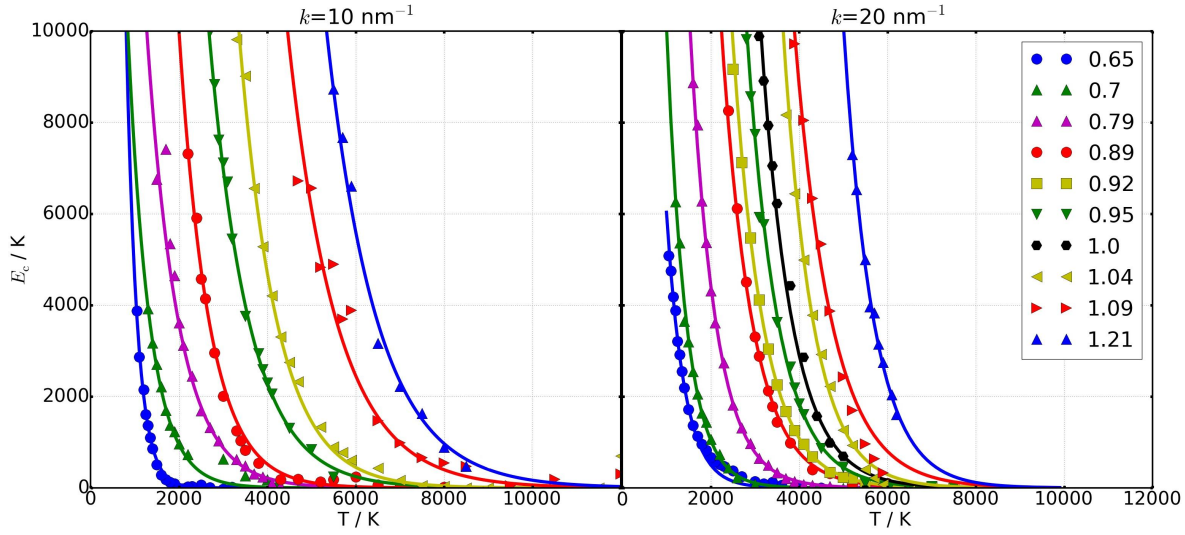

Figure 53: E_{c} calculated from Eq. 30 using the measured values of τ for two different k values and fitted with Eq. 32. The temperature variation of E_{c} explicitly shows how the correlation in dynamics decay when the temperature is increased.

The optimized parameter T_A and μ together with the glass transition temperature $\mathrm{T_g}$, as determined from extrapolation of the fits, obtained with k = 10, 20 nm^{-1} are plotted in Fig. 54. While T_{g} and $\mathrm{T_A}$ grow faster than linearly with q/q_0, we see in Fig. 54(b) that μ changes only moderately. Related to the values of the partial charges and scattering vector, μ lies in the range $\sim$ 20-30, which is lower in comparison to the generalized fragilities $\mu \approx 56$ extracted for water models from studies of rotational motion. [101] Variation of the partial charges of water models do not change the deduced generalized fragility parameter as we found here. The growing up of the fragility with the bond polarity of silica can be rationalized from the fact that the fragile regime must interpolate between the two strong regimes, with the slope in the low-temperature strong regime being steeper for larger q/q_0. This larger change of slope over an increasingly lower fragile regime requires a bigger fragility parameter. This argument is consistent with the observation that μ is somewhat lower for shorter k, for which the high-temperature-activation energy E_∞ is higher than for larger k, but the low-temperature activation energy E_0 is the same, see Figs. 49, . 51, so that a smaller difference of the slopes needs to be bridged. In any case,

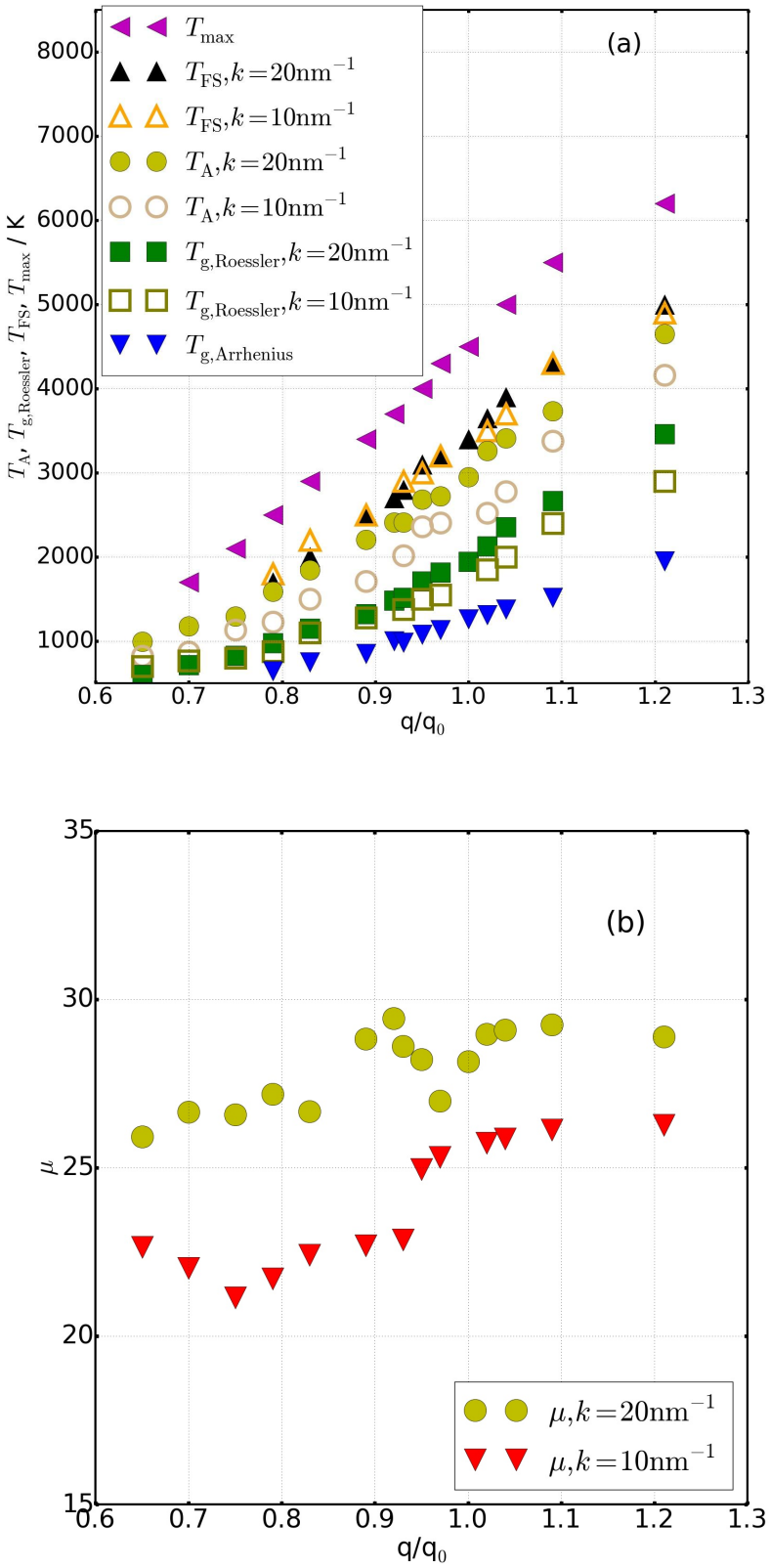

Figure 54: (a): Typical temperature describing silica systems, (b) generalized fragility parameter obtained from the *Rössler* fits.

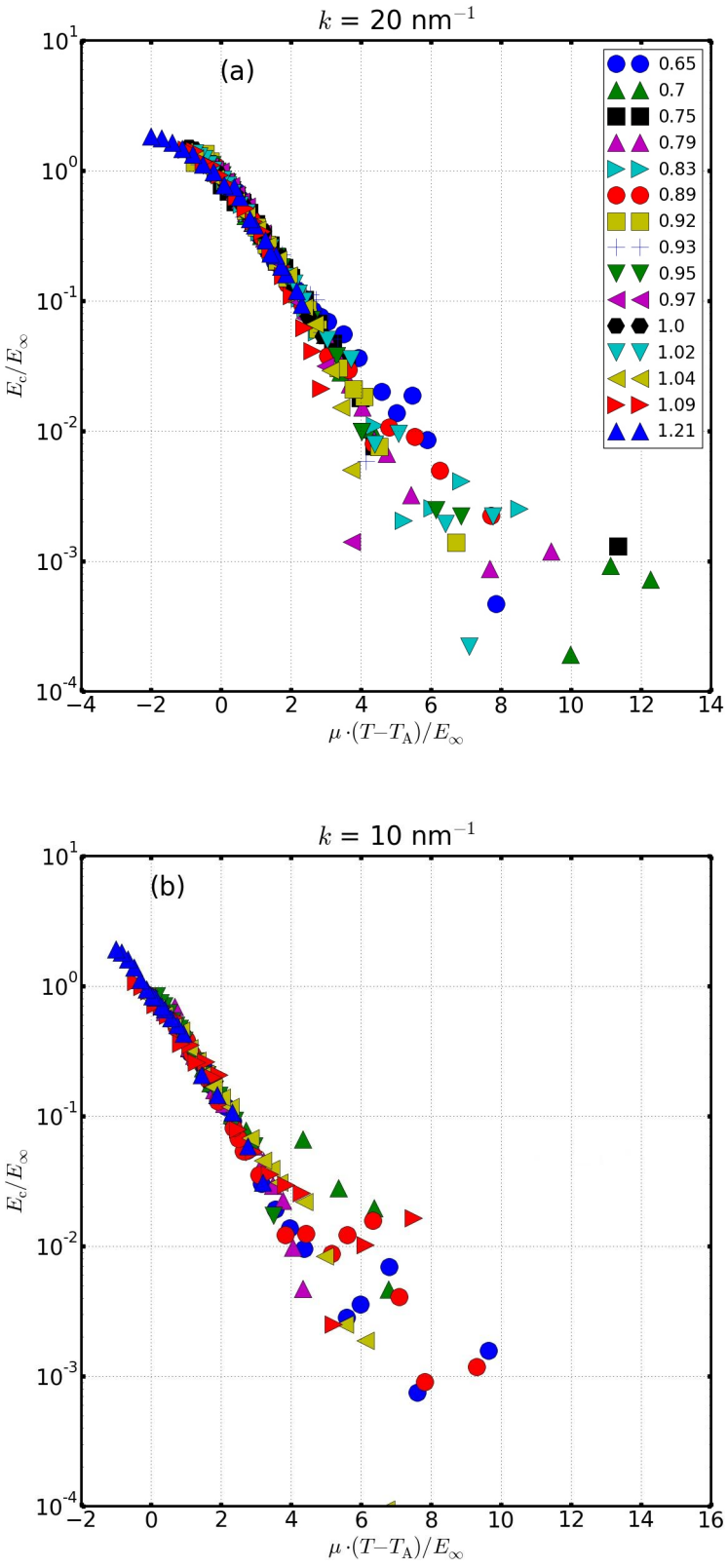

Figure 55: Representation of the ratio between the cooperative contribution E_c to the high-temperature activation energy E_∞, as a function of the reduced temperature parameter $\mu(T-T_A)/E_\infty$ for (a) k= 20 nm^{-1} and (b) k= 10 nm^{-1}.

as the fragile dynamics of silica systems is qualitatively well described by the Rössler fit functions, it is instructive to plot a similar master curve (see Fig. 55) as introduced in Refs. [184, 185, 186] which somewhat remove the charge dependence in dynamics for the respective length scale studied. A linear relation is obtained between E_c/E_∞ with respect to the reduced factor $\mu(T - T_A)/E_\infty$. The slope in the linear dependency appearing here are comparable to the slopes reported in Ref. [101] for water models with various partial charges (see Fig. 106 in appendix where data of silica and those of water are confronted.).
In the subsequent step, we inspect the self part of the van Hove correlation function, which exhibits details about the motion of individual atoms. Fig. 56 shows the distributions of the distance traveled by oxygens (a)-(b) and silicons (c)-(d) after various time intervals at particularly low temperatures. For short time intervals, there is a sharp peak at around 0.1 nm, which can be attributed to vibrational motion. For time intervals of the order of the structural relaxation time τ, we see a clear secondary peak at the oxygen-oxygen next neighbor distance, indicating hopping motions of oxygen atoms while this trend is not observed in the silicons distributions. These hopping events are observed at low enough temperature where atoms are able to then hop between energetically favorable positions, (we show in Fig. 107 of appendix that oxygen hopping disappear when the temperature is slightly increased.). We find out hopping motions for high and low charges, and notably independently of whether the system shows strong or fragile dynamics at the studied low temperatures. For this reason, the recent reports [79] that hopping motion is a signature of strong glass formers can be debatable and is certainly not fulfilled to silica-like liquids.

Finally, we examine the elastic models [205, 181, 249, 116, 250, 251] proposing relations between short-time and long-time motions by means of the short time MSD. Specifically, the shoving model of glass-forming liquids introduced in chapter. 4 assumes that relaxation events are connected to short-time molecular displacements by means of Eq. 45 which can be simplified as: [205, 101]

$$\tau(T) \propto \frac{a^2}{\langle u^2(T)\rangle}, \tag{62}$$

in which u^2 is basically the MSD at $t = 1$ ps. A semilogarithmic plot of τ versus u^2 is shown in Fig. 57. Apart from the high-temperature dynamics, the predicted linear dependency is obtained. The high temperature deviation arise from the difficulty to assign a plateau in the high temperature functions of the MSD. Basically u^2 should measure the plateau value of the MSD between vibrational and diffusive motions which is not appearing at 1 ps for most high temperature data. An intriguing aspect is that we do not obtain a master curve as the one obtained for water models in Ref. [101]. This again confirm the fact that by generating different BKS silica systems of varying polarity, one can basically move to the limit in which no FS crossover is not more obtainable. This also reveals how complex is the dynamic of the generated BKS silica systems which can not be fully captured by simplified glass transition theories.

7.4 Summary

Starting from the modified [104] BKS [105] silica model, we have generated different silica like liquids to which partial charges assigned to the silicons and oxygens are gradually rescaled. We have hence simulated various silica systems to which the silicon partial charge were between 0.65-1.21q_0, in which q_0 is the partial charge attached to silicon in the original BKS model. In this way, the effect of the electrostatic interactions on the glassy behavior of silica systems could be probed. We have found that the density enlarges when the partial charge increases since the attractive interaction between silicon and oxygens gets stronger such that silicon and oxygen are coming close to each other. Apart the silica liquids associated to the lowest partial charge, all silica liquids display a density maximum which moves to higher temperature with increasing charge. This result is somehow intuitive when one thinks about the minimization energy process namely, when the system is in the low density state characterized by a high ordering, a higher temperature is necessary to move the liquid to the state of high density with corresponding higher entropy. We have also reported the bimodal distribution displayed in the distribution

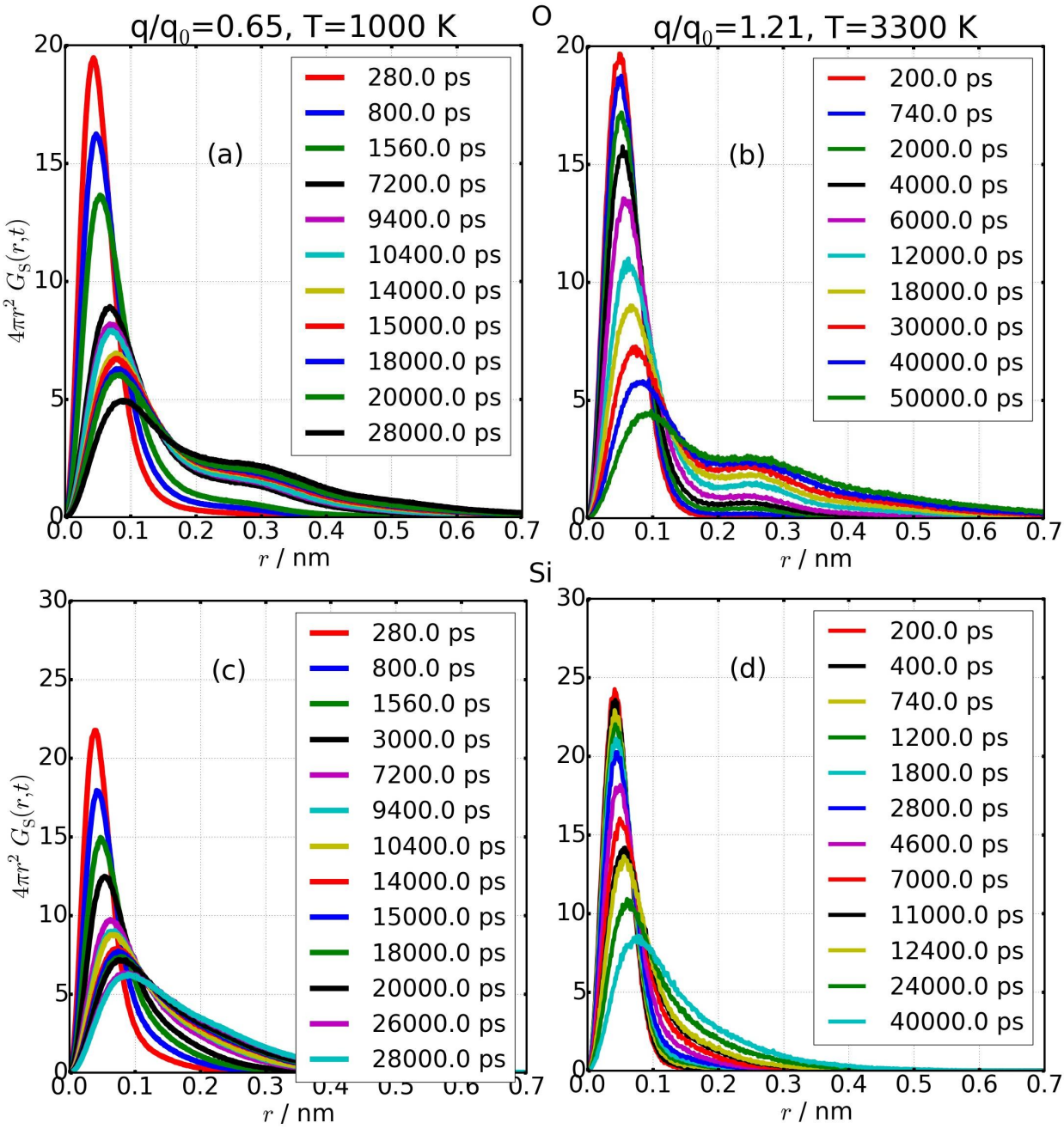

Figure 56: Self part of the van Hove correlation function of the oxygen atoms (top panels) and the silicons (bottom panels) for respectively (a)-(c) $q/q_0 = 0.65$ and (b)-(d) $q/q_0 = 1.21$ in each case at the lowest equilibrated temperature. Secondary peaks at the next-neighbor distances reveal hopping motion for oxygens atoms, while this is not observed in silicon distributions. In Fig. 107, we have added similar curves for oxygen atoms when the temperature is increased.

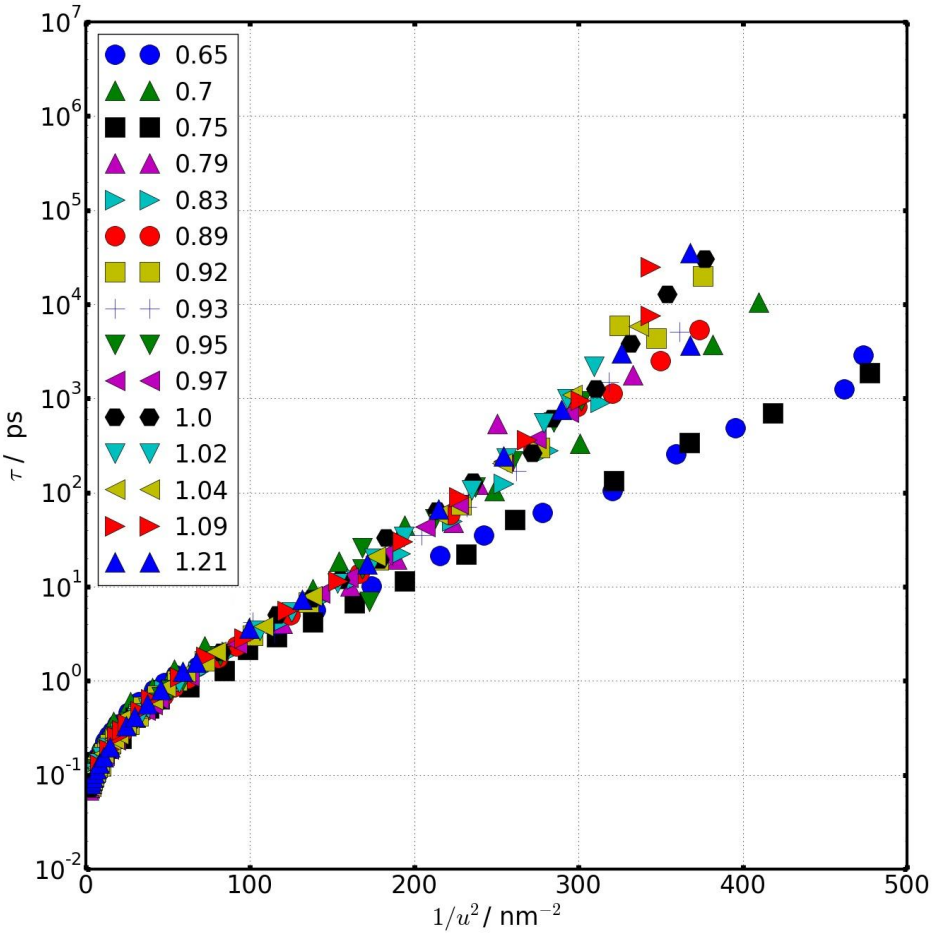

Figure 57: Structural relaxation times plotted as function of the inverse of u^2. The high-temperature data where 1 ps does not more illustrate the onset time to cage motion deviates from the linear dependence. Secondly, one can easily identify systems showing no FS crossover at low temperature in bulk, for which the behavior deviates from the master curve.

of the tetrahedral order parameter of silica like systems at the temperature of density maximum $T_{\max}$. We have further observed a bimodal function in the pair distribution of the fifth nearest neighbors of silica systems at the FS crossover temperature T_{FS}. Both observations suggest the existence of two local neighborhood in silica systems characterized by a locally high or low density. The locally high density domains are characterized by weak local ordering and are predominant at high temperature. Inversely to the low density domains which show higher local ordering and are predominant in the low temperature regime.

On top of the previous observations, the distribution of the order parameter at the FS crossover temperature T_{FS} also displays a universal behavior (the curve show a well defined peak at high Q_i=0.75 with a strong kink at Q_i=0.55) between all silica systems, confirming the existence of local density domains showing high or low local ordering, but also suggesting the strong correlation between structural and dynamical properties in silica like systems. We have as well explored the low and high temperature regime showing an analogous faster than linear increase of the high (E_∞) and low (E_0) temperature activation energy with charge, with small discrepancy appearing for small charges where the entropy effect in E_∞ has a substantial contribution. We have shown that the activation energies are related to the local bonding between closest atoms consistent with the fact that the barrier energy should be affected by local repulsion between neighboring atoms. Along with that, the glass transition temperature extrapolated with the Arrhenius low temperature data, for q's of at most 5% different than the original value q_0, agrees quantitatively well with former experimental recorded data [91, 246, 247, 88, 248] which implies that BKS silica is a good choice to probe dynamical properties of liquid silica. We have further explored the fragile regime and find out that the newly proposed *Röessler* functions describe qualitatively well the temperature-dependent relaxation times.

We have additionally inspected the k-dependent dynamics and found out that the strong dynamics observed at low temperature is almost not affected by the length scales over which correlation times are probed. This is not so surprising as the system shows a almost homogeneous highly local ordering and motions are mostly governed by local hopping between closest atomic sites. In contrast, the fragile regime is strongly dependent on the length and time scales of dynamics since it is marked by the predominance of regions containing weakly ordered clusters. This strongly impacts the SE relation which solely gives an exponent smaller as 1 whenever the length scale chosen to study motions are smaller than the average size of the weakly ordered domains in the fragile regime.

Finally, we have shown that the shoving model of the elastic glass transition theory is far to simplistic to fully represent the enriched dynamical features of silica like systems. One reason is that it does not explicitly account for dynamical transition such as the FS crossover, secondly it relies on the onset MSD separating vibrational and diffusive motions which is itself not trivial to define as the height of the vibrational amplitude and the length of the subsequent plateau are hugely related to temperature.
Hopping motions of oxygens have been obtained at low enough temperature in which atoms can diffuse by means of hoppings between energy barrier formed by the closest neighbors. They are observed for all silica systems irrespective of whether the systems show a fragile or a strong dynamic at low temperature. This implies that both for fragile and strong glass formers, at low enough temperature, the system can relax trough activation between "meta-basins". And this activated motion dominates the long time dynamics of the system. The "meta-basin" might be the low density clusters which are preponderant at low-temperature in strong glasses, and are also present in fragile glasses though in this case, they possess a smaller local ordering. It is important to keep in mind that these hopping events have been noticed at low temperature, this is relevant for the next chapter in which one can observe that hopping also develop at much higher temperature due to the confinement effects.

8 Silica with varying bond polarity in neutral confinements

In this part, we would like to study the phenomenology which drives the drastic slow-down of supercooled liquids upon cooling by inspecting the temperature-dependent length scales. This is an attempt to characterize the size growth of the emerging cooperative clusters at low temperature. Structural and dynamical length scales are easily obtainable from the neutral confinements investigations. [108, 109, 172, 119, 110, 111, 71, 112] We focus on neutral confinement of silica enabling us to inspect the temperature variation of the length scale when approaching the temperature of FS crossover T_{FS}. We will mainly report the dynamical response of silica-like liquids of different bond polarity in neutral confinements.
The neutral confinement at a given temperature is obtained using the corresponding equilibrated bulk and keeping immobile all atoms which are distant to the pore center by at least 2 nm (at a radius $(x^2 + y^2) > 2$ nm.). The rest of atoms are allowed to freely move so that we can approximate the pore diameter as 4 nm. A snapshot of the system is illustrated in Fig. 58 in which the mobile silicon (yellow spheres) and oxygens (red spheres) are positioned resolved with respect to the radius R of cylindrical coordinates, or through the distance d to the closest wall atom. Throughout this chapter, the average behavior of all atoms which are within 1.0 nm of the pore center, will be used to represent atoms at the pore center. Most of the trajectories used for the regular BKS system (q/q_0=1.00) originate from the work of *Julian Geske*. [180]

8.1 Simulation details

The simulations are performed in the NVT ensemble. We apply PBC and calculate the long-range Coulomb interactions with the PME sum and a cut-off of 1.2 nm. The time step of the integration is set to 1 fs for most simulations and 0.5 fs for systems associated with larger partial charges (q=1.09q_0, 1.21q_0) at high temperatures where, otherwise, some atoms overcome the low energy barrier to the unphysical energy minimum at short distance. Before data acquisition, the system is generally equilibrated for times longer than the structural relaxation times. The total simulation time is up to ≈ 500 ns, depending on temperature and partial charges.

8.2 Results I: Structure

The density profile showing the distribution of the mobile particles throughout the pore is added in Fig. 59. It shows that in the pore center region, the density is identical to bulk value, while in the pore wall vicinity, slight layering happen due to the combination of the static energy landscape imposed by the immobile surface as well as the surface roughness. This slight layering gets more visible at smaller temperatures in which particles move less and are therefore more localized at the preferred positions. The peak positions of the layers should then be connected to the nearest mobile oxygens or silicons atoms with respect to the matrix atoms. Indeed, the distribution of the mobile particles in pore with respect to the distance to the nearest wall atom is added in Fig. 60, in which one can identify the silicon-oxygen closest separation in the first peak; followed by the silicon-silicon nearest distance in the second peak. The main difference between the distribution of the system associated with q/q_0=0.65 and the systems associated with q/q_0=121 is that the third peak (localized at $d \approx 0.4$ nm) is considerably reduced in height for the lowest charge (independently on temperature), meaning that much less atoms are found between the first and the second neighboring shell for the lowest charge. This again rejoins the finding of chapter. 7 in which the distribution of atoms in the 5th neighboring shell was strongly correlated to the liquid ability to undergo a FS crossover.

We as well check the local structure by means of the distribution of the tetrahedral order parameter $f(Q_i)$ in Fig. 61 that displays the distribution of the order parameter at q/q_0= 0.79, 1.21 at T_{FS} (temperature of FS crossover) and T_{max} (temperature of maximum density) for the atoms layers positioned close to the pore center R= 0.35 nm or close the pore surface R= 1.95 nm. One observe the trend of the bulk

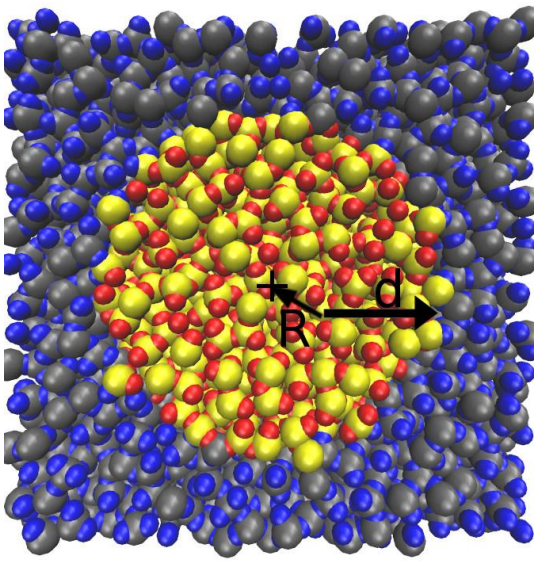

Figure 58: Top view of the neutral confinement configuration used for simulations. The yellow and red spheres indicate respectively the location of the mobile silicons and oxygens. While the immobile silicons and oxygens are marked by gray and blue spheres. The position of a mobile atom in the pore is resolved either via its cylindrical radius R with respect to the pore center, or by means of its distance d to the nearest immobile particle of the wall.

behavior that local orderings at these particular temperature do not depend on partial charges. More importantly, the distribution obtained is the same independently on the confined liquid layer which is probed. In Overall is the local structure of the mobile atoms, as expected, not distorted and comparable to the bulk structure.

8.3 Results II: Dynamics

To pinpoint the slowdown effect generated by the confinements on the structural relaxations processes of atoms, we first plot in Fig. 62, the ISF ($F_s(k,t)$) for oxygens and silicons at different distance R to the pore center or d to nearest wall atoms at 1300 K and the system corresponding to $q/q_0 = 0.65$. $F_s(k,t)$ curves decay faster for larger values of d (or short R) by roughly two orders of magnitude, revealing the enormous slowdown of structural relaxation near the pore wall though the interactions between the mobile atoms are similar with their interactions with the immobile atoms. The dynamics are slowest in the vicinity of the pore wall, and go towards the bulk behavior in the pore center; since the mobile atoms closer to the wall screen the effect of the wall on the second next mobile atoms such that the later feel much less deep potential energy minima.

The corresponding resolved relaxation times τ are extrapolated from the 1/e decay of the ISF curves decay of each mobile atoms layer inside the pore. In Fig. 63, the correlation times τ are plotted over inverse temperature for different distances d to the nearest wall atom, or to the pore center R. Oxygen and silicon atoms display analogous trend. Atoms in the pore center show a relaxation time comparable to the bulk value. For atoms in the pore center, designated by large d or low R, τ is comparable to the bulk value (maroon crosses), and increments when d enlarges or R shortens, exhibiting the ISF slower decays of atoms near the pore wall (Fig. 62). In all curves, the strong regime, when existing, is fitted with an Arrhenius equation, while the fragile regime is pictured with *Rössler* functions. In the later case, the bulk high temperature activation has been used to perform the fit for all the different layers because

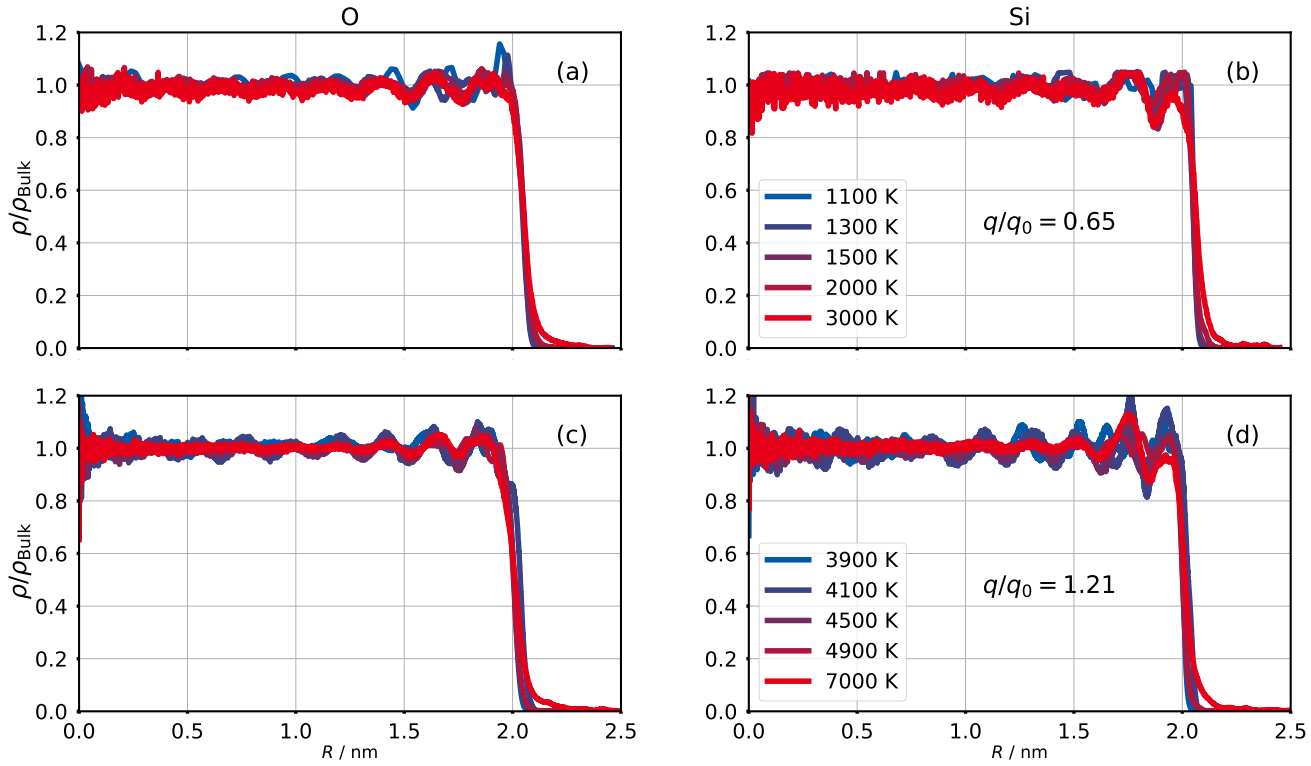

Figure 59: Radial density profile of mobile oxygens (a)-(c) and silicons (b)-(d) in the pore for q/q_0=0.65 (a)-(b), 1.21 (c)-(d). The density is weighted to the bulk density ρ_{Bulk}. In the case of oxygens data, we multiply the bulk density by 2 in order to consider the double number of oxygens atoms in silica.

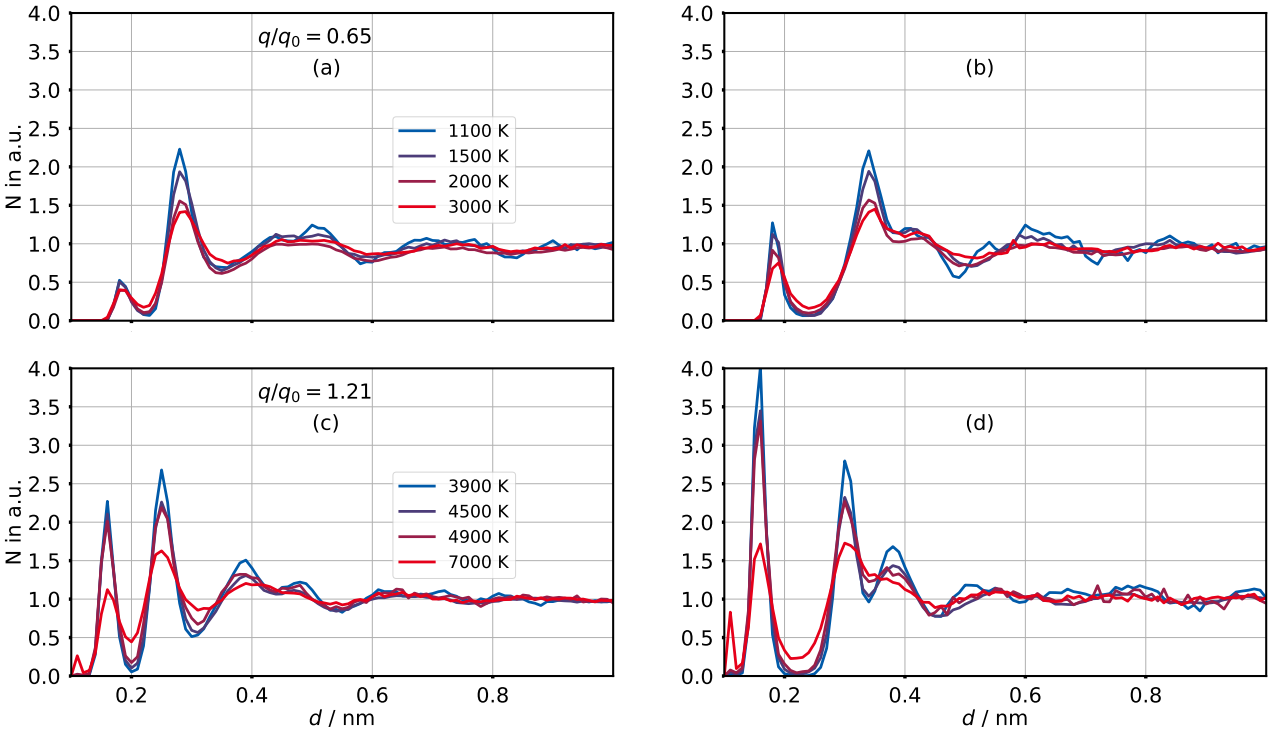

Figure 60: Distribution of mobile oxygens (a)-(c) and silicons (b)-(d) in the pore for q/q_0=0.65 in top panel, 1.21 in bottom figures. The first peak height of the top panel figures is smaller as compared to the one at 1.21, which is itself comparable to the the second peak. This is because, the density at q/q_0=0.65 is considerable smaller as the density in q/q_0=1.21 and thus we get less closest neighbors. The distribution is plotted such that for a smooth cylindrical wall, the number of atoms in each bins have equal volume. For this reason, the distribution has been normalized with the mean numbers of atoms in the distance range $1.0\,\mathrm{nm} < d < 1.5\,\mathrm{nm}$.

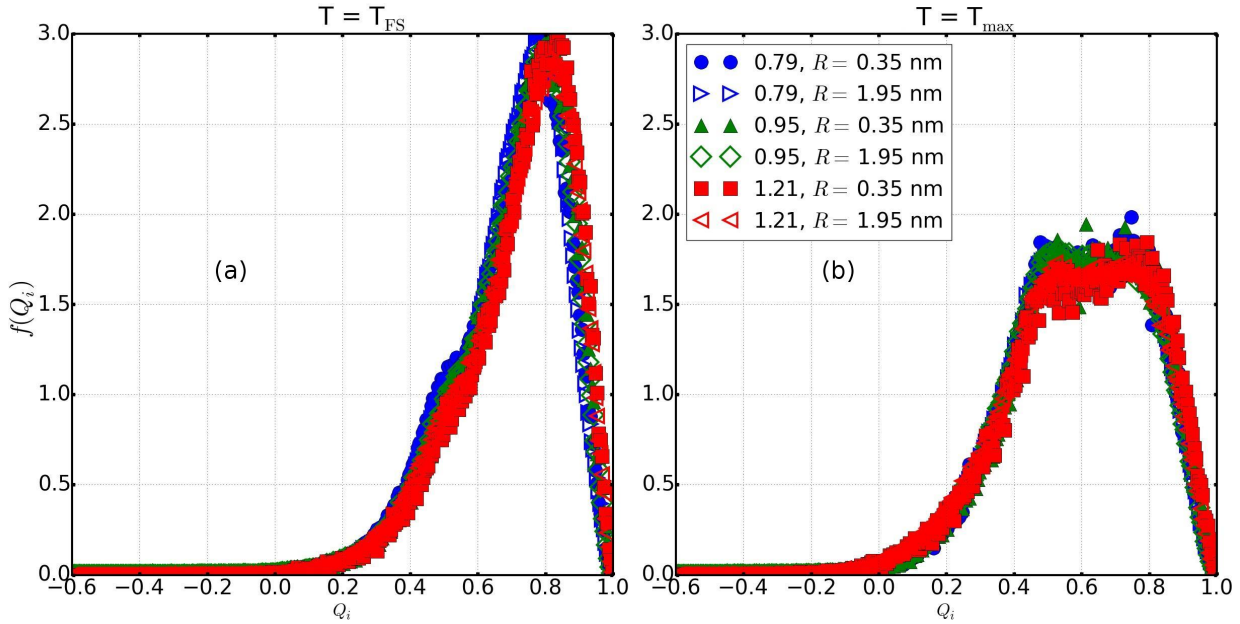

Figure 61: Distribution of the tetrahedral order parameter $f(Q_i)$ at T_{FS} and at T_{max} for atoms positioned in the pore center region (R= 0.35 nm) or near the pore surface (R= 1.95 nm) for q/q_0=0.79, 0.95 and 1.21.

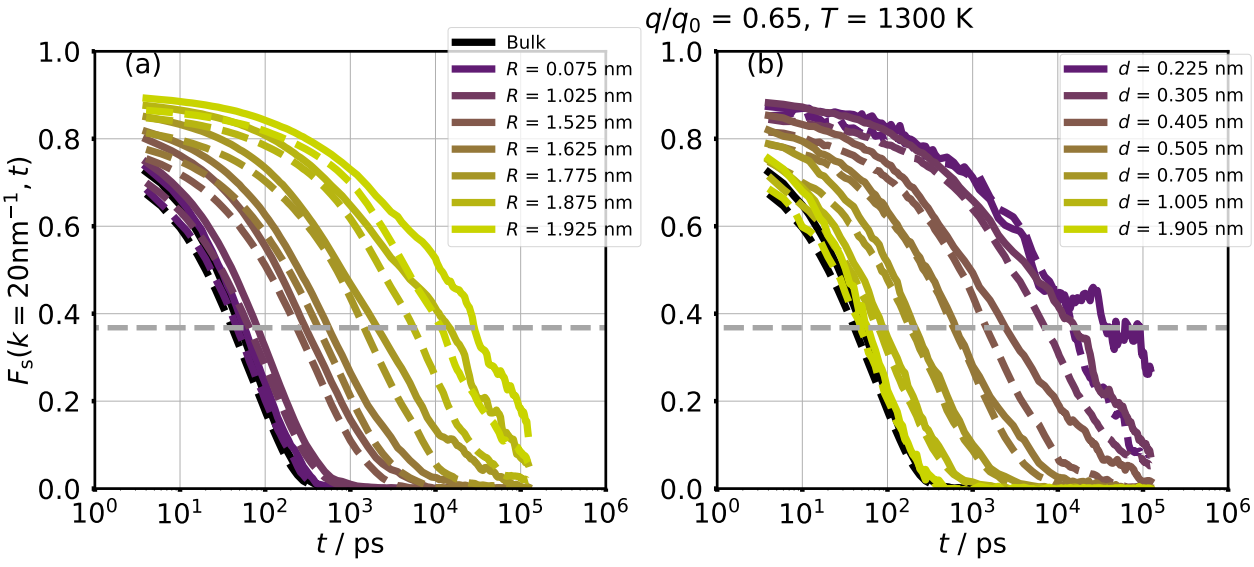

Figure 62: (a)-(b): ISF $F_s(k,t)$ for silicon (solid line) and oxygen atoms (dashed lines) at $q/q_0 = 0.65$ in which the position are resolved to pore center (a) or pore wall (b). The data are plotted at a low temperature T= 1300 K.

upon approaching the wall, it becomes tricky to distinguish high- and low-temperature dynamics.
No FS transition can be detectable in the evolution of the low-temperature data for atoms in pore center for q/q_0=0.65, consistent with the bulk behavior (reported in chapter. 7). Interestingly, the confinement induces its apparition in the dynamics of atoms positioned near the pore wall. In contrast for q/q_0=1.21, the structural relaxation in the pore center shows a FS transition at $T_{FS} \approx 5000$ K, while liquid layers near the pore wall display almost strong behavior throughout the whole temperature range investigated. The change in steepness of the τ-data when approaching the pore wall is explicitly represented by the profile of the generalized fragility μ added in Fig. 108 of the appendix, where we see that it is almost constant for pore center values and diminishes when R enlarges. Since the high-temperature dynamics is almost similar for all layers, and the fragile dynamics show a decrease in steepness, one would expect that the curves of the fragile dynamics coincide at very low temperature. This is indeed the case because the profile of the fictive glass transition (see Fig. 109(a)) extracted from the *Rössler* fits (using the usual formular $\tau(T_g) = 10^{14}$ ps) shows a constant glass transition troughout the pore.
From the strong low-temperature dynamics, one can further extrapolate the low-temperature activation energy and plot its profile throughout the pore in Fig. 64 for various systems. It is almost constant for values near the pore center and comparable between silicon and oxygens consistent with the bulk behavior reported in Fig. 104. The values at the pore center are nearly similar or within 10% different than the bulk values (see Fig. 49 for the bulk values). Interestingly, the profile changes slightly for oxygens near the pore wall while for silicon it hugely levels off; implying that silicon and oxygens dynamics near the pore wall are somewhat different. To further check this issue, we have considered silicons and oxygens mobility in different spatial regions by evaluating the Van-Hove distribution $G_s(r,t)$ (Fig. 65) at times comparable to the average relaxation time τ of the spatial resolved particles in the given region. We choose in this case a sufficiently large temperature in which no hopping events have been observed in bulk as exemplified here by the single maximum obtained for oxygens and silicons in the region within roughly 0-1.5 nm of the pore center. Thus, atoms in the pore center relax mostly via diffusive motions. Then, for layers close to the pore wall (R lying in the range [1.5-1.9) nm), a strong secondary peak at oxygens nearest neighbor distance ($r \approx 0.3$ nm) is observed in the distribution of oxygens, together with a subsequent shoulder at the second next neighbor distance ($r \approx 0.48$ nm). Similar observations can be made for silicon atoms in the pore wall vicinity but with a considerably smaller peak amplitude, suggesting that less silicons relax via hoppings near the wall in comparison to oxygens.

In the next steps, we investigate typical length scales ξ of silica systems. We disregard all length scales and corresponding data which are smaller than 0.15 nm. We can represent how much dynamics are affected by the fixed wall atoms by plotting the profile of relaxations times with respect to positions in pore. From this plot, a dynamical length scale ξ_d can be extracted. It can be deduced from the following relation (proposed in Ref. 108):

$$\ln\left(\frac{\tau(x)}{\tau_\infty}\right) = a_{ISF} \cdot \exp\left(\frac{-x}{\xi_d}\right), \tag{63}$$

in which τ_∞ stands for the average relaxations of atoms in pore center. x defines the radial position of atoms, when the position is defined with respect to closest atoms of the pore wall $x = d$, in case the position is estimated with respect to pore center, then $x = R_0 - R$ in which R_0 represent the average radius of the pore approximately 2.0 nm. These relations can then be used to fit the profile of τ's as shown in Fig. 66 showing the fits for $q/q_0 = 0.65$ for both silicons and oxygens resolved with respect to pore center (left figures) or pore surface (right figures). It is important to point out that the residues calculated during the fitting procedure are always weighted by the corresponding number of atoms in the distance interval of interest, which is crucial for the d-resolved analysis in which local order effect is explicitly visible in the data.

When approaching the pore surface, the relaxation times present some oscillations with peak positions identical to the ones appearing in the atoms distribution of Fig. 60. They basically display the signature of pore roughness on the correlation times profile and the fact that interfacial atoms sit in preferred

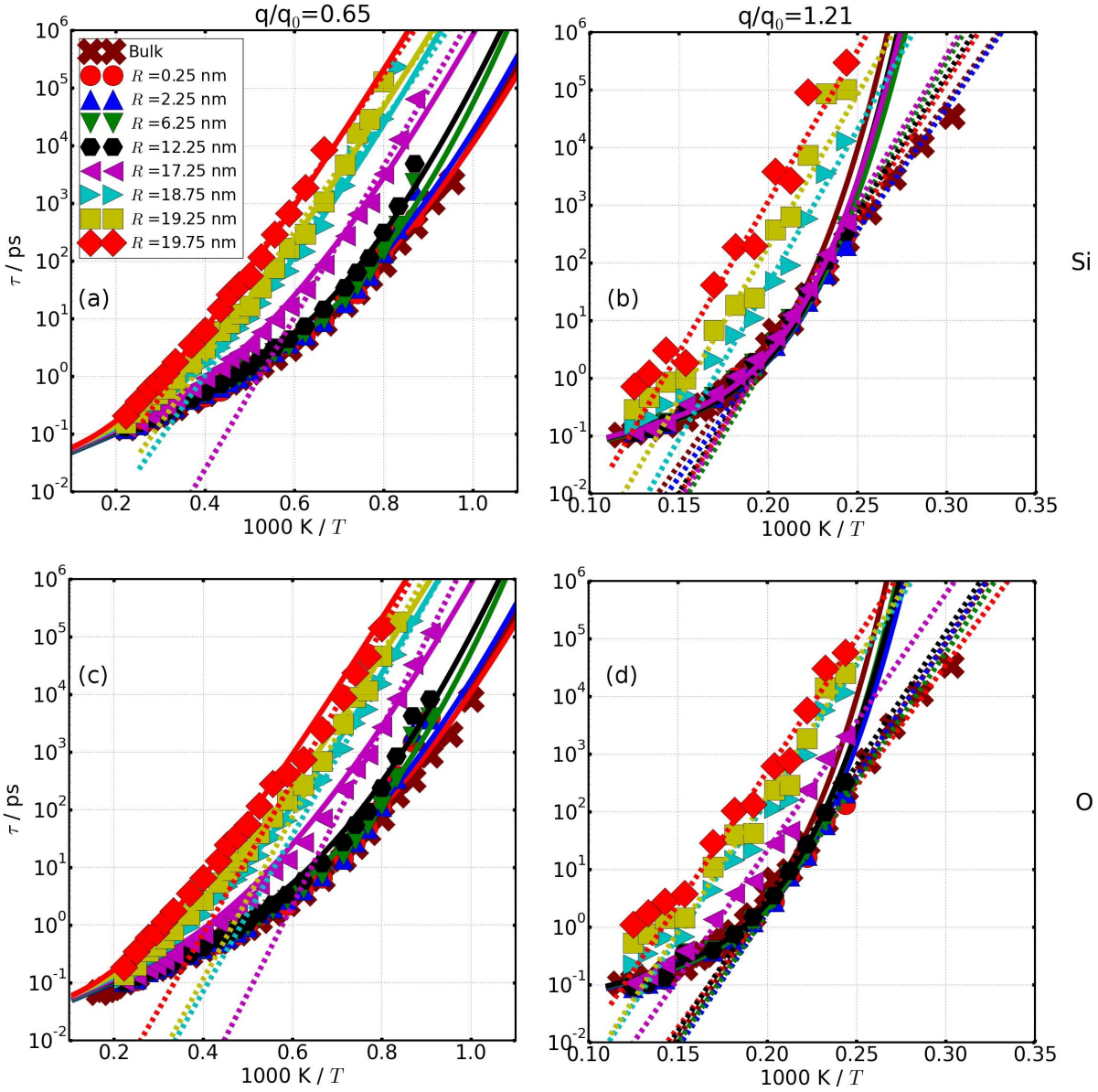

Figure 63: Temperature-dependent structural relaxation times for different liquid layers identified trough atoms position with respect to pore center. The data are added for oxygens (bottom) and silicon (top) for $q/q_0 = 0{,}65$ (left), 1.21 (right). Fits with the Arrhenius equation at low temperatures are included in dashed lines, and the ones with the *Rössler* approach are included in solid lines. The fits line of the *Rössler* functions have been performed with the bulk high temperature activation energy. Similar plots for silicon and oxygen atoms resolved with respect to pore wall are added in appendix (see Fig. 102). The resulting generalized fragility parameter for silicon and oxygens are also displayed in Fig. 108 of appendix and shows that they are of the same order of magnitude between silicons and oxygens.

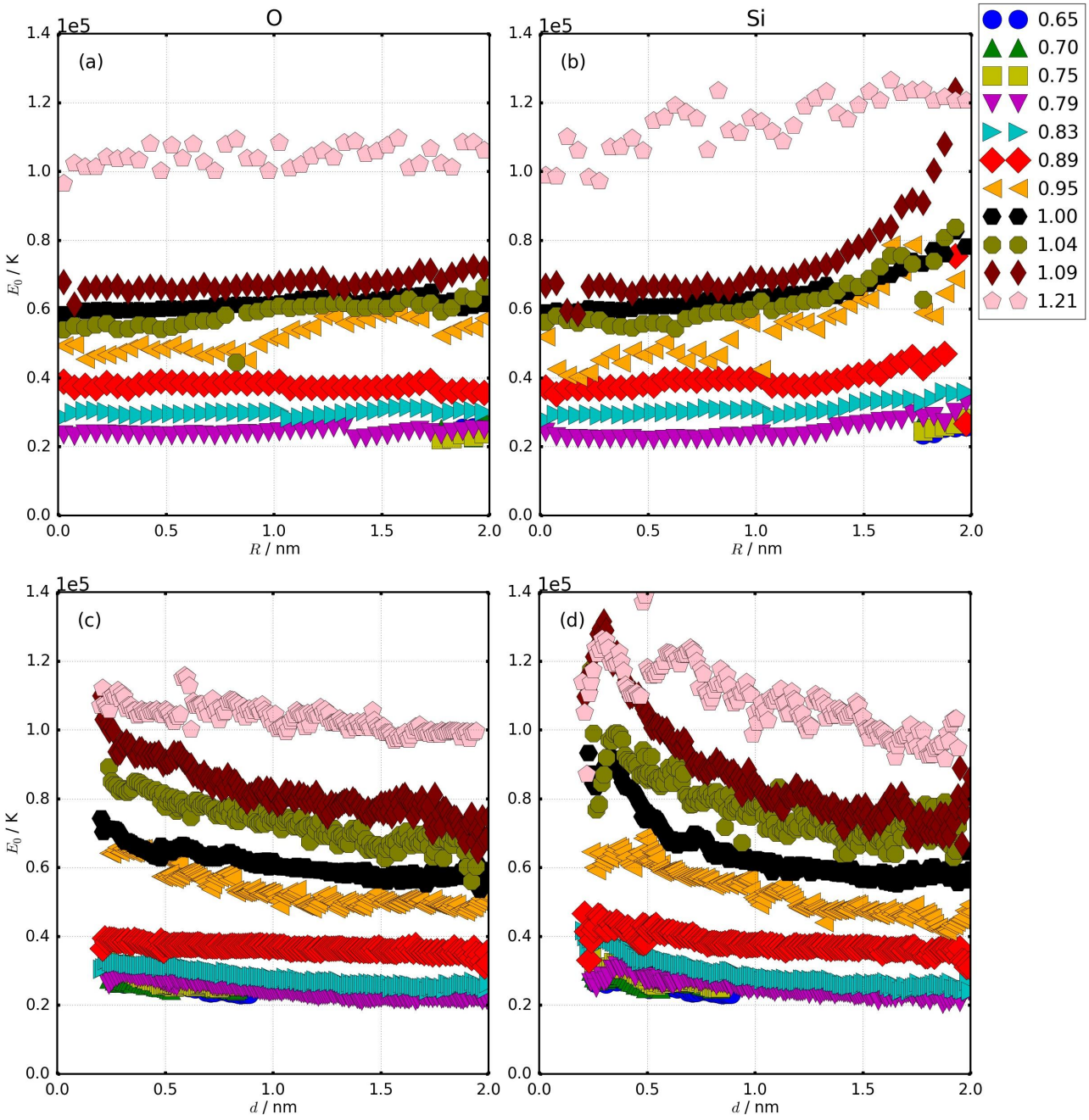

Figure 64: Top: Low-temperature activation energy for oxygens (left) and silicons (right) in the pore resolved by the distance to the pore center (top) or to the pore wall (bottom) for various silica systems.

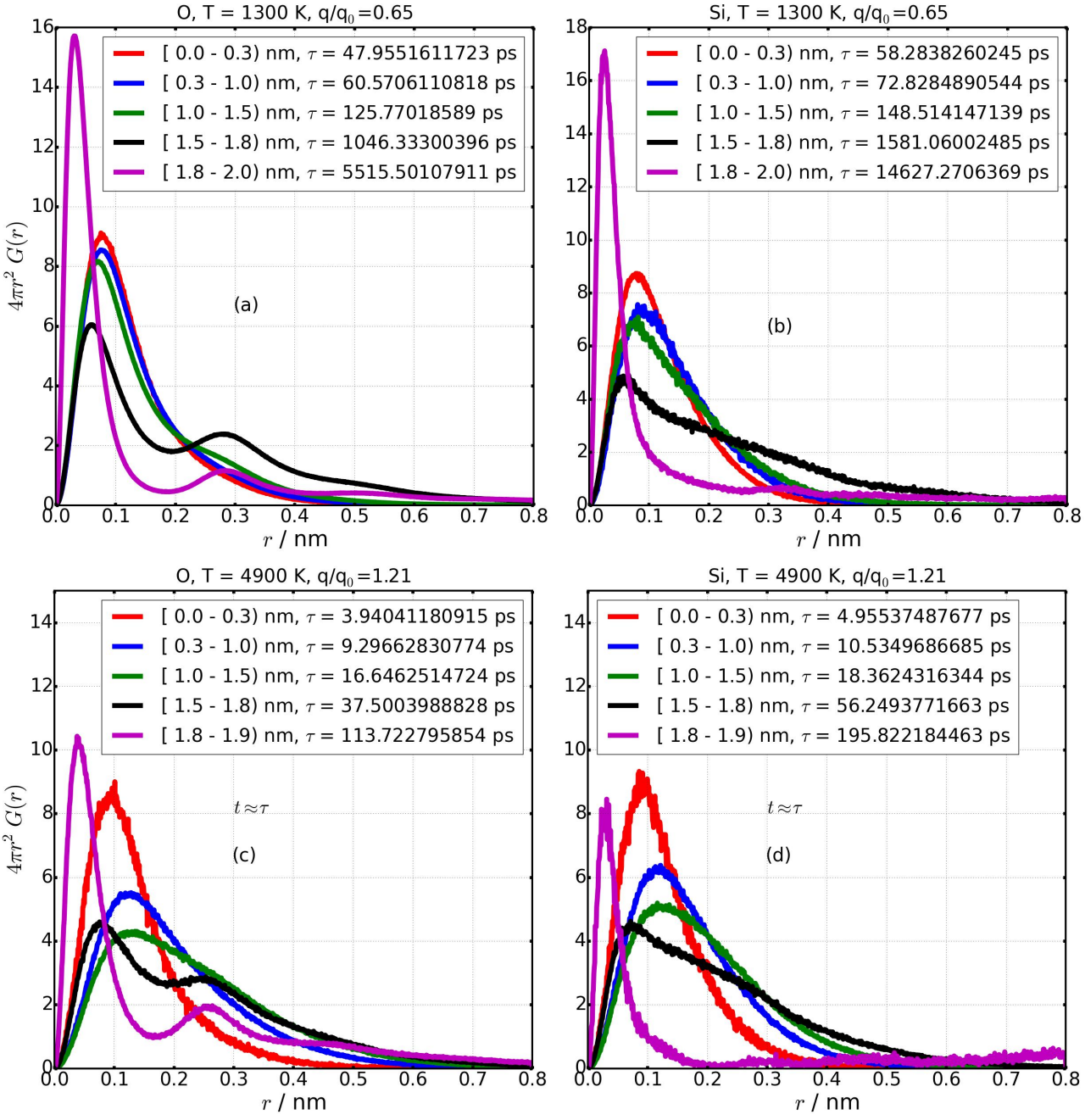

Figure 65: Self part of the van Hove correlation function of the oxygen atoms for top ($q/q_0 = 0.65$) and bottom ($q/q_0 = 1.21$) in each case at high-temperature for which no hopping motion where observed in the bulk dynamics. The timescale is the average structural relaxation of different layers in the corresponding distance interval.

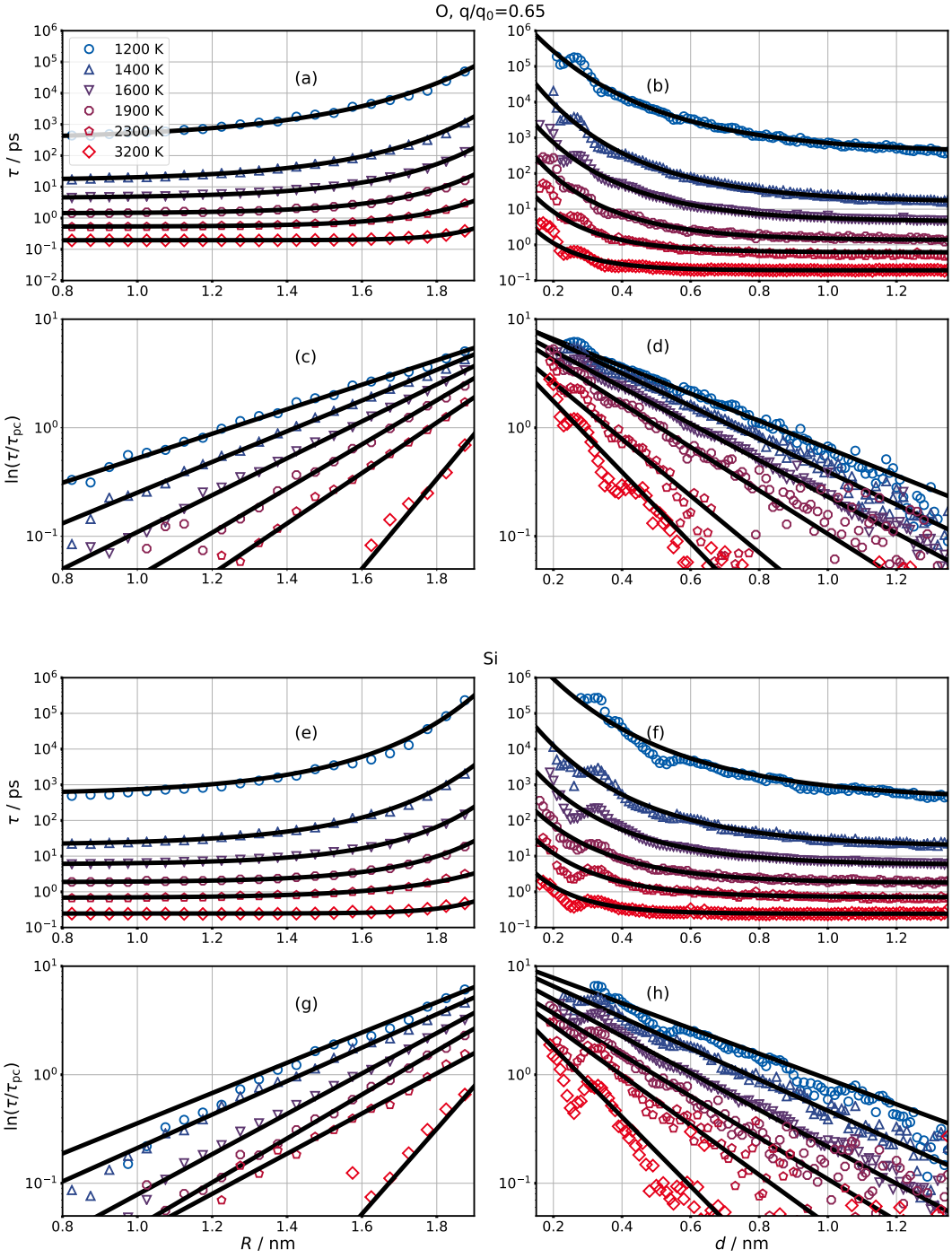

Figure 66: Distance Profile of τ of oxygens (a-d) and silicon (e-f) resolved with respect to pore center (left) or pore wall (right) fitted with Eq. 63, (c)-(d), (g)-(h) are the corresponding log log plot in which one can identify the slope at large R or small d while the fit fails at short R or large d. Here, the data correspond to the system associated with q/q_0=0.65.

positions near the pore wall. Whereas, the R-profile of τ of inter-facial layers is rather smooth as in this case, only the atom radial positions are considered and the local structure of atoms with respect to surface atoms is somewhat averaged out. Moreover, the wiggles observed for silicons (in the d-resolved profile) are of larger amplitude as compared to the ones recorded for oxygens. This implies that silicon are sitting in deeper energy minima imposed by the fixed wall atoms as oxygens do, which is understandable because silicon atoms interact with twice as many neighbors compared to oxygens in the first coordination shell.
The double exponential increase of τ qualitatively reproduces the behavior near the immobile surface. It has been formerly tested for LJ liquids near neutral walls [108] and then applied for water [71, 112] and several other liquids. [110, 111] For silica systems, τ_∞ amounts $10-20\%$ of the average relaxation times τ_{pc} of atoms in the pore center region. τ_{pc} values roughly lie also between $10-25\%$ of the bulk values. τ_∞ and τ_{pc} should represent the limiting case of an infinitely larger pore, the small deviations noticed can be attributed to weak finite-size effects as we simulate a confinement with finite pore radius. Moreover, the fits curves do not match well with τ data of atoms at the pore center, but the slope in the log log plots of Fig. 66 (c)-(d) and (g)-(h) are approximately well describing the trend near the pore wall. The constant parameters a_{ISF} out-coming from the fits are added in Fig. 111 and are varying between 0 and 15. a_{ISF} increase with pore center relaxation times with a slope which varies with partial charges. The resulting dynamical correlation length ξ_{d} are displayed in Fig. 67(a-b) for all silica variants. ξ_{d} deduced from both distance resolved analysis increase with cooling. In Fig. 68 (a)-(b), we compare dynamical length scales obtained between both analysis and found that the values obtained from the R-resolved analysis are up to 10% smaller than the values from the d-resolved analysis, especially in the low temperature range, while the deviation is small in the high temperature domain. We as well compare oxygen and silicon dynamical length scales in Fig. 68 (c)-(d) and found that they are in the same order of magnitude. Observing the left panel of Fig. 68 reveal that one can claim a slope change in the temperature varation of ξ_{d} below the temperature of FS crossover T_{FS}, but one can not make a strong statement because the data are still a bit scattered.
Since we have various temperature range between different silica variants, we compare the length scale on time scale in order to better understand the effect of charge (see Fig. 69). The dynamical length scales increase roughly linearly with the logarithm of relaxation times. In both resolved analysis and for both atoms type, a charge dependence is observed, specifically ξ_{d} grows faster with relaxation times when the partial charge is reduced.

We can at this point approximate quantitatively the slow-down effect of confinement by comparing the ratio of τ for a pinned layer of atoms close to the wall with pore center atoms. Fig. 70 displays the ratio of τ for silicon and oxygen atoms lying at $R = 1.75$ nm to pore center in one hand (top figures); and on second hand for distance $d = 0.265$ nm for oxygen (corresponding to oxygen-oxygen first neighbor shell) and $d = 0.3$ nm for silicon (corresponding to silicon-silicon first neighbor shell). A almost linear dependency is noticeable for all relaxation times ratio, and in particular for low temperatures, the slow-down amounts several hundred of magnitude. On top of the linear increase, the oxygen τ's ratio saturate at about 100, i.e two orders of magnitude larger than the pore center times. This saturation effect is less noticeable for silicon data. This is again some indication that the relaxation process of oxygens positioned at the pore wall vicinity slightly differs from those of silicons at low temperature. Much more oxygens near the pore surface are able to relax via hoppings to the next energy minimum available. And as a consequence, the structural relaxation processes at some temperature for layers near the pore wall get a bit fast such that we obtain qualitatively a plateau for the ratio of relaxation times. Nevertheless, this saturation trend is also almost less visible for the lowest partial charges q/q_0=0.65, 0.70, 0.75 in which no FS is observed in bulk.
More importantly, the data show a pronounced charge dependence in the supercooled regime. Indeed (at least from the d-resolved analysis), one can notice that the slope of the ratio tends to diminish with increasing charges revealing that the extrapolated slowdown gets huge for systems with weaker intramolecular interactions. One can rexplain this finding by suggesting that systems associated with smaller

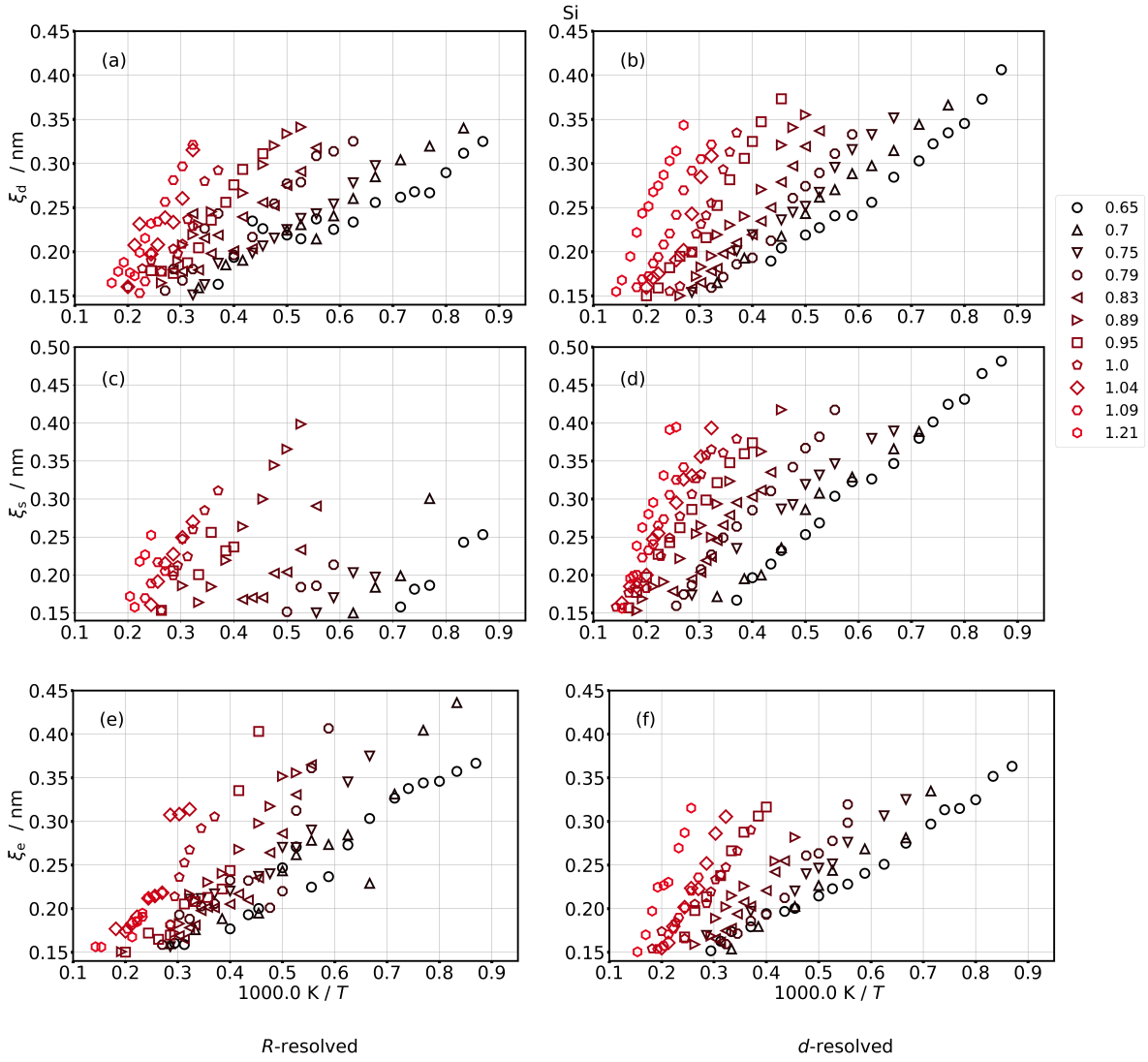

Figure 67: Dynamical ξ_d (a-b), structural ξ_s (c-d) and elastic ξ_e (e-f) length scales plotted for silicon atoms of all silica variants. Here, only the data resolved to pore center are in the left panels, and the ones with respect to pore wall in the right panels. Similar plots for oxygens are added in appendix (see Fig. 113).

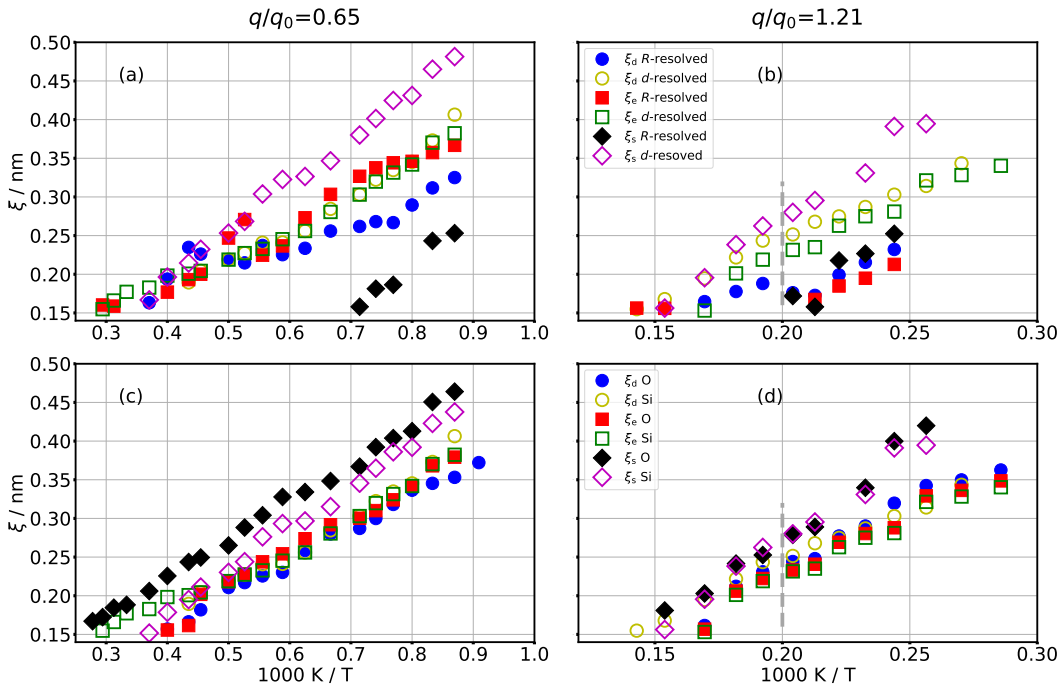

Figure 68: Comparison of the dynamical ξ_{d}, structural ξ_{s} and elastic ξ_{e} coherent length scales obtained from a fit of the R-resolved and d-resolved analysis (a-b) for silicon atoms. (c-d) show a comparison of length scales between oxygen and silicon for the d-resolved analysis. 2 silica variants data are displayed q/q_0=0.65 in (a),(c), and 1.21 in (b),(d). The gray dashed lines in the left panel indicate the position of T_{FS} for q/q_0=1.21.

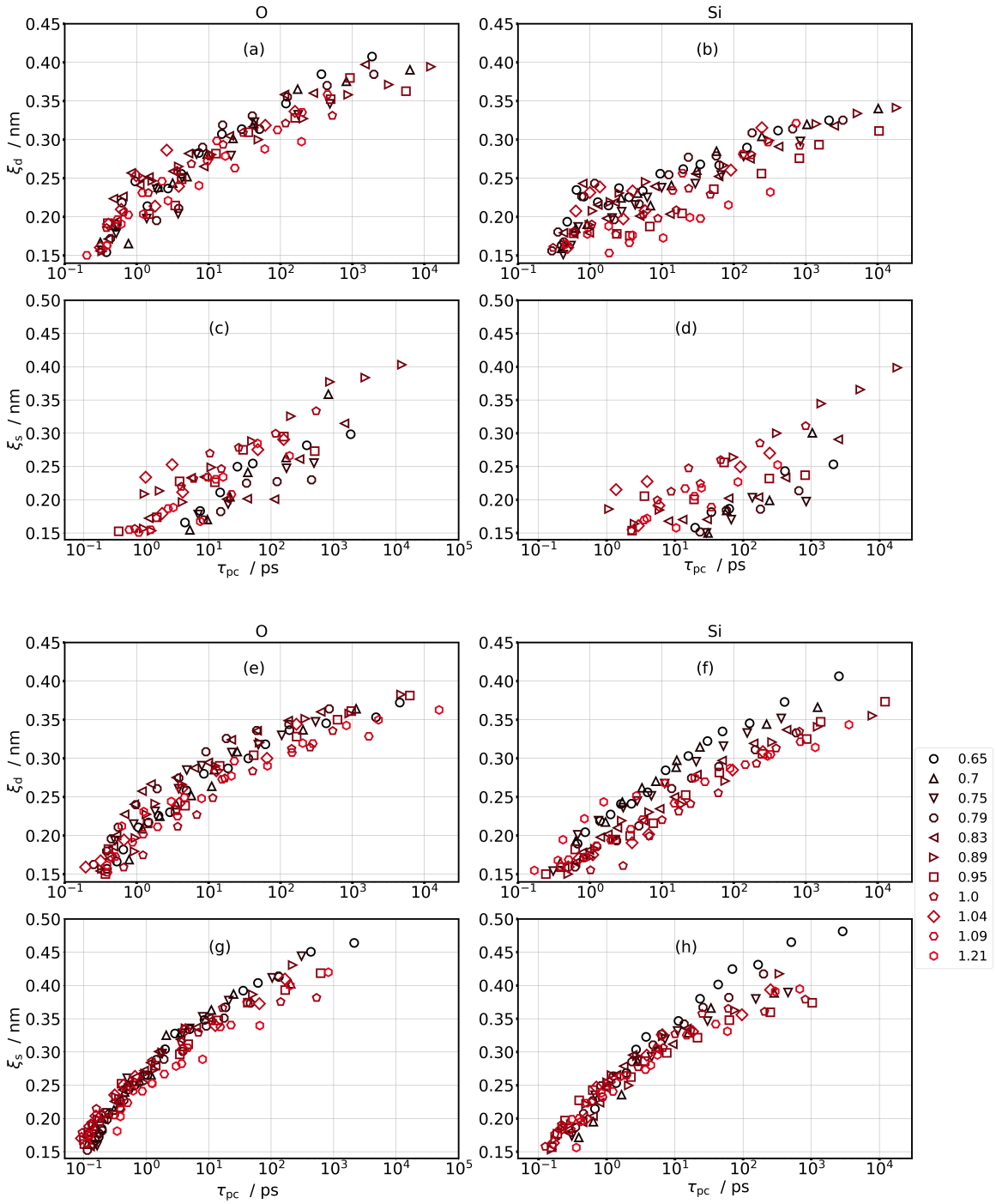

Figure 69: Relation between correlation times of oxygen and silicon atoms in the pore center with dynamical ξ_d (a)-(b) and (e)-(f), as well as structural ξ_s (c)-(d) and (g)-(h) length scales for different silica variants. (a)-(d) are corresponding to the R-resolved analysis and the (e)-(h) indicate the d-resolved analysis. oxygen (silicon) data in the left (right) panel.

charges present a smaller energy barrier that needs to be overcome during motion. This in combination with their lower density in bulk induces a shallower energy landscape compared to the thermal energy. When approaching the immobile atoms of the wall, they feel a static energy landscape and are constrained to slow down therefore they feel a stronger wall effect. In conrast with atoms in systems associated with large charges which are feeling a barrier imposed by fixed wall atoms which gets more and more comparable to the barriers imposed by the surrounding mobile atoms, upon cooling. When considering the R-resolved analysis, one can claim a charge independent effect, but the silicon data are much more scattering. As the d-resolved analysis is more precise when describing the roughness of the wall, one would more rely on the corresponding observations. The observations got from the d-resolved analysis agree well with the obersations that ξ_d change faster with slowing down earlier reported.

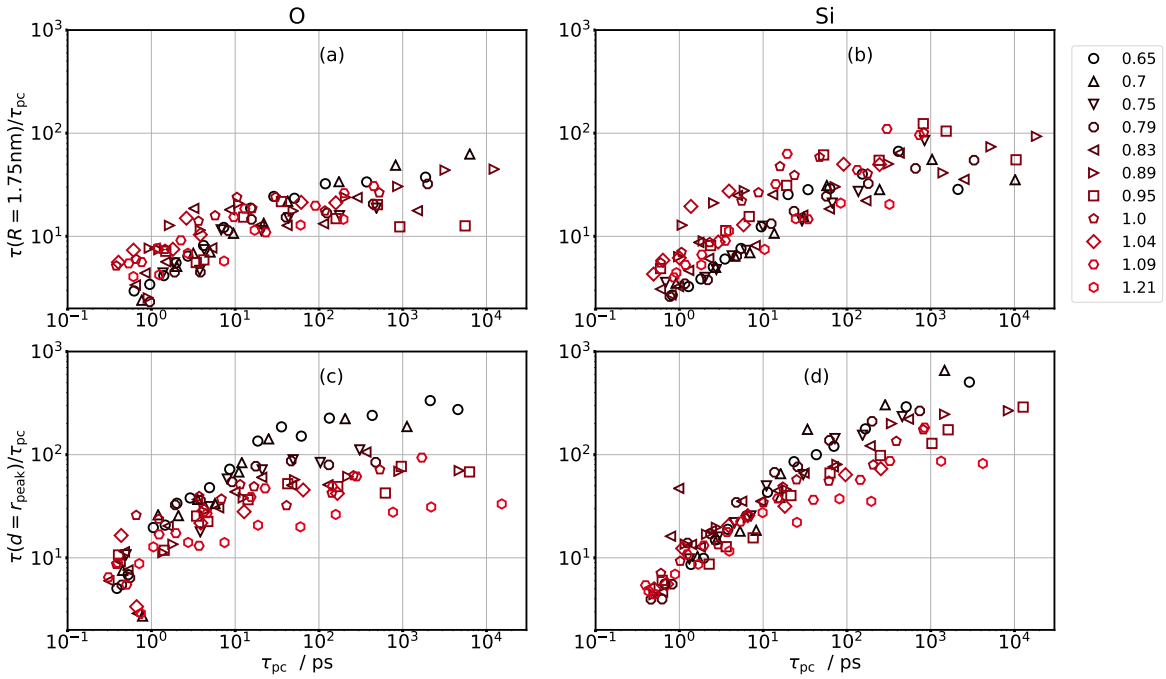

Figure 70: Ratio between structural relaxation times of a layer near the pore wall with the one in the pore center. Top: the outer layer is at $R \approx 1.75$ nm. Bottom: the outer layer at $d \approx 0.265$ nm for oxygen and 0.3 nm for silicon.

Along with the dynamical correlation length, a structural correlation length has been introduced. It is deduced from a study of density fluctuations upon approaching the pore surface which can be probed from the overlap function $P(t)$. $P(t)$ for silicon atoms at different distances from the pore center R (left panels) and from the pore surface d (right panel) for two systems $q/q_0 = 0.65$, 1.21 with respectively $T = 1300$ K and $T = 4100$ K. $P(t)$ is well pictured by a KWW-like function of Eq. 26 (see Fig. 71). $P(t)$ decays towards a plateau of increasing height upon approaching the pore wall. This is its long time limit labeled as P_∞ describing static density correlations which are basically arising from the preferred atomic positions near the pore surface. The profile of P_∞ can be equally described by the following relations

$$P_\infty(x) = P_0 + (1 - P_0) \cdot \exp\left(-\left(\frac{x}{\xi_S}\right)^\beta\right), \tag{64}$$

for the d-resolved analysis $x = d$ and for the R-resolved analysis $x = \mathrm{R}_0 - x$. Here R_0 is the pore radius that is roughly 2 nm. The sum of the stretched-exponent prefactor and the long distance limit

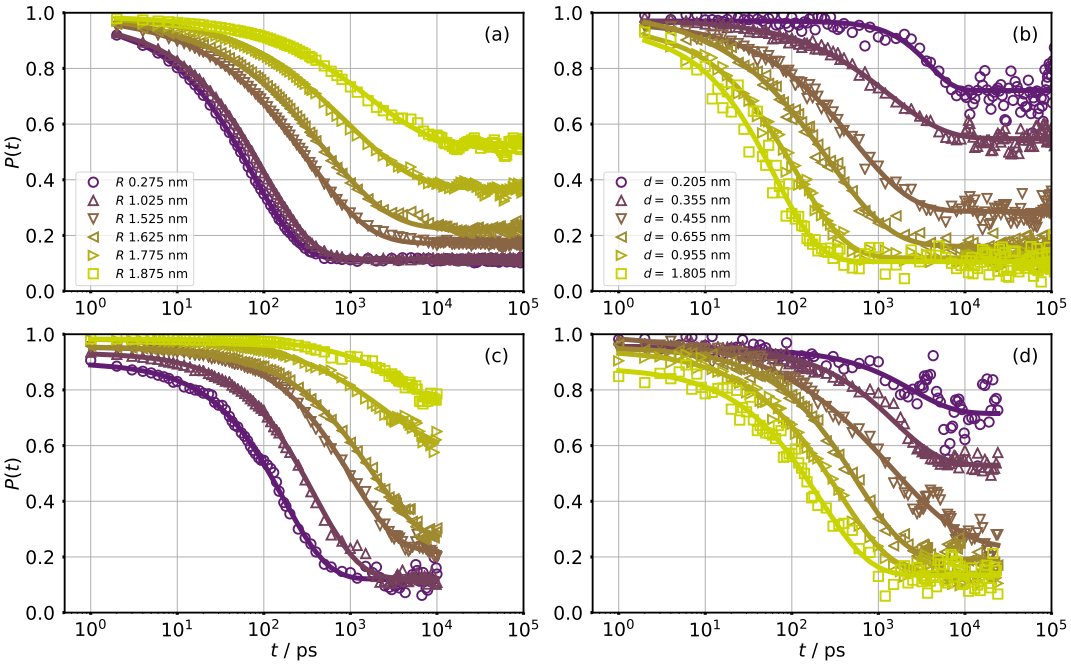

Figure 71: Overlap decays of the configurations of oxygens (left) and silicons (right) with position resolved with respect to pore center R (a),(c) or to closest wall atom d (b),(d). The data are plotted for silicon atoms of the system associated with q/q_0=0.65 and $T = 1300$K (top) and 1.21 with $T = 4100$ K (bottom). The solid lines show the result of the KWW fit (Eq. 26).

P_0 should be equal for accounting the finite pore size volume and so atoms at the pore surface (x=0) have the maximum of overlapping correlations. Fits of P_∞ are added in Fig. 72 for q/q_0= 0.65, 1.21

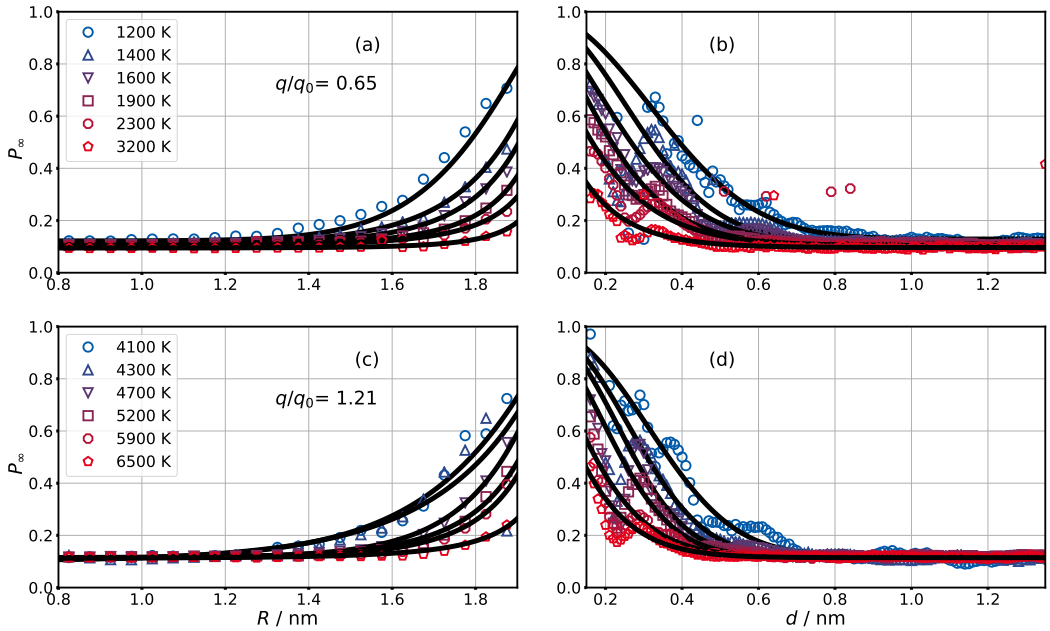

Figure 72: Left panels indicate the fit of the R-resolved overlap offset with Eq. 64, right panels display the fit of d-resolved offset with Eq. 64. We show the plot for q/q_0=0.65 (a)-(b) and q/q_0=1.21 (c)-(d) for silicons.

for R- (left) and d- (right) distance resolved. The oscillations characteristic of the pore surface roughness are also observed here. The resulting ξ_S are compared (see Fig. 68) for each liquid between both methods (R-resolved and d-resolved). Here, the effect of pore roughness is substantial since the length scales extracted from the R-resolved analysis are always smaller as the ones obtained from the d-resolved analysis. This is reasonable as one would expect more structural correlations and development of more preferred positions near a rough surface. And this should imply larger correlated clusters. These conclusions should be taken cautiously as the fits lines are only estimating the rapid and oscillating growth of P_∞ (deduced from the d-resolved analysis) near the pore surface. In any case, similar effect is also observed when comparing dynamical length scales extrapolated from both analysis, and one might conclude that the effect of the R-resolved analysis averages out too much the effect of the pore.
The fit parameters P_0 values (see Fig. 114 in appendix) are agreeing between both methods. P_0 should be similar to the bulk value in the limiting case of an infinitely large pore. It is always double for oxygens in comparison to silicon since oxygens are twice numerous. Meanwhile, it slightly increases with partial charges which is in good agreement with its expected relation with atoms density of Eq. 27. Indeed Fig. 73 shows a comparison of P_0 with N_{OF} which represents the number of atoms inside the sphere of of radius r_{OF}=0.1 nm in which the time occupation numbers of atom is analyzed. One sees that for both atom types, P_0 is roughly within 5% of N_{OF}, so as expected nearly comparable to the local bulk density.
The resulting exponent β (added in Fig. 112 of appendix) increases with cooling as already reported for regular BKS silica [177] and other liquids.[112, 172] This implies a sharp transition between overlaps of configurations in low and high temperatures. β roughly increases linearly with reducing temperature. β mostly vary between 0.5 to 2.5, and are at low-temperature comparable to the values of 2 reported for liquid water [112] and considerably smaller than 4 recorded for soft-sphere mixtures. [172] A general trend with partial charges can not be postulated and one can state that β is strongly dependent on the inferred length scales. Structural length scales ξ_s are plotted with respect to logarithm of the relaxation

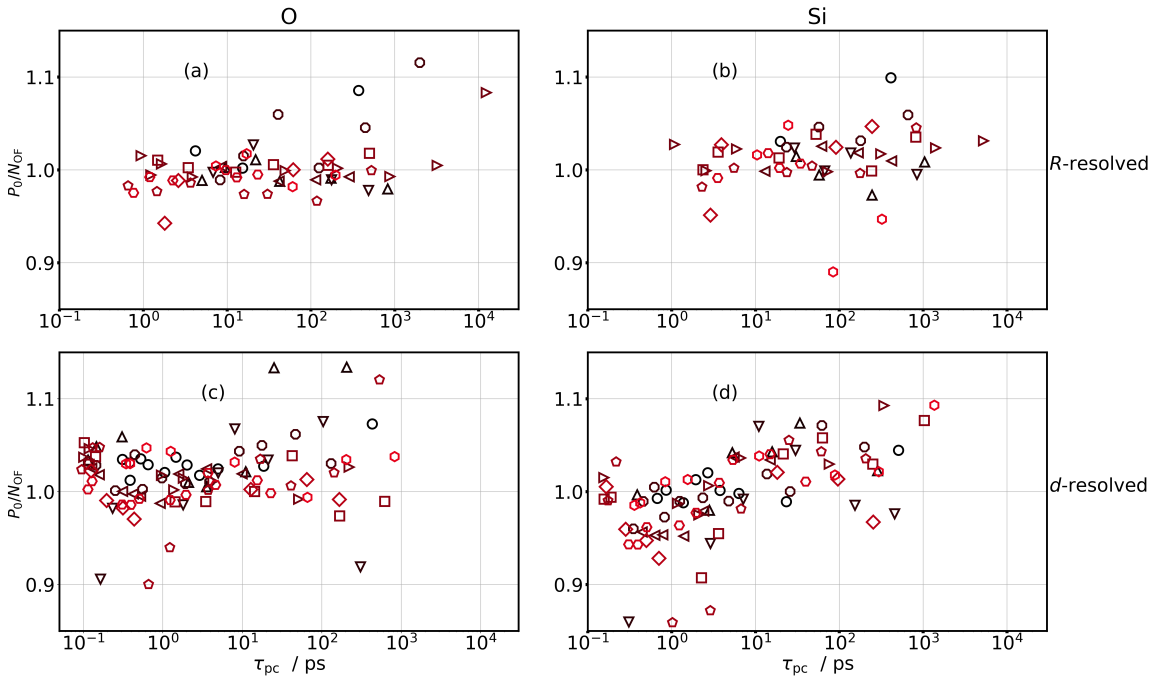

Figure 73: Comparison of P_0 with the average atoms number (N_{OF}) in a sphere of radius 0.1 nm used for determining the overlapping of configurations. The ratio is plotted with respect to τ_{pc} for an easy comparison between the different silica systems since they are studied in various temperature range. P_0 values are plotted in Fig. 114 of appendix.

times in Fig. 69 and one notice that for the R-resolved analysis, a significant charge dependence can be seen which matches well with the trend of corresponding β, while the charge dependence almost disappear with the d-resolved analysis which is also reflected in the corresponding $beta$. In order to check to which extent β and ξ_s are related, we have plotted $\langle\xi_s\rangle = \xi_s/\beta \cdot \Gamma(1/\beta)$ in Fig. 115, which vary accordingly as compared with the corresponding ξ_s and β. These observations that β and ξ_s contribute both for a complete description of the wall effect. The already noticed fact that the effect of the wall decreases with stronger atoms interactions (larger partial charges) can be in general postulated.
We have furthermore plotted the ratio of P_∞ between atoms layer positionned respectively in the pore center and near the pore surface (see Fig. 74). From the d-resolved analysis, the tendency of lowest charges to be more affected by the wall constraint (already observed from the ratio of relaxation times in Fig. 70((c)-(d)) is highlighted by the silicon data in see Fig. 74(d), while oxygen data show almost no charge dependence. From the R-resolved analysis, one can also postulate that there is in overall a slight charge dependence although a clear charge dependence trend can not be drawn. This happens because ξ_s extacted from the R-resolved analysis are always shorter than the d-resolved analysis data as can be seen in Fig. 68(a)-(b), and are mostly smaller than 0.15 nm which is the defined (in this work) cut-off length scale as it is similar to the first silicon oxygen closest distance.

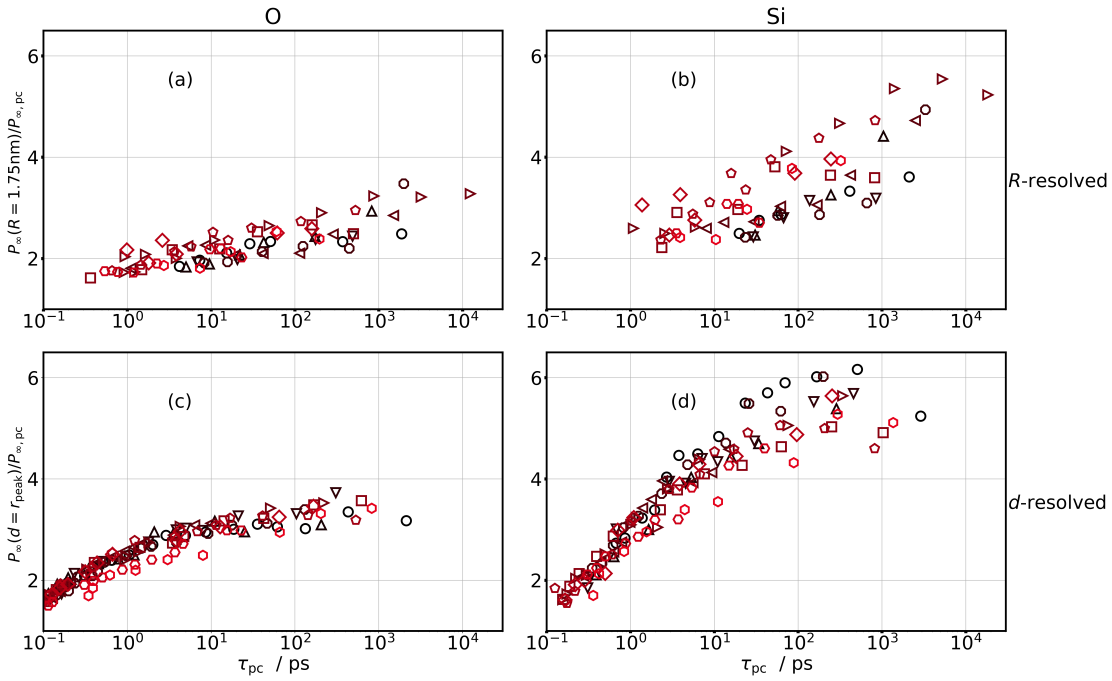

Figure 74: Ratio between long time limit plateau P_∞ of a layer near the pore wall with the one in the pore center. Top: the outer layer is at $R \approx 1.75$ nm. Bottom: the outer layer at $d \approx 0.265$ nm for oxygen and 0.3 nm for silicon.

Another way of estimating the size of correlated clusters is by estimating the elastic correlation length. This can be probed from a study of the variation of u^2 which is the MSD at 1 ps. Fig. 110 displays how u^2 are extracted from the MSD of particles resolved with respect to R (top figures) or d (down figures). The MSD in Fig. 110 indicates that the plateau between vibrational decay and diffusive regime enlarges. In particular in the pore, the 3D diffusion is not possible due to the geometric constraint imposed by the

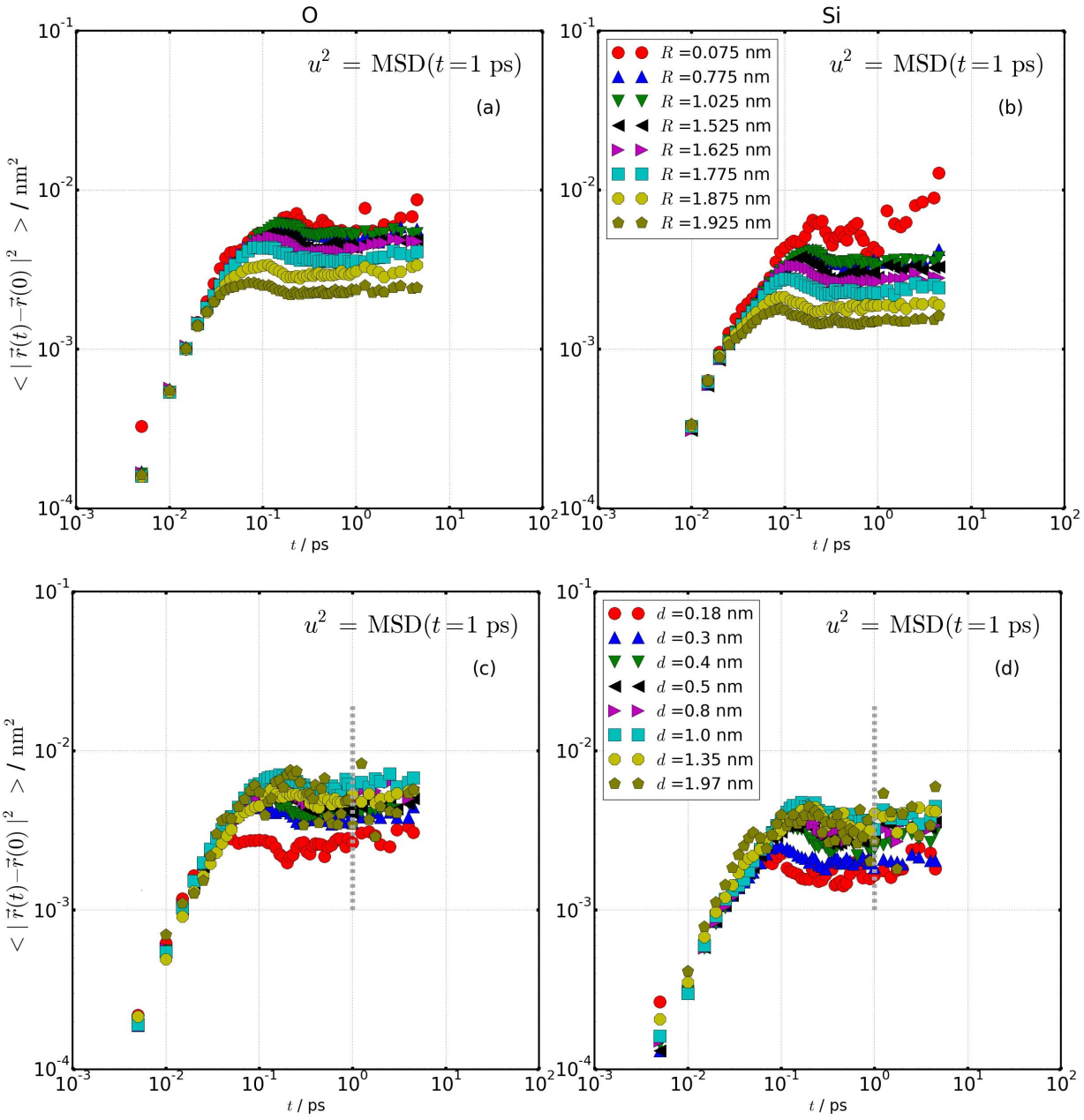

Figure 75: Short times MSD of oxygens (left) and silicons (right) to which the position are indicated with respect to pore center (top) or to the nearest atom of the pore wall (bottom). Here the data for q/q_0=1.21 and T=4100 K are shown. The vertical dashed lines illustrate the MSD at 1 ps.

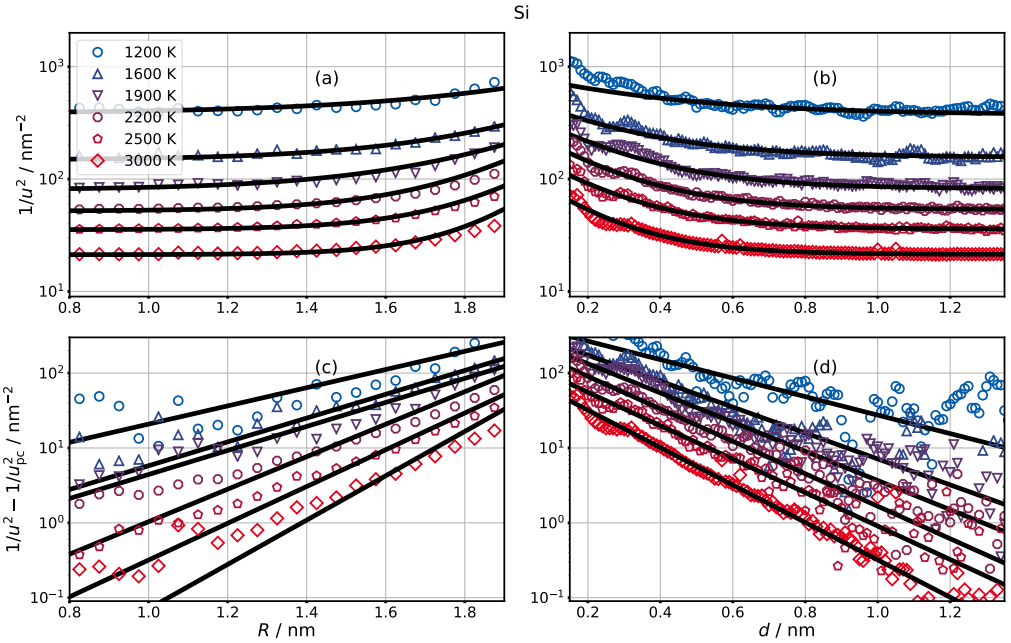

Figure 76: Distance Profile of $1/u^2$ of silicon atoms resolved with respect to pore center (left) or pore wall (right) fitted with Eq. 65. (c)-(d) are the corresponding log plot in which one can identify the slope at large R or small d. Here the data correspond to q/q_0=0.65 for different temperature.

pore. The profile of $1/u^2$ from the R-resolved and the d-resolved analysis are shown in Fig. 76, the fitted curves are given by the relation:

$$1/u^2(x) = 1/u^2_\infty + a_u \cdot \exp\left(-\frac{x}{\xi_e}\right), \tag{65}$$

in which $x = d$ for the d-resolved analysis and $x = 20 - R$ for the R-analysis. When performing the fit, we always exclude the data which are too close to the pore wall (specifally in the d-resolved analysis, we remove data of atoms which are at 0.4 nm distants to the closest wall atoms). Indeed, atoms which are next to the pore wall are not more freely moving in 3-dimension and this has a strong effect in the corresponding MSD inferred at different temperature. As a consequence, one gets spurious temperature effect, as for example that when comparing u^2 data along the pore with the pore center data u^2_{center} in Fig. 77, one sees that at $d \lesssim 0.4$ nm the high temperature data are significantly deviating from the behaviour at the pore center, as compared to the low temperature data. From the fitted lines in Fig. 76(a)-(b), the elastic coherent length ξ_e can be extracted as indicated in Fig. 68. In general, the values of ξ_e match reasonably well with the dynamical length scales ξ_d and often the structural length scale ξ_s. Relating ξ_e and τ_{pc} in Fig. 78(a)-(b) leads to similar observations as observed with dynamical and static length scales, in which length scales associated with the lowest charges are growing faster with increasing relaxation times. However, this trend is not confirmed when relating the prefactor a_u extracted from the corresponding fits with Eq. 65 as shown in Fig. 78(c)-(d), in which one almost see no charge dependence, or at least could not identify a trend with different partial charge. Fig. 67 shows the temperature dependent ξ_d, ξ_s, ξ_e for silicon atoms of all silica variants here studied, corresponding plots for oxygens are added in appendix (Fig. 113). In the temperature regime, it is almost difficult to draw a change trend of length scales with respect to charges, since the temperature range strongly shift with respect to the associated silica system. This motivates our preferred plots of Fig. 69 in which length scales are rather confronted with time scales. In Overall ξ's are comparable to inter-atomic distances

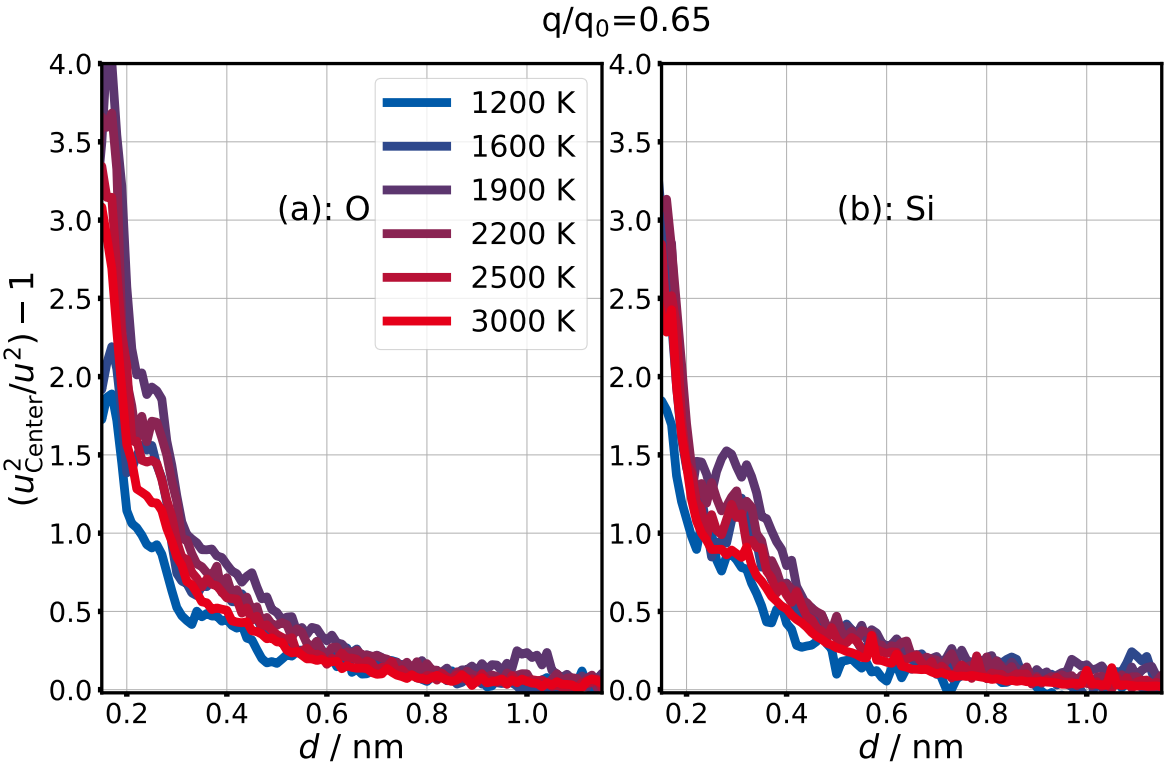

Figure 77: Distance profile of u^2 for silicon and oxygen atoms resolved with respect to pore wall data and scaled with respect to pore center data u^2_{center}. Here the data correspond to q/q_0=0.65 for different temperature.

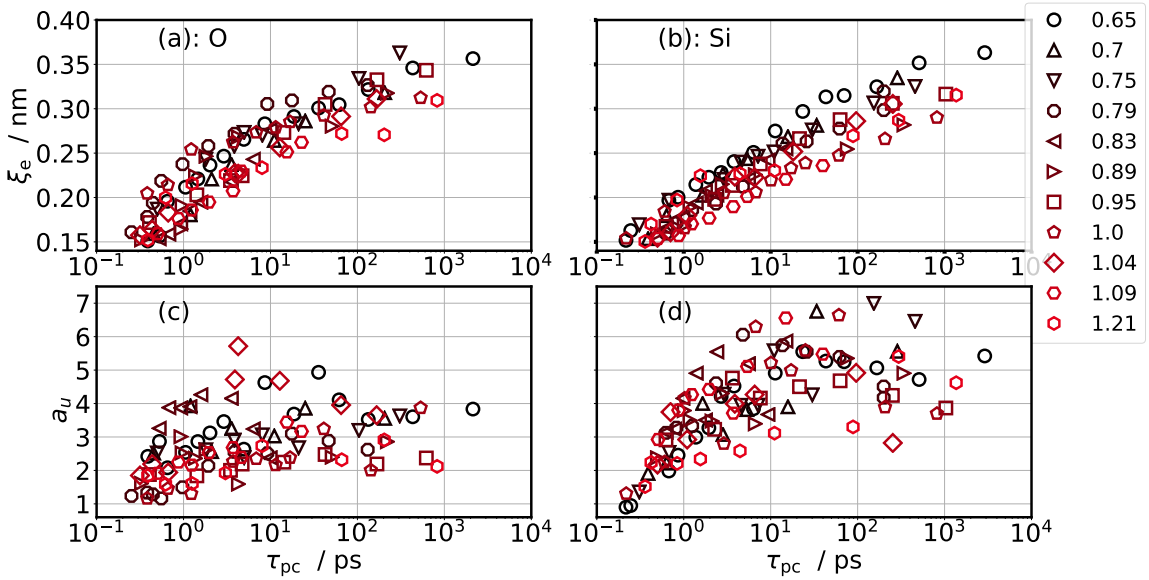

Figure 78: (a)-(b): relation between elastic length scales ξ_s and pore center relaxation times. (c) and (d) are the corresponding prefactor a_u determined from the fit with Eq. 65. Left (right) data are for oxygen (silicon) for all silica variants. These data are only plotted for the d-resolved analysis and do not dramatically differ from the R-resolved data.

in each liquid. One can almost observe a linear dependence with inverse temperature consistent with previous reports. [173, 112] Interestingly, no sign of the FS crossover as expected from Ref. 111 can be detected here since the temperature dependence is similar between systems showing no FS in bulk (as for example q/q_0=0.65, 0.70, 0.75) with the other systems. But one should be careful when drawing conclusions as the *R*-resolved analysis average out the real effect of pore roughness, while the d-resolved analysis provides some oscillation in the drastic increase of the observables near the pore wall. That means, the mere equations established to reproduce this effect should be reformulated in order to implement the local structure effect in the potential energy minima imposed by wall atoms. One would indeed expect to have correlated clusters of constant size within the low temperature range of the strong regime, which will well match with the observed temperature independent activation energy E_0.

Yet, it is still instructive to understand how the given length scales relate with the bulk behavior (here we will mostly used data of atoms at the pore center to represent the bulk behavior, as already done in Fig. 69). For this reason, we have related ξ_s with the average tetrahedral order parameter of atoms in the pore center. Fig. 79 shows that a almost linear dependence can be approximated, which is consistent with the fact that increase of local ordering in the systems implies the presence of well defined energetically favorable atom positions in the systems. And since ξ_s measures correlations in atom configurations, this might certainly contain a fingerprint of the systems local ordering. The flattening of the curves at very low temperature occurs from the saturation of the local ordering intrinsic of the BKS model already reported in the bulk behavior (see Fig. 2 of the preceding chapter).

One can as well test the RFOT theory [114, 115] (introduced in chapter. 4) which predicts that the growing of energy barrier upon lowering the temperature of glass formers scale as ξ^γ with $\gamma = 2$ for spherical correlated clusters. For silica variant not a single exponent can be observed as illustrated in Fig. 80. γ varies with partial charges and with atoms types between 1 and 2.2. It is always larger for the low partial charges and the growth of ξ_d^2/T with τ is sharper in comparison with the high partial charges. That again confirm our previous observations that the constraint imposed by the wall is more affecting systems associated with the lowest partial charges. It is also difficult to make a general conclusion about the exponent of silica like liquids. Nonetheless, the fact that different exponents are obtained for different atom species and also different probed observables of a single system might imply that the cooperative clusters might have various shape in the system. Thus depending on the quantities which is probed, a given shape is pictured.

Another alternative of checking relations between length scales and activation barriers is to confront length scales and activation energies as defined in the *Rössler* relations. For this task, we use Eq. 31 to calculate activation energy in terms of relaxation times, temperature and bulk high-temperature activation energies. Fig. 81 exhibits this relation for the three length scales types, for each atom type resolved with respect to pore center. For the low charges, the ratio of the squared-length scale with cooperative energy decreases upon cooling, revealing that collective energy barriers increase faster upon cooling than typical length scales. What is appealing in these results is that for the highest charges, the ratio is almost constant meaning that both quantities change similarly upon cooling. Strictly speaking, for the highest charges $q > 0.89q_0$, the FS crossover happens in the range 1-10 ps so this definition of activation barrier is somehow abusive. But at least it allows us to state that the length scales in strong dynamics increase with a much smaller slope as compared to the increase at similar time scales within the fragile regime. (Similar plots are added in appendix for the d-resolved analysis).

We have additionally check the ECNLE theory [116, 117, 118] (shortly described in chapter. 4) which proposes that the relaxation process involves a long-range collective elastic distortion of correlated particles, implying a relation between τ and ξ^2/u^2. The correlation between both quantities is presented in Fig. 82. Apart from the high-temperature part, a linear correlation can as well be estimated here which differs between various systems. A charge dependence is noticeable at low-temperature in particular ratio between length scales and u^2 are enlarging quickly with slowing down as the intermolecular interactions are reduced, which is again confirming our previous findings.

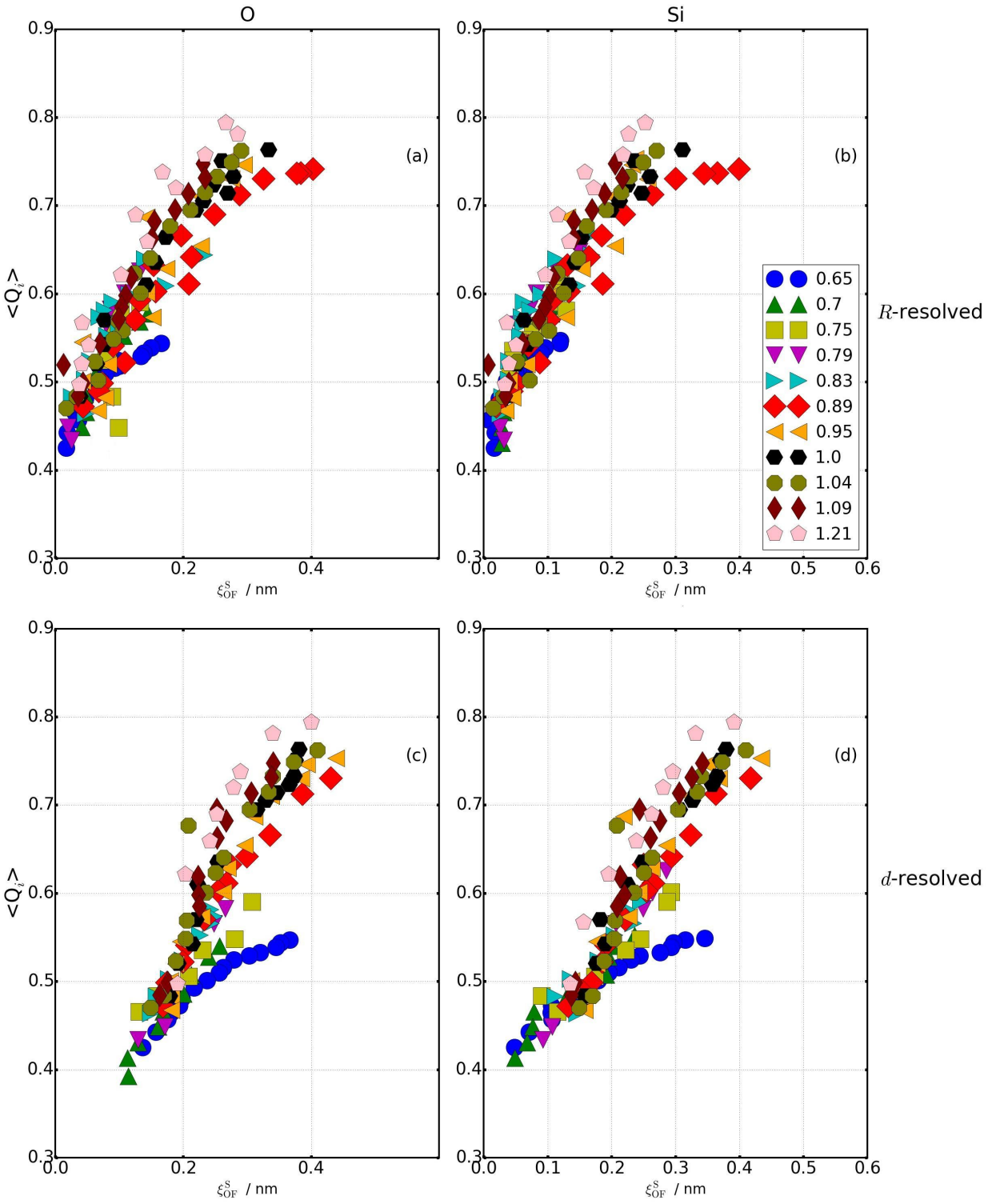

Figure 79: Relation between average tetrahedral order parameter of silicon atoms in the pore center and structural length scales ξ_S with the R-resolved (a)-(b) and the d-resolved (c)-(d) analysis.

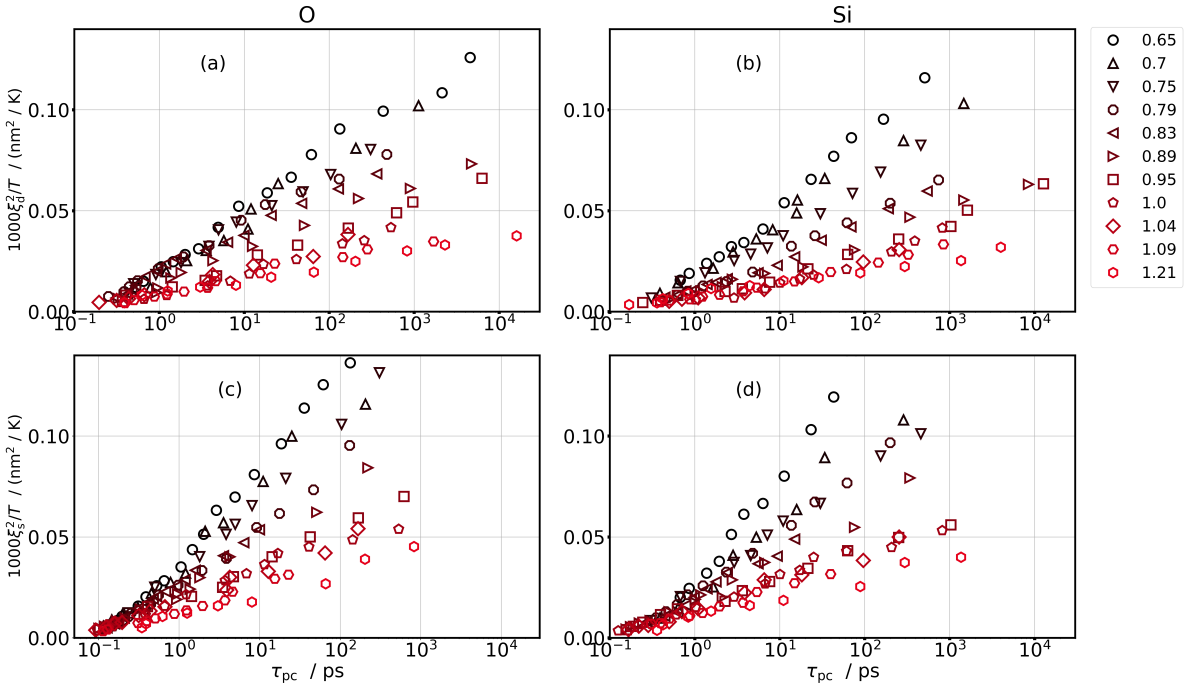

Figure 80: Relation between correlation times of oxygen and silicon atoms in the pore center with dynamical $1000 \cdot \xi_d^2/T$ (a)-(b), as well as structural $1000 \cdot \xi_s^2/T$ (c)-(d) length scales. Shown data are for the d-resolved analysis, the corresponding ones for the R-resolved analysis are added in Fig. 116.

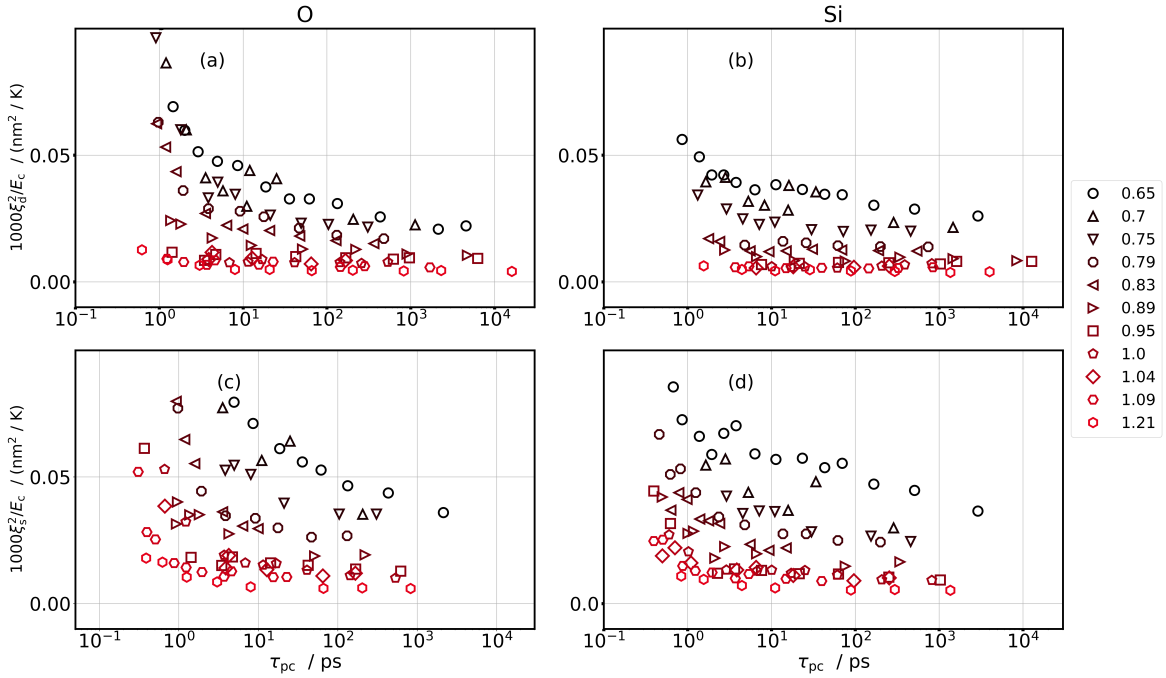

Figure 81: Relation between correlation times of oxygen and silicon atoms in the pore center with dynamical length scales $1000 \cdot \xi_d^2/E_C$ (a)-(b). (c)-(d) are similar data with structural length scales. These data are plotted with the d-resolved analysis but look alike to the R-resolved data added in Fig. 117 in appendix.

Finally, the shoving model is once more tested. We have then concentrated on atoms in the pore

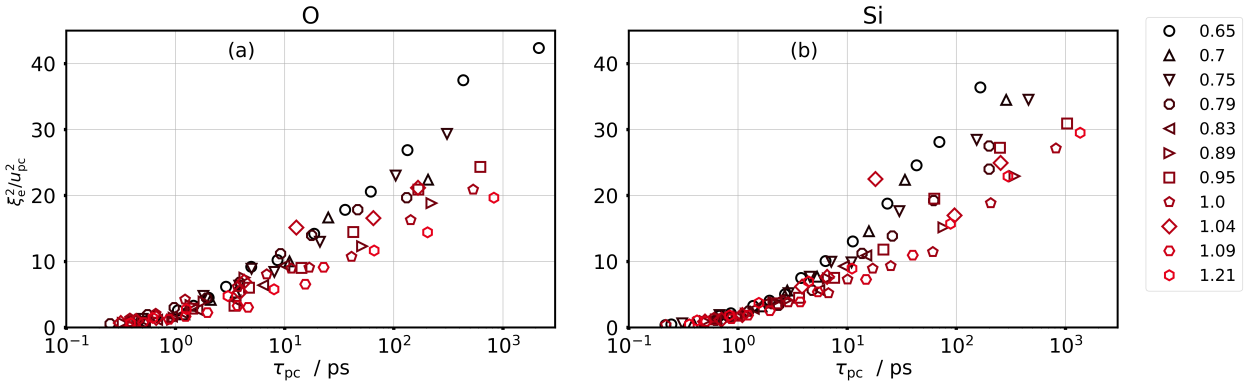

Figure 82: Relation between τ and ξ^2/u^2 namely the elastic ξ^{E} (bottom) length scales. Here the data for the d-resolved are the ones displayed since ξ^{e} data are not significantly varying between both resolved analysis.

wall vicinity (R= 1.85) and related the correlation times with the corresponding $1/u^2$ quantities. Fig. 83 shows a linear dependence for all silica variants. In the particular case of low partial charges for which the behavior considerably differs with the one of high partial charges, almost no difference is visible for atoms near the pore wall. This is somehow not surprising as for all silica liquids, particles relaxations in the pore wall vicinity have a temperature-independent activation energy over the whole temperature regime and thus dynamics of these particles resemble strong glassy dynamics. And hence a master curve is observed for all silica variants.

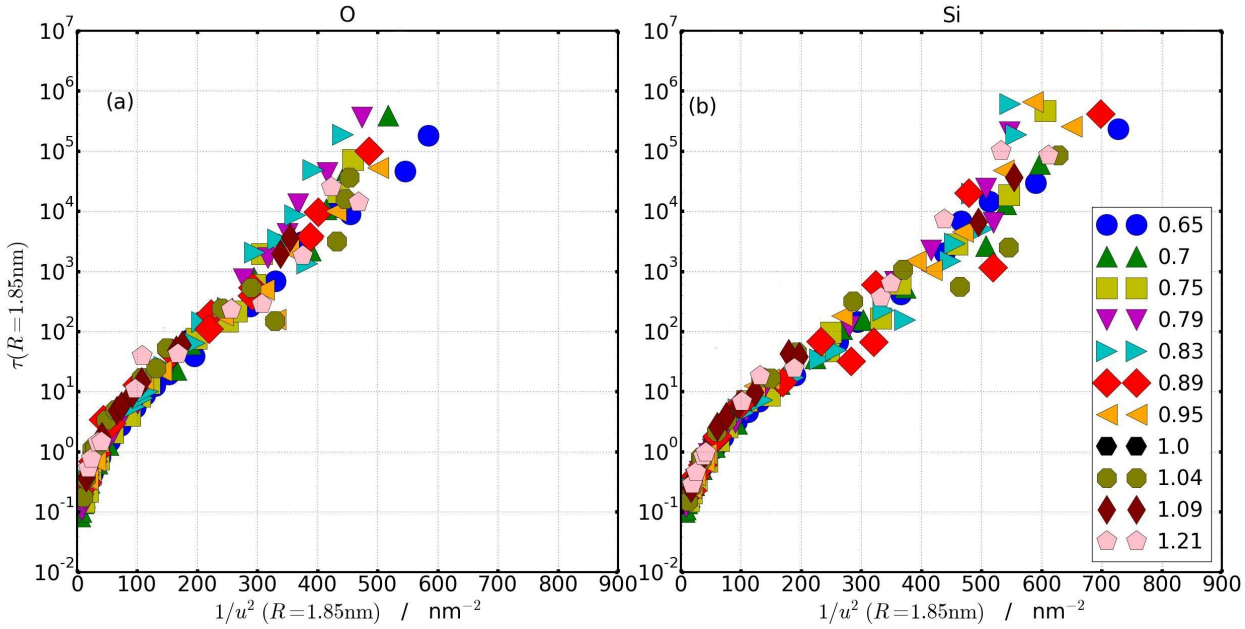

Figure 83: Relation between τ and $1/u^2$ for oxygens (a) and silicons (b).

8.4 Summary

A detailed MD study of silica-like liquids, differing with bond polarity, in neutral confinement has been performed. Neutral confinements were the focus as they permit to precisely analyze the effect of spatial constraint on structural relaxation processes. We have shown that the structure of the confined liquid is nearly identical to bulk irrespective of the positions of the probed liquid layers. This is quite predictable as the mobile liquid in the pore is of the same nature as the confined matrix, we have the same atoms type with identical attached partial charges and assigned interaction parameters. The only difference is that atoms within a distance of roughly 2 nm of the pore center are able to move while the rest are fixed. In other to study the distance-dependent dynamics of atoms, we have used the radial coordinates of atoms to label each atom and this has been referred as the R-resolved analysis. We have as well used the d-resolved analysis in which atoms position are indicated with respect to distance to nearest wall atoms. The latter explicitly describes the effect of the short local ordering on the structural and dynamical correlations.
We have found that dynamics hugely slow down for atoms in the pore wall vicinity. This suggests that the potential energy landscape imposed by atoms in the pore wall is gradually feel by mobile atoms such that the ones which are in the immediate vicinity of the pore wall feel deeper energy minima with a energy landscape which is in average temperature independent consistent with the found low-temperature Arrhenius behavior. Similar observations have been pointed for regular BKS silica. [177] We have also shown that the motion of oxygen atoms in the pore wall vicinity tends to decouple from the motion of silicon atoms since the low-temperature activation barrier barely increases near the pore wall for oxygens as opposed to the case of silicons in which the increase is significant. We have further shown (using the van Hove distribution) that much more oxygens are able to relax via hoppings to adjacent sites in comparison to silicon. Consequently, the ratio between relaxation times of atoms in the pore wall in comparison to the atoms at the pore surface increases linearly for silicon atom and somewhat saturates for oxygens (apart from the small partial charges).
Different length scales type have been derived. There are the dynamical length scale ξ^{d} from the growth of τ near the pore wall, the structural length scale ξ^{s} from the growth of the long time limit of the overlap function P_{∞} and the elastic length scale ξ^{e} from the growth of $1/u^2$. ξ^{d} and ξ^{e} barely differ between the R-resolved and the d-resolved analysis for both atoms types, while ξ^{s} considerably vary by a factor between 1.2-1.8 between both analysis. This difference arises from the strong oscillations observed in P_{∞} near the pore wall with the d-resolved analysis implying that the simplified R-resolved analysis averages out considerably the real effect of the pore wall when probing structural correlations.
In overall a linear increase with inverse temperature is observed for all these length scales agreeing with former works. [173, 112, 177] This temperature dependence of length scales has been explained [177] as originating from the decrease of confinement effect with increasing temperature due to arising fluctuations affecting the gradual transmission of the static energy landscape of the immobile wall atoms on the adjacent mobile layers inside the pore. Indications of FS crossover as expected from Ref. [111] are not clearly detectable in this plot since the temperature dependence at the low-temperature regime corresponding to strong dynamics do not display a noticeable modification from the high-temperature dynamics. This observation is somehow counter-intuitive as one would expect in the fragile regime a huge increase of correlated clusters size upon cooling in agreement with the activation barrier increase. An increase which is even sharper as postulated by the RFOT [194] as length scales relate to the activation barrier with an exponent γ. In contrast, in the strong regime with temperature-independent energy barrier, one would thus predict a constant length scale.
The RFOT has been tested and we find that the γ exponent slightly changes with charges especially when using the dynamical length scale. γ inferred from the structural length scales is roughly 1.7-2.1 for q/q_0 values between 0.65 and 0.89 while it amounts 1.0-1.5 for larger scaling factors. This charge dependence suggests that the dimension of the clusters formed in silica variants vary with bond polarity by a non-trivial manner. It is however interesting to point out that at a given time scale, the growth observed with

low partial charges is always sharper as compared with the one for high partial charges. This affirmation can also be stated when only looking how length scales vary with respect to times scales, in general, the length scales associated with the lowest partial charges increase quickly with time as compared to the length scales associated with the highest partial charges. This illustrate the effect of modifying the partial charges, which reveal that the confining wall effect enlarges.
A more appealing manner in which one can postulate a change of length scale behavior upon approaching the FS crossover is to confront squared-length scales and activation barriers as defined in the *Rössler* relations. Eq. 31 is utilized to calculate activation energy in terms of relaxation times, temperature and bulk high-temperature activation energies. For the low charges, the ratio of squared-length scale with cooperative energy suggests that collective energy barrier increases faster upon reducing the temperature than typical length scales, while the ratio is almost constant for the highest partial charges. From these results, we can thus propose that length scales in strong dynamics increase much more slower upon cooling than length scales in fragile dynamics. One can simply understand this phenomenon by considering a mobile atom in the pore wall vicinity for systems associated with small charges. This mobile atom feel the shallow energy of the surrounding mobile atoms which is considerably different to the static energy exerted by the nearby immobile atoms of the wall; the combination of both interactions result in a stronger confining effect.
Finally, we have reviewed the elastic models on silica variants and show that the shoving model applied to layer of atoms close to the pore wall leads to a master curve for all silica variants. This observation exhibits the fact that near the wall, all silica variants behave alike, and in particular, systems showing no FS in bulk are not distinguishable. We have additionally scrutinized the ECNLE theory and shows that it fails with our defined elastic length scale ξ^e. This suggests that elastic models are not adequate to check dynamics in confinements because there are defined for bulk systems while in the pore, atoms dynamics is three dimensional in the pore center, while close to the pore surface atoms loose one degree of freedom due to the immobile wall. Therefore, the inferred elastic features such as the Debye-Waller factor and subsequent length scales should be affected by these modifications in degrees of freedom.

9 Radon accumulation in water and non-polar solvents

Radon is a quite heavy chemical gas compound and its most stable isotope is ^{222}Rn. It is particularly interesting due to its medical relevance. It has been demonstrated that radon can be used as a therapeutic paint killer or releaser of rheumatism, arthritis and other inflammatory diseases. [252, 253] Interestingly, it has been reported that radon tends to accumulate more in fat cells [124, 122, 125, 254] than in other cells. That means radon accumulate easily in fat than in alkaline solutions, or liquid water. Previous simulations [255, 256, 257, 258, 259] have been concentrated on studying the diffusion of small quantities (2-5 atoms) of rare gas atoms (He, Ne, Ar, Kr, Xe) in water in order to understand the hydrophobic effect. The aim has been to compare the diffusion of each of these gas in liquid water and to probe the local structure and dynamics of the water layer surrounding the solvated gas atom. The outcome is that the bigger the atom, the slower is the dynamic of the atom in water, as the hydrogen bond network of water molecules gets more disrupted, and the first hydration layer of water molecules surrounding the solute shows a slower dynamics compared to the bulk dynamics. However, an analysis of the accumulation process of a rare gas in water compared to a non-polar substance has not yet been proposed.
Since radon is one of the largest rare gas atoms, it can be expected that its diffusion in water is even more hampered. In order to elucidate the mechanisms responsible for the particularly high (low) concentration of radon in fat (water), molecular dynamics (MD) simulations of radon diffusing in liquid water and liquid oil are performed. For testing the hypothesis that the molecular polarity of liquids is responsible for the lower concentration of radon atoms, we changed artificially the hydro-affinity of water by making it more or less polar. With respect to fat, we chose hexane which is an non-polar liquid as well as butyric and capric which are saturated fatty acids. This work is mostly inspired by the possibility to compare the simulation data with experimental results from the biophysics group of *Prof. Gerhard Kraft* and *Prof. Claudia Fournier* in the GSI institute of Darmstadt.

9.1 Simulations details

The SPC/E [136] model is also used in this part to describe liquid water. To generate water systems of varying polarity, the partial charges attached to oxygen and hydrogen atoms are increased (Water Q_+) or reduced (Water Q_) by 15 % from the original value defined in the SPC/E water model. In order to mimic the human living cell ambient fluids, alkaline solutions of 5% of NaCl and 1.9% of Ca_2Cl are simulated. Although, the salt concentrations are higher than the physiological density (0.9%), they are the ones often used in MD simulations to investigate dynamical properties of ions in salt solutions. [260, 261] The interaction parameters of the alkaline ions have been extracted from Ref. 262, 263. The parameters used to simulate hexane originate from the CHARMM22 force field, [148] and those for butyric and capric acid from the work of Clifford et al. [264]. Radon atoms interact solely via the VdW interaction with other atoms or with itself, implemented by means of the LJ potential defined in Eq. 60.

The isotope ^{222}Rn is used to describe radon. In order to set the LJ parameters corresponding to the gaseous phase of radon, the well depth ϵ is deduced from the radon bulk cohesive energy [265] (U_{coh}): $\frac{U_{coh}}{N_0} = -(2.15)\cdot 4\epsilon$ for ^{222}Rn. The value of σ used in the present study is chosen appropriately in order to reproduce accurately the density of radon gas. Some simulation using the parameters suggested by other authors [266, 267, 268, 269] have been performed, but the deriving density at room temperature is at least 5% higher than the empirical radon density. The set of parameters that we are proposing further reproduces qualitatively well the radon diffusion in atmospheric pressure (see Fig. 84 and Table. 10.). The interaction of radon with other atoms is defined with the LJ potential, and the corresponding parameters are calculated using the *Lorentz-Berthelot* mixing rules. [142]

Table. 7 recapitulates the different LJ parameters as well as the partial charges assigned to the different atoms types simulated. The temperature of simulations is set equal to the room temperature (T = 298

K) using a Langevin thermostat [137] with a coupling coefficient of 1.0 ps^{-1}. An integration time step of 1 fs was utilized in order to precisely follow the motion of fast radon atoms. The simulations are run for roughly 10 ns for the equilibration of each pure liquid, while the accumulation of radon in each liquid is studied during a time interval of at least 2 ns. We used PBC which enables the calculation of the long-range Coulomb electrostatic interactions with the PME summation, using a cut-off of 1.5 nm and a switching distance of 1.2 nm. All runs were carried out within the NPT ensemble keeping the pressure constant and equal to 1 bar using the Langevin-Piston method. [141]

Atoms	ϵ (Kcal/mol)	σ (nm)	q_i (e)
O_W	0.155	0.317	-0.847
H_W	0.000	0.179	0.423
C_e	0.078	0.363	-0.270
C_b	0.0560	0.358	-0.180
H_e	0.024	0.238	0.009
H_b	0.035	0.238	0.009
C	0.081	0.390	0.750
$O=(C)$	0.156	0.305	-0.550
$O-(H)$	0.184	0.302	-0.610
H	0.000	0.179	0.009
CH_2	0.091	0.395	-0.180
CH_3	0.194	0.375	-0.270
N_a	0.046	0.251	1.000
Cl	0.150	0.404	-1.000
C_a	0.023	0.324	2.000
Rn	0.541	0.453	0.000

Table 7: LJ parameters and partial charges assigned to each atomic site used in the simulation. O_W and H_W stand for the oxygen and hydrogen atoms of water. C_b and C_e are the carbons of the hexane chain linked respectively to 2 (H_b) and 3 (H_e) hydrogens. C, $O=(C)$ and $O-(H)$ are the atoms of the fatty acids carboxylic group. CH_2 and CH_3 are the carbons of the fatty acids linked respectively to 2 and 3 hydrogen atoms, and H represent the hydrogens. Na, Ca and Cl represent the sodium, calcium and chloride ions.

The systems characteristic sizes are mentioned in Table. 8. The number of molecules used in the simulations were 9999 for water, 3479 for hexane, 3375 and 1122 for butyric and capric acid respectively, and 9702 for radon. The first set of simulations have been devoted to bulk systems in order to check the aptitude of the interactions parameters in describing the expected density at normal pressure and room temperature. Secondly, to access the diffusion of radon in liquids, we have simulated the diffusion of one radon in each liquid and we have derived from the MSD, the diffusion coefficients. The third set of simulations are the ones settled for measuring radon solubility. We start with the equilibrated liquid droplet and surrounds it by 159 radon atoms. These simulations are also done within the NPT ensemble and thus the periodic cell varies in size accordingly whenever a radon atom enters inside the liquid or goes out from the liquid. VMD snapshots of an equilibrated configuration of radon surrounding capric and water + 5% NaCl solution are displayed in Fig. 85. It indicates some radon (silver spheres) which are inside the capric liquid volume (see Fig. 85 (a)), while they show a high tendency to surround the surface of the alkaline solution (see Fig. 85 (b)).

Table 8: Periodic box sizes of the different systems simulated and respective contained number of molecules.

Simulation Types	Systems	L_X (nm)	L_Y (nm)	L_Z (nm)	N
Bulk	Water Q_+	6.56	6.56	6.56	9999
	Water Q_0	6.69	6.69	6.69	9999
	Water Q_-	7.03	7.03	7.03	9999
	Water + 5% NaCl	6.77	6.77	6.77	9999 of water and 550 NaCl
	Water + 1.9% CaCl	6.91	6.91	6.91	9999 of water and 550 NaCl
	C_6H_{14}	9.18	9.18	9.18	3479
	$C_4H_8O_2$	7.88	7.88	7.88	3375
	$C_{10}H_{20}O_2$	7.03	7.03	7.03	1125
	Rn	73.16	73.16	73.16	9702

9.2 Results

The density of each liquid simulated is added in Table. 9. Water-like liquid systems are in general denser than liquid hexane and also than fatty acids, except capric acid which consists of large molecules (see 9). Water molecules which are highly polarized, are strongly attracted to each other by electrostatic interactions, whereas hexane and fatty acids molecules stick together mainly by the VdW interaction which are weak interaction in comparison to electrostatic forces. Obviously, the liquid density of the water Q_- is reduced in contrast to the one of water Q_+ which increases in comparison to the water density of the standard SPC/E water model (Q_0). As for the alkaline solutions, the concentration of the added salt in water is chosen as small as possible to approach the physiological value but large enough to provide a MD-sensible salt concentration in the liquid. Ca is almost 2 times bigger than Na and its oxidation state is +2e so for each Ca ion, 2 Cl ions of (-1e) are added. The number of Na and Cl ions in the Na-solution are $550 \cdot 2 = 1100$, and the number of Ca and Cl ions in the Ca-solution are $190 \cdot 3 = 570$ but as Ca is two times bigger as Na, the mass of this proportion of calcium salt should be comparable to the proportion of NaCl. One atom of radon is allowed to diffuse in each liquid droplet. Then the diffusion

	R_{NN}	D
	(nm)	($g \cdot cm^{-3}$)
Water Q_+	0.298	1.058
Water Q_0	0.310	0.995
Water Q_-	0.352	0.852
C_6H_{14}	0.446	0.662
$C_4H_8O_2$	0.451	1.014
$C_{10}H_{20}O_2$	0.463	0.921
Rn	0.453	$9.36 \cdot 10^{-3}$

Table 9: Nearest neighbor distance (R_{NN}) between water, hexane, butyric and capric acid molecules. The radius of radon is added for comparison. The density (D) of the liquid simulated compared with the density of the radon gas. The simulations have been performed at normal pressure p = 1 bar and room temperature T = 298 K.

coefficient of the radon inside each liquids and compare to the diffusion at ambient air and atmospheric pressure. Fig. 84 shows the MSD of a radon atom inside each liquid, or of radon bulk. Not surprisingly, radon diffuses fastest in the gas phase, and it is faster in less polarized systems (hexane, liquid water Q_-) than in highly polarized systems (water Q_0, water Q_+). Although hexane is less polar than water Q_-, the

diffusion coefficient in both liquids are of the same order of magnitude (see Table 10), since a hexane molecule is ≈ 4 times bigger and the motion of radon might be affected by the slower motion of hexane molecules. The diffusion coefficients of radon gas phase or radon in water agree qualitatively well with the literature values recorded. [270] The ballistic regime (illustrated by the red line in Fig. 84) is only observed in water Q_+ because the dynamic of radon is slow in this liquid, shorter integration timesteps would be necessary to record the ballistic regime in other liquids.

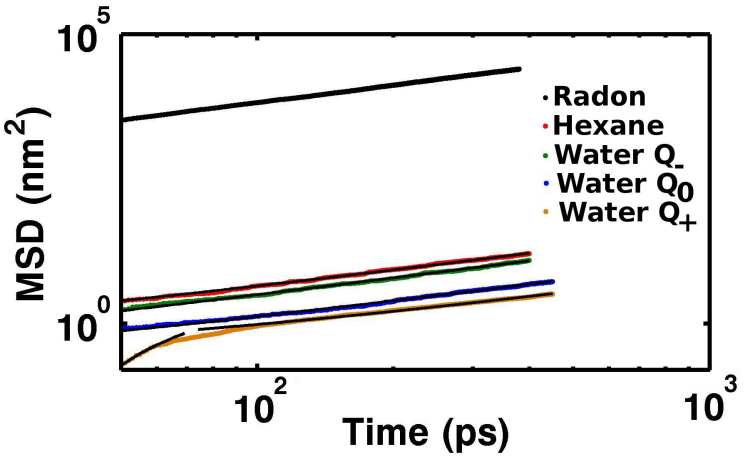

Figure 84: MSD of one radon atom diffusing in different liquid droplets. The MSD of the bulk systems of radon simulated at atmospheric pressure (p = 1 bar) is also displayed.

System/Quantities	Diffusion	Diffusion
	(nm^2/ps)	(nm^2/ps)
	This study	literature [270]
water Q_+	$1.3 \cdot 10^{-3}$	
water Q_0	$1.7 \cdot 10^{-3}$	$1.4 \cdot 10^{-3}$
water Q_-	$5 \cdot 10^{-3}$	
hexane	$6.7 \cdot 10^{-3}$	n.a.
radon	$1.41 \cdot 10^{-3}$	11.03

Table 10: The diffusion coefficients of radon in the different systems are added. No literature have been found for the diffusion of radon in hexane.

From the third group of simulations, we have evaluated the solubility (S). It is deduced from the relation

$$S = C/\mathrm{D_{Rn}}\,, \tag{66}$$

where C is the concentration of radon in the liquid and $\mathrm{D_{Rn}}$ is the radon density $\mathrm{D_{Rn}}$ in the surrounding gas, which was chosen in MD simulations as a pure radon gas at room temperature and normal pressure.s. The solubility data are added in Table. 11 while the densities have been previously presented in Table. 9.

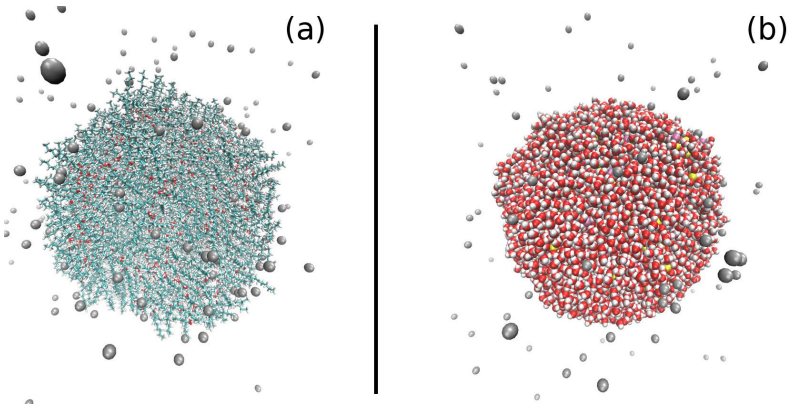

Figure 85: VMD snapshot of the equilibrated configurations obtained when investigating radon accumulation in liquids. Radon gas are surrounding the liquid droplet, the density of the surrounding gas is its one at atmospheric pressure (bulk density notified in Table. 9). (a) shows the capric liquid and (b) is water + 5% NaCl, the Na and Cl ions are marked respectively with yellow and mauve spheres. The silver spheres are representing radon atoms.

Liquid	C $(g.cm^{-3})$	$S = C/\mathrm{D_{Rn}}$
Water Q+	≈ 0	≈ 0
Water Q0	$6.45 \cdot 10^{-4}$	0.07
Water Q-	$2.09 \cdot 10^{-3}$	0.22
Water + 5% NaCl	$1.37 \cdot 10^{-3}$	0.14
Water + 1.9% CaCl	$1.46 \cdot 10^{-3}$	0.15
C_6H_{14}	$1.33 \cdot 10^{-2}$	1.42
$C_4H_8O_2$	$2.16 \cdot 10^{-2}$	2.3
$C_{10}H_{20}O_2$	$2.26 \cdot 10^{-2}$	2.4

Table 11: Radon concentration C and solubility $S = C/\mathrm{D_{Rn}}$ in different liquids. $\mathrm{D_{Rn}}$=9.73 $\cdot 10^{-3}$ g·cm^{-3} is the density of radon at ambient air (normal pressure and room temperature). Water Q_+ (Q_-) is liquid water with molecules which are highly (weakly) polarized compared to the normal liquid water Q_0. Isotonic solutions of water with respectively 5% of NaCl and 1.9 % $CaCl_2$ solvated are also used. As for fat, hexane (C_6H_{14}), butyric acid ($C_4H_8O_2$) and also capric acid $C_{10}H_{20}O_2$ are used.

The derived results for radon solubility are displayed in table 11. They are in good agreement with each other for all the fatty acids, with solubility values around 2 and they match well the experimental results. [135] These values are also comparable to the values reported by Nussbaum and Hursh, [133] and no influence of the chain length of the fatty acids could be observed. In water, solubility is lower by a factor of the order of 20 compared to data in fatty acids. For the Q_+ water, the concentration of solved radon is almost not detectable in the simulations because radon are hardly going into this liquid. Overall, the results confirm that radon solubility differs vastly between polar and non-polar liquids.
We next explore how this solubility difference can be understood from the interaction of radon with the respective liquids. Since radon is a large atom, its presence should distort the structure of the surrounding solvent molecules. Fig. 86(a) shows the radial distributions functions of the different solvents in the absence of radon. The first peak of each curve gives the nearest-neighbor distance of each liquid. This distance is much more smaller for water than for fat (which has larger molecules), and it further

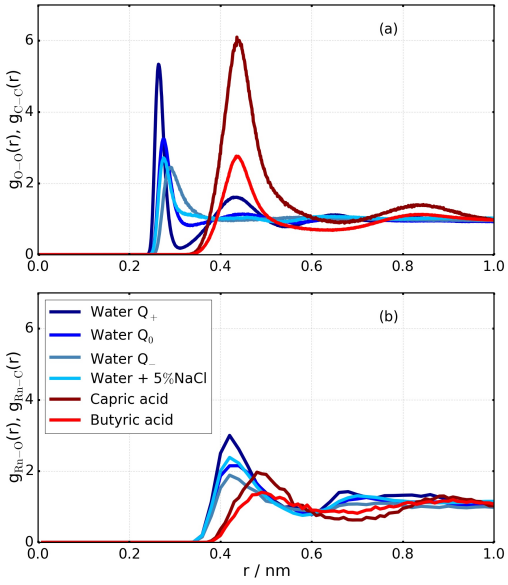

Figure 86: (a) Radial distribution function of the different types of water used in the simulations (based on the location of the oxygen atoms) and of the fatty acids (based on the location of the first carbon atom namely the carbon of the -COOH group). (b) Radial distribution function of the different solvent molecules around a solved radon atom, based again on the oxygen resp. carbon atoms.

decreases with increasing polarity, i.e., with increasing attractive interaction.
Fig. 86 (b) shows the radial distribution function of solvent molecules around radon atoms. The distance to the nearest solvent atom is $\approx 0.4\,\mathrm{nm}$, which is comparable to the radius of a radon atom. It is nearly similar to the distance between fatty acid molecules and considerably smaller than the distance between water molecules. This reveals that the local structure of water is much more disrupted by the presence of a radon atom than the structure of fatty acids. That means a solved radon atom in liquid water breaks more bonds between water molecules than bonds between fat molecules, and additionally the energy cost associated with breaking a bond is considerably larger in water than in fat since the energy of hydrogen bonds is larger by one order of magnitude than the energy of the VdW interactions. Introducing radon in water necessitates a high cost of free energy, leading to a low solubility. And as expected, the amount of radon solved in water increases when the energy of the hydrogen bonds is reduced (Q_ water) or when the tetrahedral short range order of water is decreased by dissolving salt in water (see the solubility data in Table. 11).
Oppositely to water, hydrocarbon aggregates provide free volume in which radon can enter without distorting the molecular structure. We have pictured this mechanism by the snapshot in Fig. 87 showing how radon disrupt the local structure of water but sits in the interstitial sites provided by hydrocarbon agglomerates.

Moreover, radon accumulates a bit more in fatty acids than in linear oily chains. This can be rationalized by the fact that fatty acids contain more large atoms (C and O), and that they further possess a heterogeneous structure with aliphatic groups that can form hydrogen bonds.

9.3 Summary

We have investigated the accumulation of radon in water-like liquids differing by the molecular polarity, in salt solutions and in fatty liquids. This has allowed us to test the hypothesis that radon concentrates

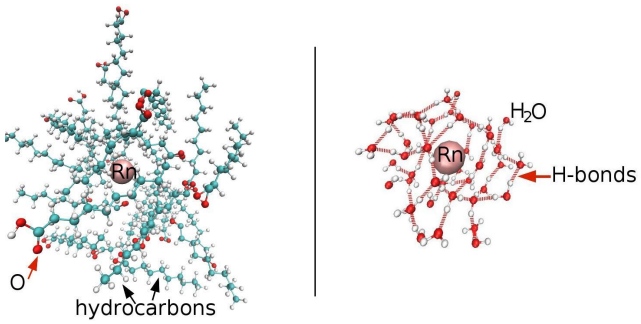

Figure 87: VMD snapshot of a radon atom surrounded by capric acid molecules (a) and water molecules (b). Interstices are noticeable in the structure of capric acid due to the hydrocarbons packing, and radon can easily find a vacant site to sit in. The opposite happens for the tetrahedral network of water providing no vacant site and therefore, some H-bond should be break in order to accommodate for radon.

easily in non-polar liquids compared to polar liquids such the polarization has a crucial role in the accumulation process. We have found that the radon solubility is at least 20 times larger in fatty acids in comparison to the solubility in water or salt solutions. Our recorded data for fatty acids are in the same order of magnitude as experimental results and also as previously reported results by Nussbaum and Hursh. [133] The recorded data in water are 3 times higher in simulations as compared to experimental data. This difference should originate from the fact that the radon solubility is strongly sensitive on the water polarization such that the solubility data in water Q_+ avoisinates 0. Hence, it can be said that the difference between simulation and experiment is related to the fact that water molecules used in simulations have fixed partial charges that cannot sensitively respond to different types of interaction partners. In future studies, the experimental and theoretical methods presented in this paper will be extended to more tissues, enabling to estimate the radon distribution in various organs. From these studies the respective dose and hence the risk and therapeutic effects of radon exposure will be determined more precisely.

10 Summary

The aim of this thesis was on the understanding of the structure and dynamics of network forming liquids in confinements based on two types of confinements: non-neutral and neutral confinements. Non-neutral confinements are the ones in which the confined liquid component is different as the elementary particle of the confining matrix and then the matrix-liquid and the liquid-liquid interaction are distinct giving rise to competitive contributions to the preferred position of liquid atoms in the wall vicinity. Consequently the structure of the confined liquid is substantially distorted. One example is liquid water in silica pores offering hydrophilic surfaces to which water can bind. Oppositely, neutral confinements are of the same nature as the confined moving liquid and therefore offer the possibility to scrutinize the slowing down process near immobile wall without the hampered effect caused by surface interactions. One example is liquid silica confined in a silica immobile matrix.

The first part of the work was devoted on inspecting the behavior of water in silica confinements. Our simulations of water in partially filled silica pores have revealed that the GT silica model describes qualitatively well the wetting mechanism of water in silica pores as reported by formers experimental works. [11, 17] As in experiment, the filling procedure of a pore starts with putting a water droplet on the top surface of the pore and enabling it to flow and enters towards the pore. For this reason, in this MD study several starting configurations are tested in the case of partially filled pores. Based on the evaluation of the radial and angular profiles, the H-bond profile, the distribution of the tetrahedral-order of the network structure of water molecules in the pore vicinity, we show that the GT [42] silica surface is more hydrophilic than the conventional and generally used BZ [40] model. Even at very low pore filling ratio, the pore surface described with the GT model is always adequately wetted by water molecules and we have proposed that approximately 1 and a half layer of water fully covered the pore surface (of 2 nm radius). In contrast, the often used BZ model leads to a partial coverage of the pore surface. And in the particular case of pores with moderate filling percentage, water can undertake different equilibrated configurations which sometimes slightly depend on the starting configurations. These configurations are plausible states arising from the surface energy minimization process of the wetting water droplet on silica surface presented in a theoretical approach based on the work of Ref. 180.
We have also performed several other simulations of water on top of silica slabs with varying thicknesses. Again, we find a contact angle nearly equal 25° with the BZ model which is larger than the close to 0 contact angle found with the GT model consistent with previous experimental reports. [44, 45] We have furthermore show that the contact angle decreases with slab thickness and reaches a limit when the thickness avoisinates 2.5 nm which is very close to 3 nm reported by Goodman in Ref. 43. We conclude that the minimum thickness required to completely capture the wetting properties of water on silica surface amounts 2.5-3 nm.
What could be interesting in future works is in the case of moderate filling ratio, to simulate a reservoir out of which water can move to fill the pore. It is certainly computationally costly but it is worthwhile since in this way, the filling procedure of the pore is more alike to experimental conditions and the starting configurations of water in pore will be spontaneous instead of the pre-defined initial configurations of our work.

We have next investigated the structure of water/octanol mixtures in silica confinements. We have used the GT silica model since our previous investigation has certified that the wetting of water are properly well depicted with this surface. We find out that the hydroxyl groups of octanol and water stay near the pore surface through hydrogen bonds with silica sites. These results have been confirmed by NMR studies of the group of *Prof Buntkowsky* at the TU Darmstadt which have analyzed in addition to linear octanol, branched octanol; and they show evidence of the presence of hydroxyl groups of octanol near the pore surface. Interestingly, NMR studies have shown that the orientation of the hydroxyl groups near the surface tend to not depend on the ratio between water and octanol molecules. This has been

approved by MD calculation of electrostatic energy between surface atoms and water, contrasting with the energy between octanol and surface atoms.
Oppositely, the effect of water content considerably affects the formation of hydrogen bondings between octanol-octanol and octanol-silica, as the number of H-bonds shared is essentially reduced when water is added. This is intuitive as with increasing water content, water molecules come with free H-bond sites than can connect to silica or octanol. Consequently, some silica sites and octanol sites form hydrogen bondings with water instead of octanol. Interestingly, for a given mixing ratio, the density of water oxygens near the pore wall is at least 1.4 times larger than the density of octanol oxygens. This effect can be explained when thinking that the large size of octanol somewhat limits the amount of hydroxyl groups which can point towards the pore wall contrasting with the small size of water molecules which enable water molecules to easily sit near free silica sites present in the pore surface. And thus, water molecules accumulate more near the pore wall vicinity when water is added. This observation can also be rationalized when thinking about the fact that water molecules attached to the wall are slow down due to the fixed potential energy landscape imposed by the immobile wall. This fixed energy landscape affects also the motions of octanol in the pore wall vicinity. But as octanol are longer compared to water, their slow mobility near the wall impose another restriction to the mobility of water. For this reason, water molecules approaching the wall are stacked there due to the combined effect of the fixed wall and slow mobility of octanol molecules.
Furthermore, the accretion of water molecules near the pore surface leaves some vacant sites in the pore center in which some carbons of the hydrocarbon tail can sit in. As a consequence, octanol density profile shifts a bit near the pore center when the water/octanol ratio is increased. In the special case for which the pore size is roughly 2 times larger than the length of a octanol molecule, MD studies have shown that, in addition to the hydroxyl groups of octanol and water present in the pore surface, other hydroxyl groups of both liquids can be identified in the pore center region, meanwhile the hydrocarbon chains are located in the range between surface and center. A bilayer-like structure is then observed, it vanishes with larger pore size and is replaced by a bulk-like structure at the pore center.
Within this study, we can conclude that we get a behavior similar to a micro-phase separation in which water molecules aggregate more near the pore surface to the detriment of octanol molecules which concentrate less in the vicinity of the pore surface when water is added. We preferably refer that as a micro-scale segregation rather than a micro-phase separation because we do not have a well defined water phase near the pore wall separated to an octanol phase out of the pore surface since hydroxyl groups of octanol are still significantly present in the pore wall vicinity and also a small amount of water molecules is visible in the pore center and intermediate region.
What is still remaining from this examination is the temperature dependent dynamical response of octanol and water in pore. It can bring more insights about the temperature effect on the orientation of the hydroxyl groups of both liquids type near the silica surface. Moreover a simulation of branched octanol in the 2 nm pore might be instructive to check whether the bilayer-like formation observed with linear octanol can as well form. Last, we have shown that increasing the pore size not only distort the bilayer-like formation observed at the 2 nm pore radius but also increases the density of water near the pore wall. The density peak of water oxygens in the pore wall vicinity varies (with pore size) from about 1.5 to 2 times larger than the one of octanol oxygens in the pore wall vicinity. This result rises the question of possible structure of water/octanol mixture in a pore of radius 1 nm which would be comparable to the length of an octanol chain, as well as the associated dynamics.

The succeeding chapter is devoted on investigating silica-like liquid in bulk and in neutral confinements. We present a comprehensive survey of structural and dynamical properties of silica-like liquids differing to each other through the partial charges q attached to silicon and oxygen atoms; explicitly the relative contribution of the Coulomb and the Van der Waals interactions between atoms pairs. It comes out that the density of these silica systems grows with increasing bond polarity since the stronger electrostatic attraction between silicon and oxygen atoms even push them closer to each other. Similarly, the tem-

perature of the density maximum, T_{max}, enlarges since the more ordered low-density structure is still visible over certain higher temperatures for stronger attractive interactions. One interesting point is that the distribution of the tetrahedral order parameter displays the same bimodal curve for all studied partial charges at T_{max} suggesting the existence of two different types of local neighborhoods in the liquid differing by the degree of local order. An evaluation of the partial pair distribution functions reveals that these two local structures can also be discriminated based on the spatial arrangement of neighbors between the first and second neighbor shells, namely trough the preferred distance of the fifth and six neighbors. These preferred positions are lying at shorter and larger distances in the high-temperature and low-temperature structures, respectively, and as a consequence the average local density reduces and the average tetrahedral order increases upon cooling. Similar observations have been reported for water with varied partial charges, [101] showing that the density maximum appearing in water is intrinsically connected to the removal of interstitial molecules between the first and second neighbor shell upon cooling. This again asserts that water and silica are intimately related.
Along with the vanishing of maximum density with lowering bond polarity, the dynamical fragile-to-strong transition also vanishes for some silica systems of smaller partial charges (roughly 75% smaller than the standard value). An intriguing aspect is that the distribution of the tetrahedral order parameter is similar around the temperature T_{FS} at which this dynamical transition appears. It shows a peak at large $Q_i \approx 0.75$ and a shoulder at small $Q_i \approx 0.55$. This again confirms that going towards the strong regime in the low temperature regime, the amount of locally highly ordered domains in silica enlarges. This as well goes in accordance with the observation obtained from the pair distribution function of the fifth neighbor at T_{FS} that the number of atoms located at the fifth interstitial positions is constant at this temperature, and reduces when the temperature is lowered leading to low density domains which are highly ordered.
We have thus added evidence that the fragile-to-strong transition of silica mainly originates from modifications of the local particle arrangements in the first and second neighbor shells with reducing temperature. This relation between structural and dynamical changes in silica have inspired *Poole et al.* [83, 84] to propose that the fragile-to-strong crossover should be correlated to a possible liquid-liquid critical point in silica systems. Although, the existence of such critical point in silica is still questioned. [221, 220, 222] Our data does not display an indication for a critical point of the BKS model and its studied variants and could be due to the fact that our study have been performed at ambient pressure, while *Lascaris et al.* [89] have shown a critical point at $\approx$ 0.1-1 GPa. However, several authors suggest that at ambient pressure the fragile-to-strong transition could be related with a crossing of the Widom line, [84, 220] which is the extrapolation of the phase transition line into a regime displaying no phase transition. From our work, it comes out that the density anomalies could be associated with a Widom line in the studied silica models, however this seems to not be significant for the FS transition because the liquid then presents a high degree of order at the FS transition. Instead, at the Widom line, one would expect not only equal weights but also roughly equally distributed local ordering of the high- and low-density liquids, and this occurs at a temperature considerably larger than that of the FS transition. We propose that both phenomena, the dynamical FS transition and the structural transition between high and low density, are both massively correlated with the occurrence of strong directed bonds, but the physical parameter at which these two transitions happen, are not necessarily identical.
What can be interesting for future works is to access thermodynamical properties of BKS silica variants such as heat capacity, thermal compressibility as well as isochores of the PT diagram. For silica variants in which a maximum in the heat capacity is detectable, one can confront it to the fragile-to-strong temperature. We can as well compare the temperature of heat capacity maximum with the temperature at which the isochores (if existent) will cross. This would reveal more indications about the possible existence of a LLPT in BKS silica variants and in particular how it is modified by bond polarity.

Finally, we address the question of BKS silica variants in neutral confinements, in order to test whether one can see a trend in the possible growing mechanism of correlated clusters. In particular, whether the

typical size of the correlated regions show a peculiar behavior at the FS dynamical transition which is often associated with the MCT dynamical transition. [96, 97, 216, 110, 104, 78, 233, 79] To clarify this issue, 3 different length scales have been defined. There are: the dynamical length scale derived from the position resolved ISF, the structural length scale defined from the position resolved overlap functions and the elastic length scale extracted from the position resolved of the inverse MSD at one 1 ps ($1/u^2$). We have as well applied two types of analysis differing by the manner in which atoms position in pore are defined. One can use as reference the pore center and then label each atom by its radial position R. Or one can either search the nearest wall atom corresponding to each mobile atom in the pore center and then assign its position with respect of the found closest wall atom. The former analysis has been referred as the R-resolved analysis and the latter the d-resolved analysis.
We have a found a linear increase of length scale with inverse temperature which is in accordance with previous reports. [173, 112, 177] In general, our analysis has been affected by the varying contributions of short time vibrational motions with temperature as well as with the distance resolved quantities. What is new is that we have solved this issue (at least at low temperature) by probing the elastic length scale at which the monotonically linear growth is as well observed. Given the fact that, the temperature range covered varies with charges q, it is insightful to compare length scales and relaxation times for the different systems. Interestingly, a almost linear relation between length scales and bulk relaxation times is seen, with slope reducing with charges. Especially for the systems corresponding to the high q's, the slope diminishes in the low-temperature range, which can be a fingerprint of strong dynamics.
An alternative approach to address the question is to compare squared-length scales and activation barriers as defined in the *Rössler* relations. Here, we use no fit parameters and we define the collective energy by calculating it using its relation with relaxation times, temperature and bulk high-temperature activation energies. The obtained ratio of squared-length scale with cooperative energy of low charges indicate that collective energy barrier increases faster upon cooling as compared to the increase of length scales upon cooling. In contrast, for the high partial charges, the ratio is almost constant revealing that both quantities have a analogous variation with temperature. We therefore use these results together with the previous observations to conjecture that length scales characterizing strong dynamics increase much more slower upon cooling than typical length scales describing fragile dynamics.
These trends are thus crucial as they imply that the length scales studied are not related to activation energy barriers in a trivial way. Since one would have expected a temperature independent length scale in the low temperature strong dynamics characterized by a constant activation barrier. Nevertheless, each length scale here studied presents a drawback. First, the dynamical length scale extraction is strongly affected by the different contribution observed when varying the temperature and/or the particle position on the vibrational motions amplitude which hinders a precise extraction of relaxation times. Secondly, the elastic length scale is connected by the definition of the onset MSD between vibrational and cage regime and the timescale which should be considered since it varies with temperature and also between the different silica systems. Thirdly, the structural length scale definition suffers from the massive oscillations observed in the distance profile of the long time limit of the OF hampering an accurate fit with the simple relation proposed to extract the length scale. This can be improved by an explicit modification of the relation to account for local structure of mobile atoms near the pore surface. Looking at overlapping of the bond orientational order deduced from the spherical harmonics between atoms involved in a bond formation recently introduced by *Shi* & *Tanaka* in Ref. [271] might be acute in determining the length scale which will measure bonds correlation upon approaching the pore wall.
Our data do not display a decoupling between structural and dynamical length scale in the nearby of the MCT critical temperature $T_C \sim T_{FS}$. Results which contradict former studies on a disordered spin model [272] and a HS mixture. [111] We have also shown that the γ-exponent of structural length scale in RFOT theory tends to not be a universal constant for silica variants but instead varies between 1 to 2.2. Again this might be related to the previous limits noticed in the structural length scale determination prohibiting to make a general statement. Furthermore, the ECNLE theory applied to the elastic length scale does not perform well at low temperatures.

In addition to the major topics presented, we have also shortly investigated the accumulation process of radon in non-polar solvents and compare with the accumulation in water-like liquids. To create water variants, we have rescaled the partial charges of the original SPC/E water. In this way, we could check the effect of the solvent polarity on the accumulation of radon. Salt solutions have been used to depict the ambient solution of biological cells. Fatty acids have also been used to picture fatty cells found in human body. We found out that radon accumulates more in fatty acids with a solubility comparable to experimental data. The concentration of radon solved in water increments when the energy of the hydrogen bonds between water molecules is reduced, as for example in the case of water $Q\_$. It also increments when the local tetrahedral order of water has already been distorted by dissolving salt in water. Oppositely, hydrocarbon aggregates provide vacant sites in which radon can fit without disrupting the molecular structure. Indeed, the energy cost associated with breaking a bond is larger by one order of magnitude in water (or in polar solvents) than in fat. Therefore, introducing radon in polar solvents leads to a huge cost of free energy, and consequently to a low solubility.

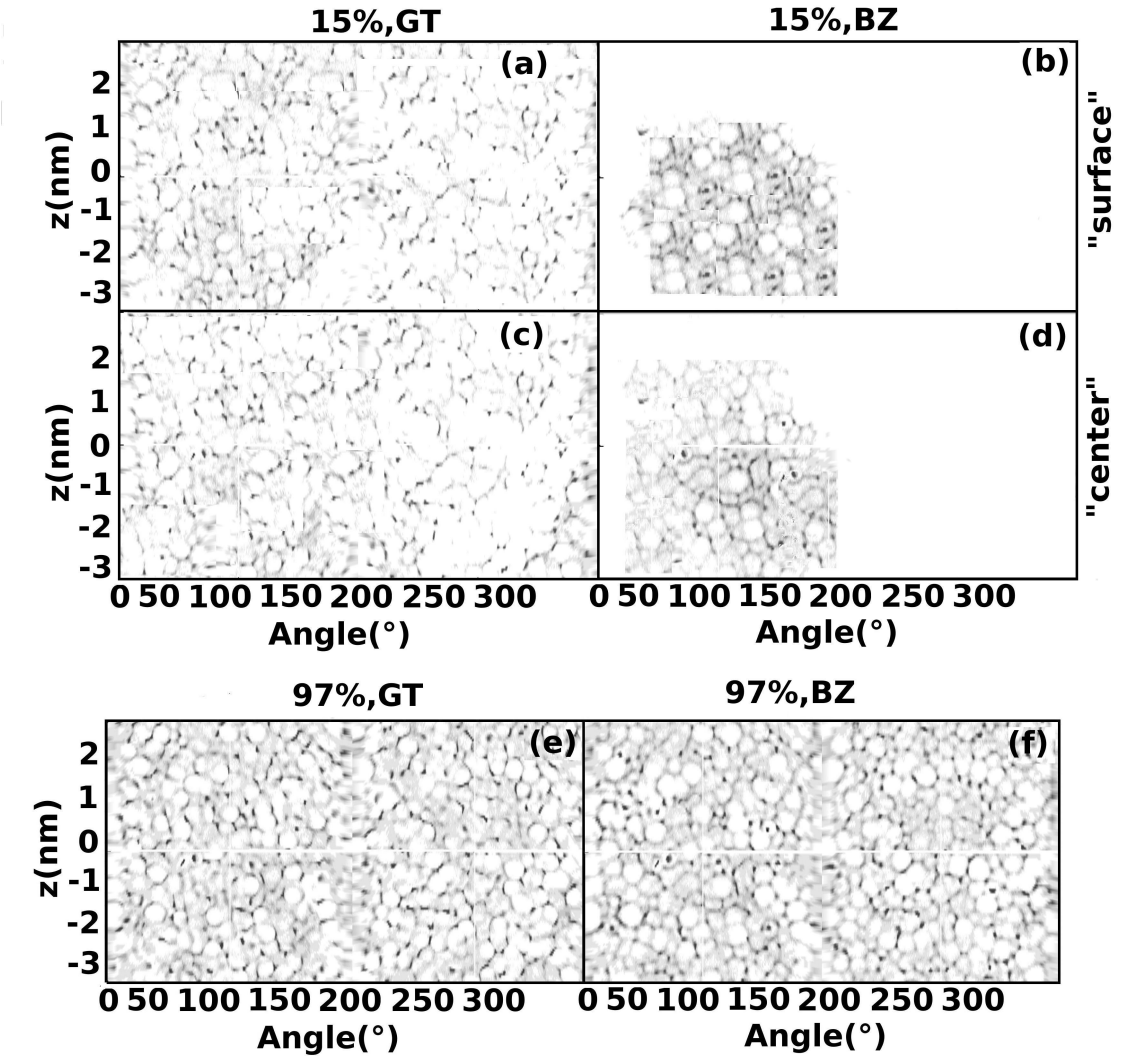

Figure 88: The water density at the pore surface for 15 % (a-d) and 97 % (e-f) filling ratio, showing water molecules that are within a distance of 0.3 nm of the silica surface, the left graphs show the density on the GT surface and the right graph on the BZ surface. The distribution agrees well with the phase diagram of Chapter. 5 showing that phase 7 is expected for filling ratio lower than 15 %. The GT surface is uniformly covered by water molecules even at this low filling ratio and phase 2 of the phase diagram is observed.

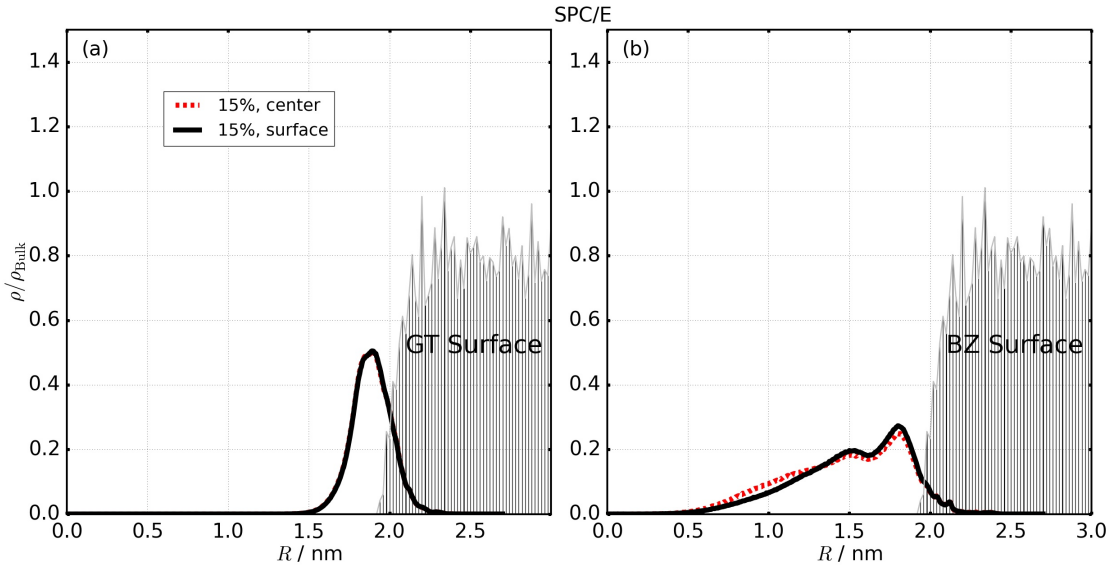

Figure 89: Number density profile of water oxygens in the case of 15 % filling ratio. One sees almost no difference on the end configurations obtained from both starting when the surface is described with the GT model (a), while a slight difference is noticeable near the BZ surface.

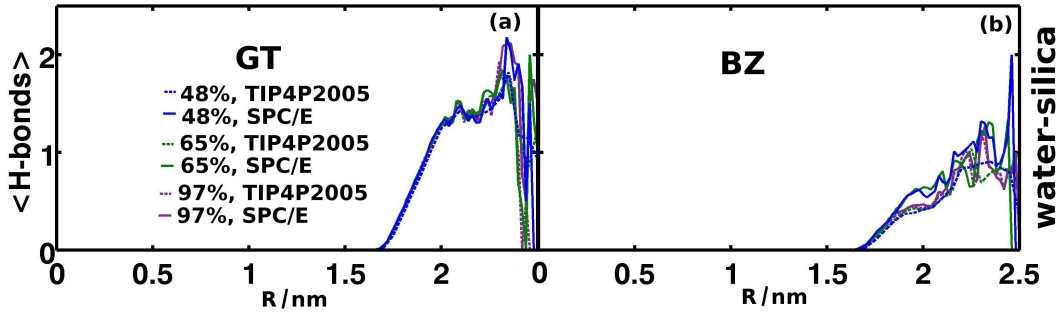

Figure 90: Average number of hydrogen bonds per water molecules for water–silica contacts, for different filling ratios and water models, as indicated in the legends. The results for the GT silica surface are given on the left-hand side (a), and those for the BZ silica surface on the right-hand side (b). There are a little bit more water–silica hydrogen bonds shared with the SPC/E water molecules than with the TIP4P/2005 molecules near the BZ surface. This is expected as TIP4P/2005 water molecules are a bit more strongly bonded to each other than SPC/E water molecules and near the less hydrophilic BZ surface, less water molecules are available for water–silica hydrogen bonds formation. This effect is not seen close to the GT surface and the water–silica hydrogen bonds are always higher close to the GT surface for the two water models than near the BZ surface. Thus, independly of the water model used, the GT model surface provides a strong hydrophilic surface.

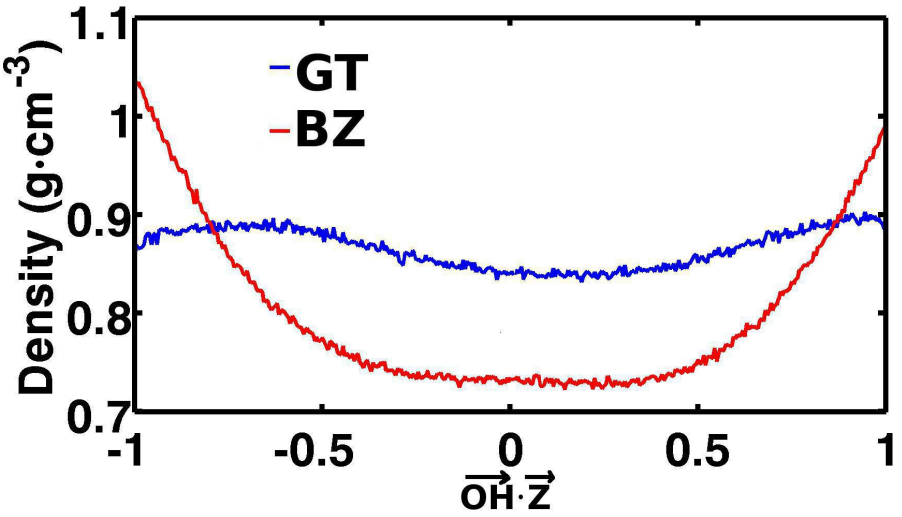

Figure 91: Density distribution of the scalar product between a $\vec{\mathrm{OH}}$ vector of the water molecules and a unit vector of the z-axis. It shows the orientation trend of the $\vec{\mathrm{OH}}$ vector of the water molecules (lying within 0.3 nm of the pore surface) with respect to the pore axis (z-axis). In the BZ model surface, the $\vec{\mathrm{OH}}$ vectors prefer to orient themselves parallel to the z-axis and this preference reduces the number of hydrogen bond donors which can form hydrogen bonds with the oxygen acceptors lying in the silica surface. This preference is not observed near the GT model surface, there is almost no preferential orientation and thus all water molecules have an equal probability to act as hydrogen bond donors or acceptors for the silica hydrogen bond sites.

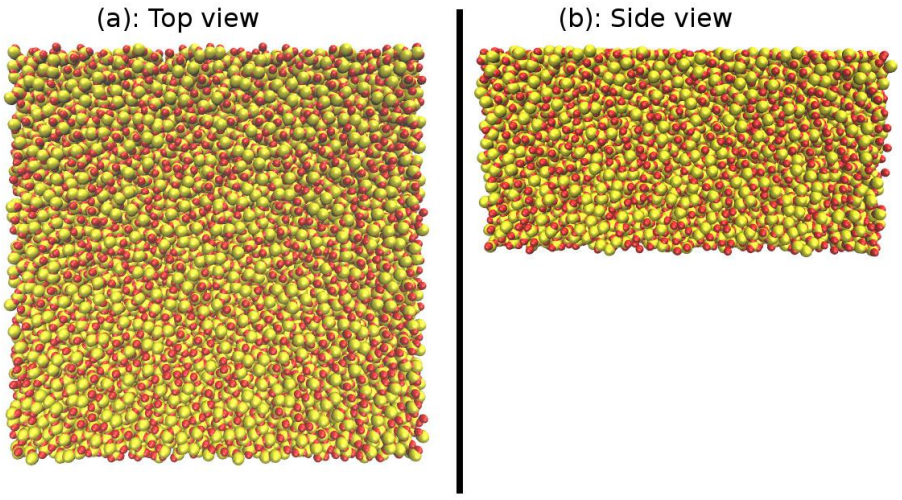

Figure 92: Top (a) and side (b) view of the larger cooled silica block utilized to create larger silica pore. The block is created from duplicating 4 times the equilibrated cooled silica block utilized by Geske and Vogel to propose a method for fabricating realistic silica pore. [230] The box size characteristic is 12.16 nm x 12.16 nm x 6.08 nm. The snapshots are generated using the VMD program. [234]

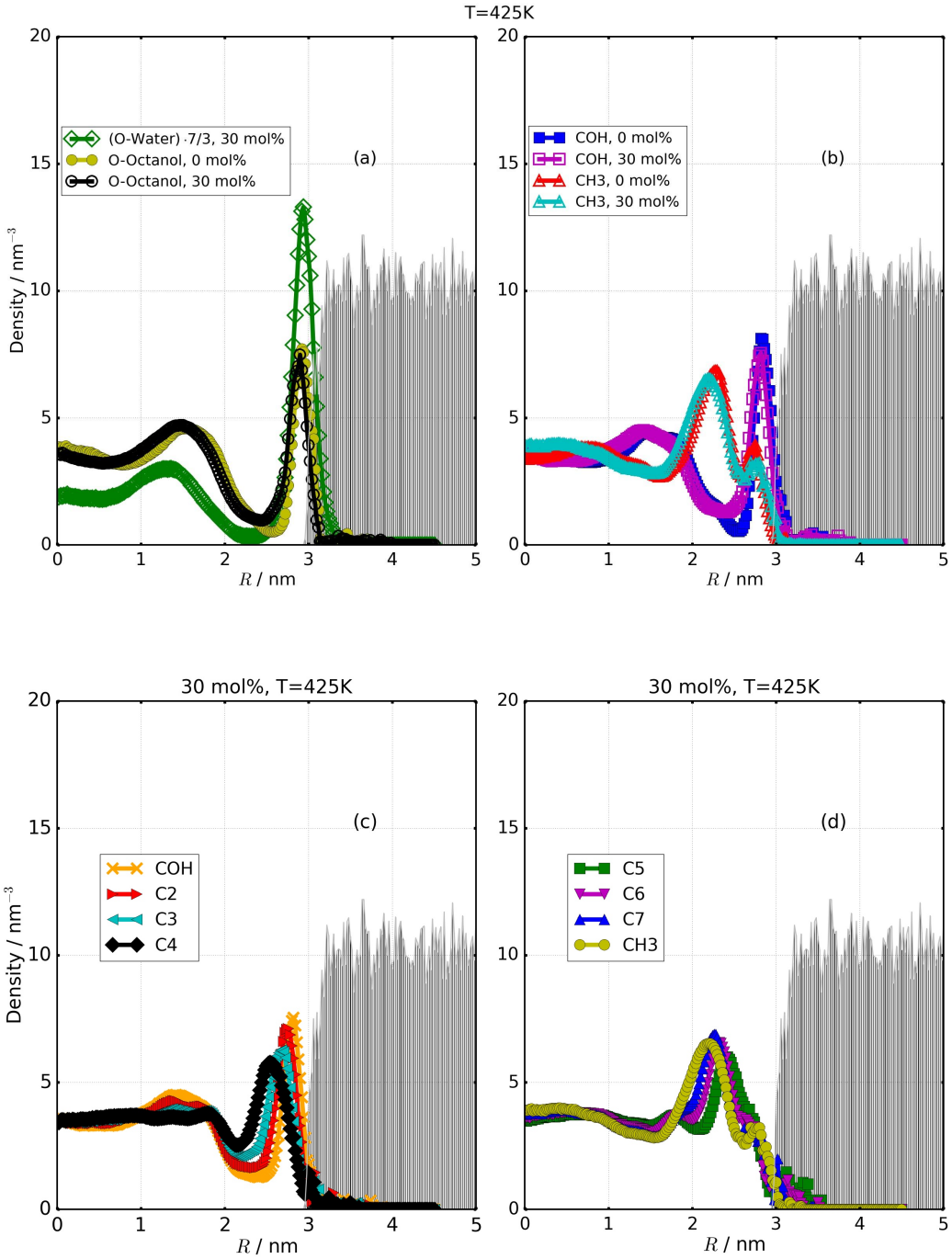

Figure 93: Number density profile of carbons of 1-octanol at T=425 K for the 3 nm pore. The effect of water content (0, 30 mol%) is illustrated in (a)-(b). (a) shows the density profile of water and octanol oxygens, while (b) shows the profile of COH and CH3 carbons. The distribution shows a peak near the pore wall and is flat within the pore. (c) and (d) display the carbons distribution in the case of 30 mol %. CH3,C2-C4 (d) each shows a peak in the intermediate pore region, next to the peak of C5-C7, COH (c) which is localized directly in the pore surface vicinity.

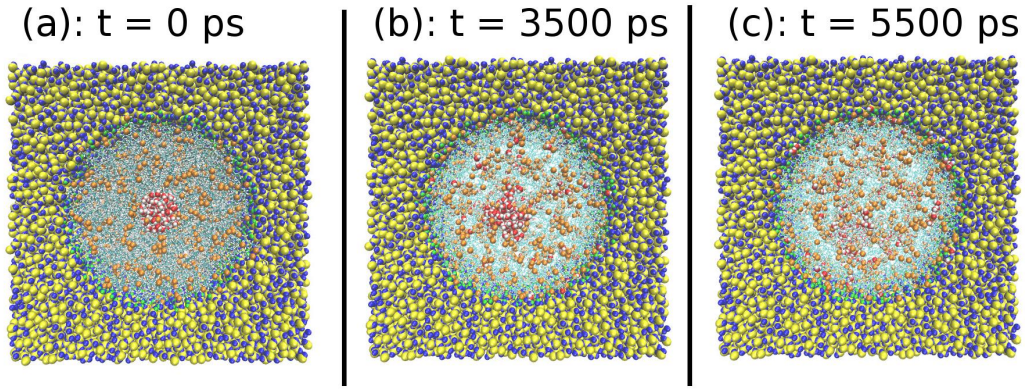

Figure 94: Snapshot showing the top views of the simulation set-ups of a mixture of 30 mol% water and 70 mol% 1-octanol in 8 nm silica pore. (a) Initial configuration of the simulation. (b) Snapshot after 3.5 ns and (c) configurations roughly 5.5 ns. The yellow, blue and green spheres are the silicon, oxygen and hydrogen atoms of the silica pore, respectively. The red and white spheres are oxygen and hydrogen atoms of water molecules. The octanol oxygen atoms are represented as orange spheres. It can be seen that water molecules move from the center to the pore surface. The snapshots are generated using the VMD program. [234]

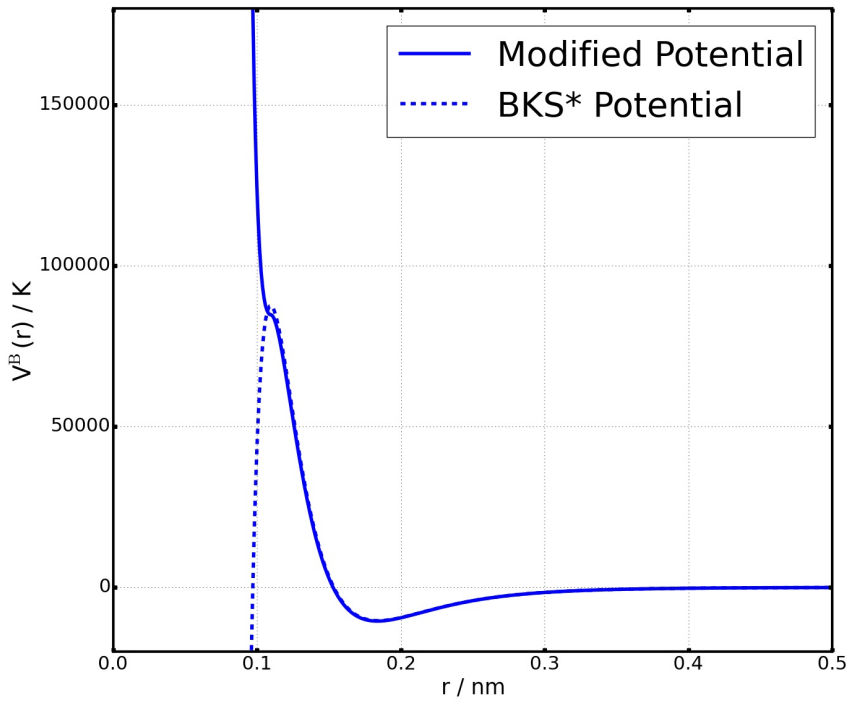

Figure 95: Buckingham part of the BKS potential [105] plotted in dashed lines as compared to the modified potential used in this study plotted in solid lines. The star added in the legend is to notice that only the Buckingham part of the BKS potential is plotted. Here, we illustrate the potential between silicon and oxygen.

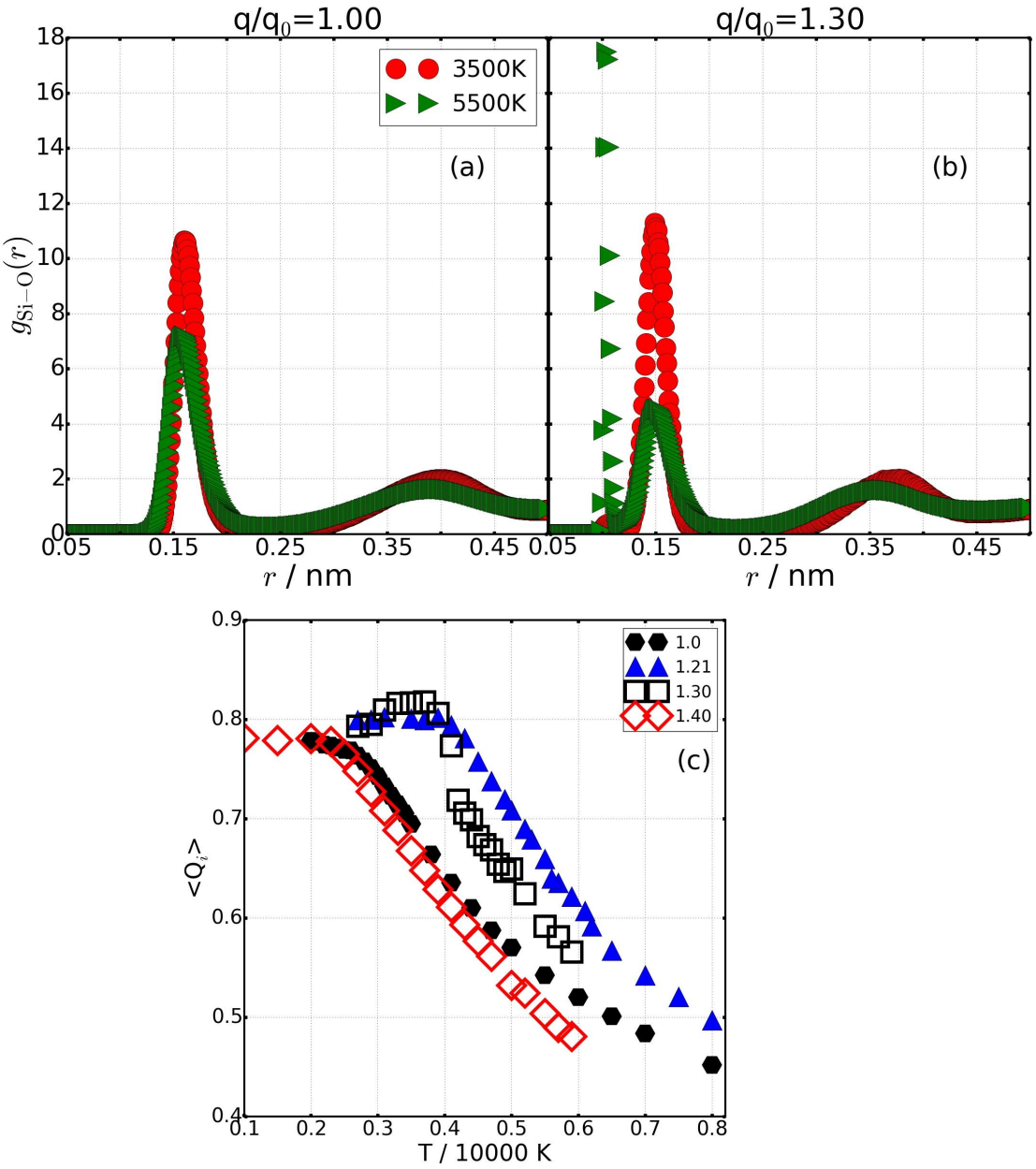

Figure 96: Radial density distribution of oxygen atoms surrounding silicon atoms at 3500 K and 5000 K for two exemplary silica systems q/q_0=1.00 (a) and q/q_0= 1.30 (b). (c) is the average order parameter of silicon atoms, the opened-symbols illustrate the temperature dependence for high scaling factors for which the local order suddenly diminishes.

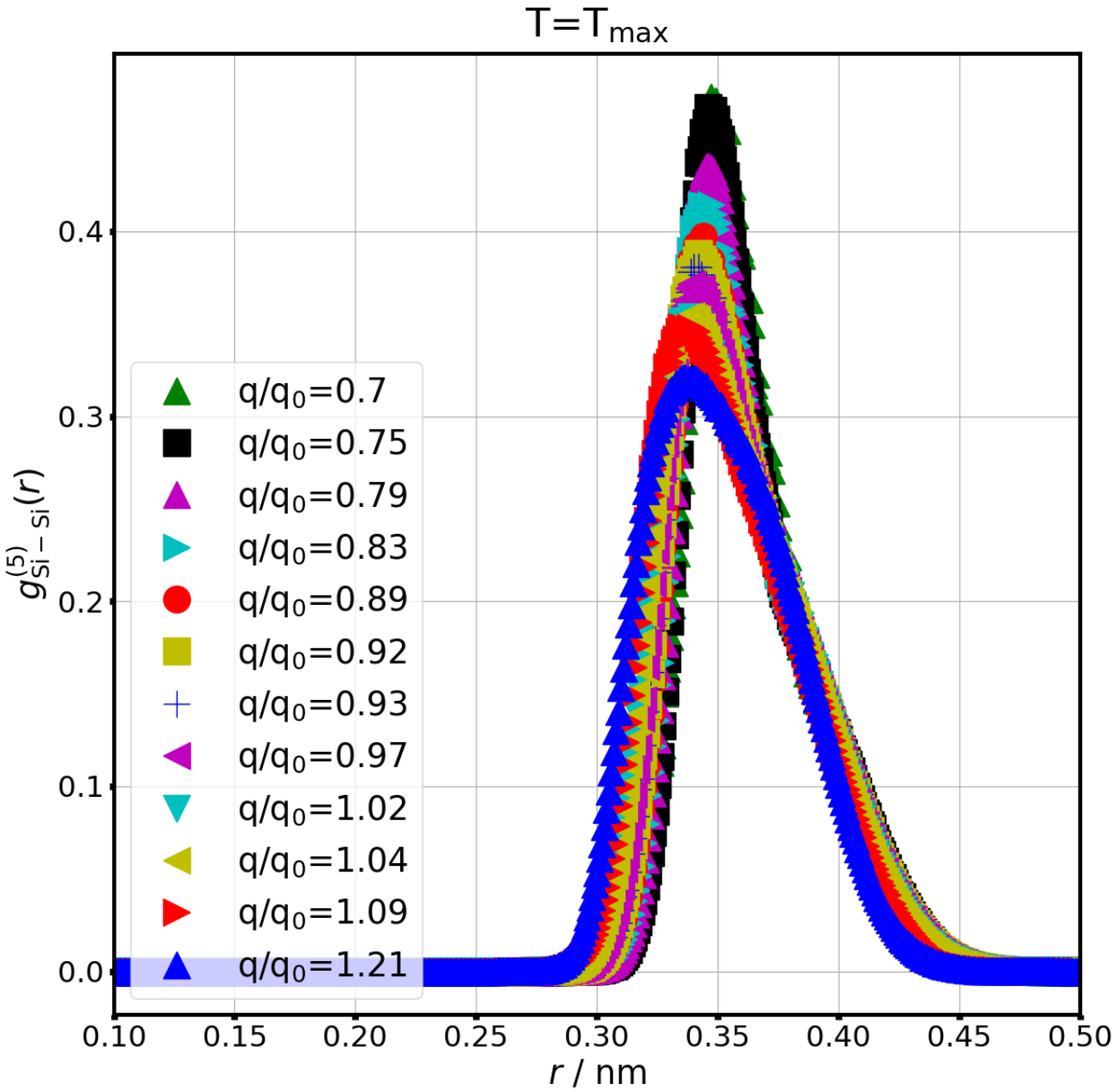

Figure 97: $g^{(5)}(r)$ showing the radial distribution of the 5th nearest atom of any chosen silicon atom, plotted for different systems showing a density maximum. The temperature chosen is the temperature of density maximum. The distribution is unimodal at this specific temperature and becomes bimodal when the temperature is closest to the temprature of fragile-to-strong transition (see Fig. 42 (b)).

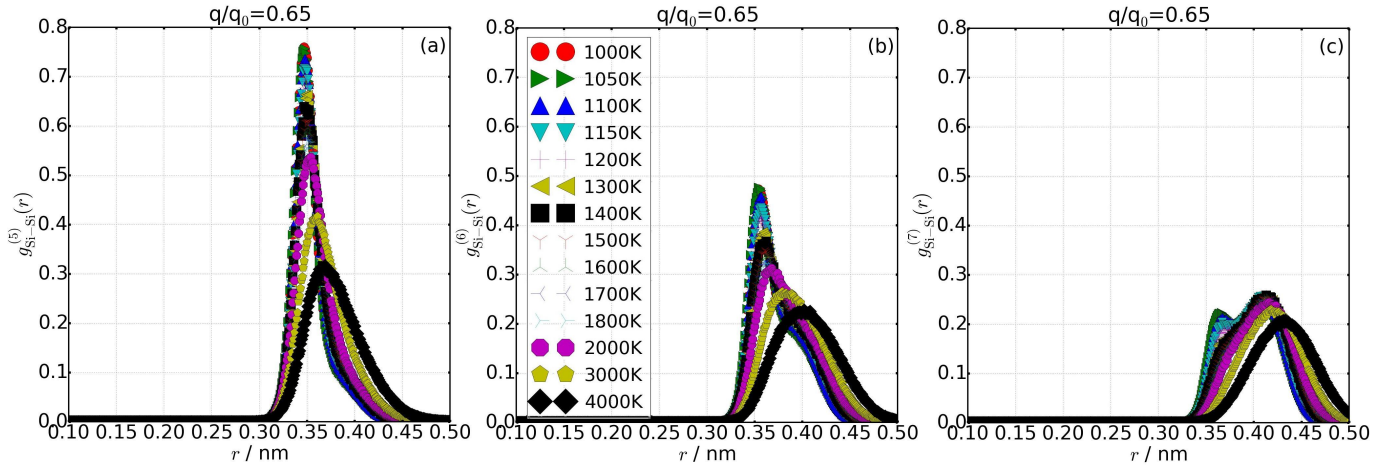

Figure 98: (a) $g^{(5)}$, (b) $g^{(6)}$ and (c) $g^{(7)}$ showing respectively the radial distribution of the 5th, 6th and the 7th nearest atom of any chosen silicon atom, plotted for different temperature for the scaling factor 0.65. This is to show that the system is more frustrated at lower charges such that at low-T the high density domains are still preponderant and the liquid behaves dynamically as a fragile glass.

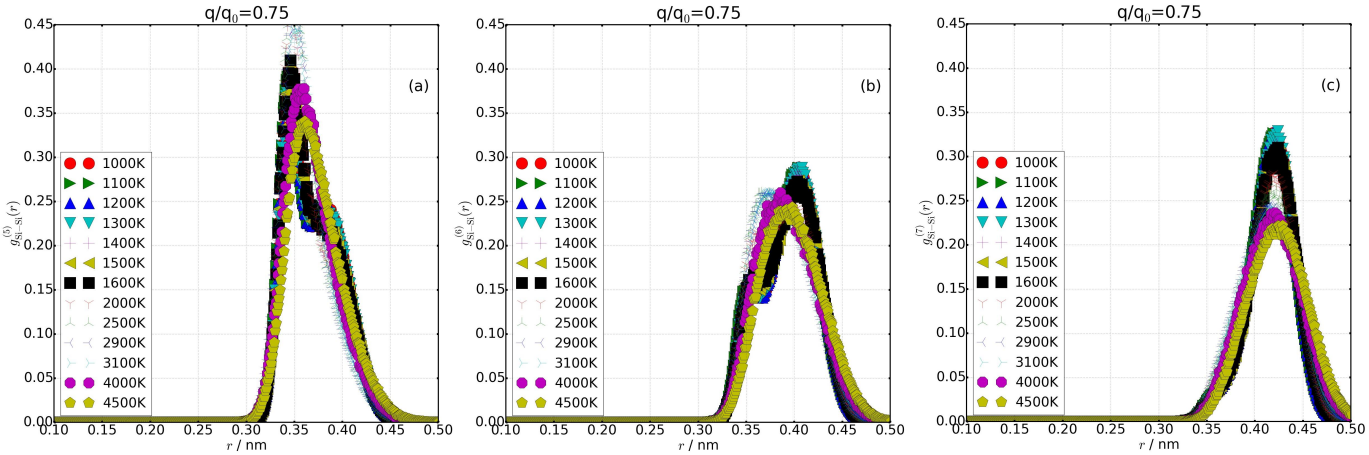

Figure 99: (a) $g^{(5)}$, (b) $g^{(6)}$ and (c) $g^{(7)}$ showing respectively the radial distribution of the 5th, 6th and the 7th nearest atom of any chosen silicon atom, plotted for different temperature for the scaling factor 0.75. This is to show that the system is more frustrated at lower charges such that at low-T the high density domains are still preponderant and the liquid behaves dynamically as a fragile glass.

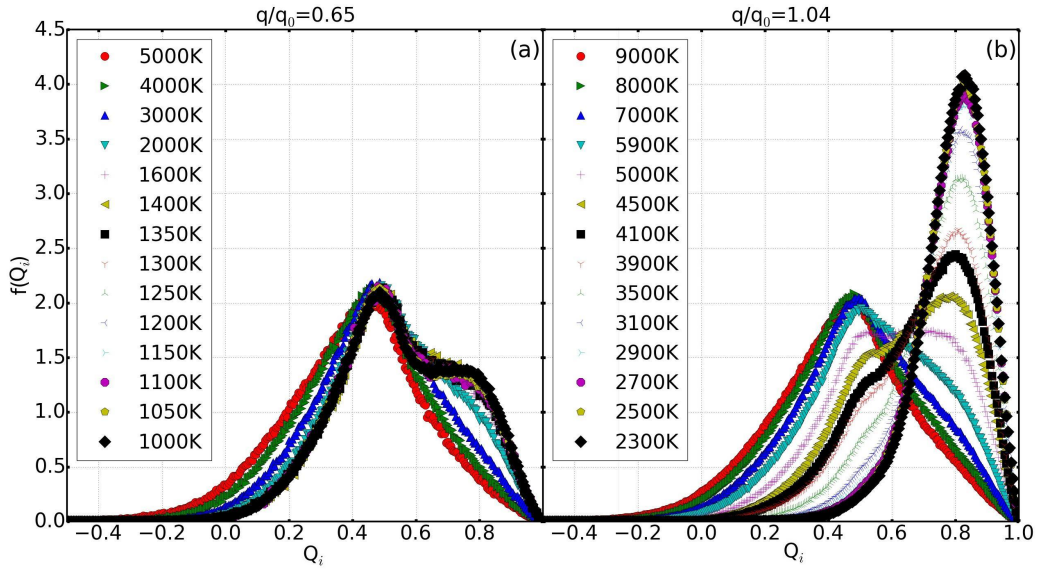

Figure 100: Distribution of the tetrahedral order parameter for different temperature and q/q_0=0.65, 1.04. For large q/q_0, at low-temperature (high-temperature) the distribution is unimodal showing a peak at high (low Q_i) while at intermediate temperature the distribution is either bimodal or unimodal with a shoulder. At small q/q_0, the distribution remains unimodal with a small kink at high Q_i appearing for low-temperature. Both temperature evolution reflect qualitatively the trend observed with $g^{(5)}(r)$ in Fig. 98 (a). and Fig. 42 (a) of the thesis.

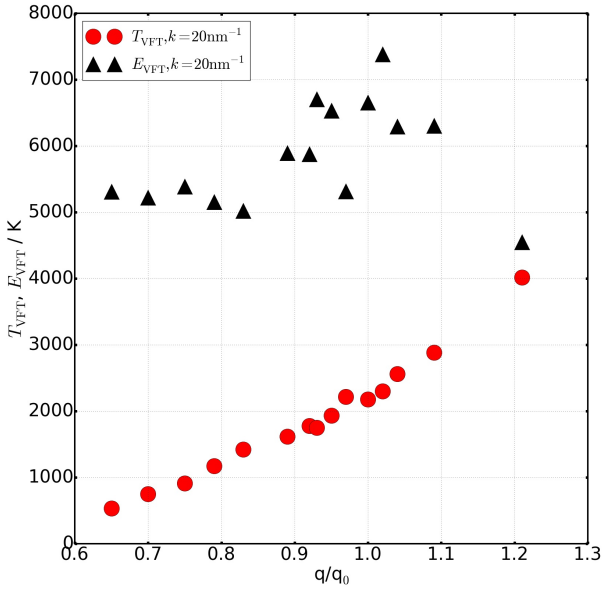

Figure 101: VFT fit parameters from the ISF correlation times over nearest neighbor walks i.e. k= 20 nm^{-1}. E_{VFT} slightly changes with partial charges contrasting with T_{VFT} wich shows a faster than linear increase with charges.

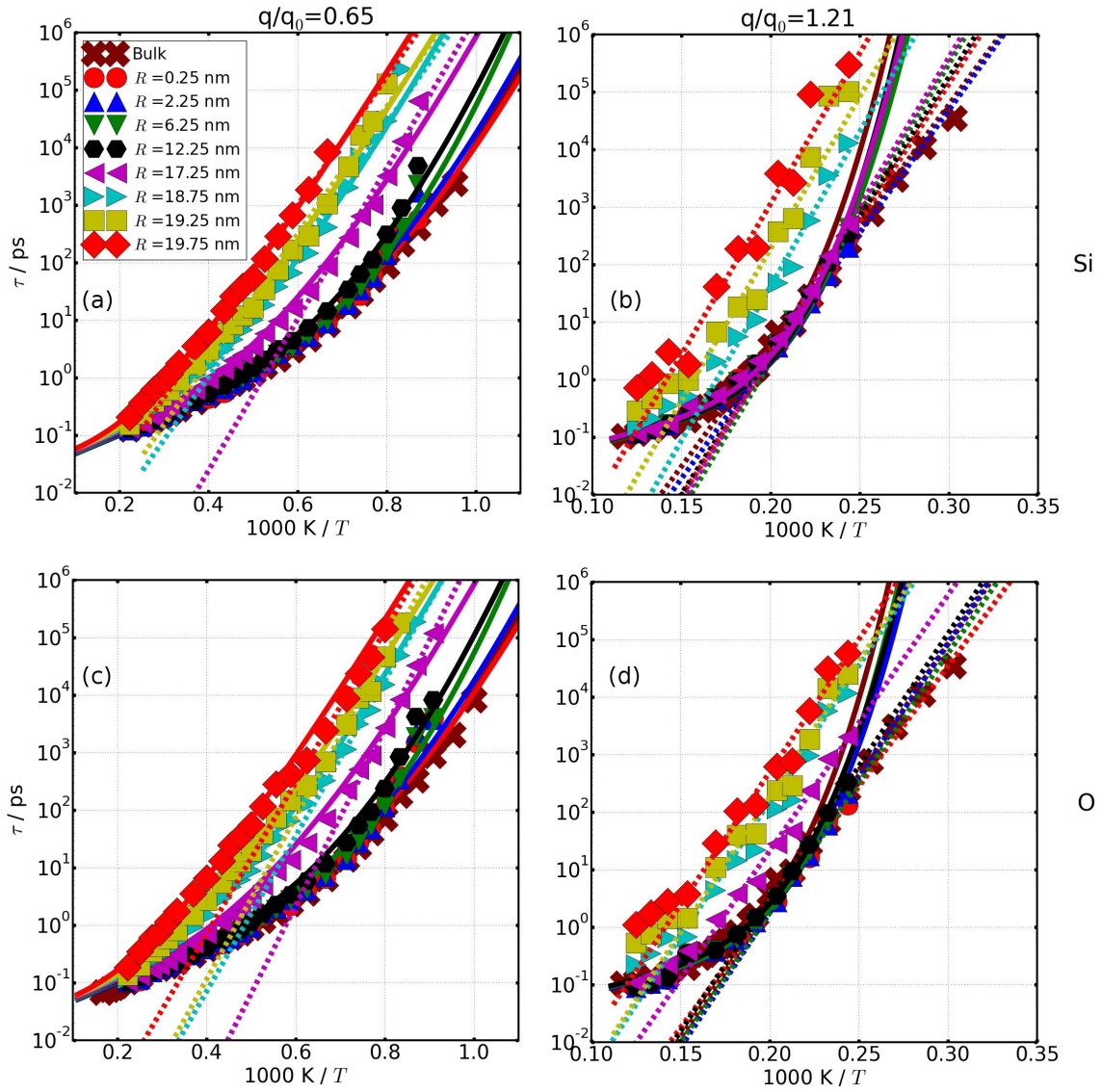

Figure 102: Temperature-dependent structural relaxation times for different liquid layers identified trough atoms position with respect to pore wall. The data are added for oxygens (bottom) and silicon (top) for $q/q_0 = 0{,}65$ (left), 1.21 (right). Fits with the Arrhenius equation at low temperatures are included in dashed lines, and the ones with the *Rössler* approach are included in solid lines. The fits line of the *Rössler* functions have been performed with the bulk high temperature activation energy.

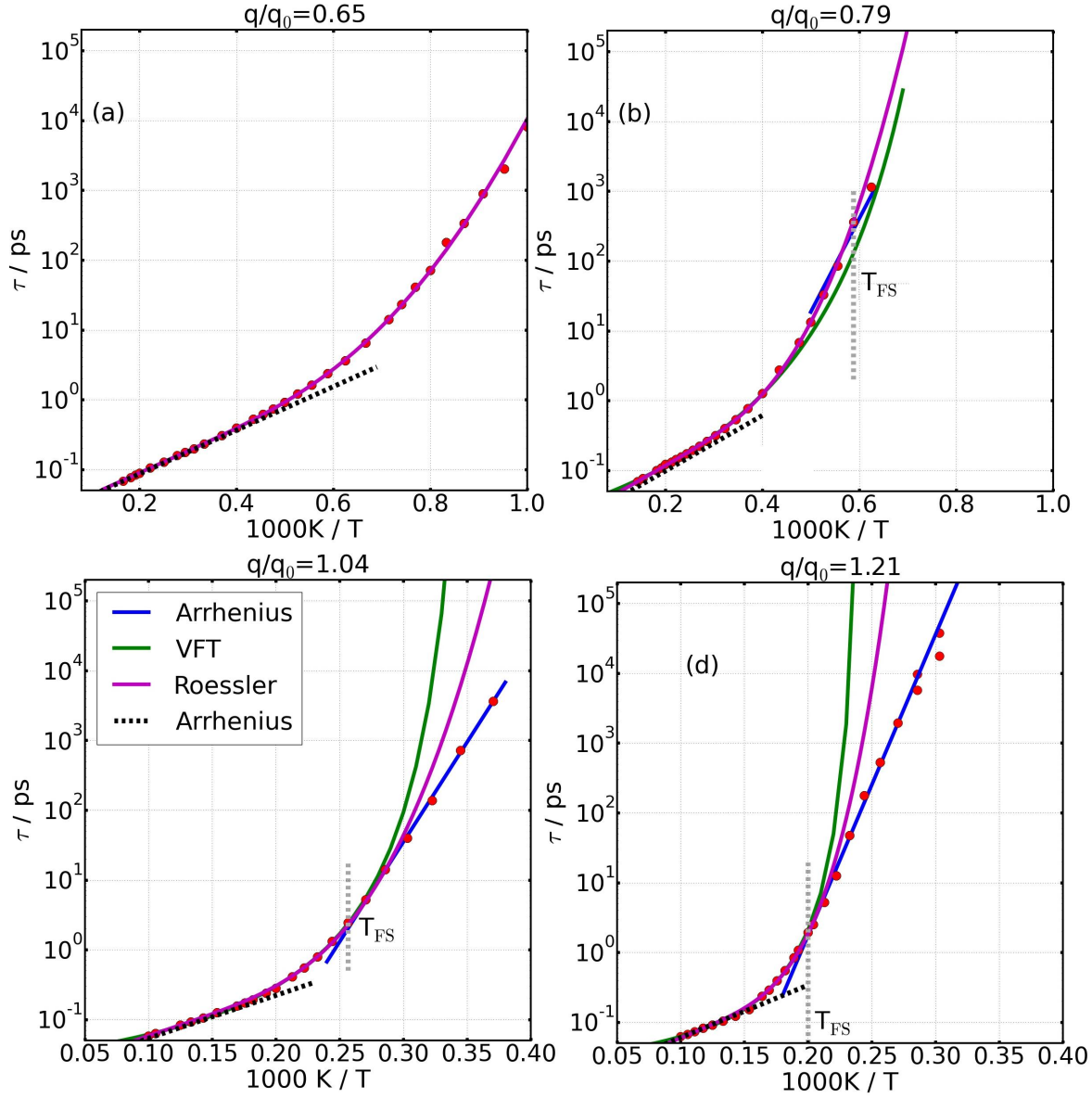

Figure 103: (a)-(d) Correlation times τ (extrapolated from $F_s(k = 20\text{nm}^{-1}, t)$) of oxygens fitted with Arrhenius function at high and low-T. In the intermediate fragile regime, the VFT and the Rössler functions are used. T_{FS} agrees reasonably well with the silicon data, along with the slopes of the high- and low-temperature of τ which are also comparable to the values of silicons (see Fig 104).

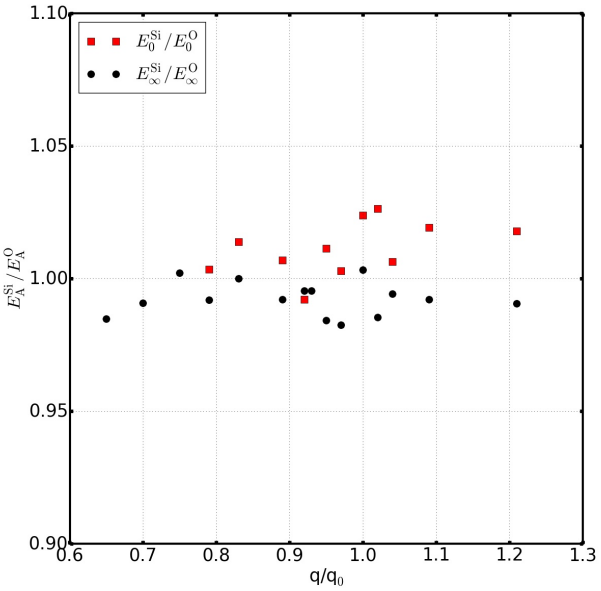

Figure 104: Ratios between the high- and low-temperature activation energies of silicons and oxygens over closed neighbor length scale i.e k= 20 nm^{-1}. The values are up to 5% varying.

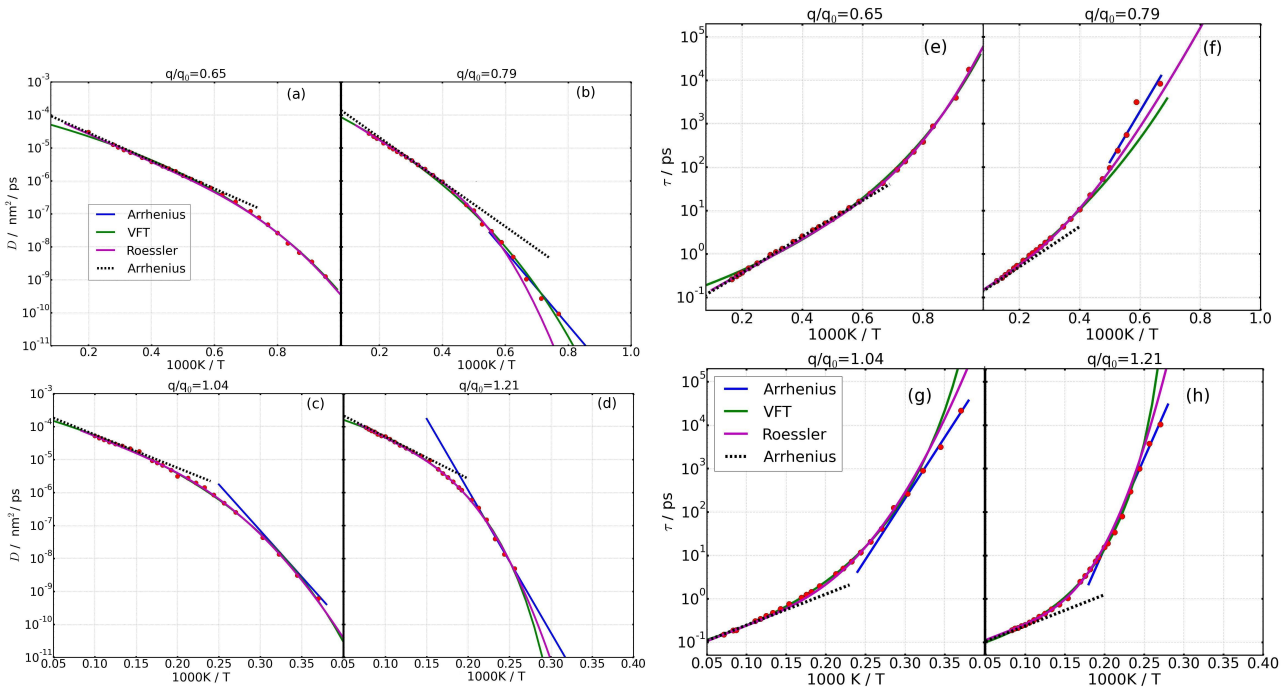

Figure 105: (a)-(d) Diffusion coefficient (D), (e)-(h) τ (extrapolated from $F_s(k = 10\text{nm}^{-1}, t)$) fitted with Arrhenius function at high and low-T. In the intermediate temperature regime, the VFT and the Rössler functions are used. The FS crossover does not appear clearly using the diffusion data but the low-T activation energies resulting from the slopes at low-T match good with the corresponding values obtained with the correlation times.

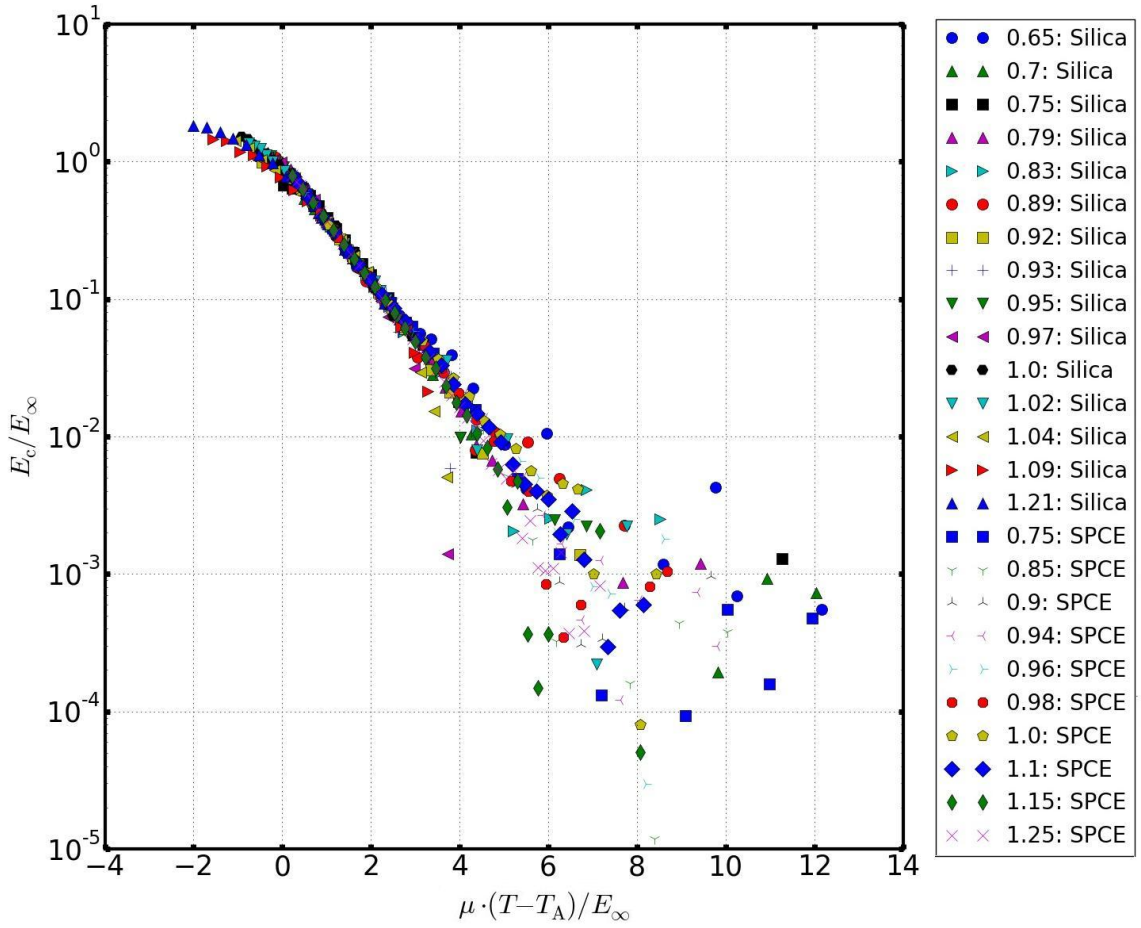

Figure 106: Representation of the ratio between the cooperative contribution E_c to the high-temperature activation energy E_∞, as a function of the reduced temperature parameter $\mu(T - T_A)/E_\infty$ for silica at k= 20 nm^{-1} and water rotation dynamics as reported in Ref. [101]. We obtain a comparable slope between water and silica.

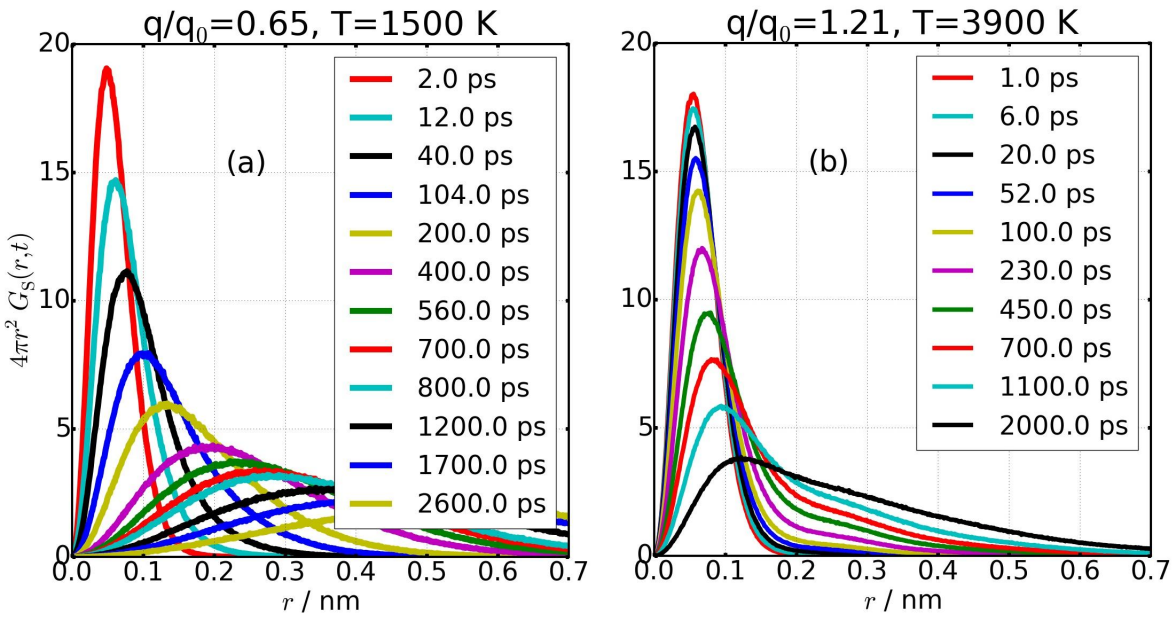

Figure 107: Self part of the van Hove correlation function of the oxygen atoms (top panels) for respectievely (a) $q/q_0 = 0.65$ and (b) $q/q_0 = 1.21$ in each case at the lowest simulated temperature at which the secondary peaks characteristic of hopping events for oxygens atoms are not noticeable.

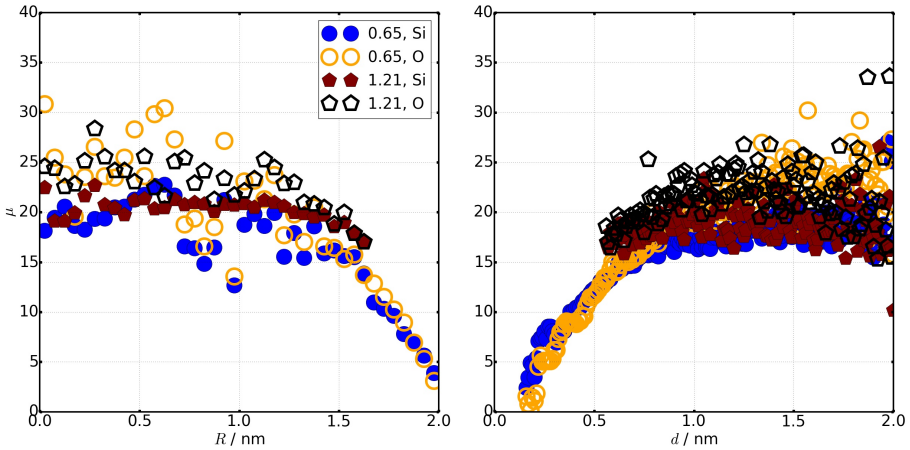

Figure 108: Profile of the fragility parameter resulting from the *Rössler* fits within the R-resolved (left) and the d-resolved (right) analysis. The comparison is performed for the two exemplary liquids associated with the lowest scaling factor q/q_0=0.65 and the highest scaling factor q/q_0=1.21.

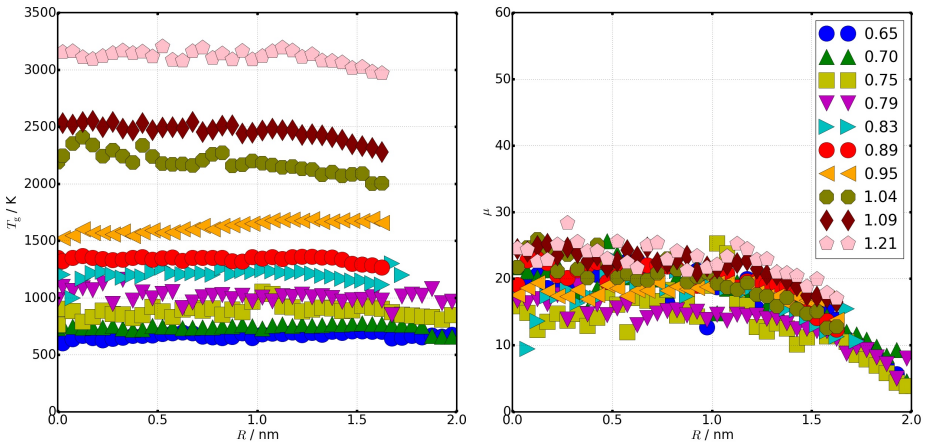

Figure 109: Profile of the glass transiton temperature (a) and fragility parameter (b) resulting from the *Rössler* fits. Here, only the R-resolved analysis data are compared for different silica variants.

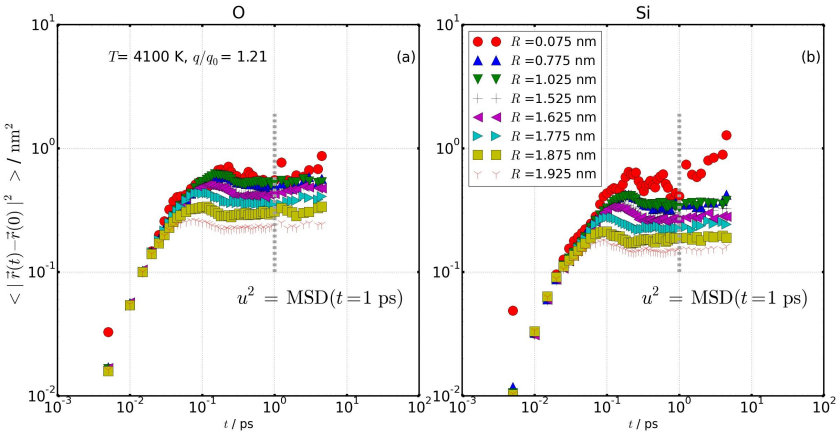

Figure 110: Short times MSD of oxygens (left) and silicons (right) to which the position are indicated with respect to pore center (top) or to the nearest atom of the pore wall (bottom). Here the data for q/q_0=1.21 are shown.

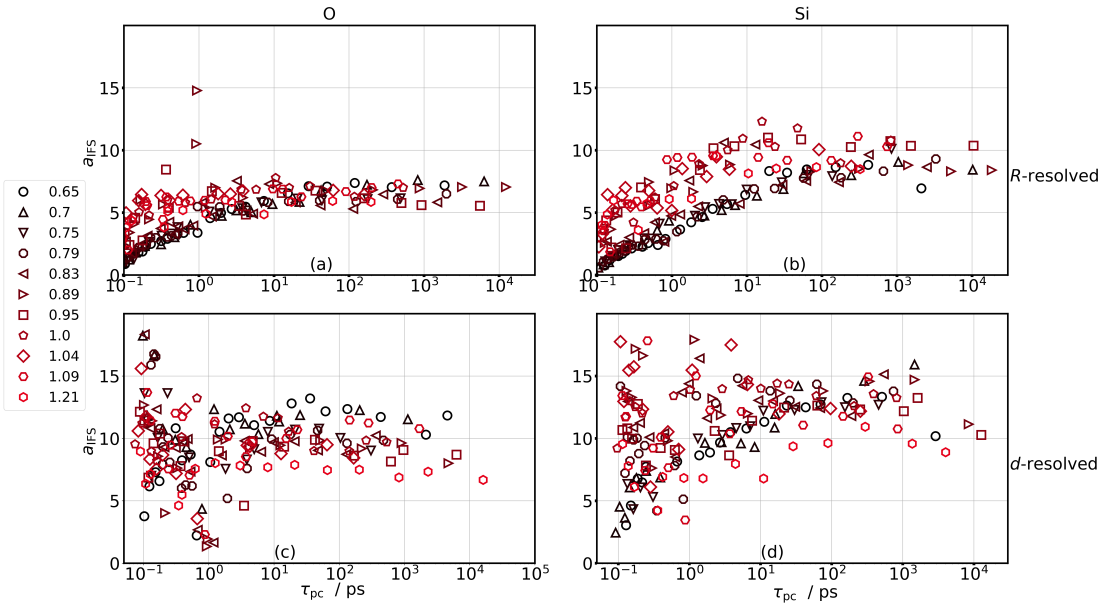

Figure 111: Prefactor a_{ISF} derived from the fit of the distance profile of τ with Eq. 63. Top figures are from the R-resolved analysis and the bottom figures for the d-resolved analysis.

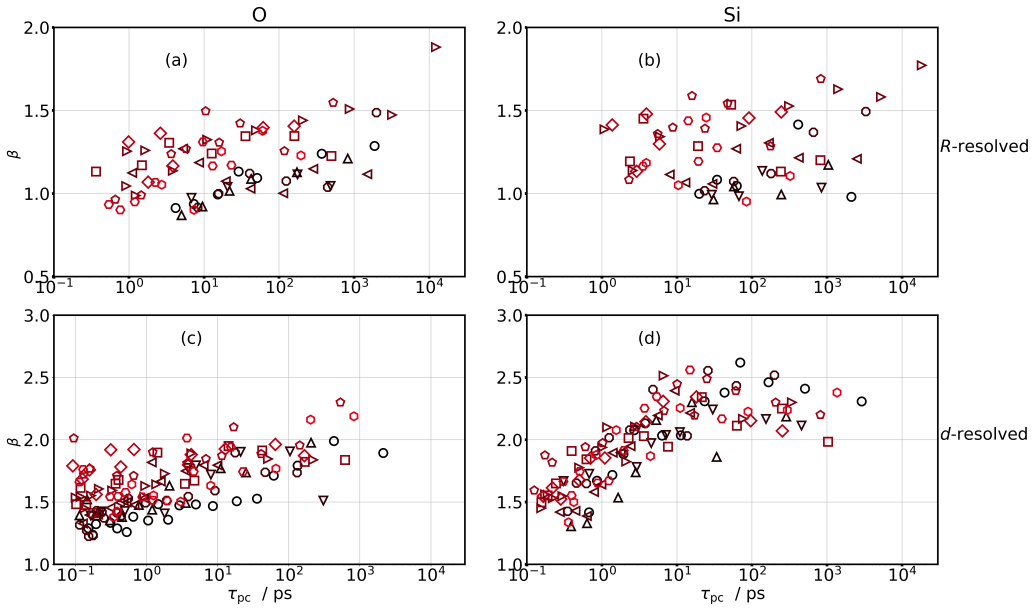

Figure 112: β derived from the fit of the distance variation of P_{∞} with Eq. 64 for the R-resolved data of top figures and Eq. 64 for the d-resolved data (bottom figures).

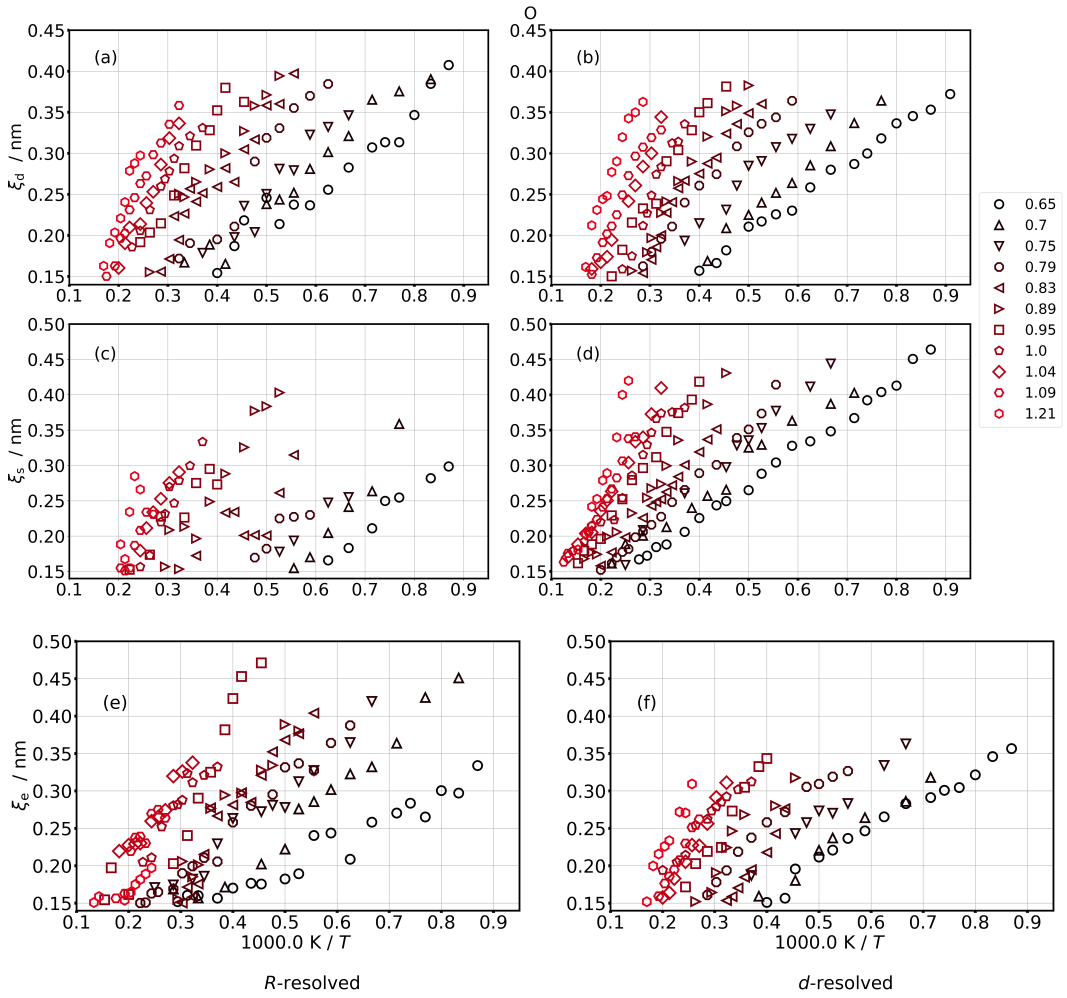

Figure 113: Dynamical ξ_d (a-b), structural ξ_s (c-d) and elastic ξ_e (e-f) length scales plotted for oxygens of all silica variants. The data resolved to pore center are in the left panels, and the ones with respect to pore wall in the right panels.

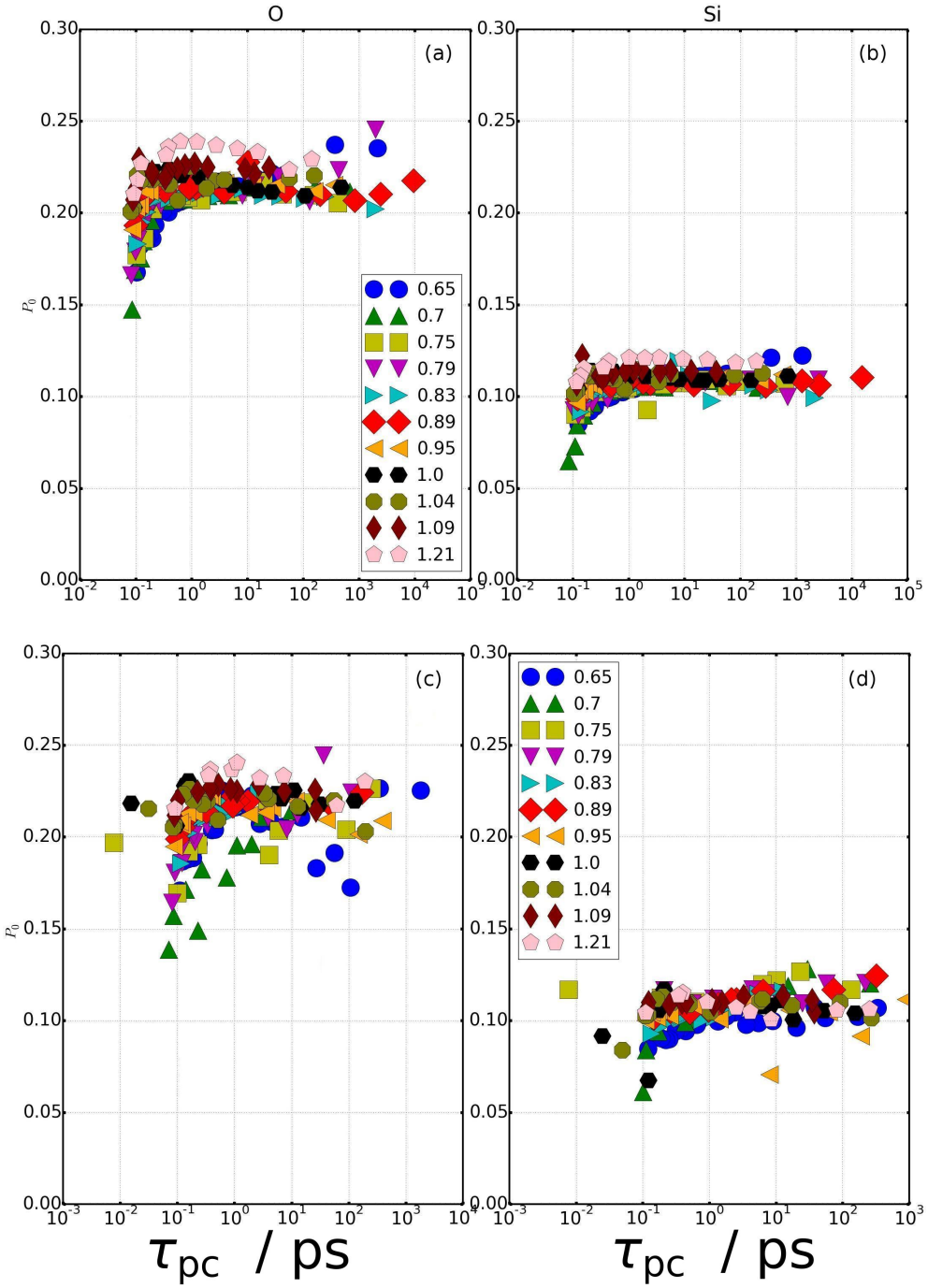

Figure 114: P_0 derived from the fit of the distance variation of P_∞ with Eq. 64 for the R-resolved data of top figures and Eq. 64 for the d-resolved data (bottom figures). P_0 represents the limiting case of P_∞ for atoms in the pore center.

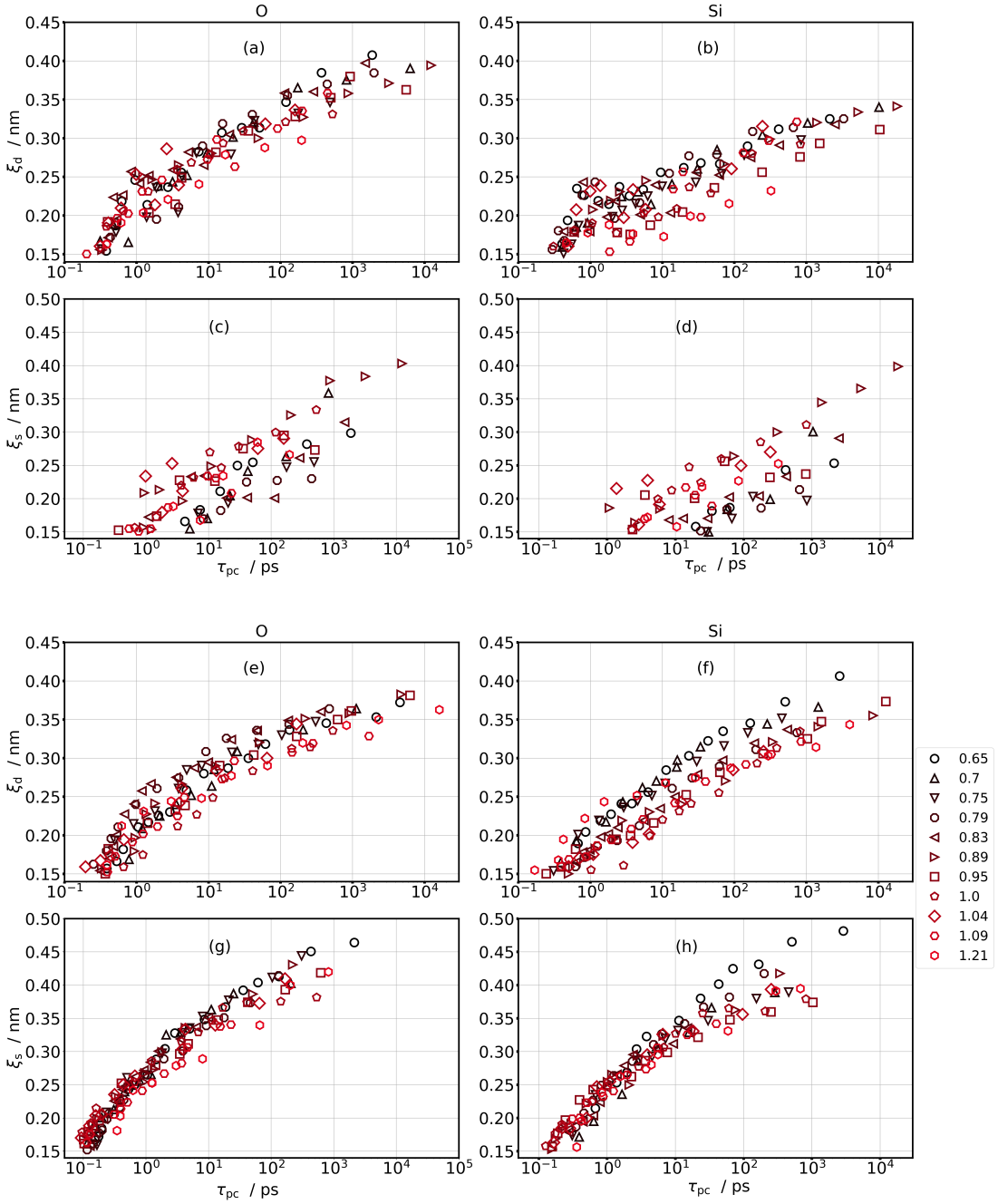

Figure 115: Relation between correlation times of oxygen and silicon atoms in the pore center with average structural length scales $\langle \xi_s \rangle = \xi_s/\beta \cdot \Gamma(1/\beta)$ (a)-(b) (R-resolved) and (c)-(d) (d-resolved) for different silica variants. oxygen (silicon) data in the left (right) panel.

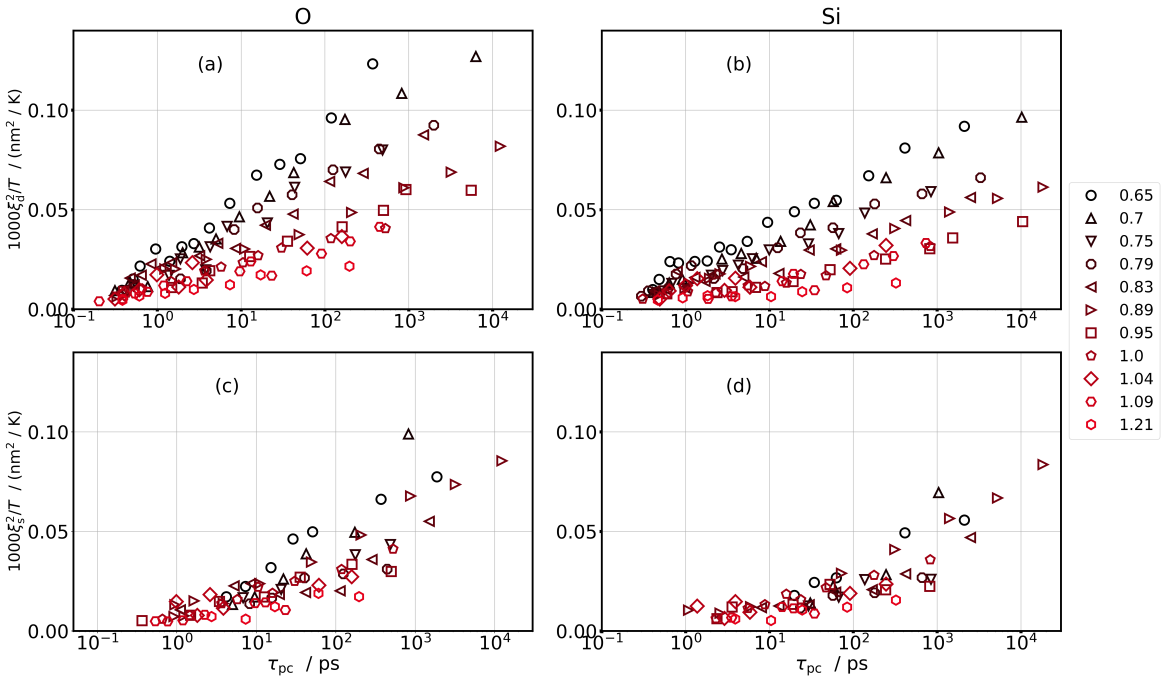

Figure 116: Relation between correlation times of oxygen and silicon atoms in the pore center with dynamical $1000 \cdot \xi_d^2/T$ (a)-(b), as well as structural $1000 \cdot \xi_s^2/T$ (c)-(d) length scales. Shown data are for the R-resolved analysis.

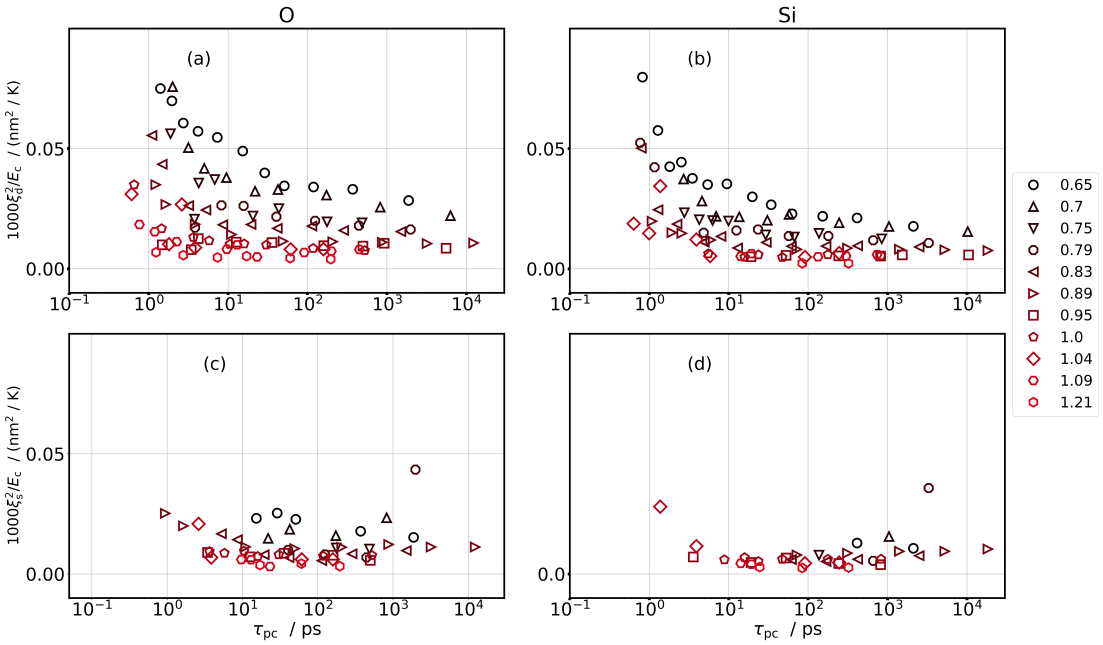

Figure 117: Relation between correlation times of oxygen and silicon atoms in the pore center with $1000 \cdot \xi_d^2/E_c$ (a)-(b), and $1000 \cdot \xi_s^2/E_c$.

References

[1] J. A.Rupley, and G. Careri. Protein hydration and function. *Advances Prot. Chem.*, **41**:37, (1991).

[2] H. D. Middendorf. Neutron studies of the dynamics of biological water. *Phys. B*, **226**:113, (1996).

[3] K. Hu, Y. Zhou, J. Shen, Z. Ji and G. Cheng. Microheterogeneous structure of 1-octanol in neat and water-saturated state. *J. Phys. Chem. B*, **111**:10160, (2007).

[4] W. T. Gozdz, K. E. Gubbins, and A. Z. Panagiotopoulos. Liquid-liquid phase transitions in pores. *Mol. Phys.*, **84**:825, (1995).

[5] M. Sliwinska-Bartkowiak, R. Sikorski, S. L. Sowers, L. D. Gelb, and K. E. Gubbins. Phase separations for mixtures in well-characterized porous materials. *Fluid Phase Equilib.*, **136**:93, (1997).

[6] M. Sliwinska-Bartkowiak, S. L. Sowers, and K. E. Gubbins. Liquid-liquid phase equilibria in porous materials. *Langmuir*, **13**:1182, (1997).

[7] A. Scodinu, and J. T. Fourkas. Comparison of the orientational dynamics of water confined in hydrophobic and hydrophilic nanopores. *J. Phys. Chem. B*, **106**:10292, (2002).

[8] S. Takahara, M. Nakano, S. Kittaka, Y. Kuroda, T. Mori, H. Hamano, T. Yamaguchi. Neutron scattering study on dynamics of water molecules in mcm-41. *J. Phys. Chem. B*, **103**:5814, (1999).

[9] P. Smirnov, T. Yamaguchi, S. Kittaka, S. Takahara, and Y. Kuroda. X-ray diffraction study of water confined in mesoporous mcm-41 materials over a temperature range of 223-298 k. *J. Phys. Chem. B*, **104**:5498, (2000).

[10] A. Faraone, L. Liu, C.-Y. Mou, P.-C. Shih, J. R. D. Copley, and S.-H. Chen. Translational and rotational dynamics of water in mesoporous silica materials: Mcm-41-s and mcm-48-s. *J. Chem. Phys.*, **119**:3963, (2003).

[11] B. Grünberg, T. Emmler, E. Gedat, I. Shenderovich, G. H. Findenegg, H.-H. Limbach, and G. Buntkowsky. Hydrogen bonding of water confined in mesoporous silica mcm-41 and sba-15 studied by 1h solid-state nmr. *Chem. Eur. J.*, **10**:5689, (2004).

[12] S. Takahara, N. Sumiyama, S. Kittaka, T. Yamaguchi, and M.-C. Bellissent-Funel. Neutron scattering study on dynamics of water molecules in mcm-41. 2. determination of translational diffusion coefficient. *J. Phys. Chem. B*, **109**:11231, (2005).

[13] S. Kittaka, S. Takahara, H. Matsumoto, Y. Wada, T. J. Satoh, and T. Yamaguchi. Low temperature phase properties of water confined in mesoporous silica mcm-41: Thermodynamic and neutron scattering study. *J. Chem. Phys.*, **138**:204714, (2013).

[14] J.-C. LI, D. K. Ross, and M. J. BENHAM. Small-angle neutron scattering studies of water and ice in porous vycor glass. *J. Appl. Cryst.*, **24**:794, (1991).

[15] F. Bruni, M. A. Ricci, and A. K. Soper. Water confined in vycor glass. i. a neutron diffraction study. *J. Chem. Phys.*, **109**:1478, (1998).

[16] H. Thompson, A. K. Soper, M. A. Ricci, F. Bruni, and N. T. Skipper. The three-dimensional structure of water confined in nanoporous vycor glass. *J. Phys. Chem. B*, **111**:5610, (2007).

[17] A. Vyalikh, T. Emmler, E. Gedata, I. Shenderovicha, G. H. Findeneggb, H.-H. Limbacha, G. Buntkowsky. Evidence of microphase separation in controlled pore glasses. *Solid State NMR*, **28**:117, (2005).

[18] C. Alba-Simionesco, B. Coasne, G. Dosseh, G. Dudziak, K. E. Gubbins, R. Radhakrishnan, M. Sliwinska-Bartkowiak. Effects of confinement on freezing and melting. *J. Phys. Condens. Matter*, **18**:R15, (2006).

[19] A. Vyalikh, T. Emmler, B. Grünberg, Y. Xu, I. Shenderovich, H. Findenegg, H.-H. Limbach, and G. Buntkowsky. Hydrogen bonding of water confined in controlled-pore glass 10-75 studied by 1h-solid state nmr. *Z. Phys. Chem.*, **221**:155, (2007).

[20] W. H. Thompson. Solvation dynamics and proton transfer in nanoconfined liquids. *Annu. Rev. Phys. Chem.*, **62**:599, (2011).

[21] A. C. Fogarty, E. D.-Dijon, D. Laage, and W. H. Thompson. Origins of the non-exponential reorientation dynamics of nanoconfined water. *J. Chem. Phys.*, **141**:18C523, (2014).

[22] M. F. Harrach, F. Klameth, B. Drossel, and M. Vogel. Effect of the hydroaffinity and topology of pore walls on the structure and dynamics of confined water. *J. Chem. Phys.*, **142**:034703, (2015).

[23] J. C. Fogarty, H. M. Aktulga, A. Y. Grama, A. C. T. van Duin, and S. A. Pandit. A reactive molecular dynamics simulation of the silica-water interface. *J. Chem. Phys.*, **132**:174704, (2010).

[24] I. Brovchenko, A. Geiger, A. Oleinikova, and D. Paschek. Phase coexistence and dynamic properties of water in nanopores. *Eur. Phys. J. E*, **12**:69, (2003).

[25] P. Gallo, M. Rovere, M. A. Ricci, C. Hartnig, and E. Spohr. Evidence of glassy behaviour of water molecules in confined states. *Phil. Mag. Part B*, **79**:1923, (1999).

[26] A. A. Milischuk, and B. M. Ladanyi. Polarizability anisotropy relaxation in nanoconfinement: Molecular simulation study of water in cylindrical silica pores. *J. Chem. Phys.*, **141**:18C513, (2014).

[27] R. Renou, A. Szymczyk, and A. Ghoufi. Tunable dielectric constant of water at the nanoscale. *Phys. Rev. E*, **91**:032411, (2015).

[28] H. Zhang, A. A. Hassanali, Y. K. Shin, C. Knight, and S. J. Singerb. The water amorphous silica interface: Analysis of the stern layer and surface conduction. *J. Chem. Phys.*, **134**:024705, (2011).

[29] B. Berkowitz. Characterizing flow and transport in fractured geological media: A review. *Adv. Water Res.*, **25**:861, (2002).

[30] H. A. Stone, A. D. Stroock, and A. Ajdari. Engineering flows in small devices microfluidics toward a lab-on-a-chip. *Annu. Rev. Fluid Mech.*, **36**:381, (2004).

[31] A. Corma, S. Iborra, and A. Velty. Chemical routes for the transformation of biomass into chemicals. *Chem. Rev.*, **107**:2411, (2007).

[32] S. Bernèche, and B. Roux. Energetics of ion conduction through the k+ channel. *Nature.*, **414**:73, (2001).

[33] M. A. Ricci, F. Bruni, P. Gallo, M. Rovere, and A. K. Soper. Water in confined geometries: experiments and simulations. *J. Phys. Condens. Matter*, **12**:A345, (2000).

[34] J. Jelassi, T. Grosz, I. Bako, M.-C. Bellissent-Funel, J. C. Dore, H. L. Castricum, and R. Sridi-Dorbez. Structural studies of water in hydrophilic and hydrophobic mesoporous silicas: An x-ray and neutron diffraction study at 297 k. *J. Chem. Phys.*, **134**:064509, (2011).

[35] C. Hartnig, W. Witschel, E. Spohr, P. Gallo, M. A. Ricci, and M. Rovere. Modifications of the hydrogen bond network of liquid water in a cylindrical sio_2 pore. *J. Mol. Liq.*, **85**:127, (2000).

[36] P. Gallo, M. Rovere, and E. Spohr. Glass transition and layering effects in confined water: A computer simulation study. *J. Chem. Phys.*, **113**:11324, (2000).

[37] P. Gallo, M. Rovere, M. A. Ricci, C. Hartnig, and E. Spohr. Non-exponential kinetic behaviour of confined water. *Eur. phys. Lett.*, **49**:183, (2000).

[38] E. Spohr, C. Hartnig, P. Gallo, M. Rovere. Water in porous glasses. a computer simulation study. *J.Mol. Liq.*, **80**:165, (1999).

[39] P Gallo, M Rovere, and S-H Chen. Anomalous dynamics of water confined in mcm-41 at different hydrations. *J. Phys. Condens. Matter*, **22**:284102, (2010).

[40] A. BródkA, and T. W. Zerda. Properties of liquid acetone in silica pores: Molecular dynamics simulation. *J. Chem. Phys.*, **104**:6319, (1996).

[41] H. Margenau, and N. R. Kestner. *Theory of Intermolecular Forces*. Pergamon, Oxford, (1969).

[42] T. S. Gulmen, and W. H. Thompson. Testing the two-state model of nanoconfined liquids: The conformational equilibrium of ethylene glycol in amorphous silica pores. *Lang*, **22**:10919, (2006).

[43] R. Williams, and A. M. Goodman. Wetting of thin layers of sio2 by water. *App. Phys. Lett.*, **25**:531, (1974).

[44] M. Lessel, P. Loskill, F. Hausen, N. N. Gosvami, R. Bennewitz, and K. Jacobs. Impact of van der waals interactions on single asperity friction. *Phys. Rev. Lett.*, **111**:035502, (2013).

[45] P. Loskill, H. Hähl, T. Faidt, S. Grandthyll, F. Müller, and K. Jacobs. Is adhesion superficial? silicon wafers as a model system to study van der waals interactions. *Adv. Coll. Inter. Sci.*, **179**:107, (2012).

[46] E. Pafong, J. Geske, and B. Drossel. On the influence of the intermolecular potential on the wetting properties of water on silica surfaces. *J. Chem. Phys.*, **145**:114901, (2016).

[47] J. L. MacCallum, and D. P. Tieleman. Structures of neat and hydrated 1-octanol from computer simulations. *J. Am. Chem. Soc.*, **124**:15085, (2002).

[48] P. Sassi, M. Paolantoni, R, S. Cataliotti, F. Palombo, and A. Morresi. Water/alkohol mixtures: a spectroscopy study of the water-saturated 1-octanol solution. *J. Phys. Chem. B*, **108**:19557, (2004).

[49] B. Chen, and J. I. Siepmann,. Partitioning of alkane and alcohol solutes between water and (dry or wet) 1-octanol. *J. Am. Chem. Soc.*, **122**:6464, (2000).

[50] N. M. Garrido, A. J. Queimada, M. Jorge, E. A. Macedo, and I. G. Economou. 1-octanol/water partition coefficients of n-alkanes from molecular simulations of absolute solvation free energies. *J. Chem. Theory Comput.*, **5**:2436, (2009).

[51] A. P. Lyubartsev, S. P. Jacobsson, G. Sundholm, and A. Laaksonen. Solubility of organic compounds in water/octanol systems. a expanded ensemble molecular dynamics simulation study of log p parameters. *J. Phys. Chem. B*, **105**:7775, (2001).

[52] R. N. Smith, C. Hansch, and M. M. Ames. Selection of a reference partitioning system for drug design work. *J. Pharm. Sci.*, **64**:599, (1975).

[53] C. Hansch, J. P. Bj"orkroth, and A. Leo. Hydrophobicity and central nervous system agents: On the principle of minimal hydrophobicity in drug design. *J. Pharm. Sci.*, **76**:663, (1987).

[54] M. N. Martinez, and G. L. Amidon. A mechanistic approach to understanding the factors affecting drug absorption: A review of fundamentals. *J. Clin. Pharm.*, **42**:620, (2002).

[55] G. Schiro, A. Cupane, S. E. Pagnotta, and F. Bruni. Dynamic properties of solvent confined in silica gels studied by broadband dielectric spectroscopy author links open overlay panel. *J. Non-Cryst. Solids*, **353**:4546, (2007).

[56] K. Elamin, H. Jansson, S. Kittaka, and J. Swenson. Different behavior of water in confined solutions of high and low solute concentrations. *Phys. Chem. Chem. Phys.*, **15**:18437, (2013).

[57] J. Swenson, K. Elamin, H. Janson, and S. Kittaka. Why is there no clear glass transition of confined water. *Chem. Phys.*, **424**:20, (2013).

[58] J. Swenson, K. Elamin, G. Chen, W. Lohstroh, and V. G. Sakai. Anomalous dynamics of aqueous solutions of di-propylene glycol methylether confined in mcm-41 by quasielastic neutron scattering. *J. Phys. Chem.*, **141**:214501, (2014).

[59] K. Elamin, H. Janson, and J. Swenson. Dynamics of aqueous binary glass-formers confined in mcm-41. *Phys. Chem. Chem. Phys.*, **17**:12978, (2015).

[60] S. M. Melnikov, A. Höltzel, A. Seidel-Morgenstern, and U. Tallarek. Composition, structure, and mobility of water-acetonitrile mixtures in a silica nanopore studied by molecular dynamics simulations. *Anal. Chem.*, **83**:2569, (2011).

[61] J. Rodriguez, M. D. Elola, and D. Laria. Polar mixtures under nanoconfinement. *J. Phys. Chem. B*, **113**:12744, (2009).

[62] J. Zang, S. Konduri, S. Nair, and D. S. Sholl. Self-diffusion of water and simple alcohols in single-walled aluminosilicate nanotubes. *ACS Nano*, **3**:1548, (2009).

[63] A. Phan, D. R. Cole, and A. Striolo. Preferential adsorption from liquid water-ethanol mixtures in alumina pores. *Langmuir*, **30**:8066, (2014).

[64] C. Allolio, F. Klameth, M. Vogel, and D. Sebastiani. Ab initio h_2o in realistic hydrophilic confinement. *Chem. Phys. Chem.*, **15**:3955, (2014).

[65] T. Muthulakshmi1, D. Dutta, P. Maheshwari and P. K. Pujari. Evidence for confinement induced phase separation in ethanol–water mixture: a positron annihilation study. *J. Phys.: Condens. Matter*, **30**:025001, (2018).

[66] S. Ullman R. Schmitz, N. Müller and M. Vogel. A molecular dynamics simulations study on ethylene glycol-water mixtures in mesoporous silica. *J. Chem. Phys.*, **145**:104703, (2016).

[67] B. Kumari, M. Brodrecht, M. Werner, B. Grünberg, H.-H. Limbach, S. Forg, E. P. Sanjon, B. Drossel, T. Gutmann, and G. Buntkowsky. Mixtures of alcohols and water confined in mesoporous silica-a combined solid- state nmr and molecular dynamic simulation study. (accepted).

[68] P. H. Poole, F. Sciortino, U. Essmann, and H. E. Stanley. Phase behaviour of metastable water. *Nature*, **360**:324, (1992).

[69] O. Mishima, and H. E. Stanley. The relationship between liquid, supercooled and glassy water. *Nature*, **396**:329, (1998).

[70] S. Cerveny, F. Mallamace, J. Swenson, M. Vogel, and L. Xu. Confined water as model of supercooled water. *Chem. Rev.*, **116**:7608, (2016).

[71] F. Klameth, and M. Vogel. Structure and dynamics of supercooled water in neutral confinements. *J. Chem. Phys.*, **138**:134503, (2013).

[72] A. Faraone, L. Liu, C.-Y. Mou,, and S.-H. Chen. Fragile-to-strong liquid transition in deeply supercooled confined water. *J. Chem. Phys.*, **121**:10843, (2004).

[73] L. Liu, S.-H. Chen, A. Faraone, C.-W. Yen, and C.-Y. Mou. Pressure dependence of fragile-to-strong transition and a possible second critical point in supercooled confined water. *Phys. Rev. Lett.*, **95**:117802, (2005).

[74] M. Rosenstihl, K. K"ampf, F. Klameth, M. Sattig, and M. Vogel. Water dynamics at rough interfaces. *arXiv preprint arXiv*, **1407.5523**, (2014).

[75] K. Ito, C. T. Moynihan, and C. A. Angell. Thermodynamic determination of fragility in liquids and a fragile-to-strong liquid transition in water. *Nature*, **398**:492, (1999).

[76] R. S. Smith, and B. D. Kay. The existence of supercooled liquid water at 150 k. *Nature*, **398**:788, (1999).

[77] J. Swenson, and J. Teixeira. The glass transition and relaxation behavior of bulk water and a possible relation to confined water. *J. Chem. Phys.*, **132**:014508, (2010).

[78] P. Gallo, K. Amann-Winkel, C. A. Angell, M. A. Anisimov, F. Caupin, C. Chakravarty, E. Lascaris, T. Loerting, A. Z. Panagiotopoulos, J. Russo, J. A. Sellberg, H. E. Stanley, H. Tanaka, C. Vega, L. Xu, and L. G. M. Pettersson. Water: A tale of two liquids. *Chem. Rev.*, **116**:7463, (2016).

[79] M. De Marzio, G. Camisasca, M. Rovere, and P. Gallo. Microscopic origin of the fragile to strong crossover in supercooled water: The role of activated processes. *J. Chem. Phys.*, **146**:084502, (2017).

[80] L. Heckmann, and B. Drossel. Common features of simple water models. *J. Chem. Phys.*, **138**:234503, (2013).

[81] P. H. Poole, M. Hemmati, and C. A. Angell. Comparison of thermodynamic properties of simulated liquid silica and water. *Phys. Rev. Lett.*, **79**:2281, (1997).

[82] D. J. Lacks. First-order amorphous-amorphous transformation in silica. *Phys. Rev. Lett.*, **84**:4629, (2000).

[83] I. Saika-Voivod, F. Sciortino, P. H Poole. Computer simulations of liquid silica: Equation of state and liquid-liquid phase transition. *Phys. Rev. E*, **63**:011202, (2000).

[84] I. Saika-Voivod, P. H. Poole, and F. Sciortino. Fragile-to-strong transition and polyamorphism in the energy landscape of liquid silica. *Nature*, **412**:514, (2001).

[85] M. S. Shell, P. G. Debenedetti, and A. Z. Panagiotopoulos. Molecular structural order and anomalies in liquid silica. *Phys. Rev. E*, **66**:011202, (2002).

[86] S. Sastry and C. A. Angell. Liquid-liquid phase transition in supercooled silicon. *Nat. Mater*, **2**:739, (2003).

[87] P. H. Poole, S. R. Becker, F. Sciortino, and F. W. Starr. Dynamical behavior near a liquid-liquid phase transition in simulations of supercooled water. *J. Phys. Chem. B*, **115**:14176, (2011).

[88] C. A. Angell, and M. Hemmati. Glass transitions and critical points in orientationally disordered crystals and structural glassformers: ('strong' liquids are more interesting than we thought). *AIP Conf. Proc.*, **1518**:9, (2013).

[89] E. Lascaris. Tunable liquid-liquid critical point in an ionic model of silica. *Phys. Rev. Lett.*, **116**:127501, (2016).

[90] K-U. Hess, D. B. Dingwell, and E. Rössler. Parametrization of viscosity-temperature relations of aluminosilicate melts. *Chem. Geo.*, **128**:155, (1996).

[91] E. Rössler, K.-U. Hess, and V. Novikov. Universal representation of viscosity in glass forming liquids. *J. Non-Cryst. Solids*, **223**:207, (1998).

[92] C. Sonneville, T. Deschamps, C. Martinet, D. de Ligny, A. Mermet, and B. Champagnon. Polyamorphic transitions in silica glass. *J. Non-Cryst. Solids*, **382**:133, (2013).

[93] M. Vogel, and S. C. Glotzer. Temperature dependence of spatially heterogeneous dynamics in a model of viscous silica. *Phys. Rev. E*, **70**:061504, (2004).

[94] M. Vogel and S. C. Glotzer. Spatially heterogeneous dynamics and dynamic facilitation in a model of viscous silica. *Phys. Rev. Lett.*, **92**:255901, (2004).

[95] J. Horbach, and W. Kob. Static and dynamic properties of a viscous silica melt. *Phys. Rev. B*, **60**:3169, (1999).

[96] K. Vollmayr, W. Kob, and K. Binder. Cooling-rate effects in amorphous silica: A computer-simulation study. *Phys. Rev. B*, **54**:15808, (1996).

[97] J. Horbach, and W. Kob. Relaxation dynamics of a viscous silica melt: The intermediate scattering functions. *Phys. Rev. E*, **64**:041503, (2001).

[98] I. Saika-Voivod, F. Sciortino, and P. H. Poole. Free energy and configurational entropy of liquid silica: Fragile-to-strong crossover and polyamorphism. *Phys. Rev. E*, **69**:041503, (2004).

[99] A. Saksaengwijit, J. Reinisch, and A. Heuer. Origin of the fragile-to-strong crossover in liquid silica as expressed by its potential-energy landscape. *Phys. Rev. Lett.*, **93**:235701, (2004).

[100] E. P. Sanjon, B. Drossel, and M. Vogel. Effects of the bond polarity on the structural and dynamical properties of silica-like liquids. *J. Chem. Phys.*, **148**:104506, (2018).

[101] R. Horstmann, and M. Vogel . Common behaviors associated with the glass transitions of water-like models. *J. Chem. Phys.*, **147**:034505, (2017).

[102] R. Chen, E. Lascaris, and J. C. Palmer. Liquid-liquid phase transition in an ionic model of silica. *J. Chem. Phys.*, **146**:234503, (2017).

[103] L. V. Woodcock, C. A. Angell, and P. Cheeseman. Molecular dynamics studies of the vitreous state: Simple ionic systems and silica. *J. Chem. Phys.*, **65**:1565, (1976).

[104] J. Geske, B. Drossel, and M. Vogel. Fragile-to-strong transition in liquid silica. *AIP Advances*, **6**:035131, (2016).

[105] B. W. H. van Beest, G. J. Kramer, and R. A. van Santen. Force fields for silicas and aluminophosphates based on ab initio calculations. *Phys. Rev. Lett.*, **64**:1955, (1990).

[106] M. Sattig, S. Reutter, F. Fujara, M. Werner, G. Buntkowsky, and M. Vogel. Nmr studies on the temperature-dependent dynamics of confined water. *Phys. Chem. Chem. Phys.*, **16**:19229, (2014).

[107] M. Rosenstihl, K. K"ampf, F. Klameth, M. Sattig, and M. Vogel. Dynamics of interfacial water. *J. Non-Cryst. Sol.*, **407**:449, (2015).

[108] P. Scheidler, W. Kob, and K. Binder. The relaxation dynamics of a supercooled liquid confined by rough walls. *J. Phys. Chem. B*, **108**:6673, (2004).

[109] A. Cavagna, T. S. Grigera, and P. Verrocchio. Mosaic multistate scenario versus one-state description of supercooled liquids. *Phys. Rev. Lett.*, **98**:187801, (2007).

[110] L. Berthier, and W. Kob. Static point-to-set correlations in glass-forming liquids. *Phys. Rev. E*, **85**:011102, (2012).

[111] W. Kob, S. Roldán-Vargas, and L. Berthier. Non-monotonic temperature evolution of dynamic correlations in glass-forming liquids. *Nat. Phys.*, **8**:164, (2012).

[112] F. Klameth, P. Henritzi, and M. Vogel. Static and dynamic length scales in supercooled liquids: Insights from molecular dynamics simulations of water and tri-propylene oxide. *J. Chem. Phys.*, **140**:144501, (2014).

[113] G. Adams, and J. H. Gibbs. On the temperature dependence of cooperative relaxation properties in glass[U+2010]forming liquids. *J. Chem. Phys.*, **43**:139, (1965).

[114] T. Kirkpatrick, D. Thirumalai, and P. G. Wolynes. Scaling concepts for the dynamics of viscous liquids near an ideal glassy state. *Phys. Rev. A*, **40**:1045, (1989).

[115] V. Lubchenko, and P. G. Wolynes. Scaling concepts for the dynamics of viscous liquids near an ideal glassy state. *Annu. Rev. Phys. Chem.*, **58**:235, (2007).

[116] S. Mirigian, and K. S. Schweizer. Unified theory of activated relaxation in liquids over 14 decades in time. *J. Phys. Chem. Lett.*, **4**:3648, (2013).

[117] S. Mirigian, and K. S. Schweizer. Elastically cooperative activated barrier hopping theory of relaxation in viscous fluids. i. general formulation and application to hard sphere fluids. *J. Chem. Phys.*, **140**:194506, (2014).

[118] S. Mirigian, and K. S. Schweizer. Elastically cooperative activated barrier hopping theory of relaxation in viscous fluids. ii. thermal liquids. *J. Chem. Phys.*, **140**:194507, (2014).

[119] A. Cavagna. Supercooled liquids for pedestrians. *Phys. Rep.*, **476**:51, (2009).

[120] S. Karmakar, C. Dasgupta, and S. Sastry. Length scales in glass-forming liquids and related systems: a review. *Rep. Prog. Phys.*, **79**:016601, (2016).

[121] R. Horstmann, E. P. Sanjon, B. Drossel, M. Vogel. Effect of the bond polarity on the dynamical properties of silica and water variants in neutral confinements. (in preparation).

[122] B. F. Peterman and C. J. Perkins. Dynamics of radioactive chemically inert gases in the human body. *Radiat. Prot. Dosim.*, **22**:5, (1988).

[123] A. Khursheed. Doses to systemic tissues from radon gas. *Radiat. Prot. Dosim.*, **88**:171, (2000).

[124] C. A. Tobias, H. B. Jones, J. H. Lawrence, and J. G. Hamilton. The uptake and elimination of krypton and other inert gases by the human body. *J. Clin. Invest.*, **28**:1375, (1949).

[125] T. A. Gosink, M. Baskaran, and D. F. Holleman. Radon in the human body from drinking water. *Health Phys.*, **59**:919, (1990).

[126] D. L. Henshaw, J. P. Eatough, , and R. B. Richardson. Radon as a causative factor in the induction of myeloid leukaemia and other cancer. *Lancet*, **335**:1008, (1990).

[127] D. J. Crawford-Brown. Cancer fatalities from waterborne radon (rn-222). *Risk Analysis*, **11**:135, (1991).

[128] A. Falkenbach and N. Wolter. Radonthermalstollen-kur zur behandlung des morbus bechterew. *Complement. Med. Res.*, **4**:277, (1997).

[129] K. Becker. Is radon dangerous for our health? In *Proceedings of the 7th International Conference on Nuclear Engineering Special Symposium*, (1999).

[130] A. Franke and T. Franke. Long-term benefits of radon spa therapy in rheumatic diseases: results of the randomised, multi-centre imura trial. *Rheumatol. Int.*, **33**:2839, (2013).

[131] A. Van Tubergen, R. Landewé, D. Van Der Heijde, A. Hidding, N. Wolter, M. Asscher, A. Falkenbach, E. Genth, H. Goei Thé, and S. van der Linden. Combined spa–exercise therapy is effective in patients with ankylosing spondylitis: a randomized controlled trial. *Arthritis Care Res.*, **45**:430, (2001).

[132] E. Nussbaum and J.B. Hursh. Radon solubility in rat tissues. *Science*, **125**:552, (1957).

[133] E. Nussbaum and J. B. Hursh. Radon solubility in fatty acids and triglycerides. *Journal Phys. Chem.*, **62**:81, (1958).

[134] Y. Ishimori, H. Tanaka, A. Sakoda, T. Kataoka, K. Yamaoka, and F. Mitsunobu. Measurements of radon activity concentration in mouse tissues and organs. *Radiat. Environ. Biophys.*, **56**:161, (2017).

[135] E. P. Sanjon, A. Maier, A. Hinrichs, G. Kraft, B. Drossel, and C. Fournier. Why radon dissolves better in fat than in water. (in preparation).

[136] H. J. C. Berendsen, J. R. Grigera, and T. P. Straatsma. The missing term in effective pair potentials. *J. Phys. Chem.*, **91**:6269, 1987.

[137] J. C. Phillips, R. Braun, W. Wang, J. Gumbart, E. Tajkhorshid, E. Villa, C. Chipot, R. D. Skeel, L. Kale, and K. Schulten. Scalable molecular dynamics with namd. *J. Comput. Chem.*, **26**:1781, (2005).

[138] T. Darden, D. York, and L. Pedersen. Particle mesh ewald: An n·log(n) method for ewald sums in large systems. *J. Chem. Phys.*, **98**:10089, (1993).

[139] D. Frenkel, and B. Smit. Academic Press, San Diego, (2002).

[140] R. Kubo, M Toda, and N. Hashitsume. *Statistical Physics II: Nonequilibrium Statistical Mechanics*. Springer: New York, (1991).

[141] S. E. Feller, Y. Zhang, R. W. Pastor, and B. R. Brooks. Constant pressure molecular dynamics simulation: The langevin piston method. *J. Chem. Phys.*, **103**:4613, (1995).

[142] H. A. Lorentz. Ueber die anwendung des satzes vom virial in der kinetischen theorie der gase. *Annal. Phys.*, **248**:127, (1881).

[143] J. L. F. Abascal, and C. Vega,. A general purpose model for the condensed phases of water: Tip4p/2005. *J. Chem. Phys.*, **123**:234505, (2005).

[144] H. B. Yu et al. Biomolekulare modellierung: Ziele, probleme, perspektiven. *Angew. Chem.*, **118**:4168, (2006).

[145] S. V. Nedea, A. J. H. Frijns, A. A. van Steenhoven, A. J. Markvoort, and P. A. J. Hilbers. Hybrid method coupling molecular dynamics and monte carlo simulations to study the properties of gases in microchannels and nanochannels. *Phys. Rev. E*, **72**:016705, (2005).

[146] M. Rovere. *Lecture notes on Monte Carlo and Molecular Dynamics Simulation*. In: School of Neutron Scattering 'F. P. Ricci', Santa Margherita di Pula, Santa Margherita di Pula, (2008).

[147] S. Debolt, and P. A. Kollman. Investigation of structure, dynamics, and solvation in 1-0ctanol and its water-saturated solution: Molecular dynamics and free-energy perturbation studies. *J. Am. Chem. SOC.*, **117**:5316, (1995).

[148] A. D. MacKerell et al. All-atom empirical potential for molecular modeling and dynamics studies of proteins. *J. Phys. Chem. B*, **102**:3586, (1998).

[149] J. L. Yarnell, M. J. Katz, R. G. Wenzel, and S. H. Koenig. Structure factor and radial distribution function for liquid argon at 85° k. *Phys. Rev. A*, **7**:2130, (1973).

[150] A. H. Narten, and H. A. Levy. Liquid water: Molecular correlation functions from x[U+2010]ray diffraction. *J. Chem. Phys.*, **55**:2263, (1971).

[151] G. Hura, J. M. Sorenson, R. M. Glaeser, and T. Head-Gordon. A high-quality x-ray scattering experiment on liquid water at ambient conditions. *J. Chem. Phys.*, **113**:9140, (2000).

[152] A. K. Soper, and M. G. Phillips. A new determination of the structure of water at 25°c. *Chem. Phys.*, **107**:47, (1986).

[153] A. K. Soper. The radial distribution functions of water and ice from 220 to 673 k and at pressures up to 400 mpa. *Chem. Phys.*, **258**:121, (2000).

[154] W. A. Senior, and R. E. Verrall. Spectroscopic evidence for the mixture model in hod solutions. *J. Phys. Chem.*, **73**:4242, (1969).

[155] H. Palamarev, and G. Georgiev. Statistical distribution of hydrogen-bonded oh oscillators in hod on the basis of infrared spectra. *Vib. Spectrosc.*, **7**:255, (1994).

[156] J. B. Asbury, T. Steinel, C. Stromberg, S. A. Corcelli, C. P. Lawrence, J. L. Skinner, and M. D. Fayer. Water dynamics: vibrational echo correlation spectroscopy and comparison to molecular dynamics simulations. *J. Phys. Chem. A*, **108**:1107, (2004).

[157] R. Kumar, J. R. Schmidt, and J. L. Skinner. Hydrogen bonding definitions and dynamics in liquid water. *J. Chem. Phys.*, **126**:204107, (2007).

[158] F. H. Stillinger, and A. Rahman. Improved simulation of liquid water by molecular dynamics. *J. Chem. Phys.*, **60**:1545, (1974).

[159] F. H. Stillinger. Water revisited. *Science*, **209**:451, (1980).

[160] A. Geiger, and H. E. Stanley. Low-density patches in the hydrogen-bond network of liquid water: Evidence from molecular-dynamics computer simulations. *Phys. Rev. Lett.*, **49**:1749, (1982).

[161] W. L. Jorgensen, J. Chandrasekhar, J. D. Madura, R. W. Impey, and M. L. Klein. Comparison of simple potential functions for simulating liquid water. *J. Chem. Phys.*, **79**:926, (1983).

[162] A. Luzar, and D. Chandler. Hydrogen-bond kinetics in liquid water. *Nature*, **379**:55, (1996).

[163] A. Luzar, and D. Chandler. Effect of environment on hydrogen bond dynamics in liquid water. *Phys. Rev. Lett.*, **76**:928, (1996).

[164] M. Sharma, R. Resta, and R. Car. Intermolecular dynamical charge fluctuations in water: A signature of the h-bond network. *Phys. Rev. Lett.*, **95**:187401, (2005).

[165] J. D. Smith, C. D. Cappa, K. R. Wilson, R. C. Cohen, P. L. Geissler, and R. J. Saykally. Unified description of temperature-dependent hydrogen-bond rearrangements in liquid water. *PNAS*, **102**:14171, (2005).

[166] R. Shi, and H. Tanaka. Microscopic structural descriptor of liquid water. *J. Chem. Phys.*, **148**:124503, (2018).

[167] P. L. Chau, and A. Hardwick. A new order parameter for tetrahedral configurations. *Mol. Phys.*, **93**:511, (1998).

[168] J. R. Errington, and P. G. Debenedetti. Relationship between structural order and the anomalies of liquid water. *Nature*, **409**:318, (2001).

[169] P. Kumar, S. V. Buldyrev, H. E. Stanley. A new order parameter for tetrahedral configurations. *PNAS*, **106**:22130, (2009).

[170] F. W. Starr, S. Sastry, J. F. Douglas, and S. C. Glotzer. What do we learn from the local geometry of glass-forming liquids? *Phys. Rev. Lett.*, **89**:125501, (2002).

[171] S. Toxvaerd, U. R. Pedersen, T. B. Schroder, and J. C. Dyre. Stability of supercooled binary liquid mixtures. *J. Chem. Phys.*, **130**:224501, (2009).

[172] G. Biroli, J.-P. Bouchaud, A. Cavagna, T. S. Grigera, and P. Verrocchio. Thermodynamic signature of growing amorphous order in glass-forming liquids. *Nat. Phys.*, **4**:771, (2008).

[173] G. M. Hocky, T. E. Markland, and D. R. Reichman. Growing point-to-set length scale correlates with growing relaxation times in model supercooled liquids. *Phys. Rev. Lett.*, **108**:225506, (2012).

[174] S. Karmakar, E. Lerner, and I. Procaccia. Direct estimate of the static correlation length-scale accompanying the glass transition. *Physica A*, **391**:1001, (2012).

[175] G. Biroli, S. Karmakar, and I. Procaccia. Comparison of static length scales characterizing the glass transition. *Phys. Rev. Lett.*, **111**:165701, (2013).

[176] F. Klameth. *From Brownian motion to supercooled water in confinements - a moleculardynamics simulation study*. PhD thesis, TU Darmstadt, (2014).

[177] J. Geske, B. Drossel, and M. Vogel. Structure and dynamics of a silica melt in neutral confinement. *J. Chem. Phys.*, **146**:134502, (2017).

[178] B. Drossel. *Theorie Kondensierter Materie, Vorlesung und Vorlesungsunterlagen tu Kapitel 8*. TU Darmstadt, (SS 2013/2014).

[179] D. S. Sanditov, S. Sh. Sangadiev, and G. V. Kozlov. *On the correlation between elastic modulus of vitreous solids and glass transition temperature of melts*. Glass Physics Chemistry (Translation of Fizika i Khimiya Stekla), (1998).

[180] J. Geske. *Eine molekulardynamische Studie von amorphen SiO2 im Bulk und unter geometrischen Einschränkungen*. PhD thesis, TU Darmstadt, (2017).

[181] J. C. Dyre. The glass transition and elastic models of glass-forming liquids. *Rev. Mod. Phys.*, **78**:953, (2006).

[182] J. Langer. The mysterious glass transition. *Phys. Today*, **60**:8, (2007).

[183] K. Trachenko. The vogel-fulcher-tammann law in the elastic theory of glass transition. *J. Non-Cryst. Sol.*, **354**:3903, (2008).

[184] B. Schmidtke, N. Petzold, R. Kahlau, M. Hofmann, and E. A. Rössler. From boiling point to glass transition temperature: Transport coefficients in molecular liquids follow three-parameter scaling. *Phys. Rev. E*, **86**:041507, (2012).

[185] B. Schmidtke, N. Petzold, R. Kahlau, and E. A. Rössler. Reorientational dynamics in molecular liquids as revealed by dynamic light scattering: From boiling point to glass transition temperature. *J. Chem. Phys.*, **139**:084504, (2013).

[186] B. Schmidtke, M. Hofmann, A. Lichtinger, and E. A. Rössler. Temperature dependence of the segmental relaxation time of polymers revisited. *Macromolecules*, **48**:3005, (2015).

[187] W. Kauzmann. The nature of the glassy state and the behavior of liquids at low temperatures. *Chem. Rev.*, **43**:219, (1948).

[188] R. Richert, C.A. Angell. Dynamics of glass-forming liquids. v. on the link between molecular dynamics and configurational entropy. *J. Chem. Phys.*, **108**:9016, (1998).

[189] J. H. Gibbs and E. A Di Marzio. Chain stiffness and the lattice theory of polymer phases. *J. Chem. Phys.*, **28**:807, (1958).

[190] S. Sengupta, S. Karmakar, C. Dasgupta, and S. Sastry. Adam-gibbs relation for glass-forming liquids in two, three, and four dimensions. *Phys. Rev. Lett.*, **109**:095705, (2012).

[191] G. P Johari. A resolution for the enigma of a liquid's configurational entropy-molecular kinetics relation. *J. Chem. Phys.*, **112**:8958, (2000).

[192] I. M. Hodge. Adam-gibbs formulation of enthalpy relaxation near the glass transition. *J. Res. NIST*, **102**:195, (1997).

[193] R. A. Jones. *Soft Condensed Matter*, volume **6**. Oxford University Press, (2002).

[194] G. Biroli, and J. P. Bouchaud. The random first-order transition theory of glasses: a critical assessment. (2009).

[195] M.D.Ediger, C.A. Angell, and S.R. Nagel. Supercooled liquids and glasses. *J. Phys. Chem.*, **100**:13200, (1996).

[196] D. R Reichman, and P. Charbonneau. Mode-coupling theory. *J. Stat. Mech.*, **P05013**, (2005).

[197] U. Bengtzelius, W. Gotze and A. Sjolander. Dynamics of supercooled liquids and the glass transition. *J. Phys. C*, **17**:5915, (1996).

[198] W. Götze. The essentials of the mode-coupling theory for glassy dynamics. *Condens. Mat. Phys.*, **1**:873, (1998).

[199] W. Goetze. *Complex dynamics of glass forming liquids: a mode coupling theory*. Oxford University Press, (2008).

[200] N. J. Tao, G. Li, and H. Z. Cummins. Self-similar light-scattering spectra of β relaxation near the liquid-glass transition. *Phys. Rev. Lett.*, **66**:1334, (1991).

[201] M. Elmroth, L. B"orjesson, and L. M. Torell. Observation of a dynamic anomaly in the liquid-glass transformation range by brillouin scattering. *Phys. Rev. Lett.*, **68**:79, (1992).

[202] F. Mezei, W. Knaak, and B. Farago. Neutron spin echo study of dynamic correlations near the liquid-glass transition. *Phys. Rev. Lett.*, **58**:571, (1987).

[203] W. Doster, S. Cusack, and W. Petry. Dynamic instability of liquidlike motions in a globular protein observed by inelastic neutron scattering. *Phys. Rev. Lett.*, **65**:1080, (1990).

[204] M. Goldstein. Viscous liquids and the glass transition: A potential energy barrier picture. *J. Chem. Phys.*, **51**:3728, (1969).

[205] R. W. Hall, and P. G. Wolynes. The aperiodic crystal picture and free energy barriers in glasses. *J. Chem. Phys.*, **86**:2943, (1987).

[206] J. C. Dyre, N. B. Olsen, and T. Christensen. Local elastic expansion model for viscous-flow activation energies of glass-forming molecular liquids. *Phys. Rev. B*, **53**:2171, (1996).

[207] J. C. Dyre. Source of non-arrhenius average relaxation time in glass-forming liquids. *J. Non-Cryst. Solids*, **235**:142, (1998).

[208] J. C. Dyre, and W. H. Wang. The instantaneous shear modulus in the shoving model. *J. Chem. Phys.*, **136**:224108, (2012).

[209] K. S. Schweizer, and E. J. Saltzman. Entropic barriers, activated hopping, and the glass transition in colloidal suspensions. *J. Chem. Phys.*, **119**:1181, (2003).

[210] K. S. Schweizer. Derivation of a microscopic theory of barriers and activated hopping transport in glassy liquids and suspensions. *J. Chem. Phys.*, **123**:244501, (2005).

[211] H. E. Stanley, S. V. Buldyrev, M. Canpolat, O. Mishima, M. R. Sadr-Lahijany, A. Scala, and F. W. Starr. The puzzling behavior of water at very low temperature. *Phys. Chem. Chem. Phys.*, **2**:1551, (2000).

[212] P. H. Poole, F. Sciortino, T. Grande, H. E. Stanley, and C. A. Angell. Effect of hydrogen bonds on the thermodynamic behavior of liquid water. *Phys. Rev. Lett.*, **73**:1632, (1994).

[213] S. S. Borick, P. G. Debenedetti, and S. A. Sastry. A lattice model of network-forming fluids with orientation-dependent bonding: equilibrium, stability, and implications from the phase behavior of supercooled water. *J. Phys. Chem.*, **99**:3781, (1995).

[214] L. Xu, P. Kumar, S. V. Buldyrev, S.-H. Chen, P. H. Poole, F. Sciortino, and H. E. Stanley. Relation between the widom line and the dynamic crossover in systems with a liquid–liquid phase transition. *PNAS*, **102**:16558, (2005).

[215] J. L. F. Abascal and C. Vega. Widom line and the liquid-liquid critical point for the tip4p/2005 water model. *J. Chem. Phys.*, **133**:234502, (2010).

[216] P. Gallo, M. Rovere, and S.-H. Chen. Dynamic crossover in supercooled confined water: Understanding bulk properties through confinement. *J. Phys. Chem. Lett.*, **1**:729, (2010).

[217] D. T. Limmer and D. Chandler. The putative liquid-liquid transition is a liquid-solid transition in atomistic models of water. *J. Chem. Phys.*, **135**:134503, (2011).

[218] J. C. Palmer, F. Martelli, Y. Liu, R. Car, A. Z. Panagiotopoulos, and P. G. Debenedetti. Metastable liquid-liquid transition in a molecular model of water. *Nature*, **510**:385, (2014).

[219] E. Duboue-Dijon, and D. Laage. Characterization of the local structure in liquid water by various order parameters. *J. Phys. Chem. B*, **119**:8406, (2015).

[220] E. Lascaris, M. Hemmati, S. V. Buldyrev, H. E. Stanley, and C. A. Angell. Search for a liquid-liquid critical point in models of silica. *J. Chem. Phys.*, **140**:224502, (2014).

[221] P. H. Poole, F. Sciortino, U. Essmann, and H. E. Stanley. Computer simulations of liquid silica: water-like thermodynamic and dynamic anomalies, and the evidence for polyamorphism. *Liquid Polyamorphism*, **152**:373, (2013).

[222] E. Lascaris, M. Hemmati, S. V. Buldyrev, H. E. Stanley, and C. A. Angell. Diffusivity and short-time dynamics in two models of silica. *J. Chem. Phys.*, **142**:104506, (2015).

[223] E. F. Burton, and W. F. T. Oliver. The crystal structure of ice at low temperatures. *Proc. R. Soc. Lond. A*, **153**:166, (1936).

[224] P. Br"uggeller, E. Mayer. Complete vitrification in pure liquid water and dilute aqueous solutions. *Nature*, **288**:569, (1980).

[225] J. Dubochet, and W. A. McDowall. vitrification of pure water for electron microscopy. *J. Microsc.*, **124**:RP3, (1981).

[226] O. Mishima, L. D. Calvert, and E. Whalley. Melting ice i at 77 k and 10 kbar: a new method of making amorphous solids. *Nature*, **310**:393, (1984).

[227] O. Mishima. Relationship between melting and amorphization of ice. *Nature*, **384**:546, (1996).

[228] R. J. Hemley, L. C. Chen, and H. K. Mao. New transformations between crystalline and amorphous ice. *Nature*, **338**:638, (1989).

[229] J. N. Israelachvili. *Intermolecular and surface forces-3rd Ed.* Elsevier, (2011).

[230] J. Geske, and M. Vogel. Creating realistic silica nanopores for molecular dynamics simulations. *Mol. Simulat.*, (2016).

[231] J.-R. Hill, and J. Sauer. Molecular mechanics potential for silica and zeolite catalysts based on ab initio calculations. 1. dense and microporous silica. *J. Phys. Chem.*, **98**:1238, (1994).

[232] M. A. Gonzalez, and J. L. F. Abascal. The shear viscosity of rigid water models. *J. Chem. Phys.*, **132**:096101, (2010).

[233] M. De Marzio, G. Camisasca, M. Rovere, and P. Gallo. Mode coupling theory and fragile to strong transition in supercooled tip4p/2005 water. *J. Chem. Phys.*, **144**:074503, (2016).

[234] W. Humphrey, A. Dalke, and K. Schulten. Vmd: Visual molecular dynamics. *J. Mol. Graphics*, **14**:33, (1996).

[235] R. Seemann, S. Herminghaus , C. Neto, S. Schlagowski , D. Podzimek, R. Konrad , H. Mantz, and K. Jacobs. Dynamics and structure formation in thin polymer melt films. *J. Phys. Condens. Matter.*, **17**:267, (2005).

[236] S. Forg. A molecular dynamics study of water and octanol confined in a silica nanopore. Master's thesis, Technische Universität Darmstadt, (2017).

[237] L. D. Schuler, X. Daura, and W. F. van Gunsteren. An improved gromos96 force field for aliphatic hydrocarbons in the condensed phase. *J. Comput. Chem.*, **22**:1205, (2001).

[238] W. L. Jorgensen, D. S. Maxwell, and J. J. Tirado-Rives. Development and testing of the opls all-atom force field on conformational energetics and properties of organic liquids. *J. Am. Chem. Soc.*, **118**:11225, (1996).

[239] C. A. Angell, and H. Kanno. Density maxima in high-pressure supercooled water and liquid silicon dioxide. *Science*, **193**:1121, (1976).

[240] P. Debenedetti. *Metastable Liquids: Concepts and Principles, Physical chemistry: science and engineering*. Princeton University Press, (1996).

[241] A. Bormuth. *Untersuchung der polymerdynamik in abhängigkeit von kettenlänge, temperatur und druck mit hilfe von molekulardynamik simulationen*. PhD thesis, TU Darmstadt, (2012).

[242] R. Brückner. Properties and structure of vitreous silica. i. *J. Non-Cryst. Solids*, **5**:123, (1970).

[243] K. T. Wikfeldt, A. Nilsson, and L. G. M. Pettersson. Spatially inhomogeneous bimodal inherent structure of simulated liquid water. *Phys. Chem. Chem. Phys.*, **13**:19918, (2011).

[244] J. C. Mikkelsen. Self-diffusivity of network oxygen in vitreous sio_2. *Appl. Phys. Lett.*, **45**:1187, (1984).

[245] G. Brebec, R. Seguin, C. Sella, J. Bevenot, and J. Martin. Diffusion du silicium dans la silice amorphe. *Acta Metallurgica*, **28**:327, (1980).

[246] P. Richet, and Y. Bottinga. Glass transitions and thermodynamic properties of amorphous sio_2, $naalsi_no_{2n+2}$ and $kalsi_3o_8$. *Geochim. Cosmochim. Acta*, **48**:453, (1984).

[247] J. D. Mackenzie. High-pressure effects on oxide glasses: I, densification in rigid state. *J. Am. Ceram. Soc*, **47**:76, (1963).

[248] V. N. Novikov, Y. Ding, and A. P. Sokolov. Correlation of fragility of supercooled liquids with elastic properties of glasses. *Phys. Rev. E*, **71**:061501, (2005).

[249] D. S. Simmons, M. T. Cicerone, Q. Zhong, M. Tyagi, and J. F. Douglas. Generalized localization model of relaxation in glass-forming liquids. *Soft Matter*, **8**:11455, (2012).

[250] B. A. P. Betancourt, P. Z. Hanakata, F. W. Starr, and J. F. Douglas. Quantitative relations between cooperative motion, emergent elasticity, and free volume in model glass-forming polymer materials. *Proc. Natl. Acad. Sci. U. S. A.*, **112**:2966, (2015).

[251] J. F. Douglas, B. A. P. Betancourt, X. Tong, and H. Zhang. Localization model description of diffusion and structural relaxation in glass-forming cu–zr alloys. *J. Stat. Mech.: Theory Exp.*, **2016**:050048, (2016).

[252] K. Becker. One century of radon therapy. *Int. J. Low Radiat.*, **1**:333, (2004).

[253] B. E. Erickson. The therapeutic use of radon: a biomedical treatment in europe; an alternative remedy in the united states. *Dose-Response*, **5**:48, (2007).

[254] J. H. Harley, E. S. Jetter, and N. Nelson. Elimination of radon from the body. *Environ. Int.*, **20**:573, (1994).

[255] A. Geiger, A. Rahman, and F. H. Stillinger. Molecular dynamics study of the hydration of lennard-jones solutes. *J. Chem. Phys.*, **70**:263, (1979).

[256] A. Filipponi, D. T. Bowron, C. Lobban, and J. L. Finney. Structural determination of the hydrophobic hydration shell of kr. *Phys. Rev. Lett.*, **79**:1293, (1997).

[257] R. D. Broadbent and G. W. Neilson. The interatomic structure of argon in water. *J. Chem. Phys.*, **100**:7543, (1994).

[258] T. P. Straatsma, H. J. C. Berendsen, and J. P. M. Postma. Free energy of hydrophobic hydration: A molecular dynamics study of noble gases in water. *J. Chem. Phys.*, **85**:6720, (1986).

[259] W. C. Swope and H. C. Andersen. A molecular dynamics method for calculating the solubility of gases in liquids and the hydrophobic hydration of inert-gas atoms in aqueous solution. *J. Phys. Chem.*, **88**:6548, (1984).

[260] K.D. Collins. Charge density-dependent strength of hydration and biological structure. *Biophys. J.*, **72**:65, (1997).

[261] K. Stroh. In silico untersuchung des ionentransports in peptidfunktionalisierten nanoporen. Master's thesis, Technische Universität Darmstadt, (2017).

[262] Y. Luo and B. Roux. Simulation of osmotic pressure in concentrated aqueous salt solutions. *J. Phys. Chem. Lett.*, **1**:183, (2009).

[263] J. Aqvist. Ion-water interaction potentials derived from free energy perturbation simulations. *J. Phys. Chem.*, **94**:8021, (1990).

[264] S. Clifford, K. Bolton, and D. Ramjugernath. Monte carlo simulation of carboxylic acid phase equilibria. *J. Phys. Chem. B*, **110**:21938, (2006).

[265] C. Kittel. *Introduction to Solid State Physics, 8th Edition*. (2004).

[266] B. N. Srivastava and S. C. Saxena. Generalised relations for the thermal diffusion factor of inert gas mixtures with one invariable constituent. *Physica*, **22**:253, (1956).

[267] G. A. Miller. The intermolecular force constants of radon. *J. Phys. Chem.*, **64**:163, (1960).

[268] P. K. Chakraborti. Intermolecular potential of radon. *J. Chem. Phys.*, **44**:3137, (1966).

[269] R. Gopal. On intermolecular lennard-jones potential energy parameters for radon. *J. Indian Chem. Soc.*, **39**:791, (1962).

[270] S. Zakaria, D. Gay, J. Guillevic, and R. Améon. Eos7rn: a new tough2 module for simulating radon emanation and transport in the subsurface. *Comput. Geosci.*, **65**:72, (2014).

[271] R. Shi, and H. Tanaka. Impact of local symmetry breaking on the physical properties of tetrahedral liquids. *PNAS*, **115**:1980, (2018).

[272] S. Franz, and A Montanari. Analytic determination of dynamical and mosaic length scales in a kac glass model. *J. Phys. A: Math. Theor.*, **40**:F251, (2007).

Publications by the author

1. E. Pafong, J. Geske and B. Drossel, on the influence of the intermolecular potential on the wetting properties of water on silica surfaces, The Journal of Chemical Physics, (2016), vol. 145, pp. 114901; DOI:10.1063/1.4962516.

2. E. Pafong Sanjon, B. Drossel and M. Vogel, Effects on the bond polarity on the structural and dynamical properties of silica like-liquids, The Journal of Chemical Physics, (2018), vol. 148, pp. 104506; DOI:10.1063/1.5017681.

3. B. Kumari, M. Brodrecht, M.Werner, B. Grünberg, H.-H. Limbach, S. Forg, E. P. Sanjon, B. Drossel, T. Gutmann and G. Buntkowsky, Mixtures of Alcohols and Water confined in Mesoporous Silica: A Combined Solid-State NMR and Molecular Dynamics Simulation Study, The Journal of Physical Chemistry C,(2018), vol. 122, pp. 19540; DOI: 10.1021/acs.jpcc.8b04745.

4. E. P. Sanjon, A. Maier, A. Hinrichs, G. Kraft, B. Drossel and C. Fournier, Molecular dynamic simulation and measurement of radon solubility in fatty acids and isotone solution, submitted.

5. R. Horstmann, E. P. Sanjon, B. Drossel and M. Vogel, Dynamic and static length scales in tetrahedral liquids in confinement, in preparation.

Curriculum vitae

Date and place of Birth

18.08.1989 Yaounde, Cameroon

University Education

March 2015 - October 2018 Doctorate Physics (TU Darmstadt)

October 2012 - May 2014 M.Sc. Physics (University Stuttgart)

September 2010 - August 2012 Diploma in condensed matter physis in ICTP (International centre of theoretical physics in Trieste, Italy)

September 2009 - August 2010 First year M.Sc. Mechanics and materials, University of Yaounde 1, Cameroon

September 2006 - August 2009 B.Sc. Physics University of Yaounde 1, Cameroon

School Education

2003 - 2006 Baccalauréat in Mathematics and Physics, Biyem-Assi High school in Yaounde, Cameroon

Acknowledgments

I would like to thank all those people of the physics department at the TU Darmstadt who have assisted and supported me during my studies at the TU Darmstadt.

A very special gratitude goes to my supervisor Prof. Barbara Drossel for the continuous support, for her patience, enthusiasm, and immense knowledge during my doctoral studies. Her guidance and recommendations have helped me during the research time. Honestly, I could have not dreamed up having a better mentor for my doctoral study.

I am also grateful to Prof. Michael Vogel for his unfailing willing for advising during our MD meetings. He was always available for discussions and for providing new interesting ideas and comments for the thesis. It was really a nice experience to collaborate with him.

I would also like to thank Dr. Julian Geske who was already well experienced with the topics of glass transition and MD techniques at the beginning of my doctoral studies. His critical opinions and comments during our discussions were always helpful. We have collaborated in the project of water in silica pore, and its initial works on silica in bulk and in neutral confinements have been very useful for me to proceed with the work.

I would also like to thank my colleagues in the Drossel working group and also Vogel working group. With a special mention to Robin Horstmann for nice exchanging and our ongoing collaboration on the project of silica and water in neutral confinements, to Sandra Forg which has worked on the initial steps of the water/octanol project under my supervision; to Julian Geske, Robin Horstmann and Andreas Brechtel who have corrected my thesis.

I would also thank the DFG for grant FOR 1583, and our working groups admins, Markus Rosenstihl, Christian Kolb, Philipp Gramlich and Johannes Falk who did and are still continuously performing a great job for improving our computer systems and enabling us to actually do any MD calculations.

I am also grateful to my parents who have always advised and supported me in my decisions in life. My father who has taught me during my high school studies and specially my mother who is continually supporting me spiritually throughout my life; lately she has always been available for helping me with the kids. Many thanks to my lovely younger sister Ariane Mbekwe and my brothers which are always encouraging me.

Finally, I would like to address a grateful thanks to my best friend and husband Cedric Sanjon who has been encouraging me, inspiring me, motivating me and taking care of our two sons Jake and Isaac Sanjon when I had to concentrate on my thesis. I am indebted to him for helping me in correcting thesis drafts and for the countless conversations and debates about my work. I would have never achieved this work without his immense support, this is basically a joint achievement. At my two baby boys Isaac and Jake, thanks for giving me strengths and energies to move forward in my dreams and for bringing a smile to my heart. I dedicate this work to you.